(NASA-CR-120466)   DEVELOPMENT AND TESTING   N74-33950
OF LASER DOPPLER SYSTEM COMPONENTS FOR
WAKE VORTEX MONITORING.   VOLUME 1:
SCANNER DEVELOPMENT, (Lockheed Missiles   Unclas
and Space Co.)   190 p   50 CSCL 14B   G3/14   49796

PRICES SUBJECT TO CHANGE

Lockheed

HUNTSVILLE RESEARCH & ENGINEERING CENTER

LOCKHEED MISSILES & SPACE COMPANY, INC.
A SUBSIDIARY OF LOCKHEED AIRCRAFT CORPORATION

HUNTSVILLE, ALABAMA

LOCKHEED MISSILES & SPACE COMPANY, INC.

HUNTSVILLE RESEARCH & ENGINEERING CENTER

HUNTSVILLE RESEARCH PARK

4800 BRADFORD DRIVE, HUNTSVILLE, ALABAMA

DEVELOPMENT AND TESTING
OF LASER DOPPLER SYSTEM
COMPONENTS FOR WAKE
VORTEX MONITORING

VOLUME I

SCANNER DEVELOPMENT,
LABORATORY AND FIELD TESTING
AND SYSTEM MODELING

August 1974

Contract NAS8-29824

by

D. J. Wilson
M. C. Krause
E. W. Coffey
C-C. Huang
B. B. Edwards
K. R. Shrider
J. L. Jetton
L. K. Morrison

APPROVED: _____

J. S. Farrior
Resident Director

FOREWORD

Lockheed Missiles & Space Company, Inc., Huntsville Research & Engineering Center, conducted the effort reported herein under Contract NAS8-29824 for the National Aeronautics and Space Administration, George C. Marshall Space Flight Center.

The work was performed during the period May 1973 through August 1974. The NASA contracting officer's representatives for this contract are Mr. James W. Bilbro and Mr. Harold B. Jeffreys, alternate.

CONTENTS

Section 1
INTRODUCTION AND SUMMARY

In May 1973, Lockheed-Huntsville received a contract from NASA-MSFC to: (1) develop a servo-controlled scanner for NASA's Laser Doppler Velocimeter (LDV); (2) to perform certain field tests of LDV components; and (3) to develop a mathematical model of the scanning LDV interacting with aircraft-generated vortices. In December 1973, the contract was expanded to cover additional testing, certain hardware modifications and complete scanner manual development. Again in June 1974, the contract was expanded to include mechanical service testing at the MSFC test site and to perform planning for operation at a remote site.

Lockheed developed three range and elevation scanners — one set for each of three MSFC LDV units — and installed these subsystems at MSFC in late 1973 and early 1974. The elevation scanners provide a capability to manually point the LDV telescope at operator chosen angles from 3.2 to 89.6 degrees within 0.2 degrees or to automatically scan the units between operator chosen limits at operator chosen rates of 0.1 to 0.5 Hz. Likewise, the range scanners provide a capability to manually adjust the focal point of the system from a range of 32 meters to a range of 896 meters under operator control or to scan between operator chosen limits and at rates from 0.1 to 6.9 Hz. The range and elevation scanner controls are designed to allow simultaneous range and elevation scanning so as to provide finger scan patterns, arc scan patterns and vertical line scan patterns. The development and testing of these units are discussed in Section 2 of this volume and also in Volume II of this final report.

Numerous field and laboratory tests have been performed under this contract to evaluate vendor-provided components, to optimize marginal subsystems and to overcome unforseen hardware difficulties. Lockheed personnel

have tested numerous optical components and subassemblies of the LDV both in the field and in the laboratory. Lasers, interferometers and specific optical elements have been examined both independent of the system and while assembled into the system. Calculations and experiments have been performed to determine system efficiency from experimental and theoretical standpoints. Experiments were conducted along with analytical efforts to develop a practical means of reducing backscattered radiation from the secondary mirror of the telescope which previously saturated the detector and reduced the effectiveness of the Mach Zehnder interferometer. The translator, which earlier had been judged very inefficient, was shown to have promise of efficient operation with modifications. Spatial resolution of the system was measured both in the laboratory and in the field. A longer-than-expected spatial resolution was attributed to laser beam truncation by the telescope primary mirror. This truncation was also found to reduce system signal-to-noise ratio from hard targets at long ranges due to the increased size of the focal volume. However, system efficiency appeared quite adequate to detect wake vortices during numerous aircraft flybys at MSFC. Laboratory and field tests are discussed in Section 3 of this volume.

Lockheed developed a fluid dynamic model of the wake vortex and modeled the interaction of the laser system with the vortex. The fluid dynamic model of the vortex included such effects as the centrifugal force upon the particulate matter suspended in the vortex. The LDV model included the system spatial resolution and time of passage of particles through the focal volume. Details of this modeling effort are presented in Section 4.

Section 2

SCANNER DEVELOPMENT AND TESTING

Authors: E. W. Coffey
B. B. Edwards

Lockheed-Huntsville received a contract to fabricate three combination range-elevation scanners for the NASA-MSFC Laser Doppler System in May 1973. The units were delivered the following November, December and February. The units consisted of independent range and elevation servo systems with a digital control panel for each. The elevation scanners were designed to be pointed, using a manual mode, from 3.2 to 89 deg accurate to within 0.2 deg and scan in an automatic mode within operator chosen limits and at operator chosen rates from 0.1 to 0.5 Hz. The range scanners were likewise designed to be pointed manually from distances from 32 to 599 meters and scanned automatically between operator chosen limits and at rates from 0.1 to 6.9 Hz. Various operator designated inputs would program the units to perform finger scans, arc scans or coordinated line scans.

The details of scanner design and operator instructions are presented in Volume II, "Scanner Operations Manual," of this final report. However, a description of results of the acceptance tests plus additional tests performed on the scanners is presented in the following paragraphs. Section 2.1 presents the results of the acceptance test on unit 001. Section 2.2 presents the results of additional tests which were used to optimize the range calibration technique.

Tests referred to in this section as E-1, E-2, etc., refer to tests run to evaluate the "elevation" scanning capability of the unit. Tests referred to as R-1, R-2, etc., refer to tests run to evaluate the range scanning capability of the unit.

2.1 RESULTS OF ACCEPTANCE TEST ON LASER SCANNER 001

A description of the tests agreed upon as being suitable is given in the Appendix. This report presents the results obtained when these tests were carried out on unit 001, along with some comment as considered appropriate.

Test E-1

In this test the output of the D/A converter, which operates on the elevation command angle 12-bit word, was recorded on a strip chart with a known calibration. The front panel thumbwheel switch, which controls the upper limit of the auto-scan mode was advanced successively in 1-deg increments from 10 to 59 deg. The purpose of this test was to verify that the command word did, in fact, reverse direction when it reached an angle corresponding to the dialed-in upper limit, over the full range of variation of this variable. The other conditions of this test were:

    a. Mode: auto-scan, normal
    b. Lower limit: 0 deg
    c. Scan frequency: 0.1 Hz

The results are shown in Fig. 2-1. Note that the turnaround angles correspond exactly to those of Table A-1 of the Appendix. Since the computer, which senses when the upper limit has been reached, uses only the five most significant bits of the word it is evident that on the "up" cycle the command word corresponding to equality on the comparator for the first time will have all its lower order bits (7 through 1) equal to zero. All possible dialed-in upper limit angles having identical structure in bits 12 through 8 will thus produce the same effect on the command word, despite the fact that they represent different angles. This truncation effect* creates the "plateaus" in the input/output table of Fig. 2-1.
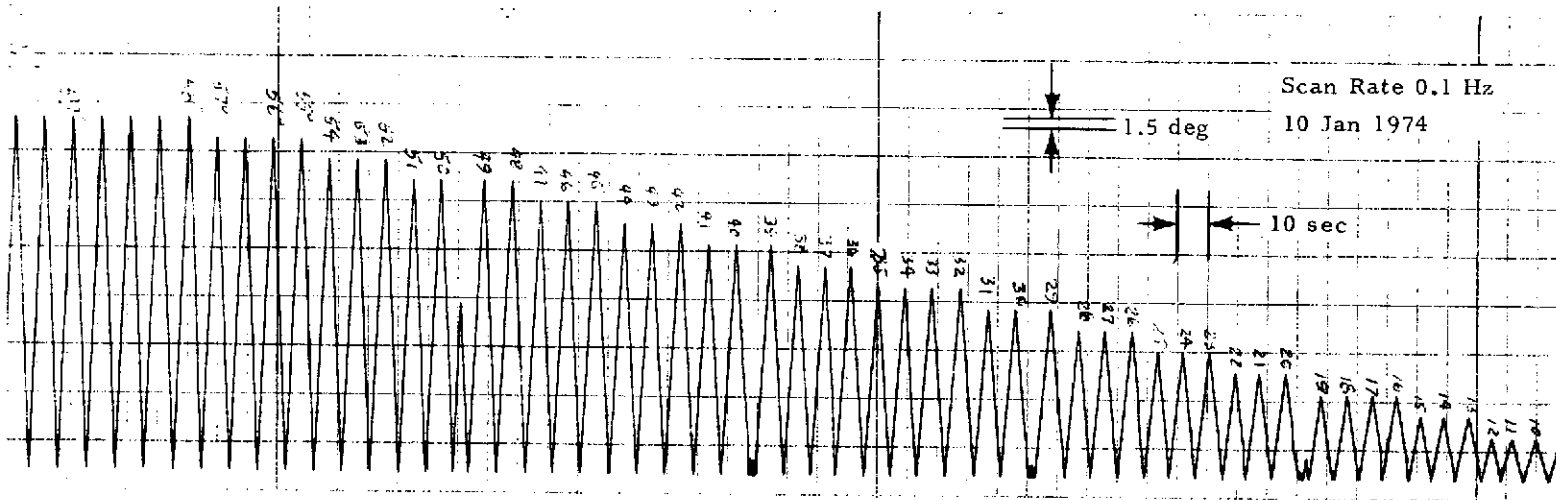
---

*The system has since been modified to reduce truncation effects.
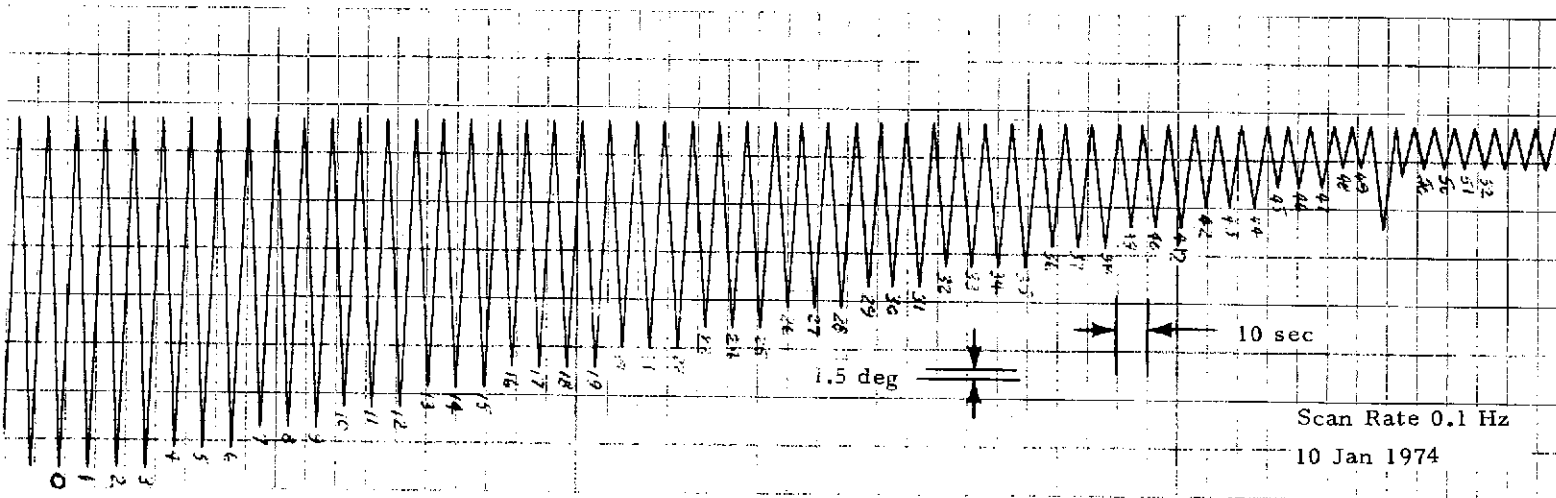
Fig. 2-1 - Elevation Angle Upper Limit Test

Fig. 2-2 - Elevation Angle Lower Limit Check

Test E-2

This test was identical to E-1 with the roles of upper and lower limit interchanged. The results are shown in Fig. 2-2. As expected, complete conformity to the input/output characteristic of Table A-2 of the Appendix was obtained. (We observe that the command word on the "down" angle will, when the equality condition on bits 12 through 8 is met for the first time, have all the lower order bits (7 through 1) in the "high" condition, creating the "staircase" effect of Table A-2. The actual scan will always be "inside" the dialed-in limit values.)

Test E-3

In this test the scanner was made to execute the normal auto-scan function in elevation between six conditions of upper and lower limits as shown in Table A-3, with five (the complete set) selected scan frequencies in each distinct upper/lower limit condition. The purpose was to verify that the logic, which is supposed to vary the counter clock rate to achieve the same dialed-in scan frequency for any condition of limit boundaries (i.e., for any scan excursion) was, in fact, accomplishing this. The recorded command-word cycle behavior is shown in Figs. 2-3-1 through 2-3-6. The scan frequency was computed from the known chart speed, with results as shown in Table 2-1. Note that all the frequencies have a slight bias toward high values. This arises from the truncation effect mentioned in Tests E-1 and E-2. The control logic uses the entire 12-bit upper and lower limit words (and the 4-bit BCD scan frequency control word) to compute and generate the appropriate counter clock rate, but the scan turn-around occurs automatically between the limits set by the 5-bit comparators. Since this excursion is always "inside" the true one (i.e., smaller), the rate is slightly high. It was agreed that this effect was acceptably small. (The bias-in rate could, if desired, be split ($\pm$) to have the correct average value by a minor hard-wire change in the fixed rate multiplier, which is now set at 12/64 ratio.)
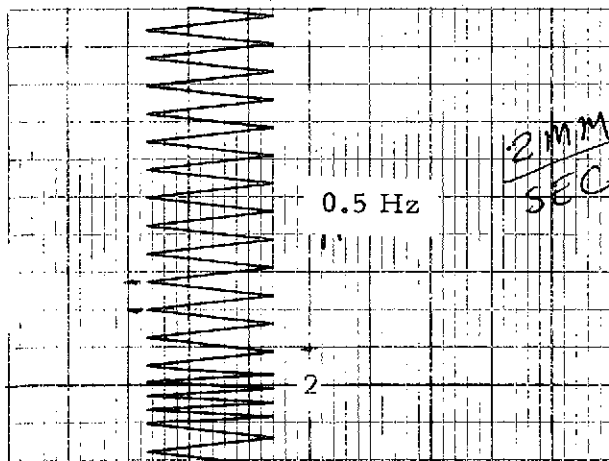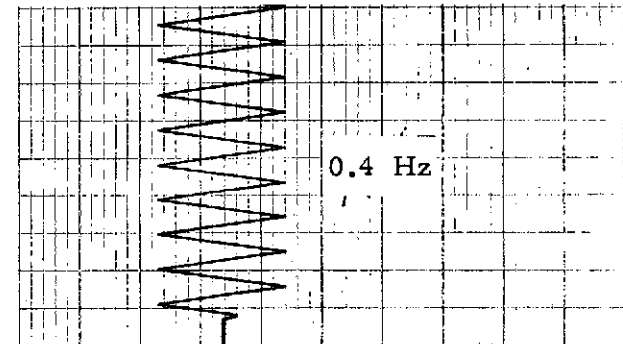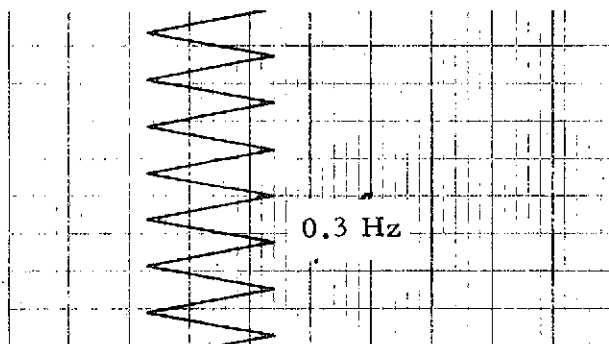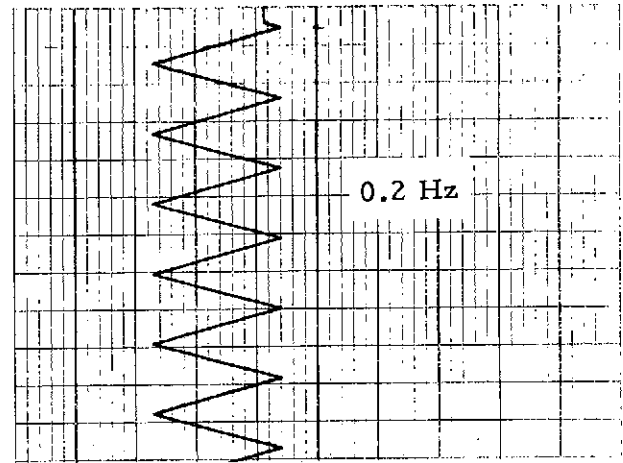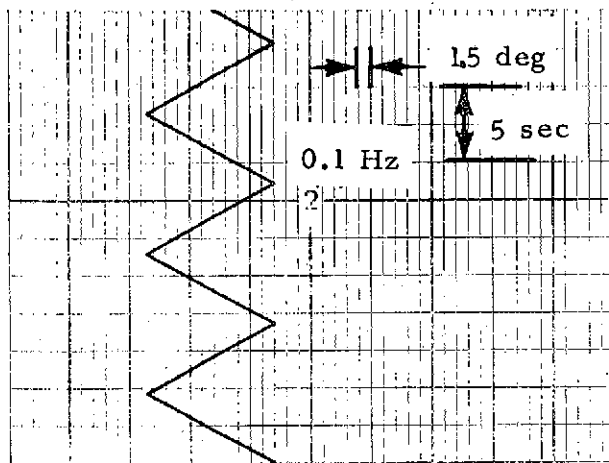
Fig. 2-3-1 - Scan Frequency Test (Elevation Scanner Between 58 and 41 deg)

1.5 deg

5 sec

0.1 Hz

0.2 Hz

0.3 Hz

0.4 Hz

0.5 Hz

NOTE: Time scale is
identical on all
figures.
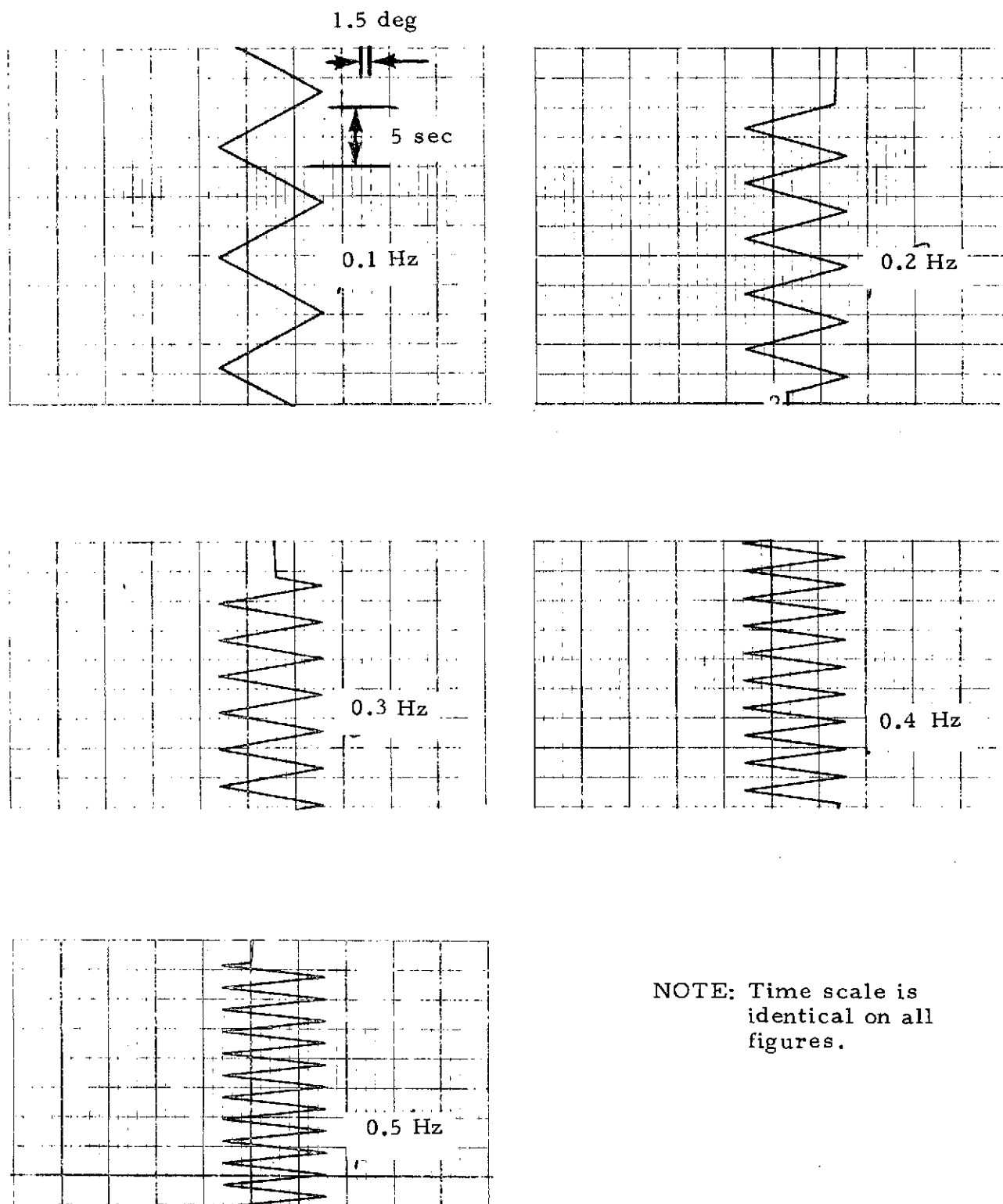
Fig. 2-3-2 - Scan Frequency Test (Elevation Scanner Between 42 and 25 deg)
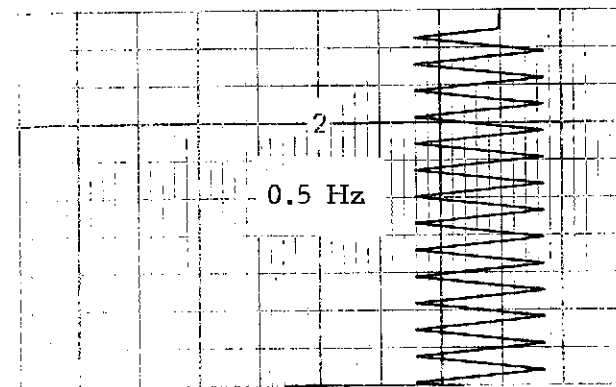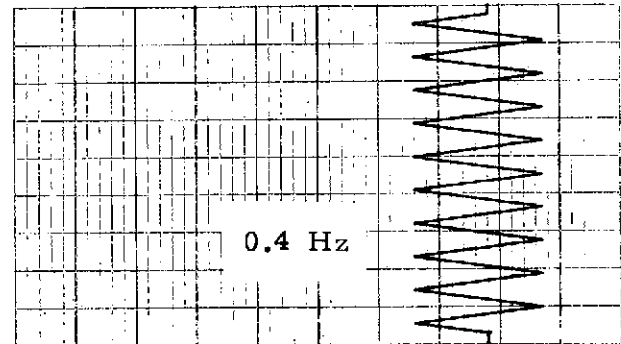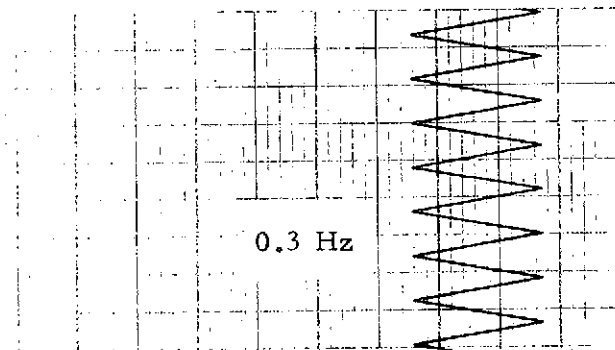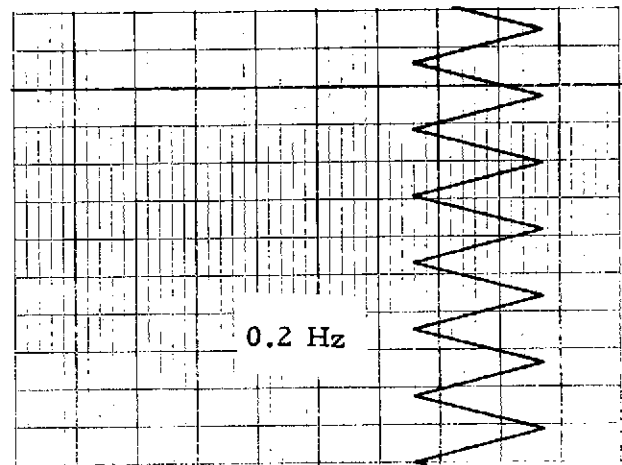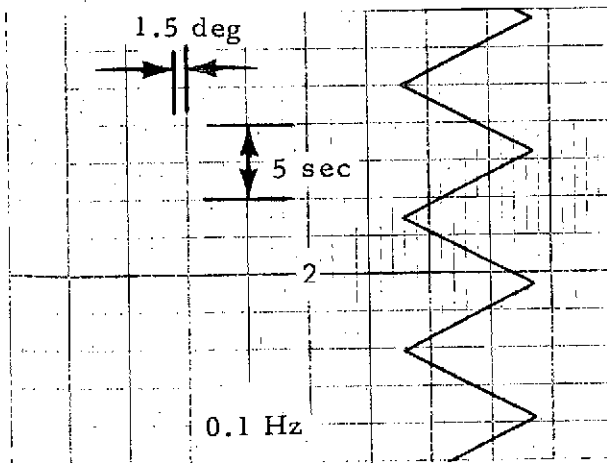
NOTE: Time scale is identical
on all figures.

Fig. 2-3-3 - Scan Frequency Test (Elevation Scanner Between 26 and 8 deg)
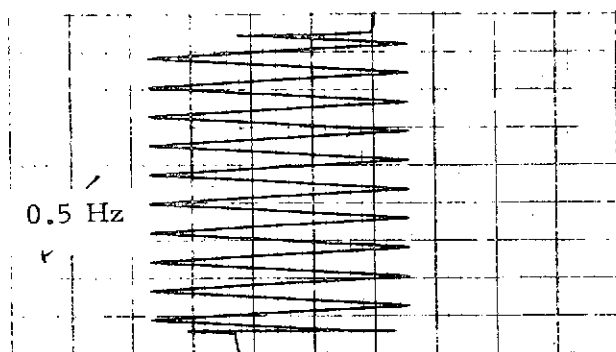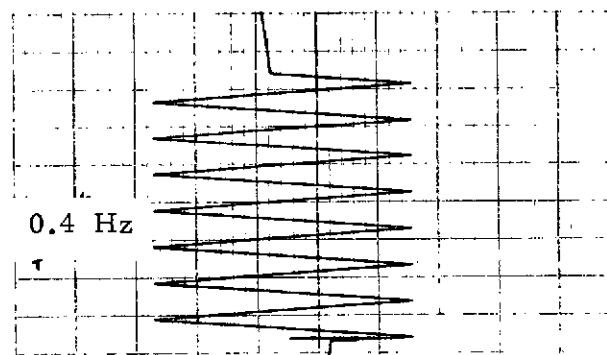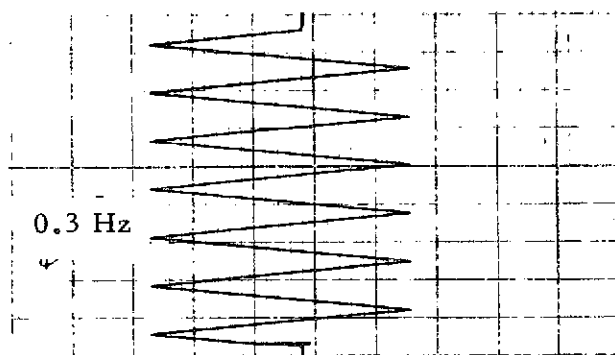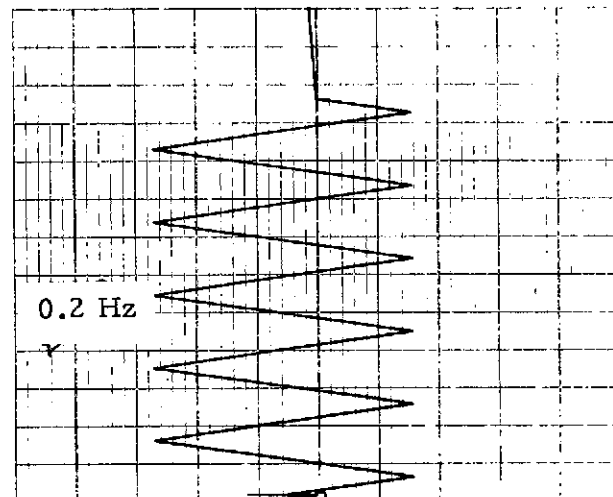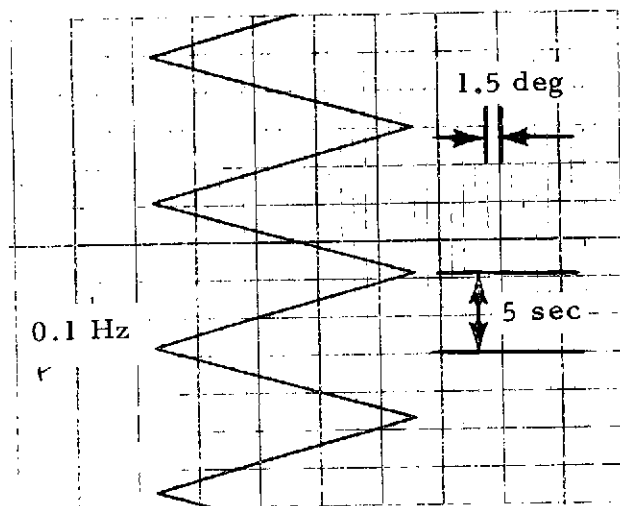
Fig.2-3-4 - Scan Frequency Test (Elevation Scanner Between 58 and 25 deg)

10
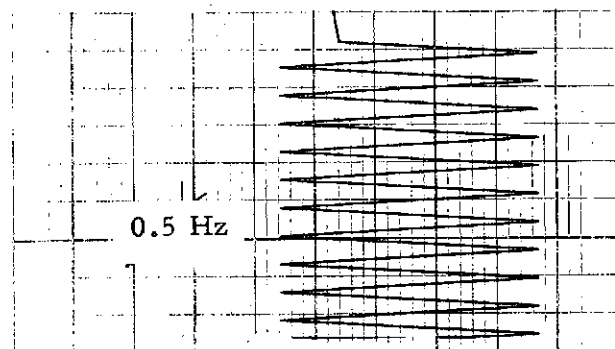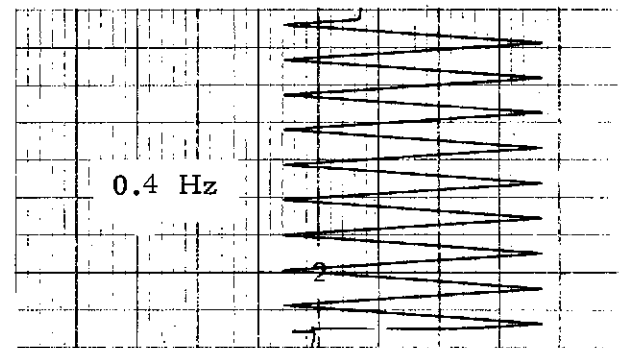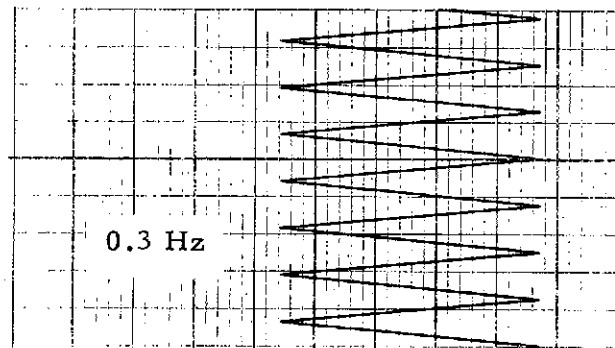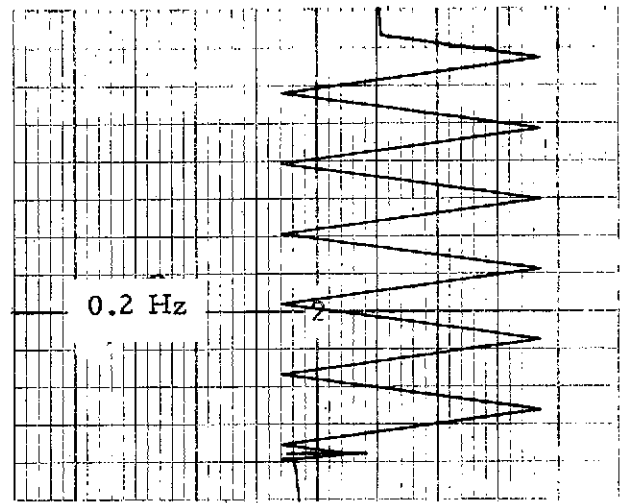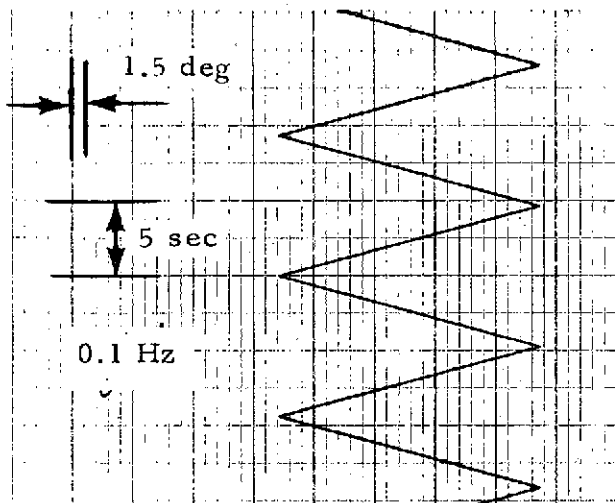
NOTE: Time scale is identical
on all figures.

Fig. 2-3-5 - Scan Frequency Test (Elevation Scanner Between 42 and 8 deg)

11
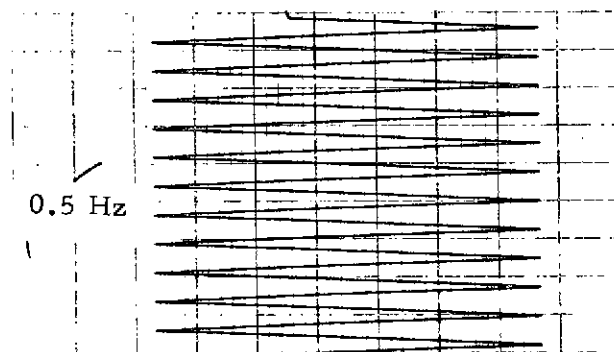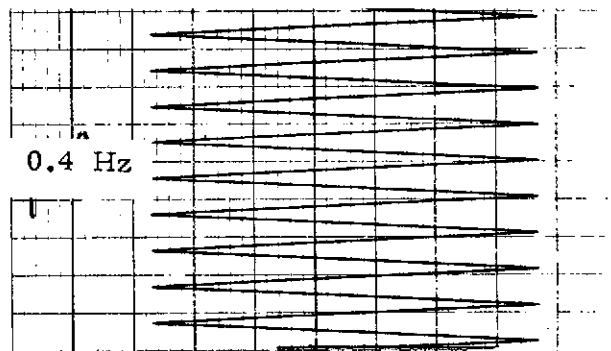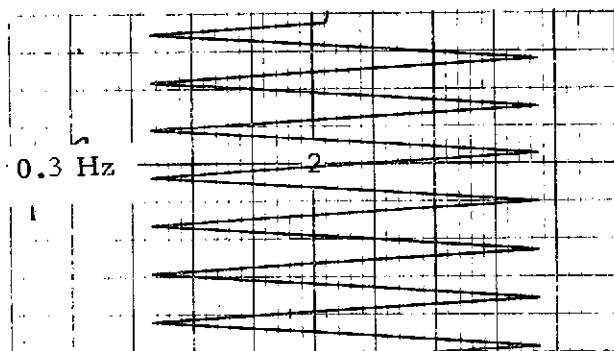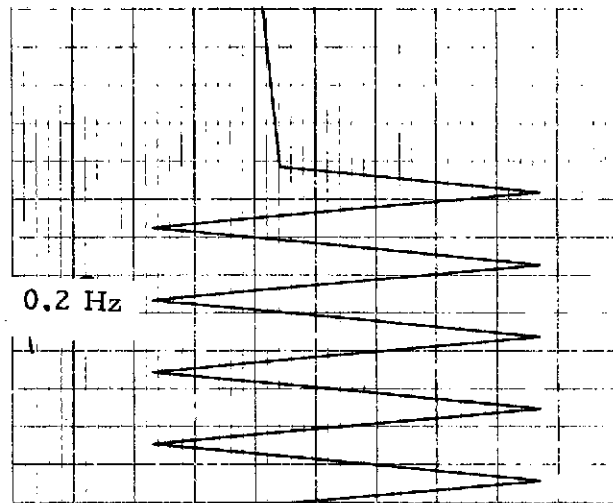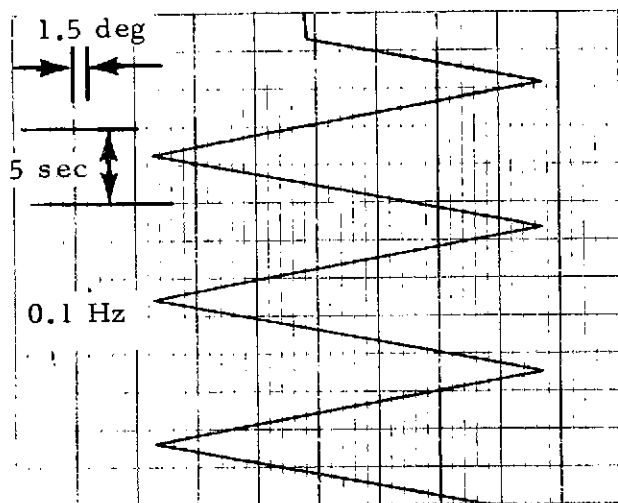
Fig.2-3-6 - Scan Frequency Test (Elevation Scanner Between 58 and 9 deg)

Table 2-1

MEASURED SCAN RATES OF TEST E3

Angle Designation	Excursion Limits (deg)	Scan Rates (Hz)				
		0.1	0.2	0.3	0.4	0.5
A	58-41	0.1065	0.216	0.32	0.430	0.534
B	42-25	0.107	0.211	0.32	0.434	0.527
C	26-8	0.113	0.224	0.337	0.445	0.565
D	58-25	0.104	0.206	0.315	0.415	0.515
E	42-8	0.107	0.213	0.32	0.427	0.54
F	58-8	0.107	0.208	0.306	0.419	0.524

Test E-4

The purpose of this test was to ascertain that the anti-crossover logic was operating correctly. This logic is constructed so as to substitute, for the dialed-in lower scan limit, a new limit equal to the (actual) upper limit minus 9.6 deg, whenever the difference between the upper limit and the dialed-in lower limit is less than 9.6 deg (and particularly whenever the dialed-in lower limit is larger than the upper limit, i.e., crosses over). The test consisted of setting the upper limit at three different values and, for each value, moving the lower limit in successive steps toward and beyond the (fixed) upper limit while recording the actual scan excursion. Figures 2-4-1 and 2-4-2 show the results, i.e., the lower limit approaching the θ_{ul} - 9.6 deg value[*] and staying there, thus demonstrating the correct operation.

Test E-5

The purpose of this test was to demonstrate correct operation of the manual mode slewing function and the single increment capability. This was done by:

  a. Operating both the fast and slow slewing through the full range and recording the command voltage to show the slew rate and automatic top and bottom limiting, and

  b. Depressing the "single increment" button a large number of times in succession in both the up and down directions and recording the successive step increments in the command word on a calibrated scale to show the step size.

The results are shown in Figs. 2-5-1 and 2-5-2. The slew rates were within 10% of their design values (34 deg/sec and 3.4 deg/sec, and automatically limited at 89 deg and 3.2 deg as required.

---

[*]In certain instances the 5-bit truncation effect is in evidence on θ_{ul} - 9.6 deg.
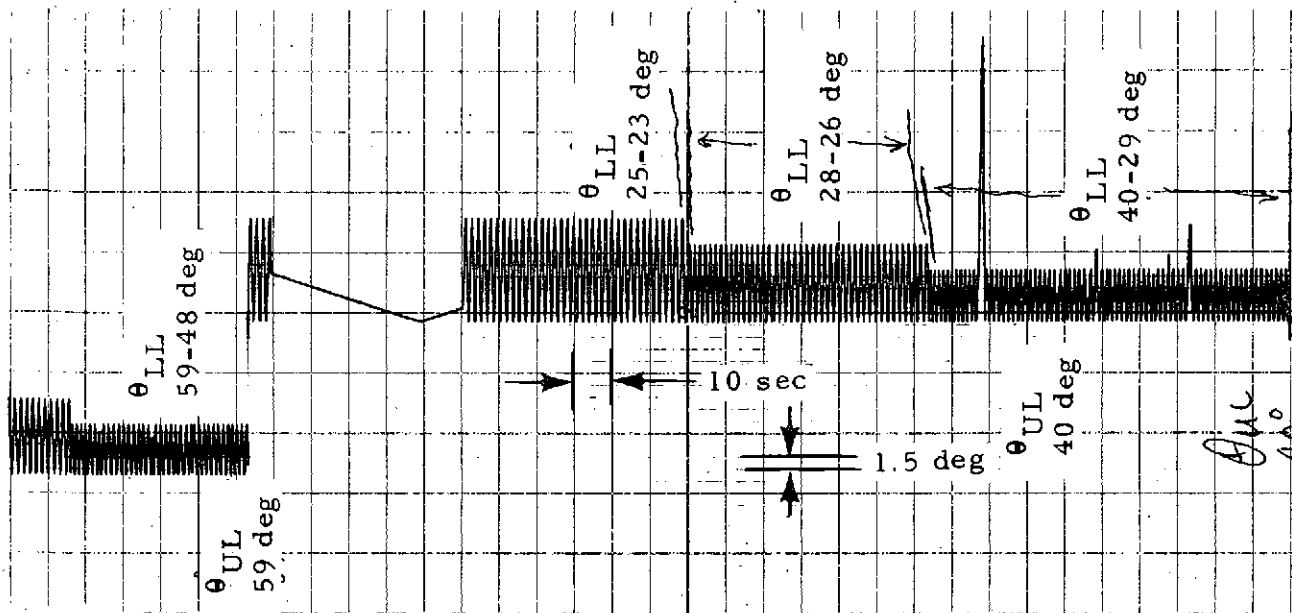
Fig. 2-4-1 - Elevation Crossover Test — 16 January 1974
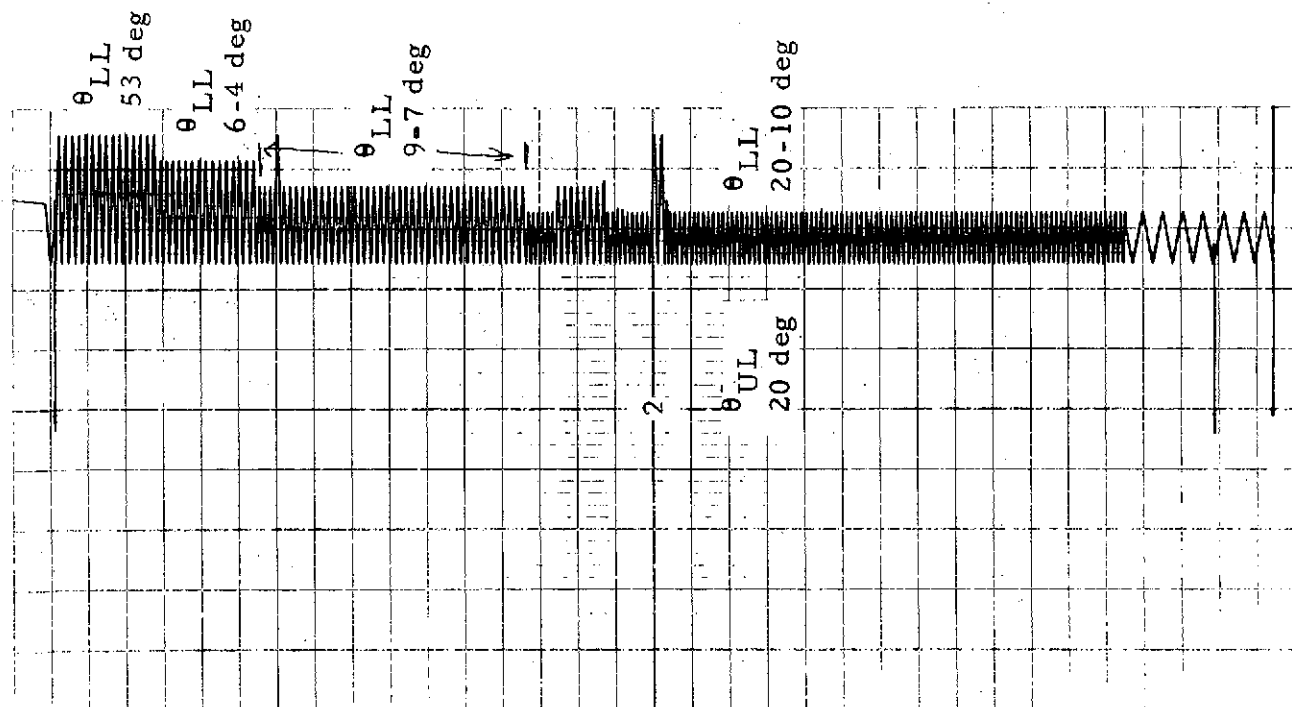
Fig. 2-4-2 - Crossover Test Continued
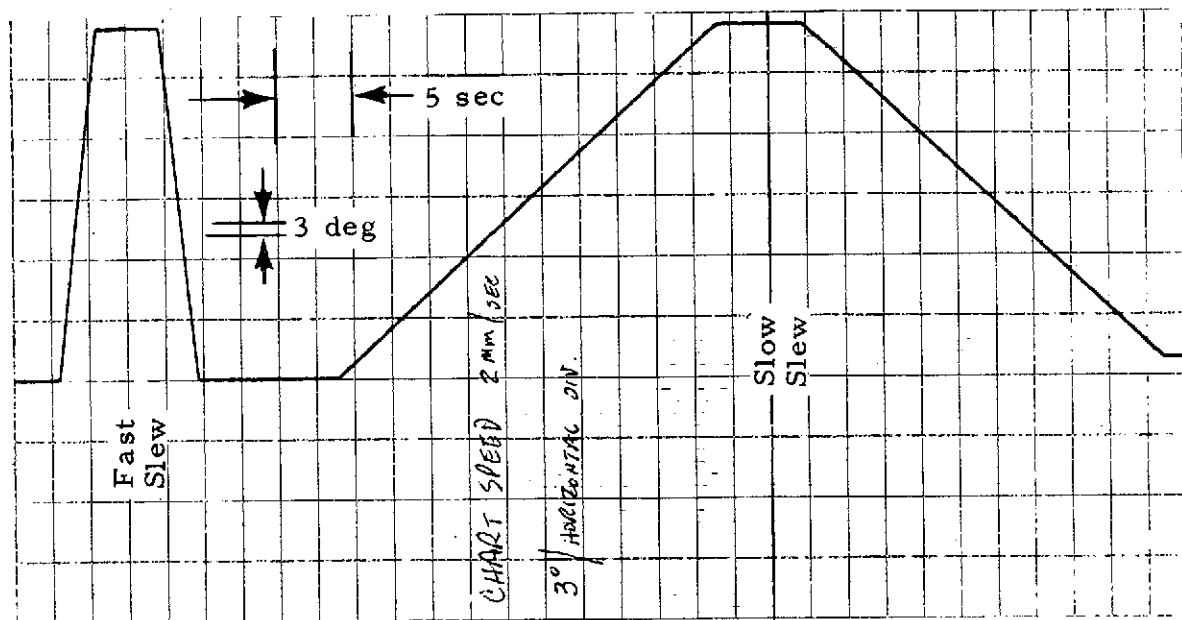
Fig. 2-5-1 - Slew Rate and Automatic Limiting Checks
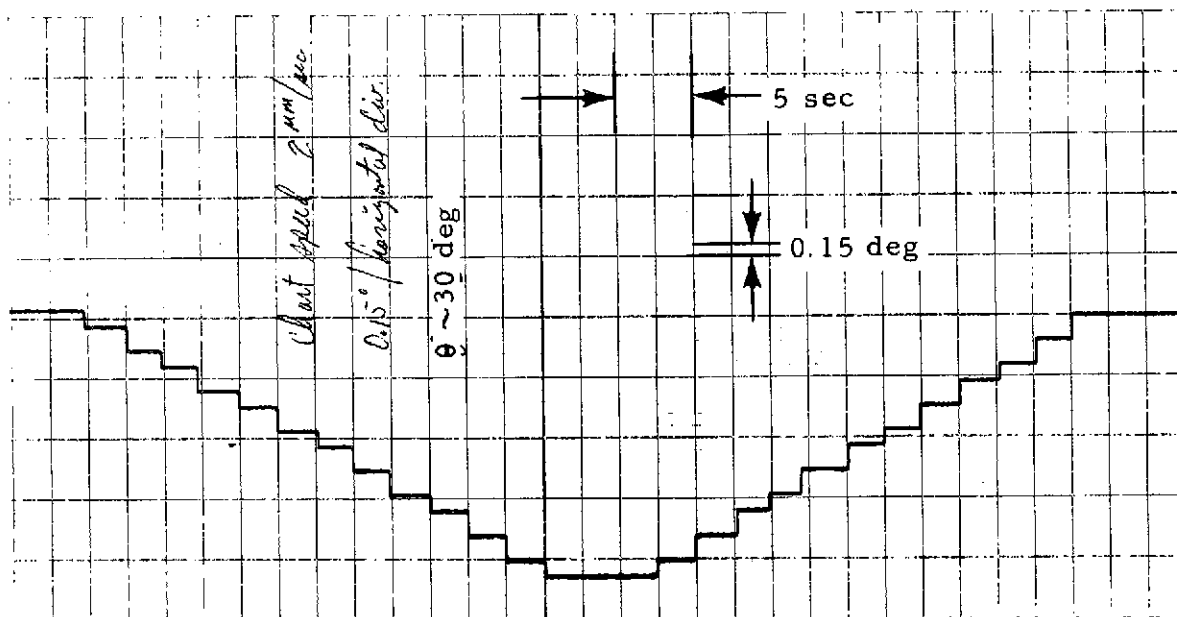
Fig. 2-5-2 - Incremental Step Size Check

The single increment operation occasionally yielded steps greater than the design value of 0.2 deg, indicating that the one-shot gate controlling this operation is slightly longer than it should be, but was considered acceptable.

Test E-6

The purpose of this test was to demonstrate the proper operation of the sector scan mode. In this mode the scan limits for the automatic mode are derived from a pair of 8-bit counters. One of these counters controls the spread between the upper and lower limits, moving both symmetrically toward or away from a center value, while the second moves the center value up or down across the elevation domain.

While the controls exhibited all the correct functions, it was clear that the slew rates used in the design were too fast, and this test was deferred pending a decision on proper slew rates.[*] The rates can easily be reduced by a factor of 10 by minor modifications to the card containing the clock generation circuitry.

Tests R-1 Through R-6

These tests were identical to their elevation counterparts, mutatis mutandis.[**] Since the circuitry is identical, acceptable performance by one confirms acceptable performance by the other.

The following series of tests was made to ascertain the static and dynamic accuracy of the servo systems.

_____

[*] Slew rates have been decreased.

[**] The range scale factor in meters is ten times that of the elevation variable in degrees, and the scan frequency range spans from 0.1 to 6.9 Hz, requiring two BCD control words.

Test E-7-1

In this test, made on the elevation servo (manual mode), a series of consecutive 5-deg increments was set with the manual slewing control,[*] and the actual elevation mirror angle was read from the vernier dial mounted on the mirror rotation axis. The percent accuracy is shown in Table 2-2. Some comments are in order:

- A zero offset was not properly nulled out so that percent error is abnormally large at the small angles.

- The percent error exceeds 0.2 at all points tested.

- A significant amount of hysteresis is exhibited.

Most of the error observed may be attributed to insufficient "stiffness" in the servo to overcome friction and small inertial moment unbalance. The system at present has a static error factor of 0.123 deg/in-oz of friction or mass unbalance. Although the static error coefficient could be reduced by the use of a higher gain in the error channel (G_1 of Fig. 2-6), there are two reasons why this is not possible:

1. The use of higher gain G_1, necessitates increasing gain G_3 in the damping (tachometer feedback) channel in order to avoid overshoot transients at the turn-around points of the sawtooth driving waveform. If both these gains are made high, the other transient term in the response, which is due to the real root of the third order polynomial of the transfer function, reaches excessive duration and magnitude.

2. The dynamic range at the final power amplifier (which subtracts the tachometer voltage from the error voltage) is exceeded, and the resultant response is very much underdamped, since proportionality cannot be maintained when saturation is reached.

---

[*]The LED readouts were used to determine the command angle actually arrived at with the slewing control.

Table 2-2

STATIC POSITIONING ACCURACY IN ELEVATION ANGLE

Command Angle (deg)	Specified Lower Limit	Specified Upper Limit	Actual	Percent Error	Command Angle (deg)	Specified Lower Limit	Specified Upper Limit	Actual	Percent Error
5	4.975	5.025	4.95	-1	65	64.675	65.325	65.4	+0.615
10	9.95	10.05	10.05	+0.5	70	69.65	70.35	70.35	+0.5
15	14.925	15.075	15.0	0	75	74.625	75.375	75.0	0
20	19.9	20.1	20.1	+0.5					
25	24.875	25.125	25.2	+0.8					
30	29.85	30.15	30.15	+0.5					
35	34.825	35.175	35.25	+0.714					
40	39.8	40.2	40.5	+1.25					
45	44.775	45.225	45.3	+0.666					
50	49.75	50.25	50.4	+0.80					
55	54.725	55.725	55.2	+0.364					
60	59.70	60.3	60.15	+0.25					

Fig. 2-6 - Elevation Servo
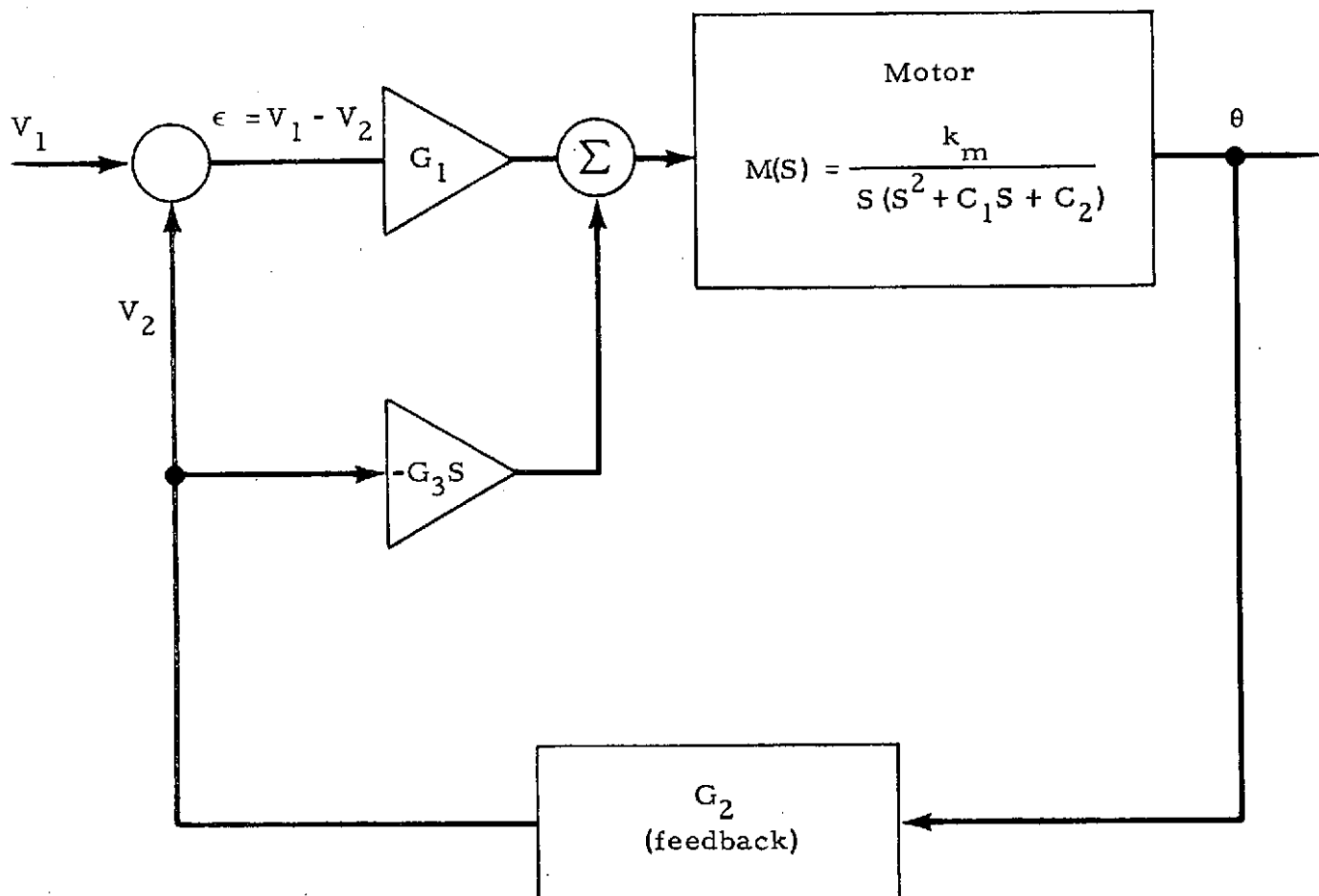
$$\frac{\theta}{V_1} = \frac{G_1 K_m}{S^3 + C_1 S + (C_2 + G_2 G_3 K_m) S + G_1 G_2 K_m}$$

For these reasons any significant reduction in the static error can only be obtained by a more exact balance of the large mirror mass distribution throughout the region of elevation angle being scanned. It should be noted that these errors, provided they are not too large, are not of major importance, since the actual pointing angle of the mirror is read by the feedback potentiometer (which is accurate to 0.1% of full scale) and small discrepancies between the command position and the actual position are tolerable (the command angle is not part of the recorded data).

Test E-7-2

During this test, simultaneous strip chart recordings were made of the command angle and the actual elevation mirror angle with the system in the auto-scan mode. Several combinations of scan excursion and scan rate were examined, the purpose being to determine the phase lag at high rates, the reduction in scan excursion, and the "rounding off" of the response at the turn-around points. The results are shown in Figs. 2-7-1 through 2-7-20.

It is clear from the response illustrated in these figures that the servo bandwidth is undersirably low. Unfortunately, this cannot be remedied by increasing the loop gain since the constraint is the upper bound on the available amplifier voltage driving the torque motor. It can readily be shown that the maximum frequency to which the servo can respond, if the maximum acceleration is applied at all times is

$$f_{max} = 1/4 \ (\alpha_{max}/\theta_s)^{1/2} \tag{2.1}$$

here

$$\alpha_{max} = \text{maximum available acceleration (rad/sec}^2)$$
$$\theta_s = \text{total scan angle (rad)}$$

and

$$\alpha_{max} = K_T \ E_{max}/R \ J \tag{2.2}$$

1.2 deg.

Mirror
Position

78.8 deg.

50 deg.

Command Signal

2

0.1 sec
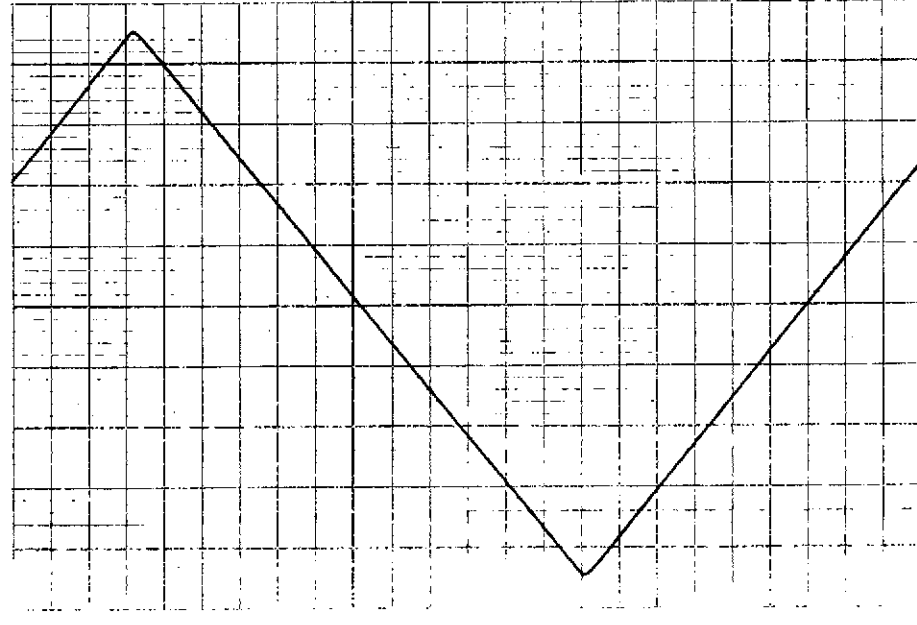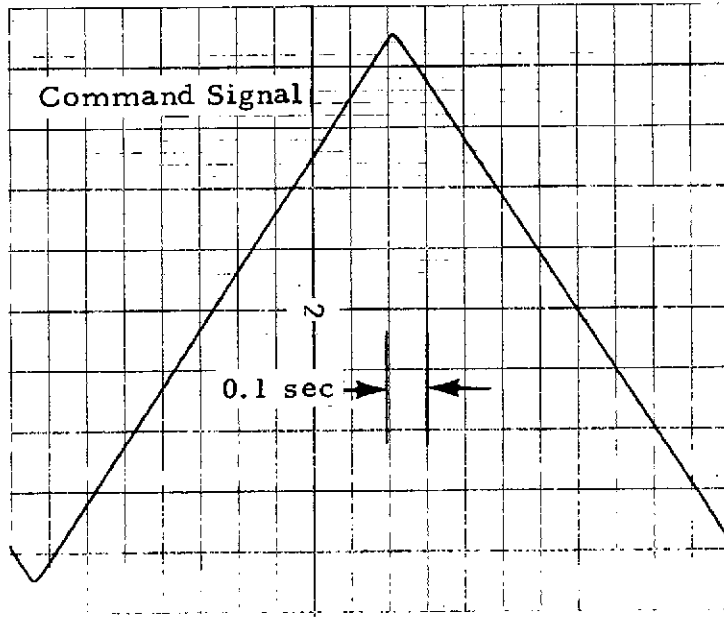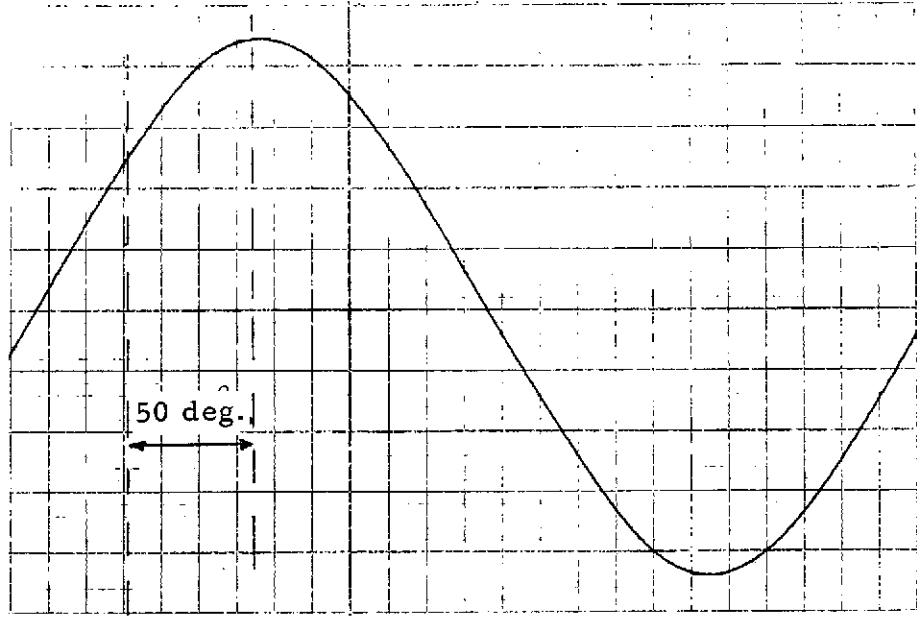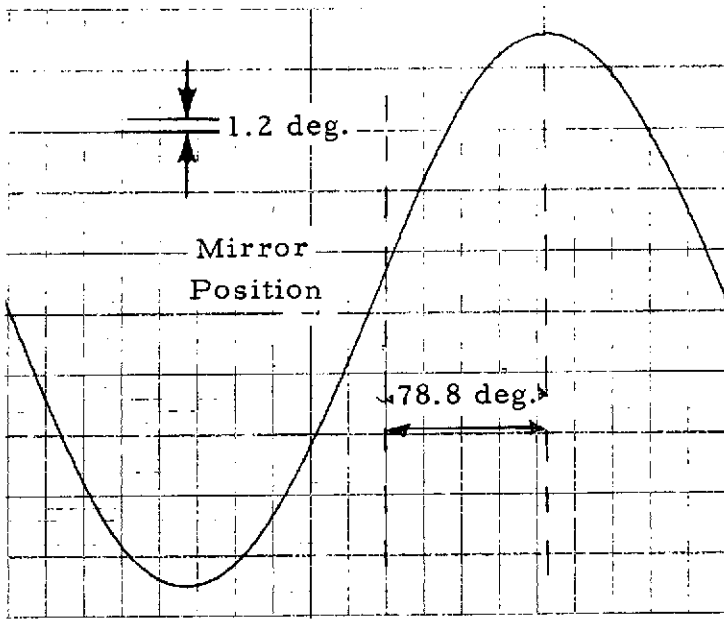
Fig. 2-7-1 - 0 to 59 Degree Excursion at 0.5 Hz

Fig. 2-7-2 - 0 to 59 Degree Excursion at 0.4 Hz
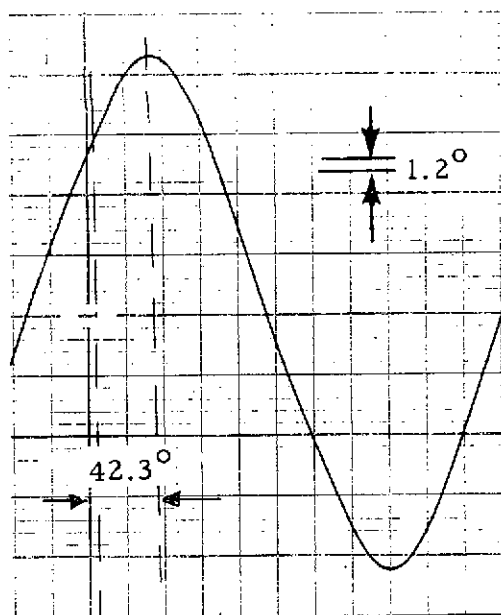
Fig. 2-7-3 - 0 to 59 Degree Excursion at 0.3 Hz

Fig. 2-7-4 - 0 to 59 Degree Excursion at 0.2 Hz

1.2°

Mirror
Position

14.2°

1 sec

Command
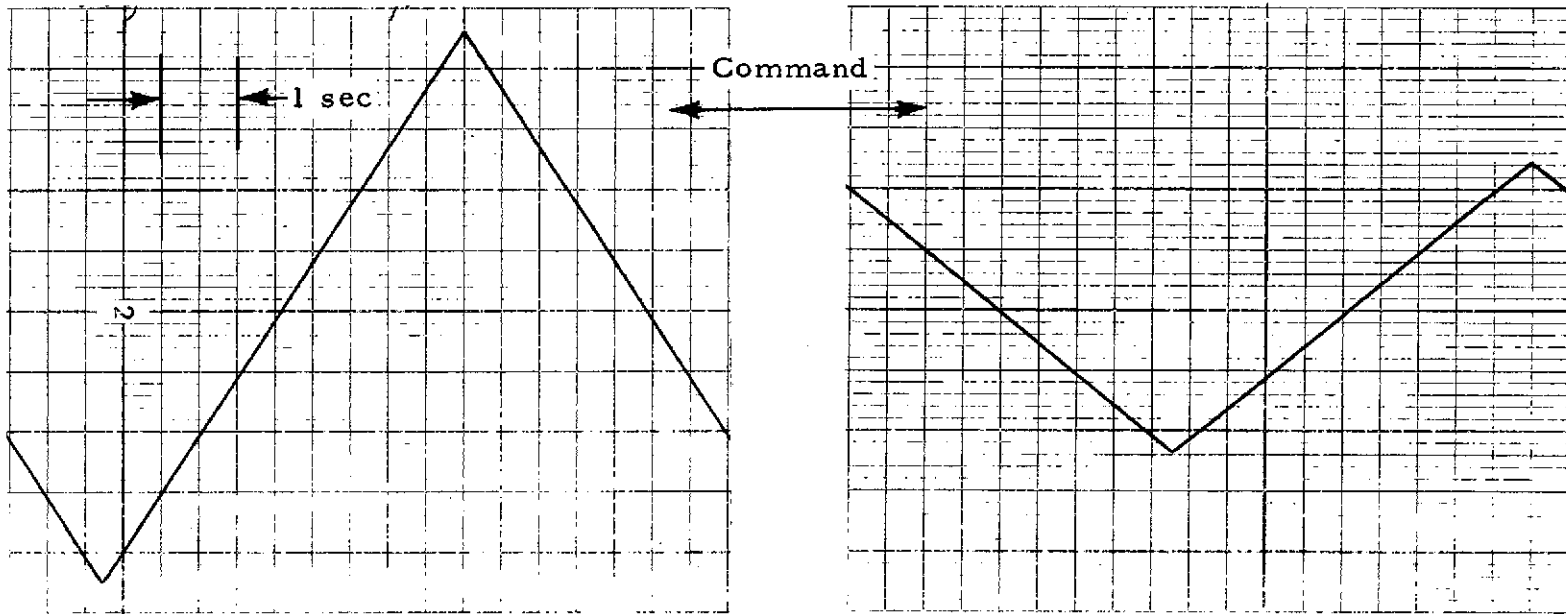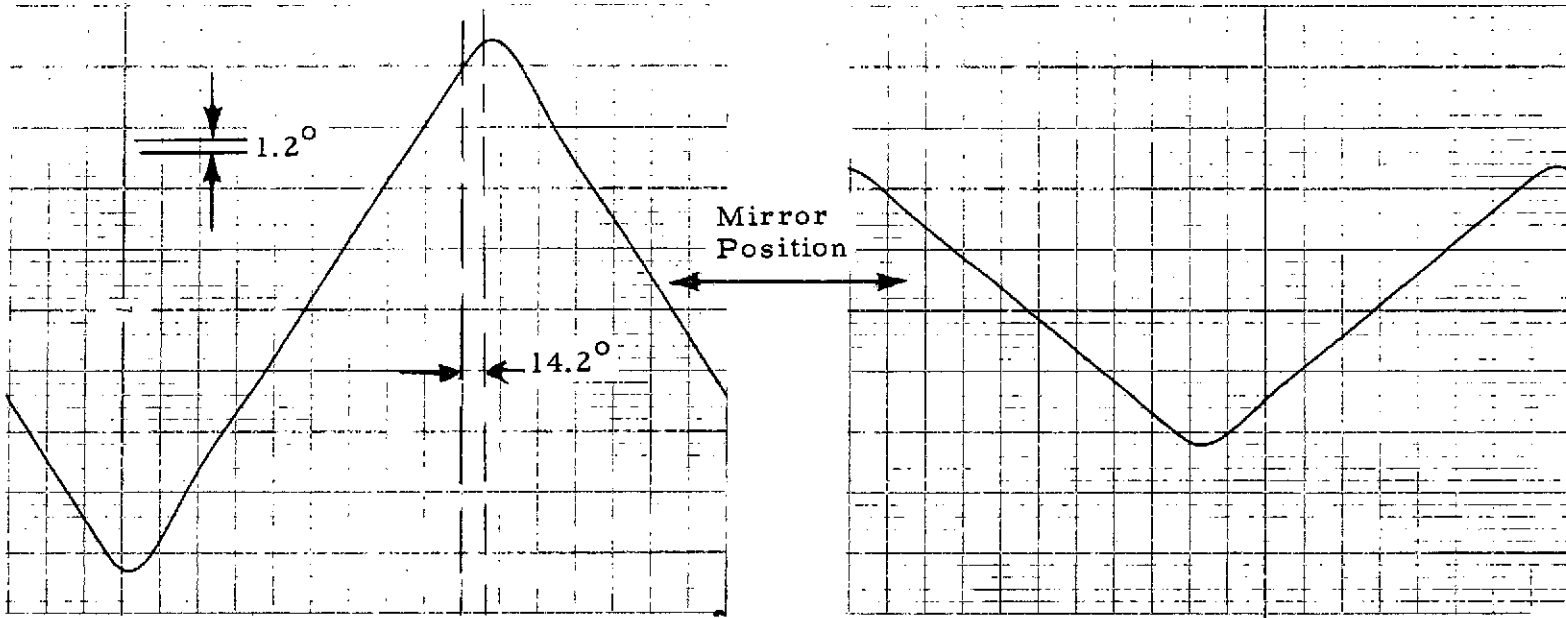
Fig. 2-7-5 - 0 to 59 Degree Excursion at 0.1 Hz   Fig. 2-7-6 - 15 to 45 Degree Excrusion at 0.1 Hz
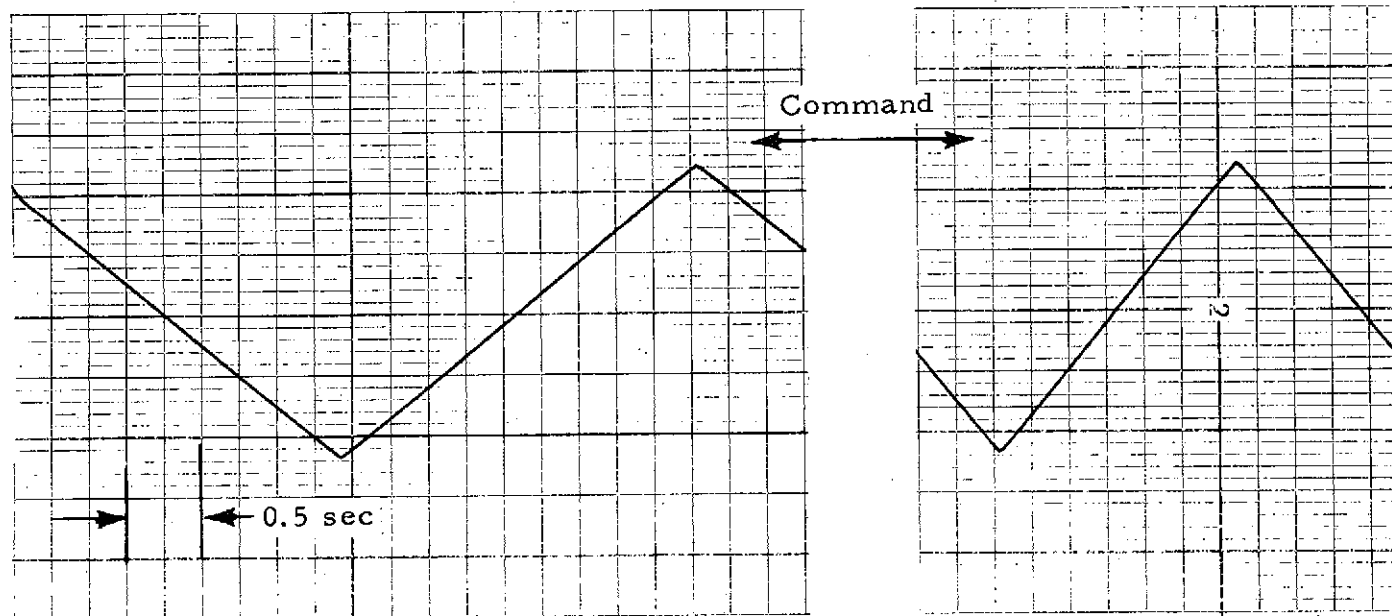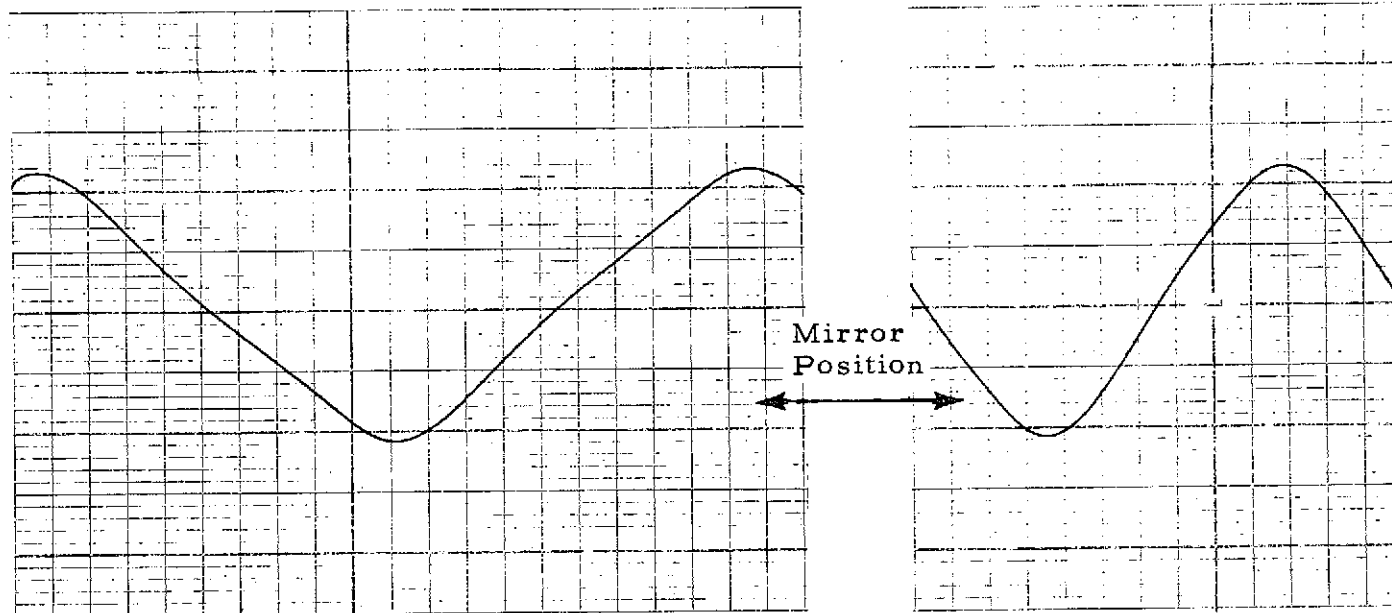
Fig. 2-7-7 - 15 to 45 Degree Excursion at 0.2 Hz

Fig. 2-7-8 - 15 to 45 Degree Excursion at 0.3 Hz

Mirror
Position

Command

2

← 0.5 sec

2

0.1 sec
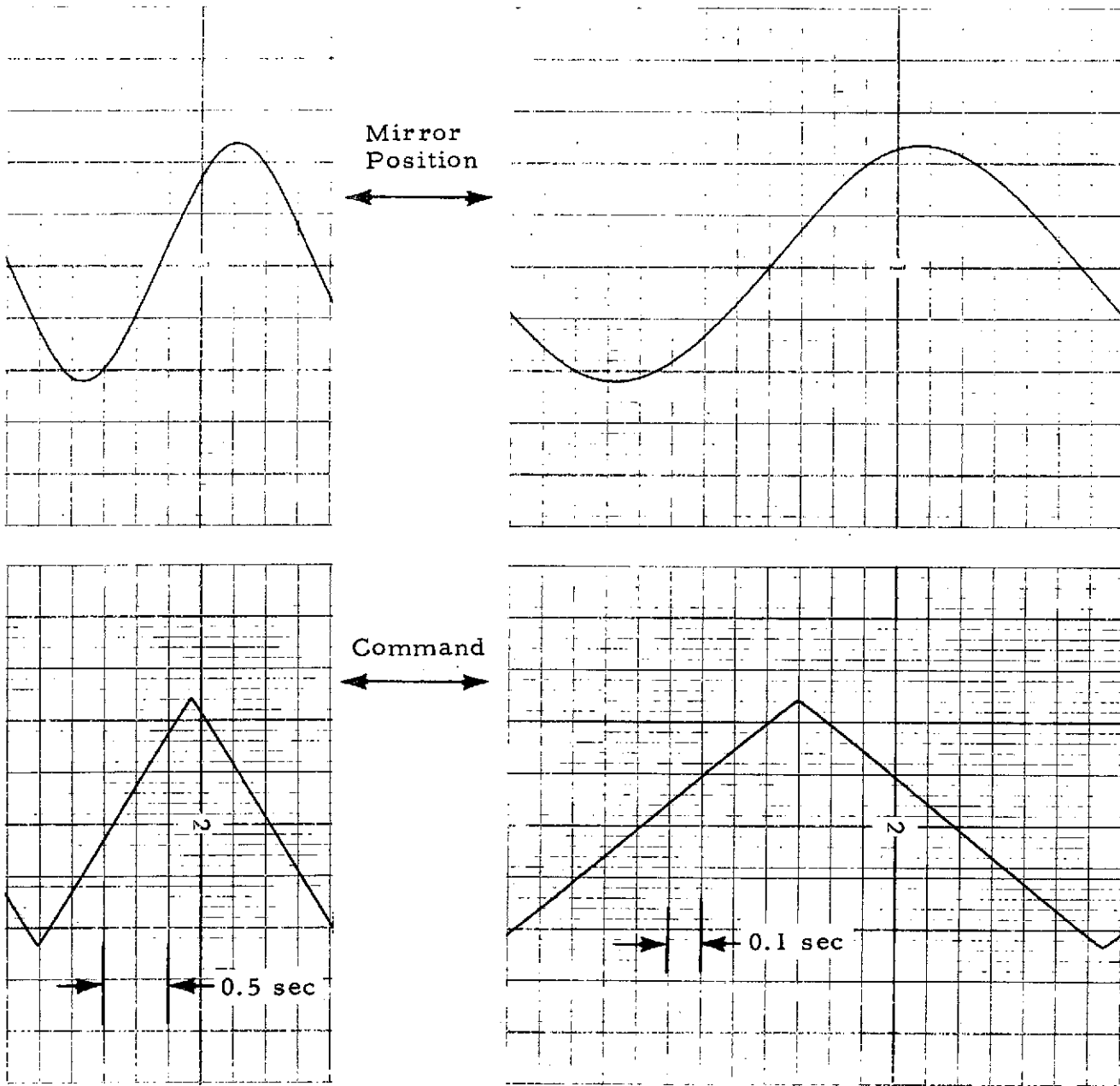
Fig. 2-7-9 - 15 to 45 Degree Excursion
at 0.4 Hz

Fig. 2-7-10 - 15 to 45 Degree Excursion at 0.5 Hz

Mirror
Position

Command

→| |← 1 sec

→| |← 2 sec
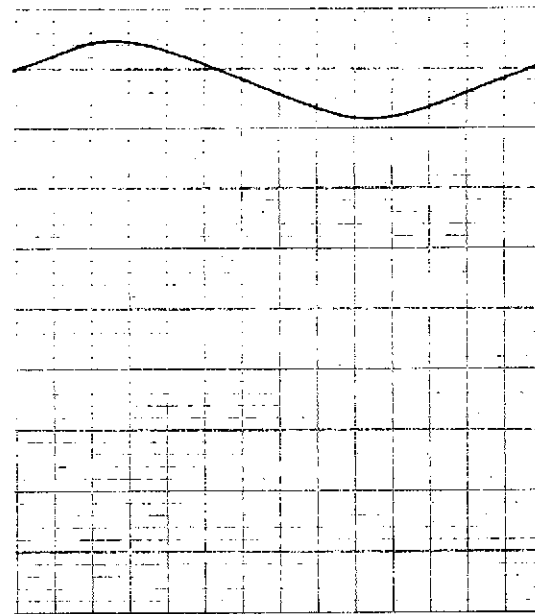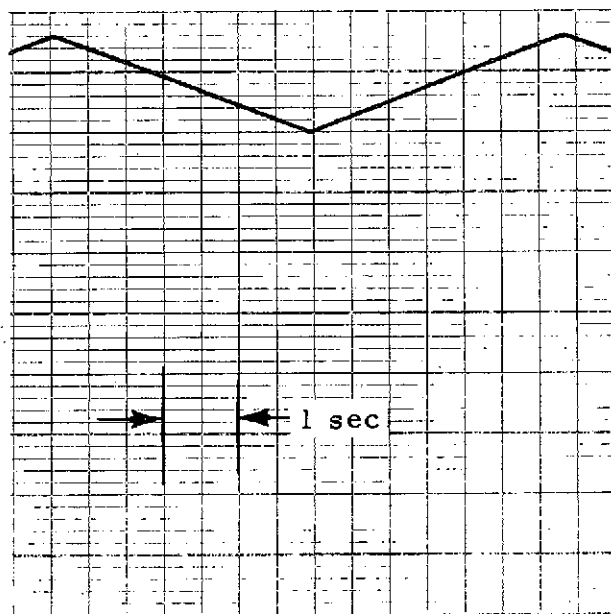
Fig. 2-7-11 - 45 to 59 Degree Excursion
at 0.1 Hz
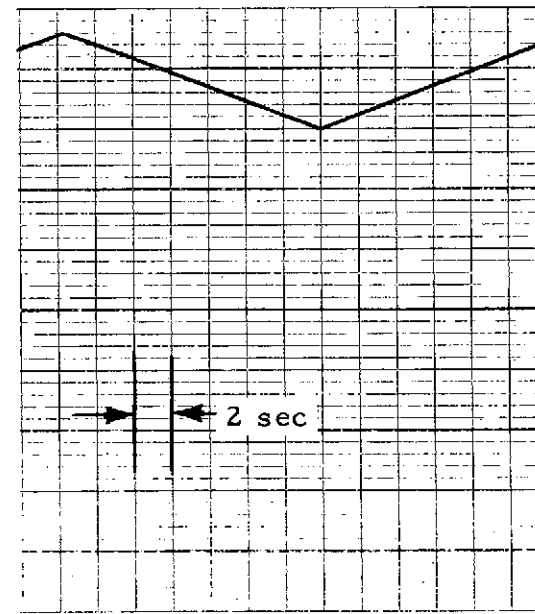
Fig. 2-7-12 - 45 to 59 Degree Excursion
at 0.2 Hz

Mirror
Position

Command

0.5 sec
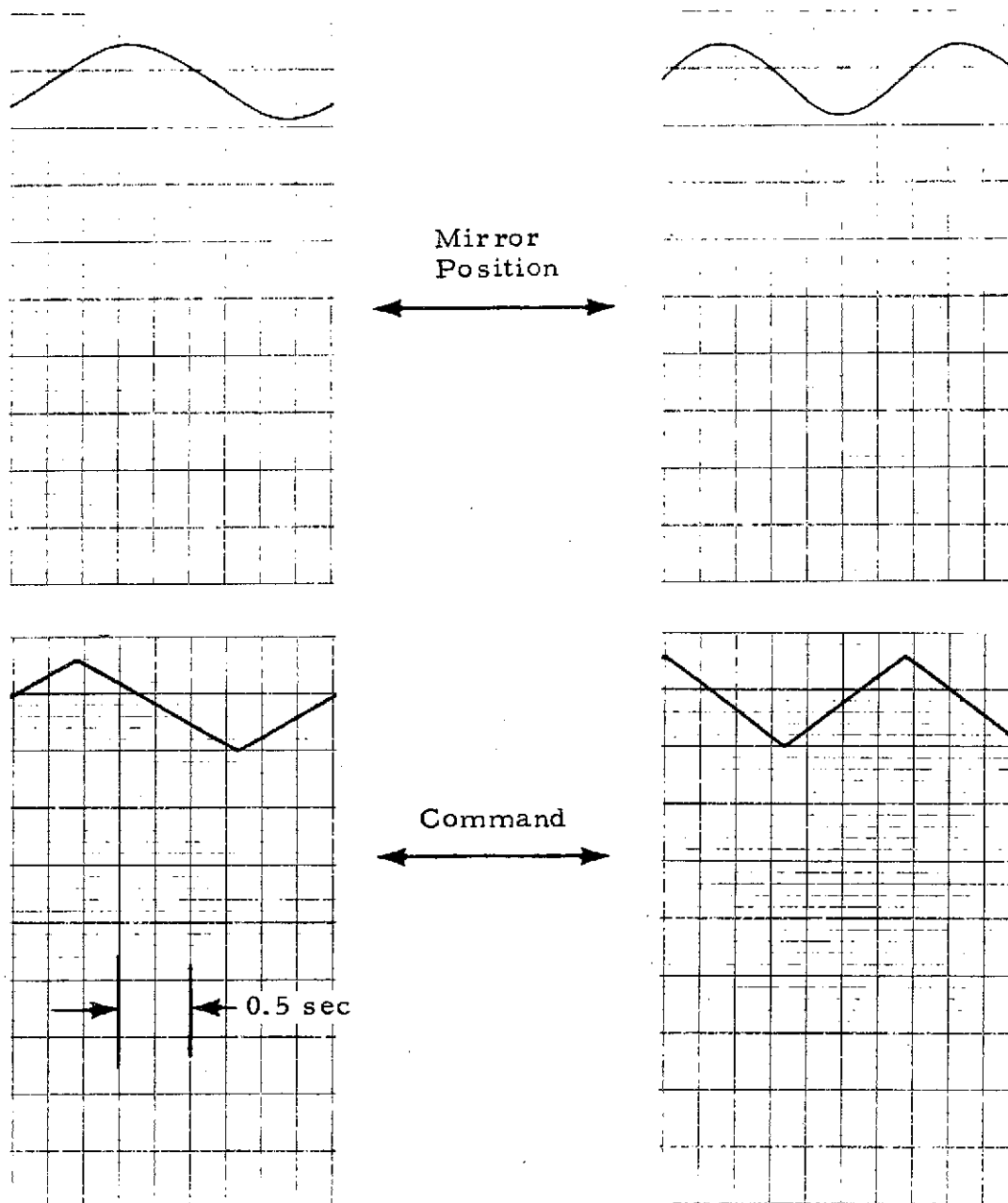
Fig. 2-7-13 - 45 to 59 Degree Excursion
at 0.3 Hz

Fig. 2-7-14 - 45 to 59 Degree Excursion
at 0.4 Hz

Mirror
Position

Command

0.1 sec

1.0 sec
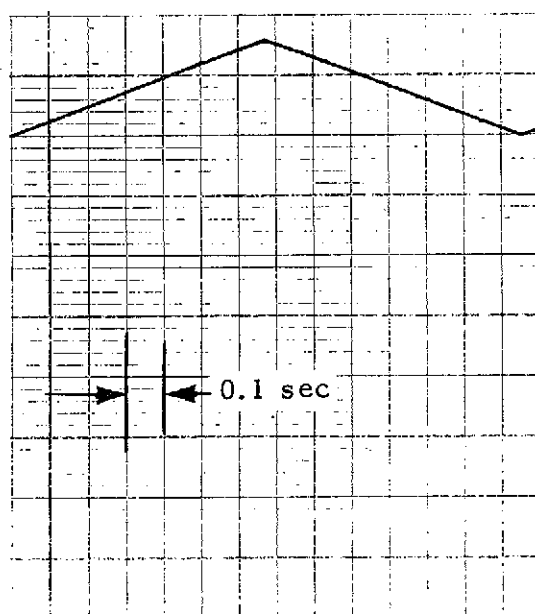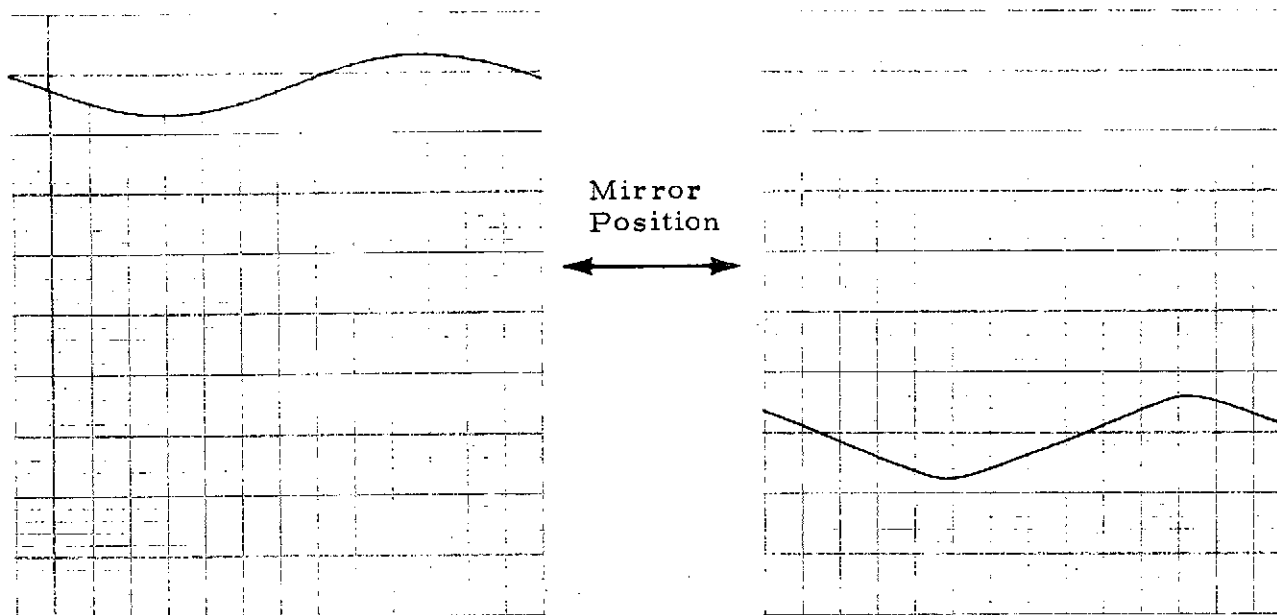
Fig. 2-7-15 - 45 to 59 Degree Excursion
at 0.5 Hz
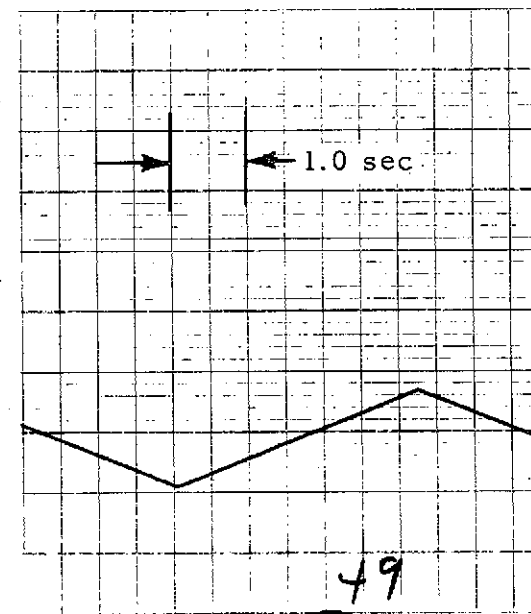
Fig. 2-7-16 - 10 to 25 Degree Excursion
at 0.1 Hz

Command

Mirror
Position

0.5 sec
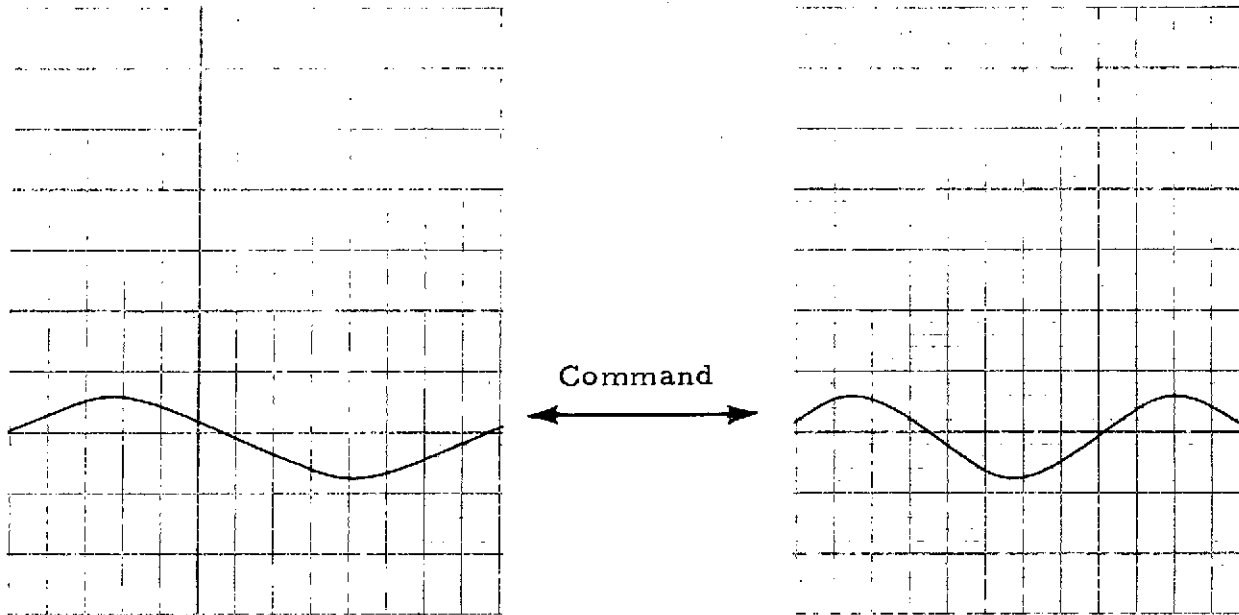
Fig. 2-7-17 - 10 to 25 Degree Excursion
at 0.2 Hz
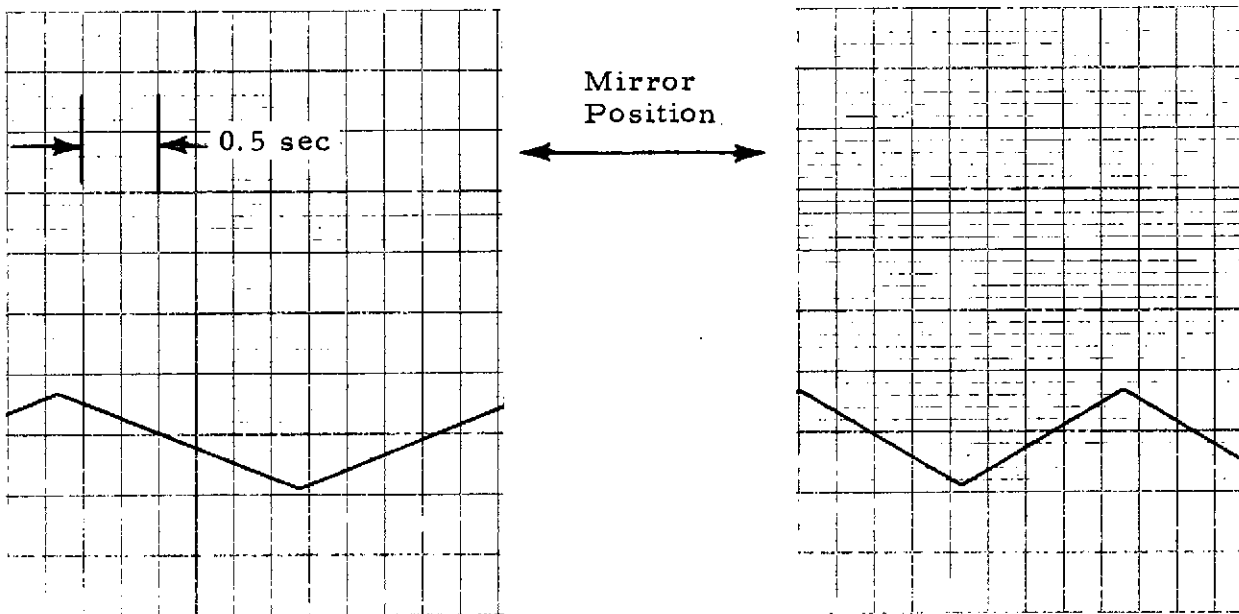
Fig. 2-7-18 - 10 to 25 Degree Excursion
at 0.3 Hz

Mirror
Position

Command
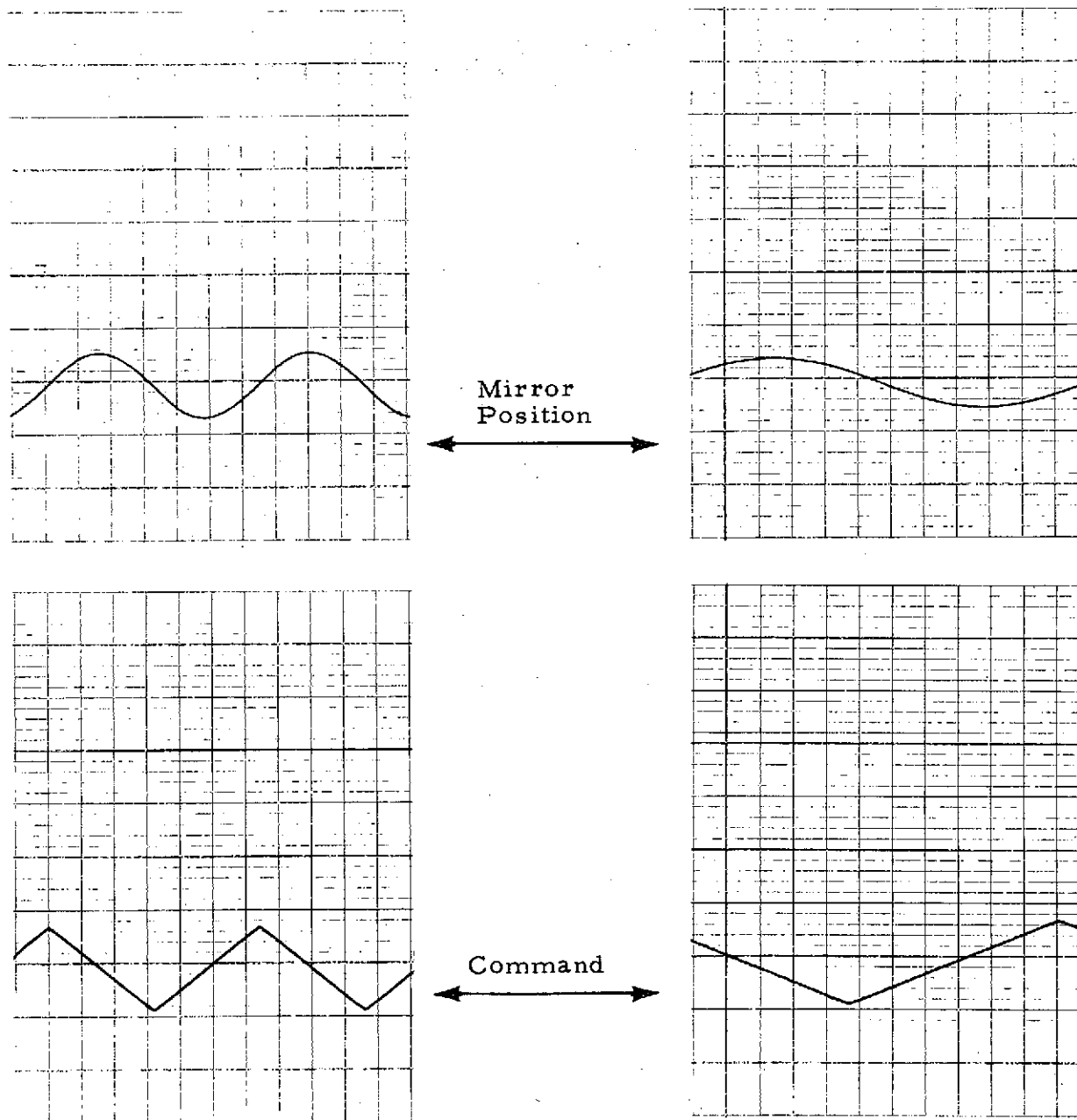
Fig. 2-7-19 - 10 to 25 Degree Excursion
at 0.4 Hz

Fig. 2-7-20 - 10 to 25 Degree Excursion
at 0.5 Hz

where

$$K_T = \text{motor torque constant (in-oz/amp)}$$
$$E_{max} = \text{maximum available amplifier voltage (volts)}$$
$$R = \text{torque motor resistance (ohms)}$$
$$J = \text{moment of inertia of load plus motor (in-oz/sec}^2)$$

In the actual design the fixed parameters are:

$$K_T = 60 \text{ in-oz/amp} \qquad R = 9 \text{ ohms}$$
$$E_{max} = 24 \text{ volts} \qquad J = 38 \text{ in.-oz/sec}^2$$

which gives

$$\alpha_{max} = 4 \text{ rad/sec}^2.$$

For an angular excursion at 0.5 rad (28.6 deg) this yields

$$f_{max} = 0.7 \text{ Hz}.$$

Since this value corresponds to a condition at 90-deg phase lag and continuous acceleration,* the actual limiting frequency will depend on the distortion criteria imposed — it certainly must be smaller than that given above. A substantial increase in bandwidth would be possible if the torque motor had a much lower resistance.

Test R-8

This test involving range scanning against an external wheel target at a known range, was performed later and is discussed in Section 2.2 of this report.

---

*Arising from the saturation, i.e., full torque is always applied and only the direction is changed to create the periodic reversals of direction.

Test R-9

Figure 2-9[*] shows the display x, y coordinates for successive 50 meter range increments; the dotted lines correspond to inward displacement and the solid lines correspond to outward displacement. The following was noted: (1) A hysteresis error, increasing linearly to about 8 meters at 500 meters, and (2) Jitter on the x, y voltage due to the truncation effect of the digital (13-bit optical encoder) feedback. It was decided to defer the x, y accuracy tests until more work had been done in adjusting offsets and gains in the range channel. It was also discovered that the feedback gain was set to a value equal to one-half of its correct value; this was later corrected.

Test R-10 — Range Servo Dynamics

The dynamic response for a variety of input range commands was examined by simultaneous comparison of the input range command and the reconstructed range voltage. The results are shown in Figs. 2-10-1 through 2-10-12.[**] The main effect at high scan rates is to reduce slightly the overall excursion in range, and to introduce a very small phase lag. (Note: The actual mirror position is obtained from the feedback voltage, so that the output x, y does not exhibit any lag.)

Test R-11 — Line Scan Mode

This mode was tested by setting in several values of horizontal range, programming the scanner through an angle at 60 deg scan and observing the x, y on an x, y recorder. Ideally, the x, y plots should be vertical lines through the x-axis values corresponding to the horizontal range. We note some hysteresis effect in the results. This test should be repeated since later realignment of the x, y channel obtained much better accuracy.

---

[*] To maintain consistency of test and figure numbers, Fig. 8 is intentionally omitted.

[**] In the figures, the input command is the lower trace and the reconstructed range voltage is the upper trace.

1-29-74

θ̇ = 0.1 Hz

59°

0°

100　　　200　　　300　　　400　　　500　　　600
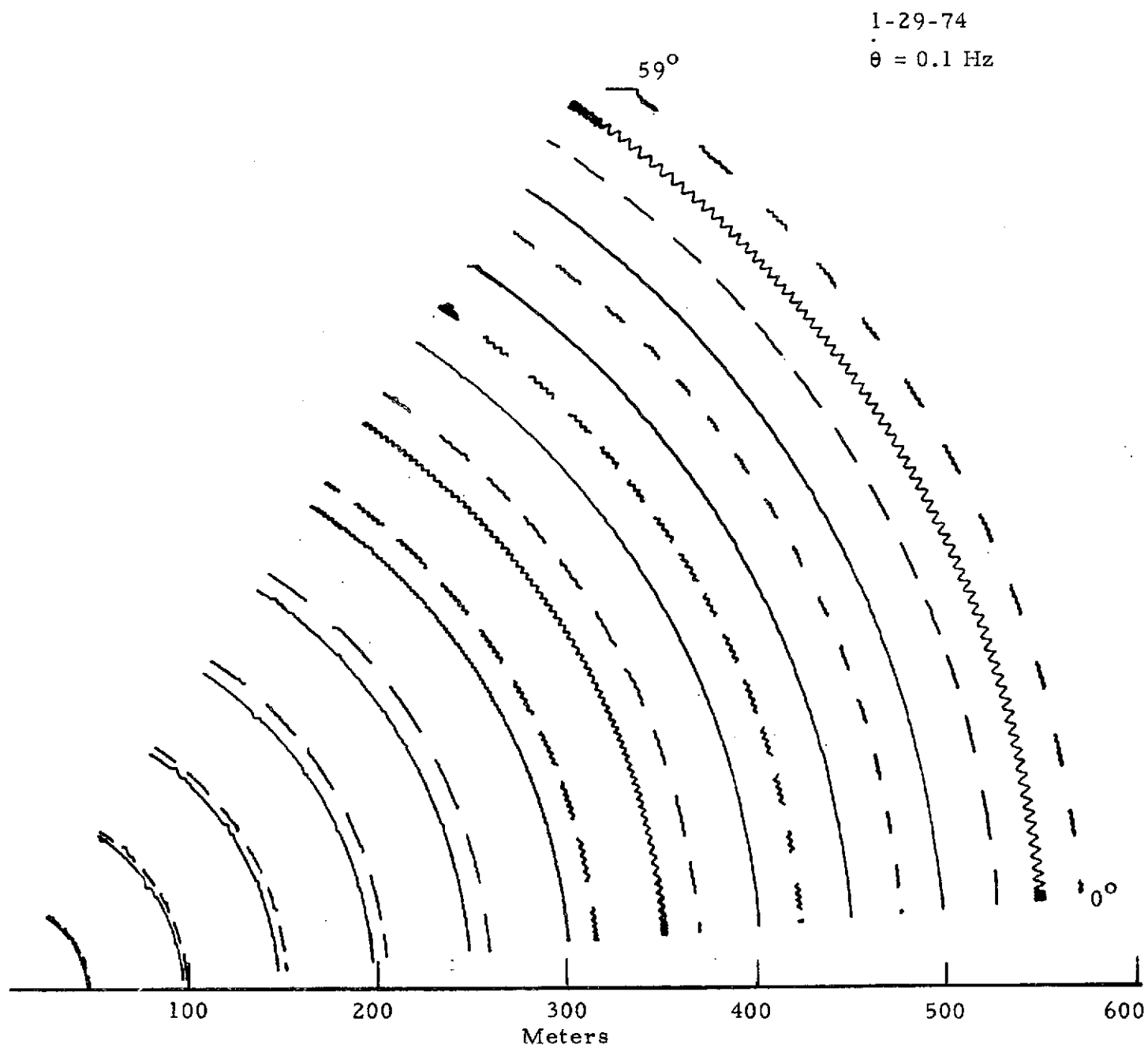
Meters

Fig. 2-9 - Elevation Scans for Successive 50 Meter Range Increments
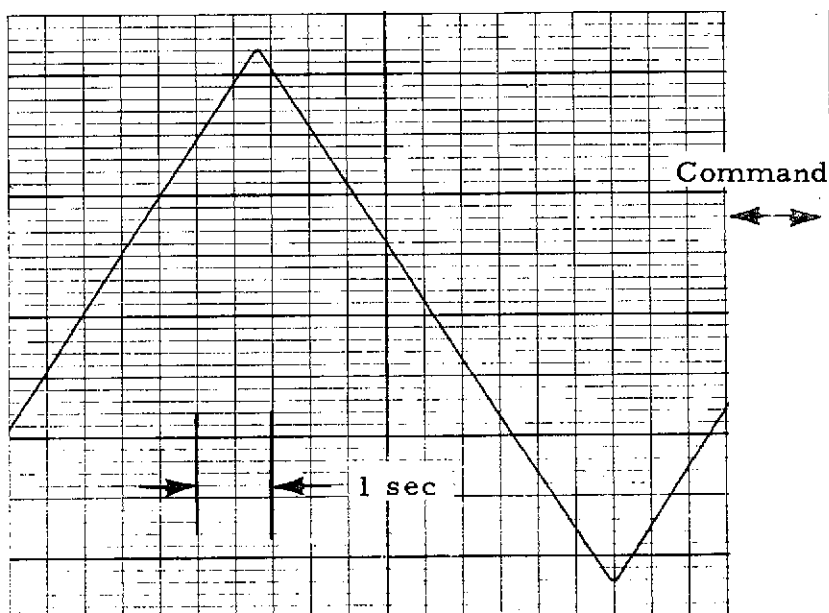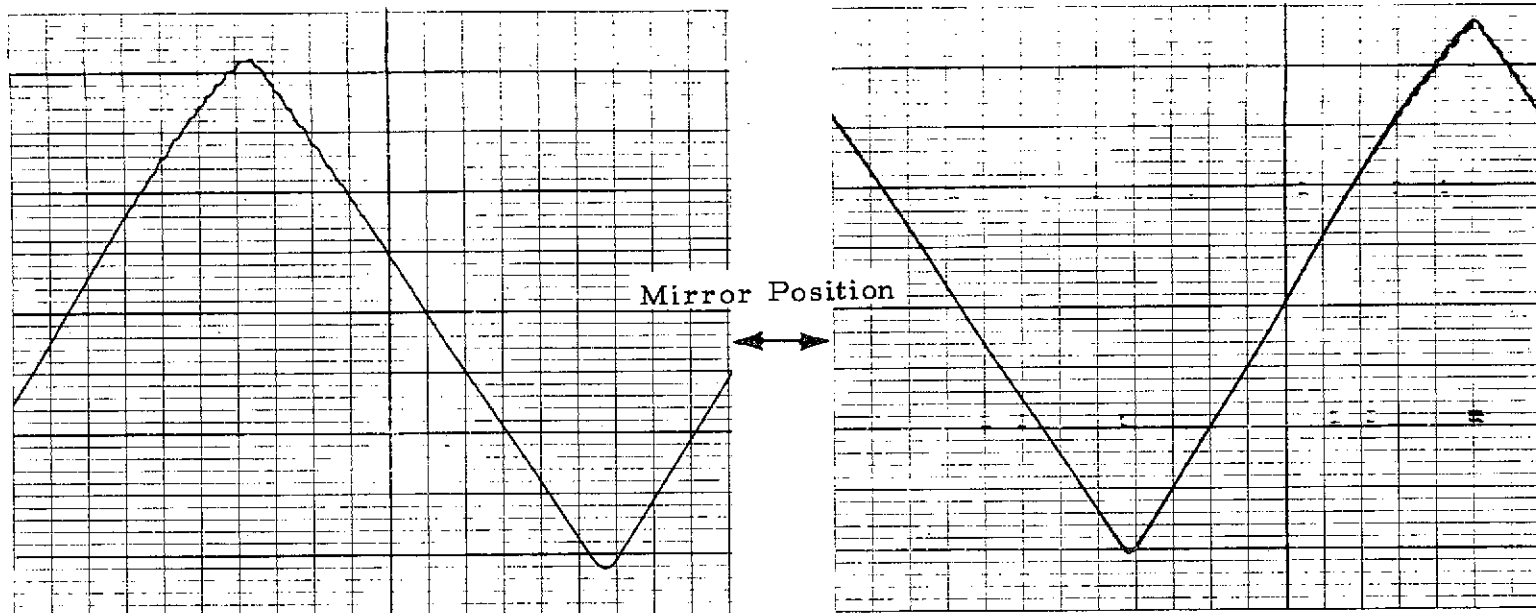
Fig. 2-10-1 – 30 to 500 Meter Excursion at 0.1 Hz   Fig. 2-10-2 – 30 to 500 Meter Excursion at 1.0 Hz
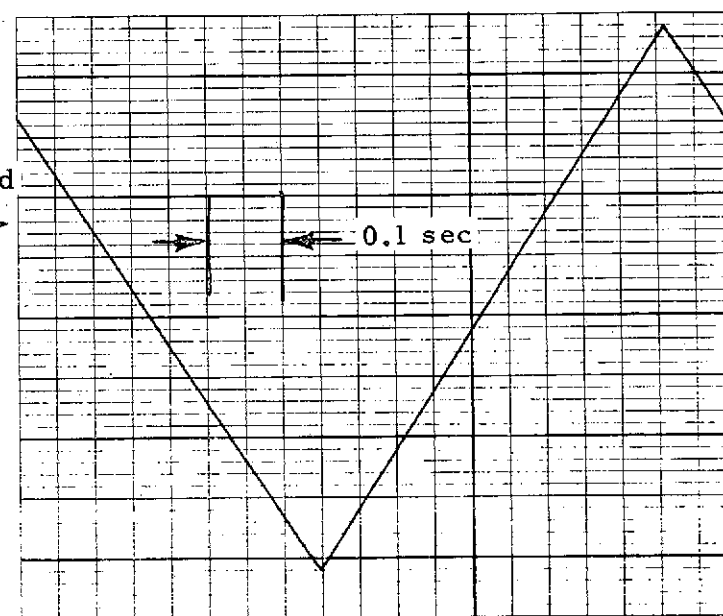
Mirror Position

Command

.05 sec
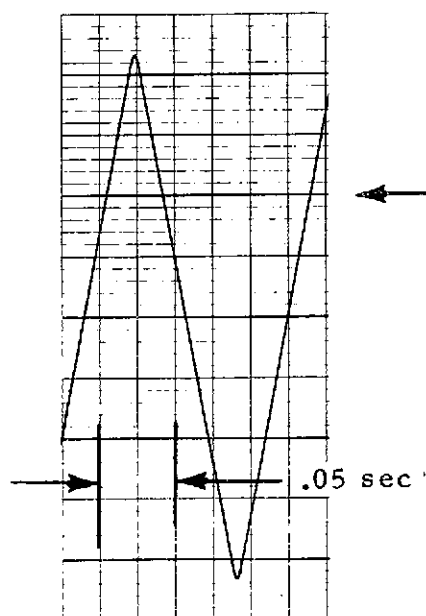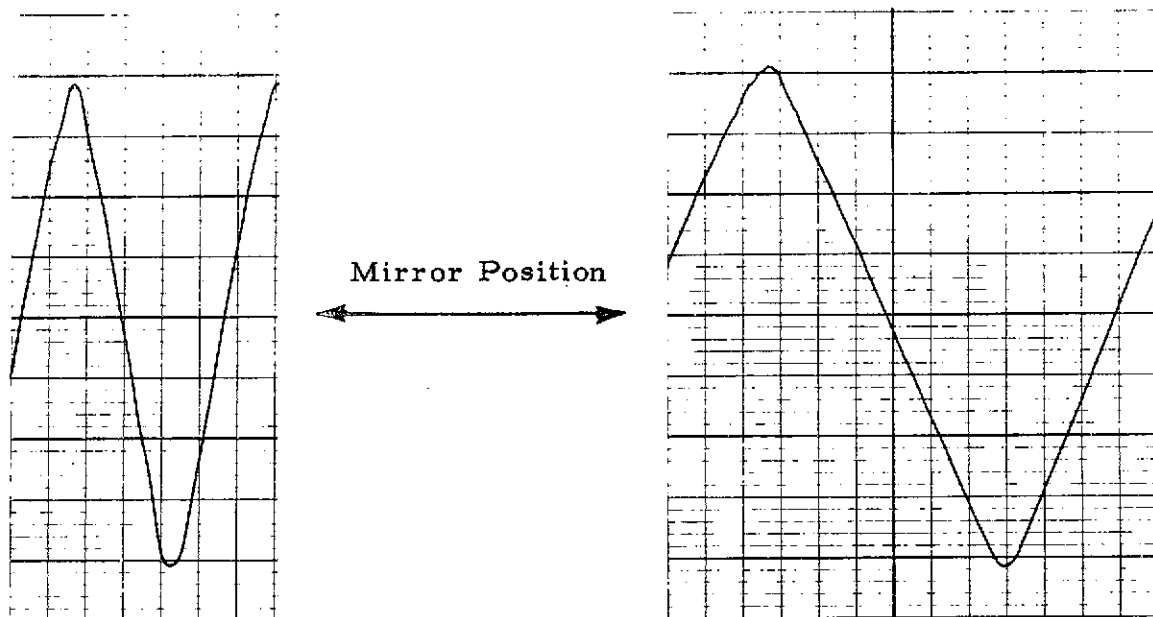
Fig. 2-10-3 - 30 to 500 Meter
Excursion at 6.9 Hz
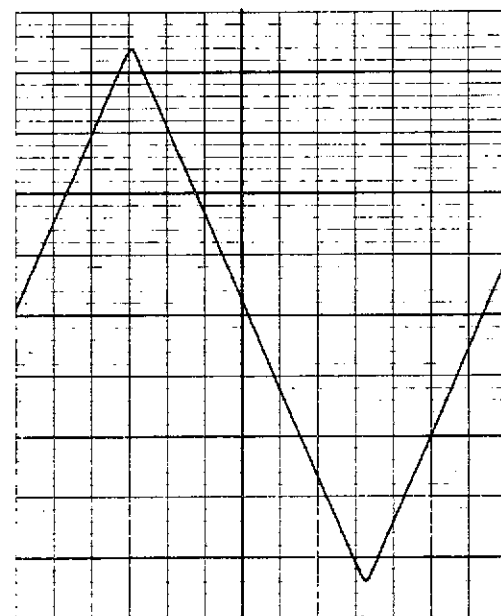
Fig. 2-10-4 - 30 to 500 Meter Excursion
at 3 Hz
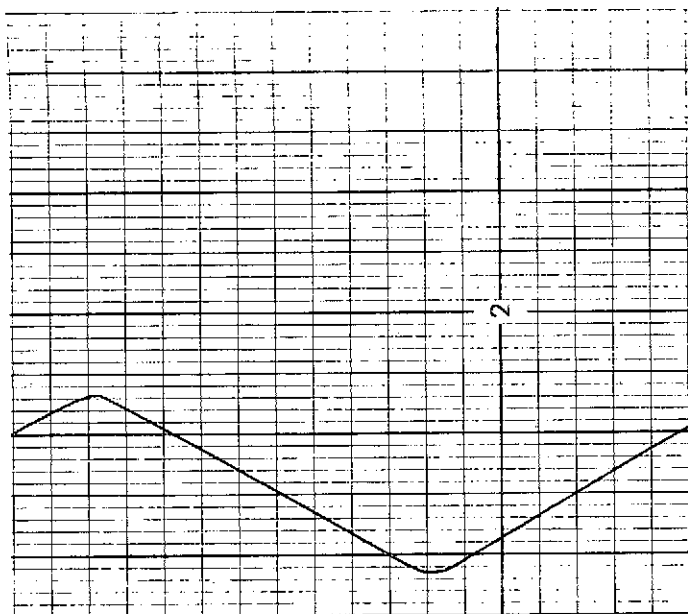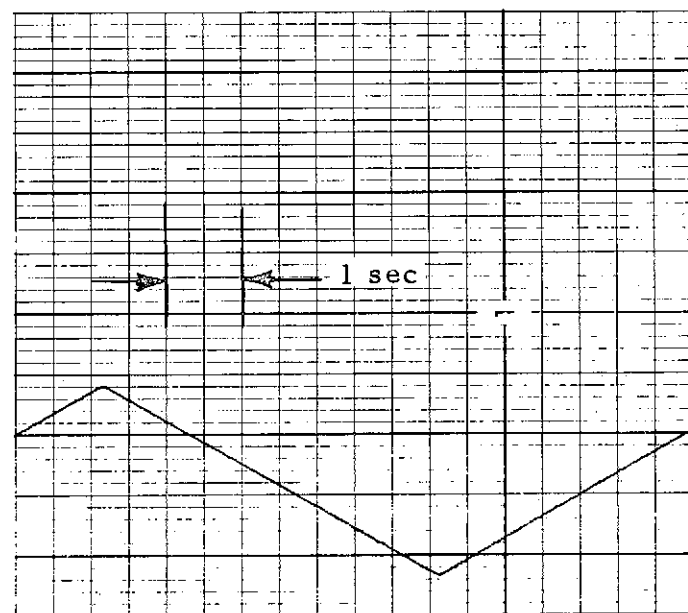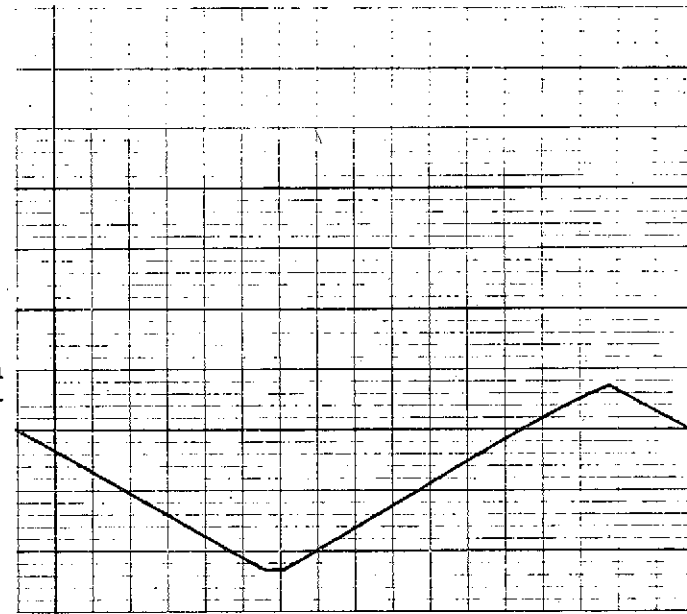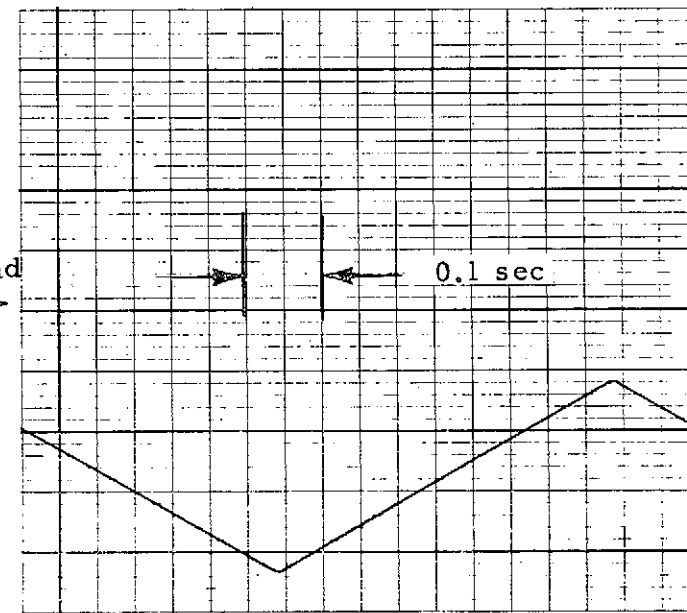
Fig. 2-10-5 - 30 to 200 Meter Excursion at 0.1 Hz   Fig. 2-10-6 - 30 to 200 Meter Excursion at 1 Hz

Mirror Position

0.05 sec
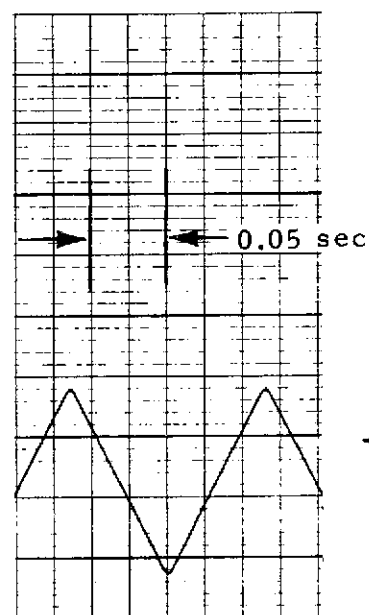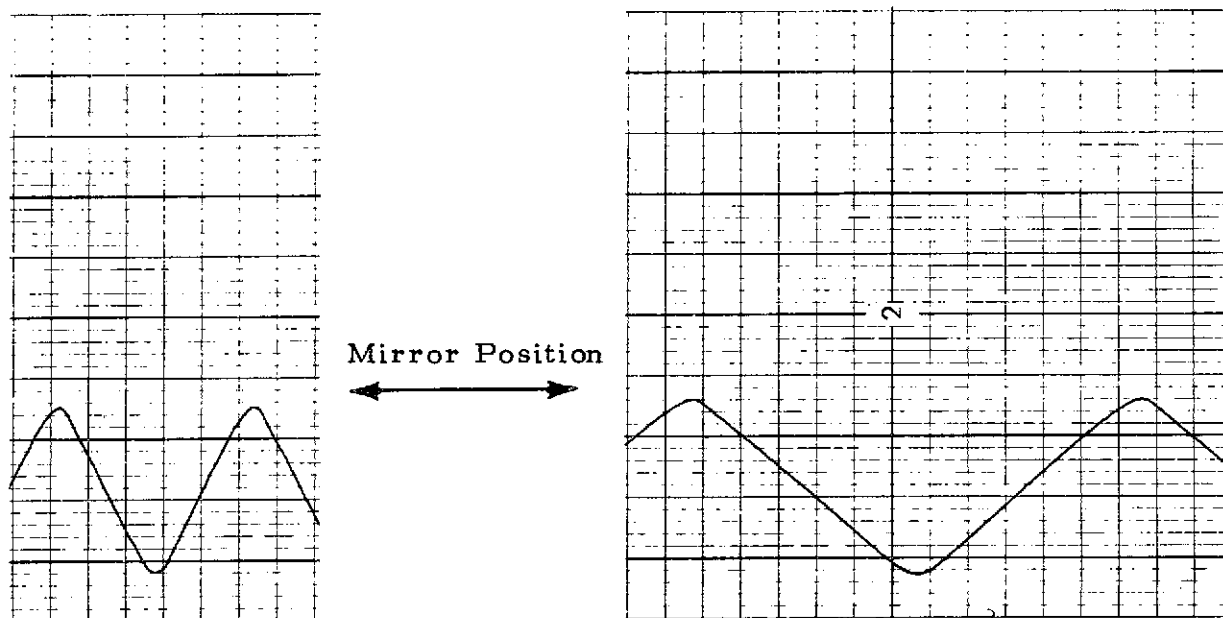
Command

Fig. 2-10-7 - 30 to 200 Meter
Excursion at 3.0 Hz

Fig. 2-10-8 - 30 to 200 Meter Excursion at 6.9 Hz
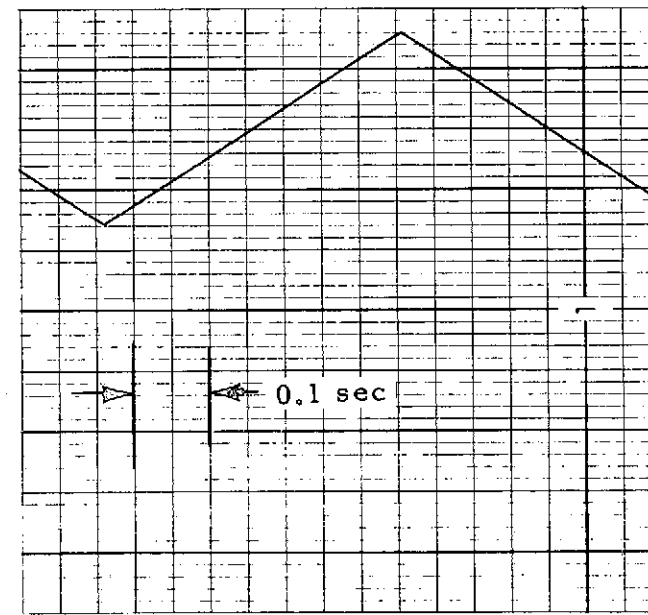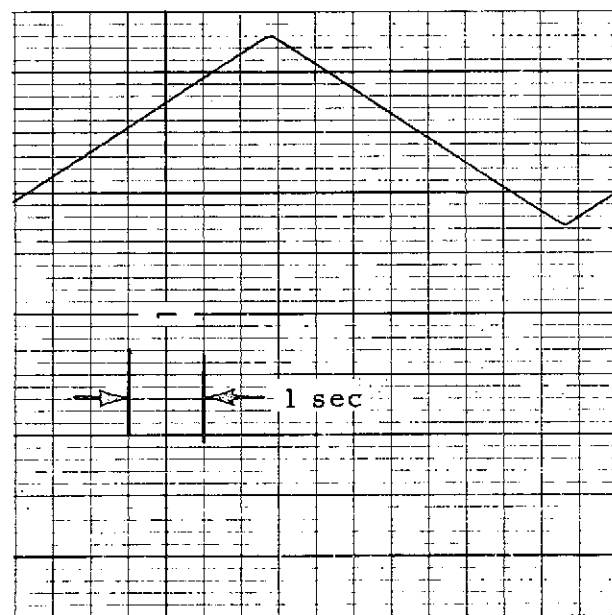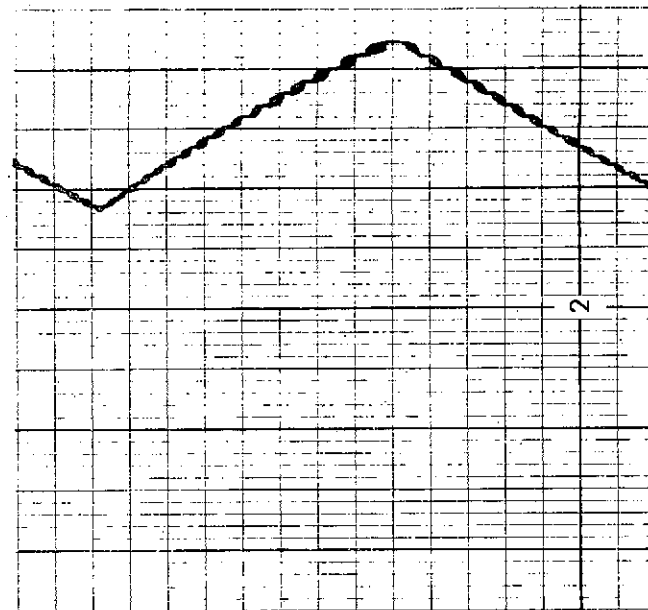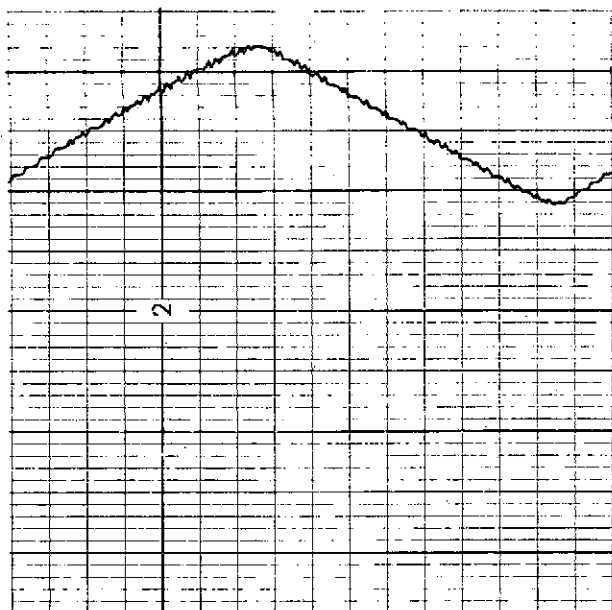
Fig. 2-10-9 - 300 to 500 Meter Excursion
at 0.1 Hz

Fig. 2-10-10 - 300 to 500 Meter Excursion
at 1.0 Hz

Mirror Position

Command

0.15 sec →

0.05 sec

.02 sec
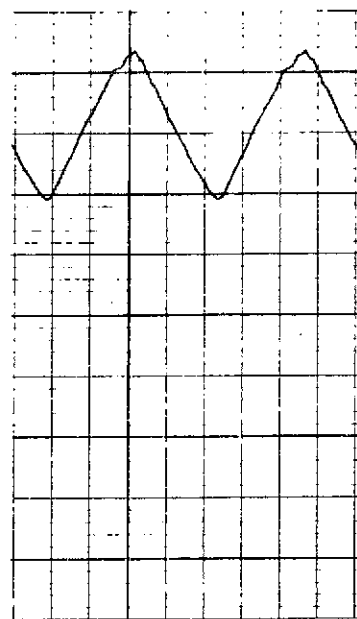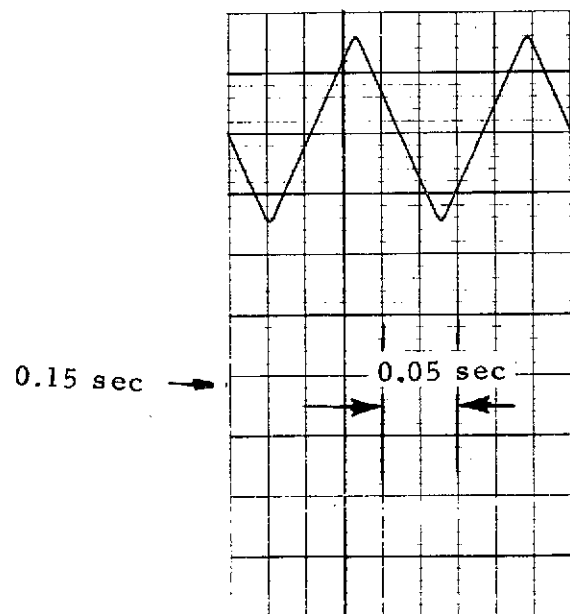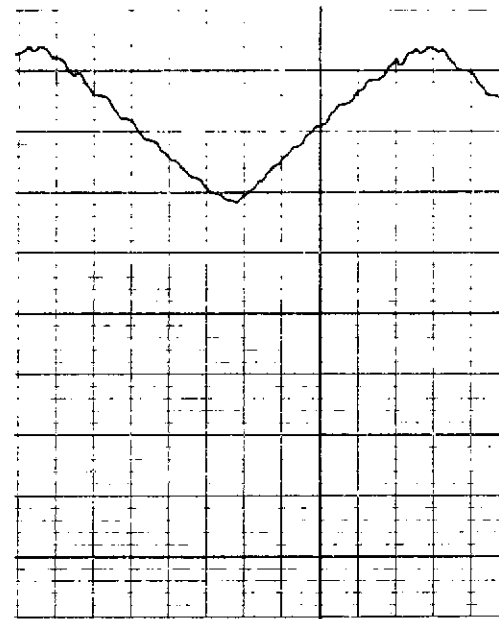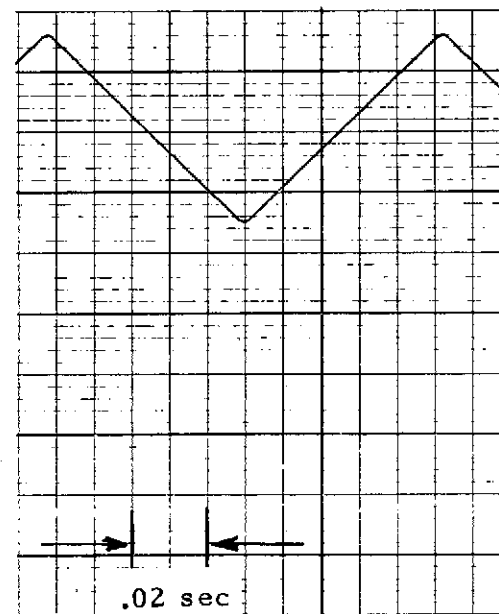
Fig. 2-10-11 - 300 to 500 Meter Excursion
at 3.0 Hz

Fig. 2-10-12 - 300 to 500 Meter Excursion
at 6.9 Hz

2.2 RESULTS OF ADDITIONAL SCANNER TESTS

2.2.1 Introduction

The data from the previous flyby tests indicated the following:

- The range coverage of both systems was considerably smaller than the programmed value.

- The system in van 2 gave elevation angles consistently lower than the programmed values, at least on the data readouts. (The actual angle, however, as judged visually, appeared correct.)

Investigation of these discrepancies revealed the following:

- Note from Fig. 2-11 that the scale factor relating secondary mirror position to input range command is determined by the ratio, G_1/G_2. In adjusting this to the correct value, a value of

$$G_5 = 10/2\pi \text{ volts/radian}$$

was used, based upon full scale voltage (10V) corresponding to full rotation ($\theta = 2\pi$ radians). Since only the lower 12 bits from the optical encoder is actually used for feedback, the true gain is

$$G_5 = 10/\pi \text{ radian/volt}$$

i.e., G_5 is really twice as large as was thought. The system was aligned for secondary mirror position offset by placing a target at a known distance

$$R_1 = 61 \text{ meters (200 feet)},$$

programming the input command to this value, and displacing the secondary mirror platform to give optimum focus on this target. With the incorrect value of G_1/G_2 used, this resulted in the relation

$$R_{actual} = \left[\frac{R_{command}}{1/2 + \dfrac{R_{command}}{2R_1}} \right]$$

41
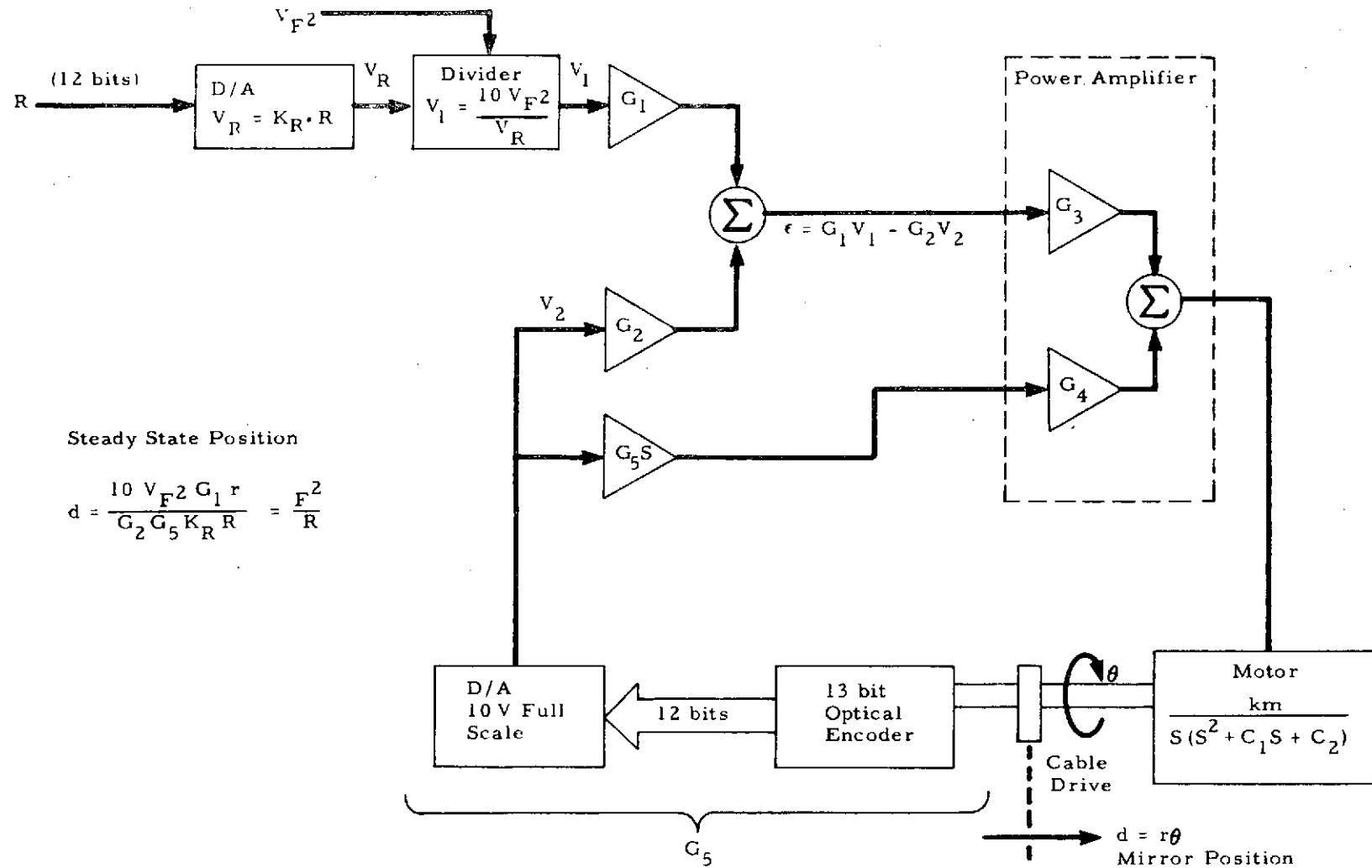
Fig. 2-11 - Range (Secondary Mirror) Positioning Servo Functional Diagram

We observe that the actual range agrees with the command only when the command is equal to R_1, but that for other values the scan coverage will be reduced. This was corrected by readjusting G_1/G_2 to the correct value.

The discrepancy in angle was found to exist only on the readout data for van 2, and was due to the method used to correct the sine/cosine potentiometer for the left-handed* configuration required in van 2. This resulted in a distortion of the sine function. The condition was corrected by using the same potentiometer connections as in van 1, and inverting the sine voltage with a unity gain operational amplifier (the previous configuration used this amplifier in the non-inverting mode).

After these corrections were made, both systems were realigned and calibrated with respect to the x, y outputs. This procedure involves adjusting a series of gains and offsets in the chain of devices generating x and y. This data output chain is shown in Fig. 2-12. (The y output is the same, with the exception that the cosine function replaces the sine function.) After alignment, the values

$$\theta_{el} = \tan^{-1} (v_y/v_x)$$

$$R = K_s \cdot \left[v_x^2 + v_y^2 \right]^{1/2}$$

were compared with the actual elevation angle (as read on the vernier dial on the elevation mirror shaft) and with the actual external focus range as computed from the relation between the optical encoder output voltage and the secondary mirror position. (This comparison relies on the validity of the lens equation relating secondary mirror position to external focus, and on the precision with which the optical encoder output indicates the true mirror position.)

Results of the calibration are shown in Figs. 2-13 and 2-14. We note that angle errors are less than 0.5 degree and range errors are a small fraction of the external range resolution length.

---

*In van 2, the opposite (from van 1) rotational sense on the potentiometer shaft occurs to indicate increasing (i.e., upward) elevation angle. This is because van 2 views the other end of the scan plane baseline, but employs the same directional layout of optical axis.

$$\theta_a = d/r$$

Optical Encoder

G_5

12 bits

D/A Converter

G_1

V_d

$V_{4}2$ (constant)

$V_R' = \dfrac{10 V_f 2}{V_d}$

V_R'

V_2

θ_{el}

Sine Pot

$G = 1$

$V_1 = K \sin \theta$

Multiplier
$V_x = \dfrac{V_1 V_2}{10}$

$V_x = \dfrac{V_R' K \sin \theta}{10}$

G_2

V_x
Output
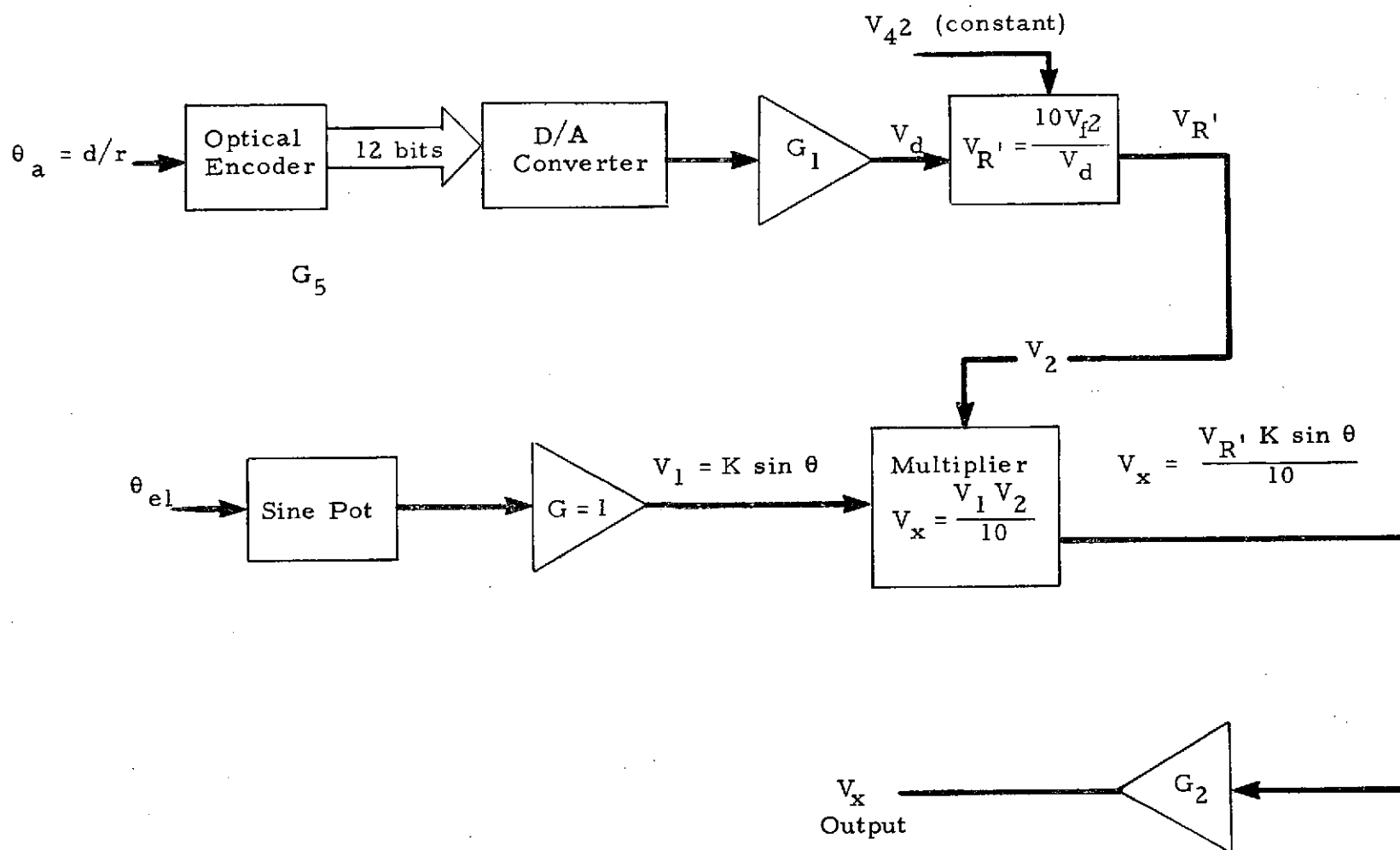
Fig. 2-12- Processing Chain for x Voltage Output

Command Angle (deg)	Actual Angle (deg)	Command Range (m)	Actual Range (m)	$\tan^{-1}$ (y/x) (deg)	$(x^2 + y^2)^{1/2}$ (m)
5.3	5.3	50	50.386	5.67	49.44
		100	99.85	5.31	97.65
		200	199.0	4.92	194.35
		350	352.6	5.03	341.51
15.0	15.2	50	50.41	15.52	48.47
		100	99.76	15.20	97.65
		200	201.40	15.27	197.71
		350	352.09	15.14	344.87
30.0	30.3	50	50.38	30.66	49.91
		100	100.32	30.43	99.66
		200	198.6	30.39	197.43
		350	352.09	30.25	345.7
45.0	45.1	50	50.66	45.36	50.66
		100	99.86	45.17	100.36
		200	200.09	45.05	200.20
		350	346.7	45.16	346.30

Fig. 2-13- Output Data Static Accuracy for Van 1 System

45
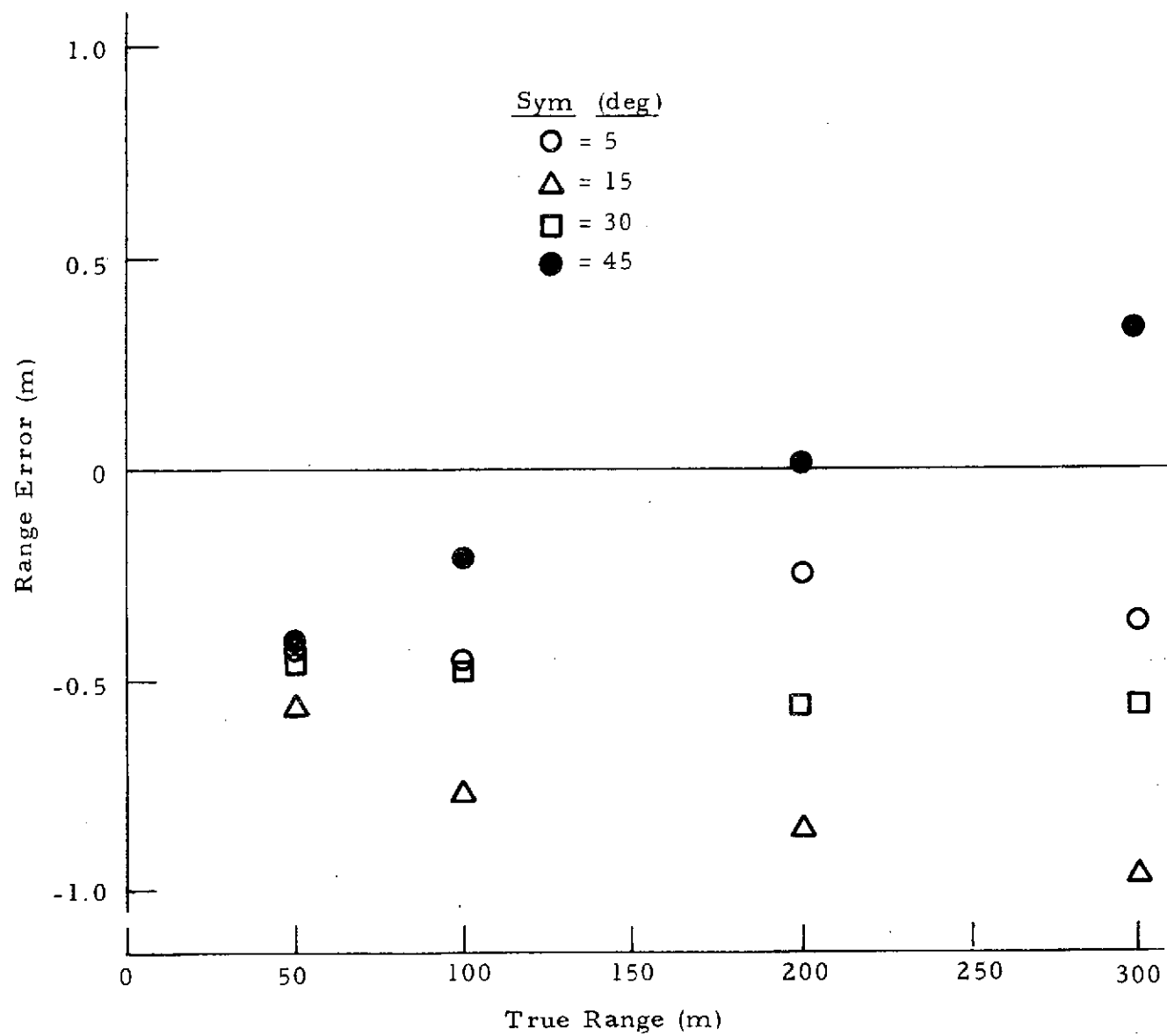
Fig. 2-14a - Errors in $R = (x^2 + y^2)^{1/2}$ After Calibration for Van 2
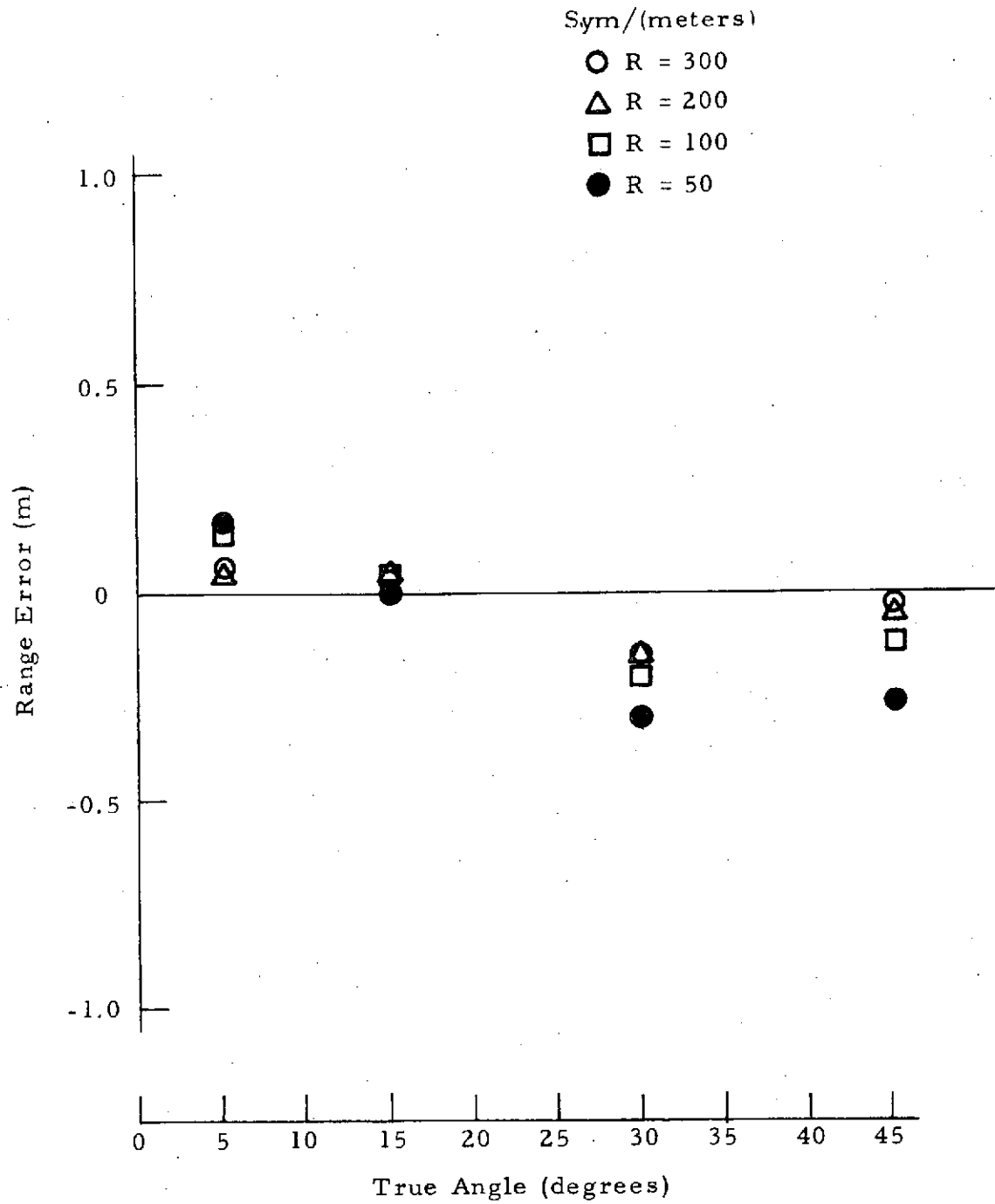
Fig. 2-14b - Errors in $\theta = \tan^{-1} (x/y)$ after Calibration (Van 2)

In addition to the above, tests were made on the shrinkage of the range scan excursion as a function of scan rate (an inevitable consequence of a finite bandwidth servo with max torque limitations, i.e., any physically realizable servo, being required to follow commands involving extremely large accelerations) and the hysteresis error between command and output range. These are shown in Figs. 2-15 and 2-16. Neither of these effects is serious, since the data readout is correct and the programmed scan excursion can always be made to yield any desired actual scan coverage; in addition, the range excursion is quite linear, hence there is no difficulty with variation of integration time in the processor.

2.2.2 Tests on Hard Target (Wheels)

After calibration the system was scanned against wheel targets at several known ranges. To obtain an indication of the behavior of the external focus, the signal back-scattered from the wheel was used as the input to a spectrum analyzer set in the non-scanning mode, with its IF bandwidth centered on the Doppler frequency, and with a video bandwidth sufficient to pass the expected modulation frequencies without distortion. Under these circumstances we would expect the signal (which is proportional to back scattered power) to indicate the variation in intensity incident upon the wheel, and to exhibit a peak at a range equal to the known target range. To determine if this was actually the case, the spectrum analyzer output and the range voltage were simultaneously recorded on a Brush recorder. Figures 2-17 and 2-18 show the results obtained at two different ranges, the computed range (obtained by projecting the time of occurrence of peak signal on to the calibrated range sweep) agrees fairly closely with the known range value.

There are two difficulties in using such a procedure:

1. The peak signal does not necessarily occur in time coincidence with the incidence of maximum intensity, since the effective backscatter is the sum of a large number of randomly phased vectors reflected from individual small grains of particulate matter (sandpaper) on the wheel surface.
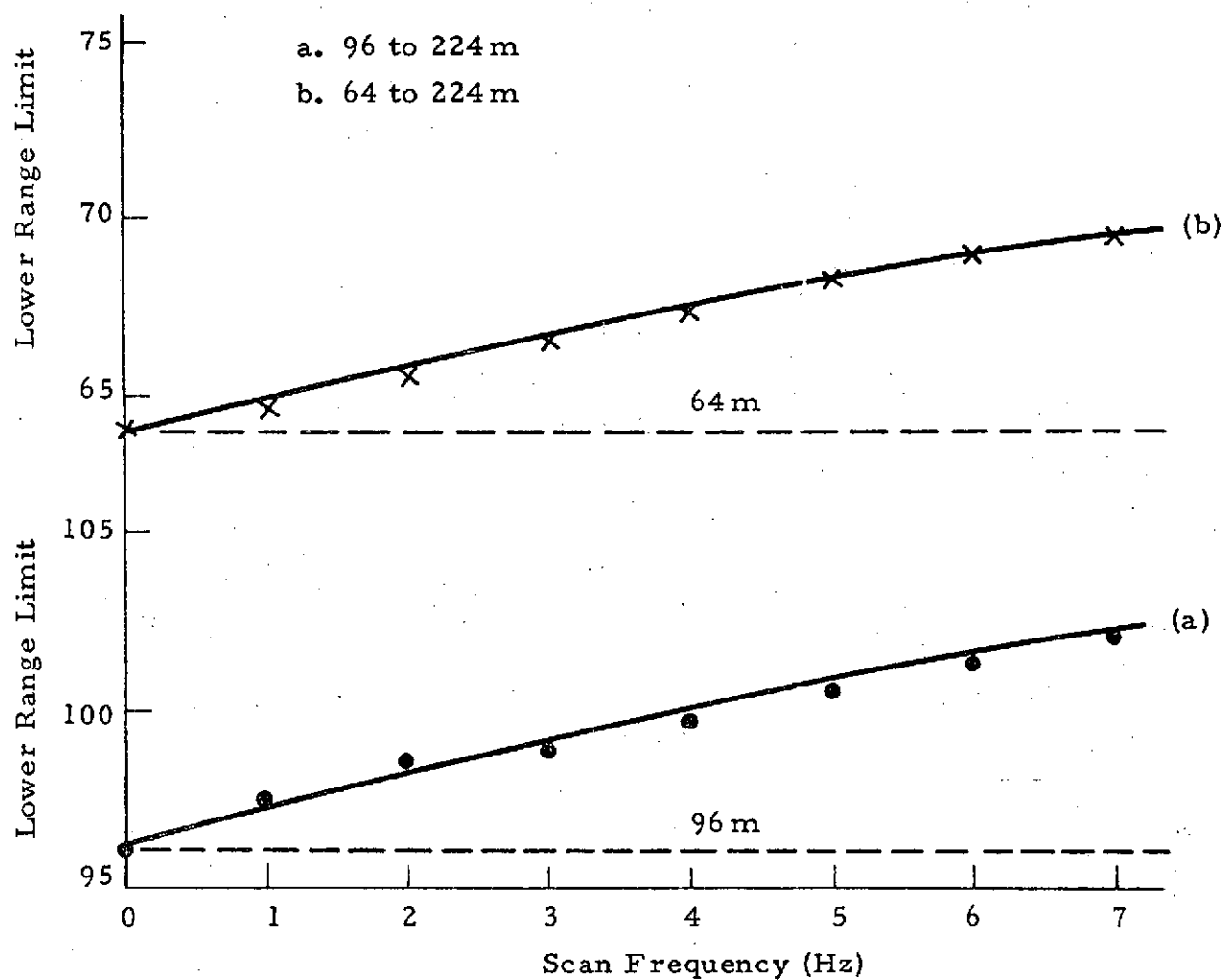
Fig. 2-15 - Range Scan Dynamic Excursion Error

Input Command	Outward Traverse R_{act}	Inward Traverse R_{act}
50	49.66	50.39
100	99.38	100.435
150	147.25	150.07
200	194.78	199.96
250	241.67	249.56
300	289.24	298.51
350	333.44	344.41

Notes: 1. Lack of symmetry with respect to input indicates gain or offset error or both.

2. Actual R determined from encoder output.

Fig. 2-16 - Static Hysteresis — Van 2 Range Servo

Range (meters)

192

76
64

0

-3 dB
points

-3 dB
points

8 m

12 m

0

Signal Level

S_{max}

Signal from Sandpaper Wheel
Video Bandwidth = 100 Hz
Scan Frequency = 4.0 Hz
Range = 76 m

Run 14, Van 1, 5-21-74
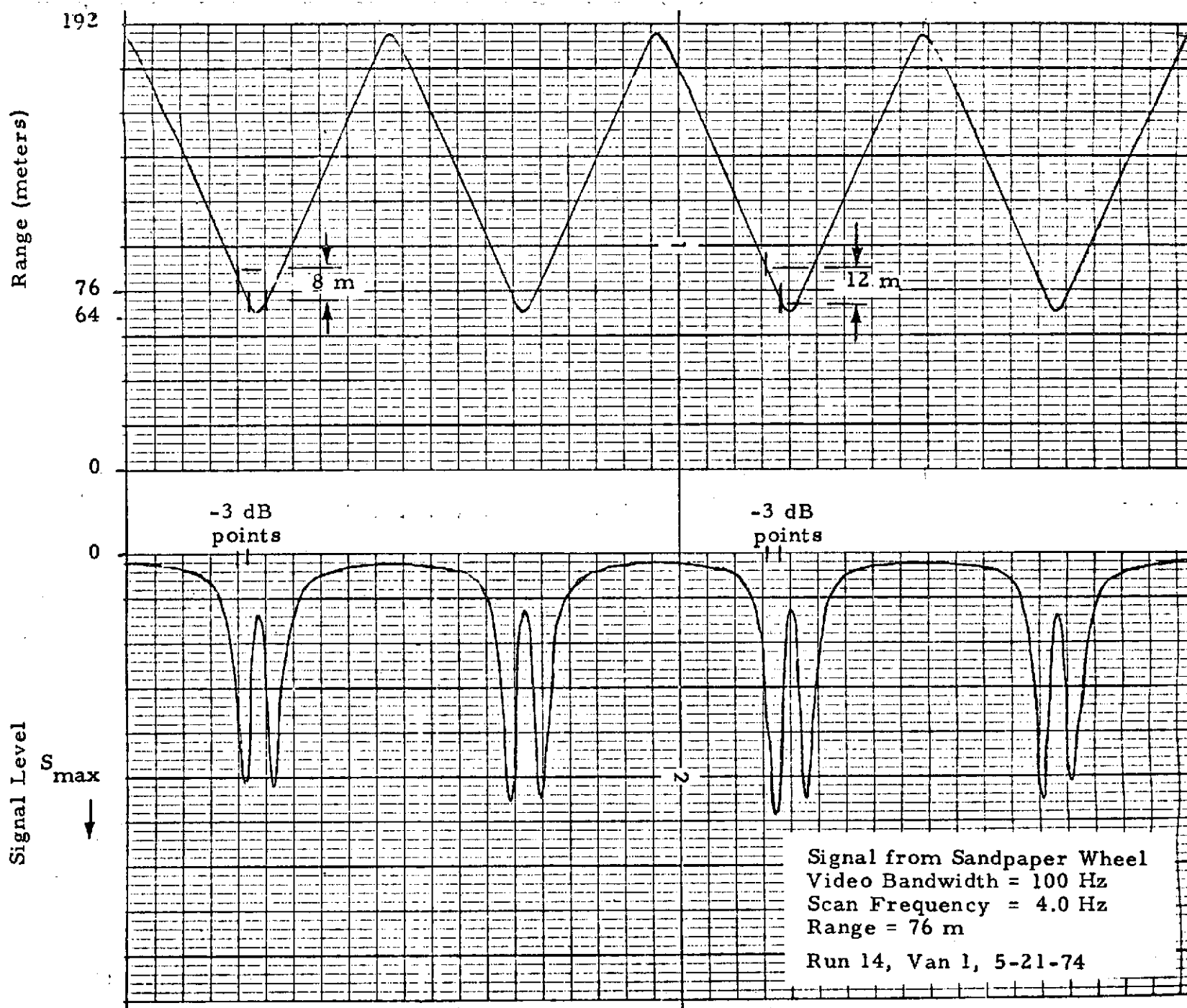
Fig. 2-17 - Signal Returned from Short Range Target

Signal from Belt Sander

Video Bandwidth = 100 Hz
Scan Freq. = 0.1 Hz
Range = 229 m
Run 1, Van 1, 5/17/74
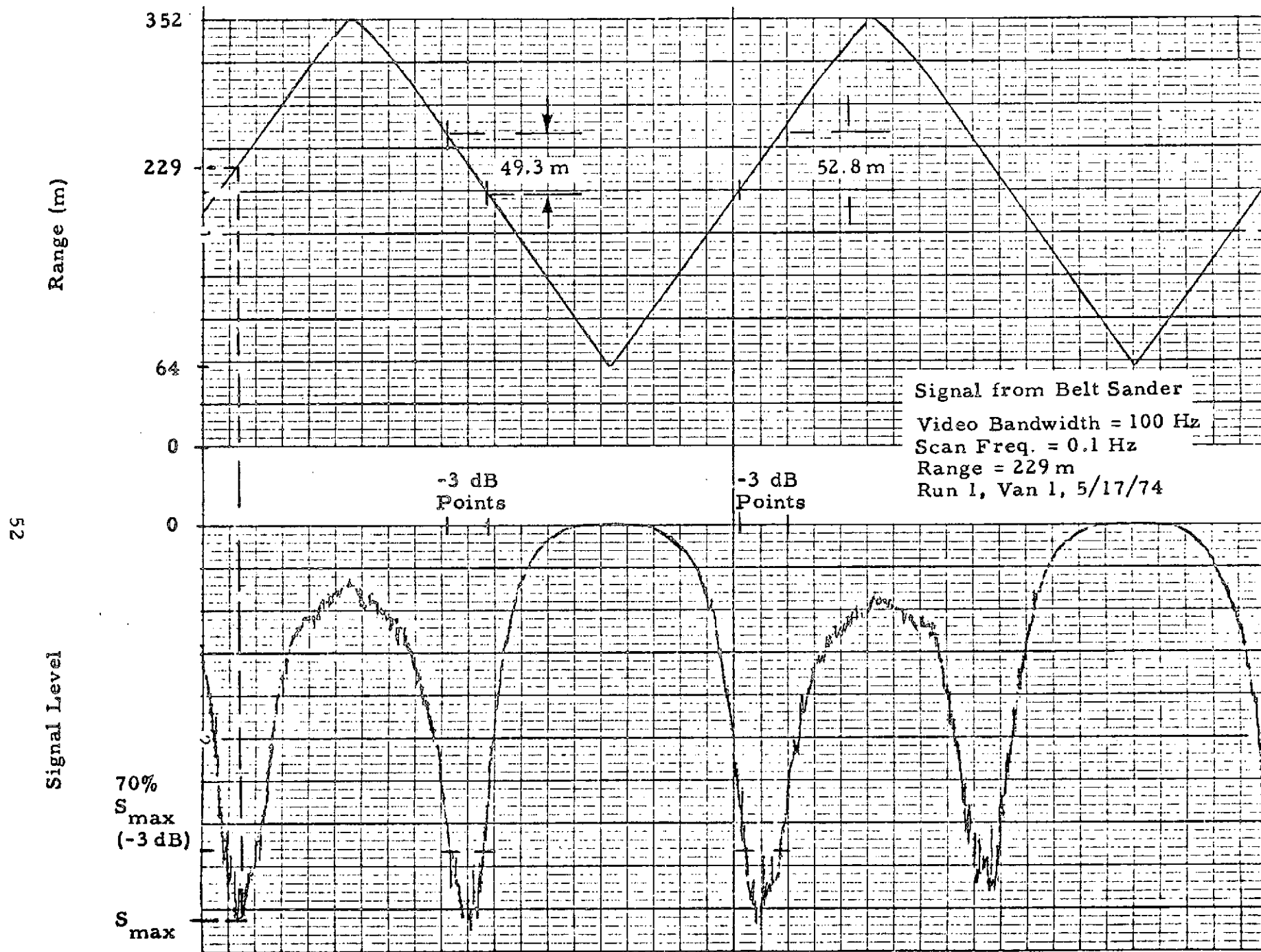
Fig. 2-18 - Signal Returned from Long Range Target

2. When the offset on the secondary mirror position is removed
    by using a target at short range, any errors in finding this
    mirror location are greatly magnified when the mirror is
    moved to a position corresponding to long range.

While it is true that the axial resolution of the system also is magnified
in the same proportion as is any setting error, this does not remove the error,
but merely makes it to be the same percentage of the axial resolution. It would,
then, be best to perform the offset alignment with a calibration target at long
range, using a very long averaging time to determine the setting corresponding
to peak value. Any setting errors resulting would be then quite small at short
range.

Since the strip chart data give the variation of signal level with focus
range, it should then be possible to determine the range interval between 3 dB
down points, i.e., the axial resolution. This was done for the ranges involved,
with results as shown in Fig. 2-19. The results are comparable to these obtained
previously on the same type of optical system using direct measurements of
the intensity variation. In Fig. 2-19 'mode' refers to heterodyning configuration.

2.2.3 Air Flow Targets

To determine the ability of the system to locate an air flow of velocity
higher than the ambient air, an airplane propeller was set up at a range of 152
meters (500 feet) and the system scanned against this in several modes. Fig-
ures 2-20, 2-21, and 2-22 show scans[*] corresponding to:

- Fig. 2-20 — Range only, with angle such as to pierce flow stream
- Fig. 2-21 — Angle only, with range fixed at 152 meters
- Fig. 2-22 — Range and angle, both dimensions enclosing target.

The expected variations are all present, i.e.,

- The peaking of the signal on the range scan, with minima
  at the extremities of the scan (Fig. 2-20).

---

[*]The recording method was as described in the preceding section, except
that now the IF filter was moved up to the neighborhood of 1.5 MHz, so
as to not respond to the (continually present) wind background signal.

Wheel, 250 ft

Scan Rate (Hz)		0.1	1	2	4	6
Mode	Van	Resolution (ft)				
Front Cavity	1	15.7	21.86	24.49	26.24	36.7
	2	X	24.20	23.70	25.80	X
Secondary L.O.	1	13.3	34.98	34.98	21.50	34.9
	2	X	31.16	35.50	38.80	X
Separate L.O.	1	16.9	14.60	X	28.90	36.2
	2	28.9	32.80	33.90	32.30	X

Belt, 750 ft

Scan Rate (Hz)		0.1	1	2	4	6
Mode	Van	Resolution (ft)				
Front Cavity	1	162.7	150.6	X	141.5	X
Secondary L.O.	1	136.8	137.8	X	144.0	X
Separate L.O.	1	134.9	144.6	X	142.7	X

Fig. 2-19 - Signal Returned from Long Range Target
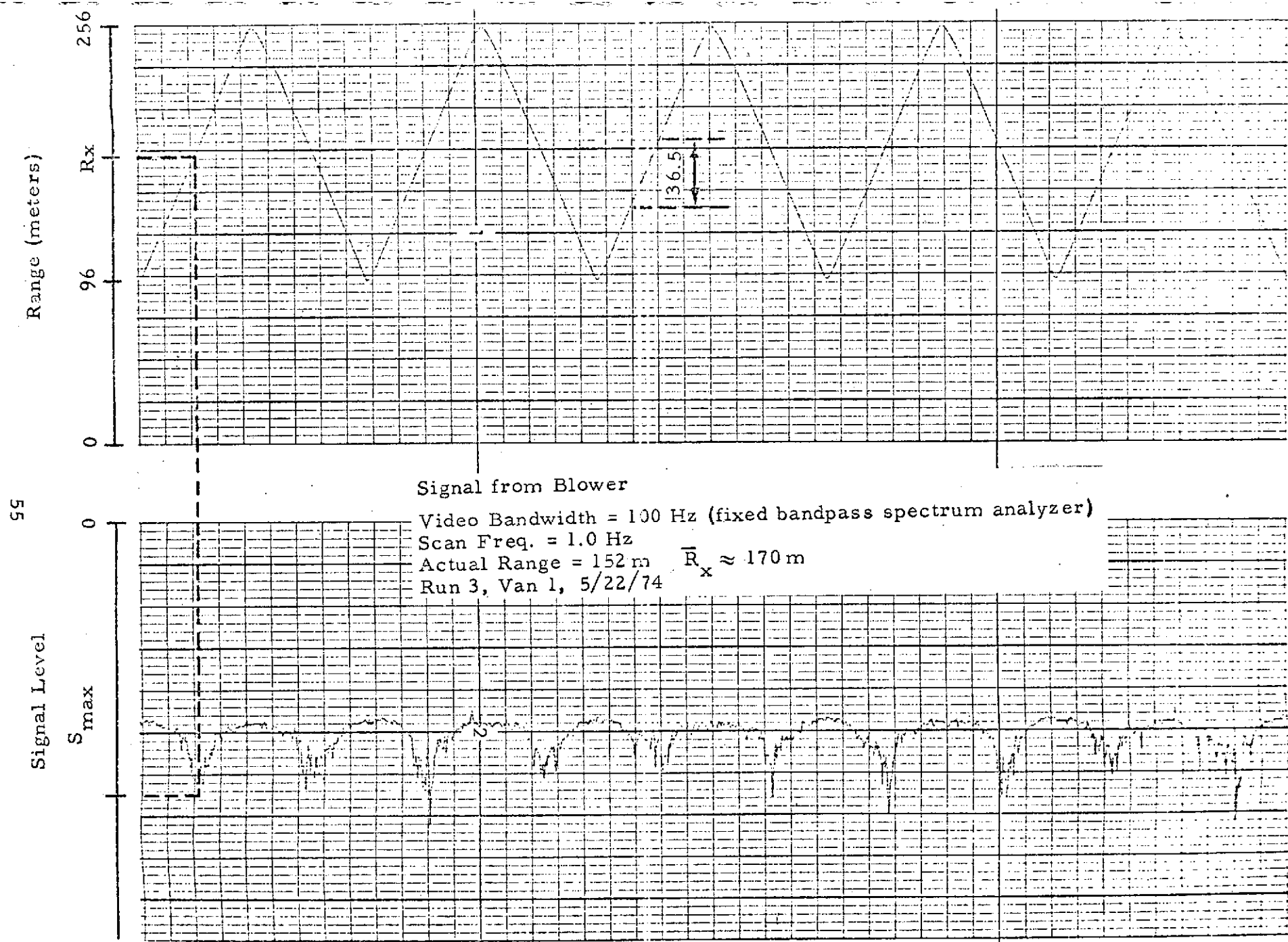
Fig. 2-20a – Signal Returned from Airstream – Slow Scan (Range Only)

Range (meters)

256

R_x

96

0

Signal Level

0

S_{max}

Signal from Blower

Video Bandwidth = 100 Hz (fixed bandpass spectrum analyzer)
Scan Freq. = 4.0 Hz
Actual Range = 152 m $\overline{R}_o \approx 172$ m
Run 3, Van 1, 5/22/74
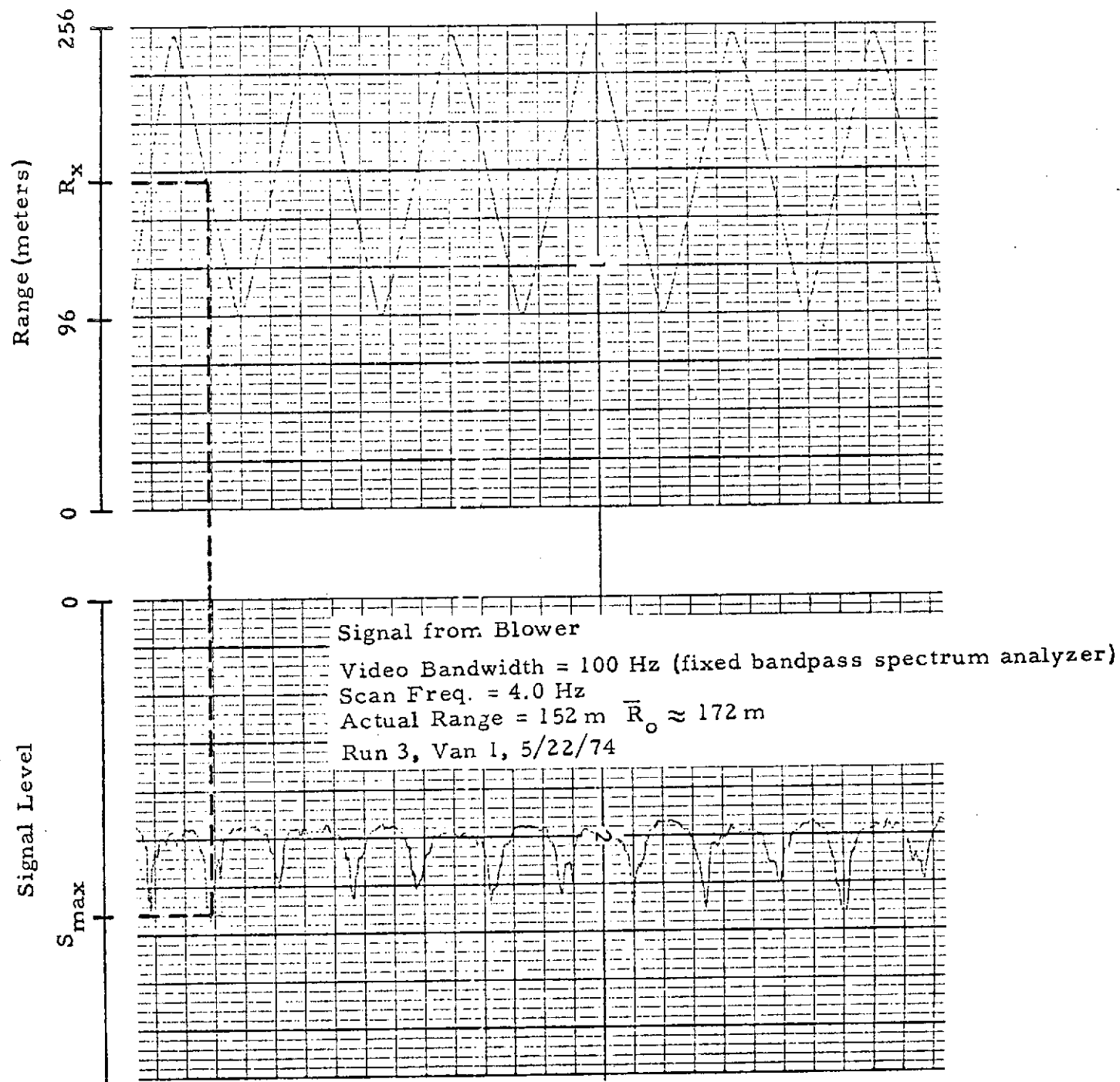
Fig. 2-20b - Signal Returned from Airstream - Fast Scan (Range Only)

Signal From Blower ... Run 14 Van 1
Angle Scan Only 3.2 to 16 deg at 0.1 Hz
Range Focused at R $\approx$ 159 m

40 Divisions ——→   ←——   30 Time Divisions ——→
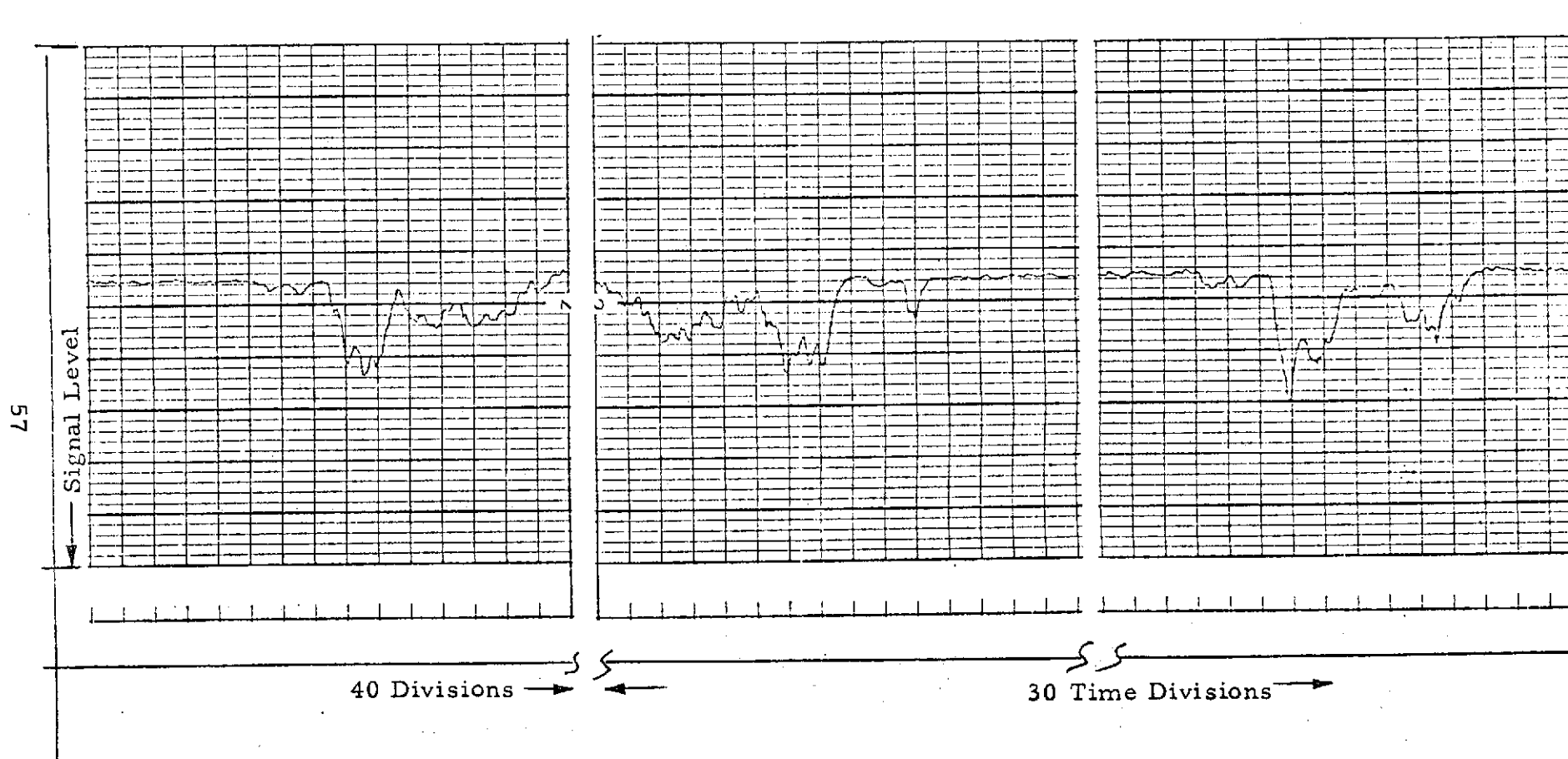
Fig. 2-21 - Signal Returned from Airstream (Angle - Only Scan)

Range (m)

256

96

0

0.1 sec

Signal from Blower Range and Angle
Scan - Run 16, Van 1

Range Scan ... 96 to 256 at 6.1 Hz
Angle Scan ... 3.2 to 16 deg at 0.1 Hz

Air Column Diam. (calculated from data) = 16 ft
Propeller Diam.   14 ft

Signal Level

0

25
Divisions

58
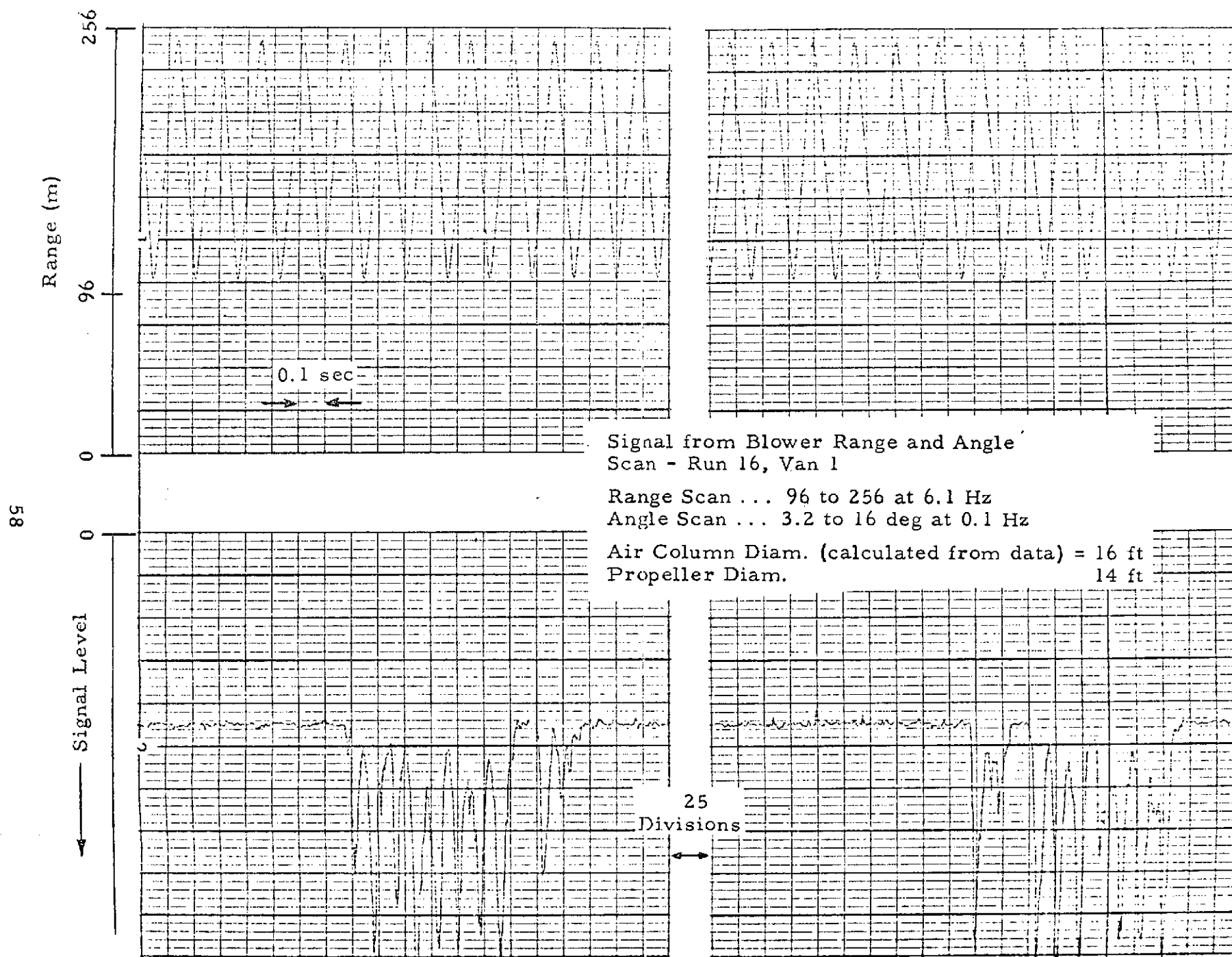
Fig. 2-22 - Signal Returned from Airstream (Range and Angle Scan)

- The (more or less) continuous signal available over a finite angular region, with noise only outside this region, as exhibited by angle-only scan (Fig. 2-21).

- The group, finite in number, of periodic signal maxima, with "dead space" between such clusters, exhibited by the range and angle scan.

Two computations were made from these data: (1) the average range to the peak signal; and (2) the physical extent of the "signal-present" region in the angular scan-only mode. The range measurement average gave a location of 170 meters, i.e., about 18 meters longer than the correct value (the individual readings were always within $\pm$ 3 meters of this average value). The second measurement gave a value of 16 feet for the diameter of the airstream containing velocities significantly higher than the wind. This compares quite well with the known diameter of the propeller span, which was 14 feet (some spreading out of the airstream is to be expected).

The range discrepancy was later checked against a wheel target, and was found to be still present. The system was then adjusted for zero offset against a target at 700 feet, and the location of the peak determined for a wheel at 500 feet. The location thus determined was within $\pm$4 meters of the true location. This result emphasizes the importance of a very careful initial offset alignment, preferably done at long range[*]. It also emphasizes that the major error in locating a flow field will not be due to inaccuracies in the system readouts, but in the displacement of the peak signal due to random signal fluctuations arising from the relative locations and backscatter magnitudes at the aerosol particles comprising the target. In order to locate accurately, the intensity pattern (illumination) must move across the particle stream at a speed such that the same assemblage of particles is present during the entire time taken to change the illumination by a significant amount. If a new array of particles enters the beam while the focus is moving, it will be impossible to distinguish signal level changes due to the changing illumination from signal level changes arising from the new array of scatterers. The latter can easily create 10 dB or more signal change.

---

[*]This is difficult to do, since movement of personnel in the van can result in a slight tilt of the floor, changing the location of the incident spot on the wheel and the corresponding Doppler shift. In addition, fluctuations at signal level are always present, obscuring the location of the maximum.

A series of similar tests scanning against the same blower airstream, now moved to 85 meters range, was made several days later. Some of the results, recorded in the manner just described, are shown in Figs. 2-23, 2-24 and 2-25. While the general nature of the signals is similar to those previously obtained, we note that only at the higher scan speeds was it possible to obtain a consistent estimate of the target location. One would expect that at short range the slower scan speeds would be acceptable, if we consider the following:

Let

$$\tau_p = \text{particle population renewal time}$$

$$\tau_p = \frac{\lambda \, R/d}{V_p \, \sin \theta}$$

$$\tau_s = \text{scan modulation time}$$

$$\tau_s = \frac{\lambda \, (\dot{R}/d)^2}{R}$$

$$\tau_p / \tau_s = (\dot{R}/v_p \, \sin \theta) \times d/R$$

where

$$\lambda \qquad = \text{wavelength}$$
$$R \qquad = \text{range to airstream}$$
$$d \qquad = \text{effective optical aperture diameter}$$
$$v_p \, \sin \theta = \text{cross-beam velocity of particles}$$
$$\dot{R} \qquad = \text{scan velocity}$$

We note that other things being equal, τ_p / τ_s varies as $1/R$. It is also true that at short range, due to the $1/R^4$ behavior of the illuminated volume, the ratio of mean to standard deviation of the wind background signal is very much diminished (the volume of the higher speed particles in the airstream is constant) so that the occasional large particles at wind velocity may cause excitation of the higher frequency filters (since their spectrum is spread out because of short signal duration) and obscure the scan modulation of the airstream. Additional tests should be made to determine the quantitative nature of these effects.
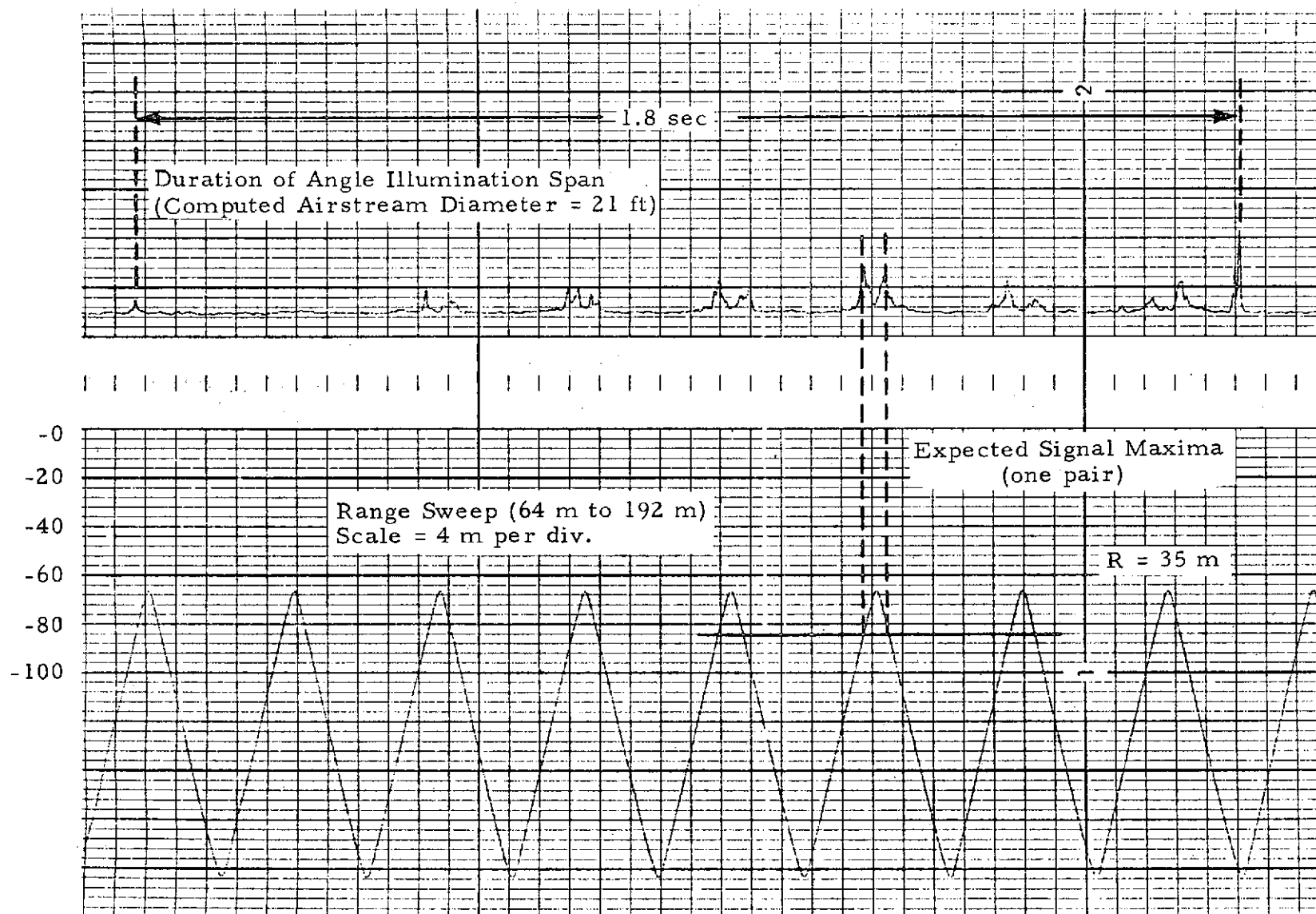
Fig. 2-23 - Range and Angle Scanning (64 to 192 m at 4 Hz, 3.2° to 16° at 0.1 Hz)
Typical Signal Segment - Propellor at R = 85 m, Van 2, 11 June 1974
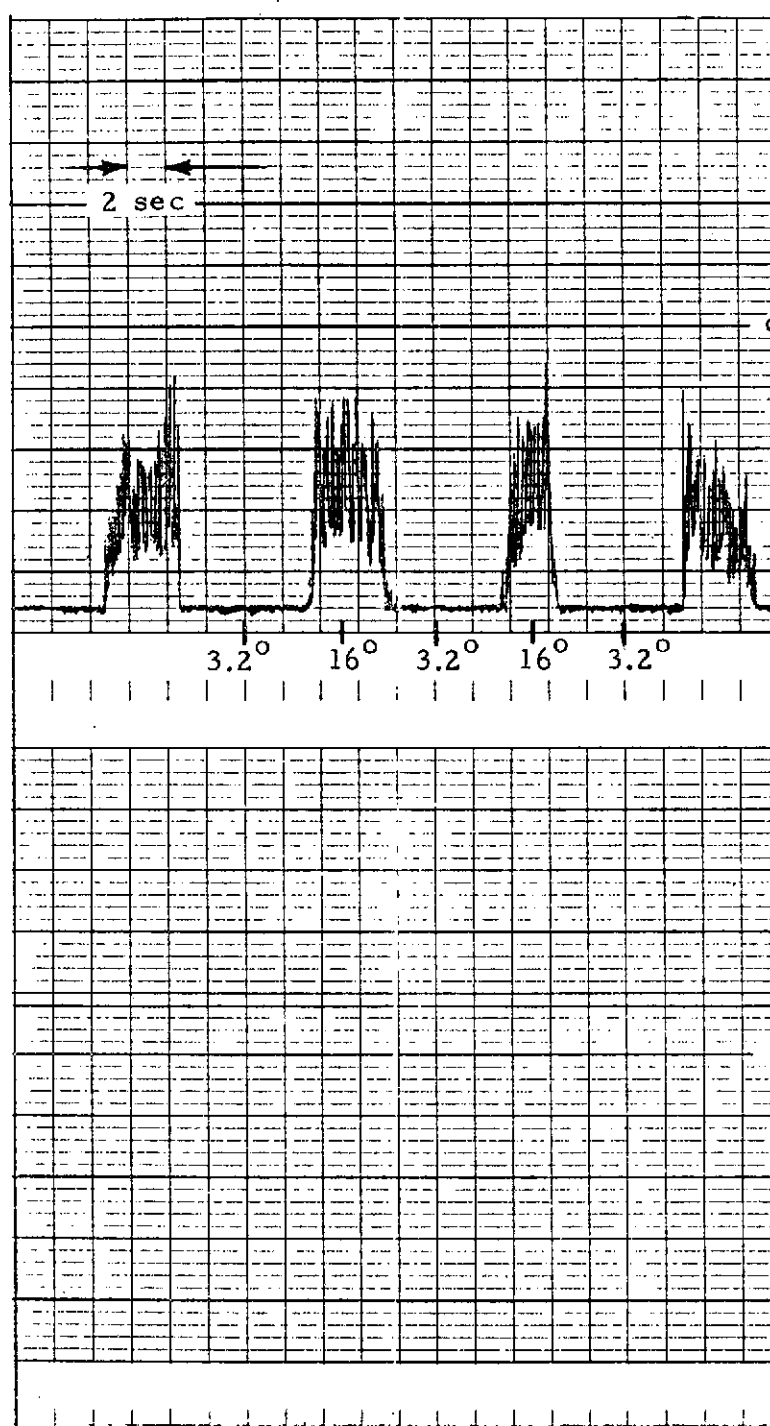
Fig. 2-24 - Angle-Only Scan (R = 85m, Target Range;
θ = 3.2° to 16° at 0.1 Hz, Van 2, 11 June 1974)

Gain Change

R = 85

R = 85
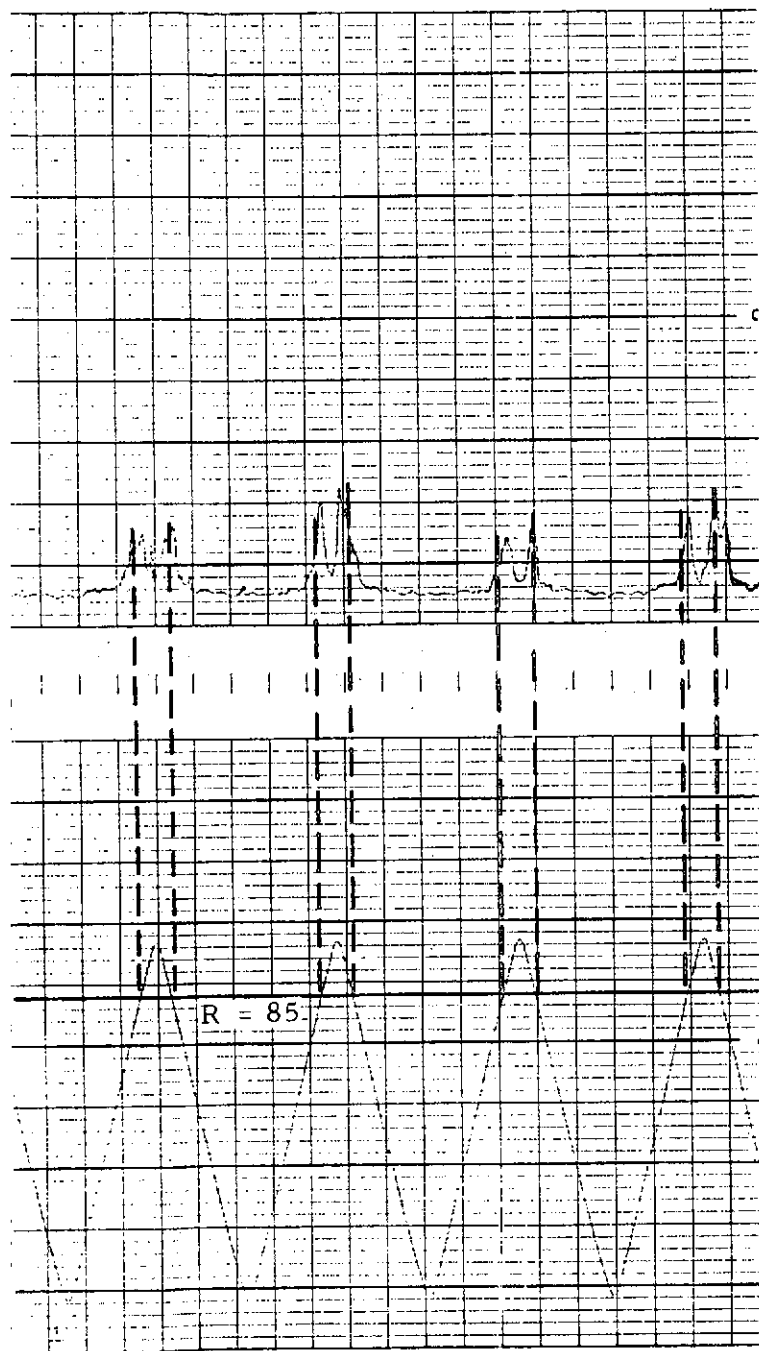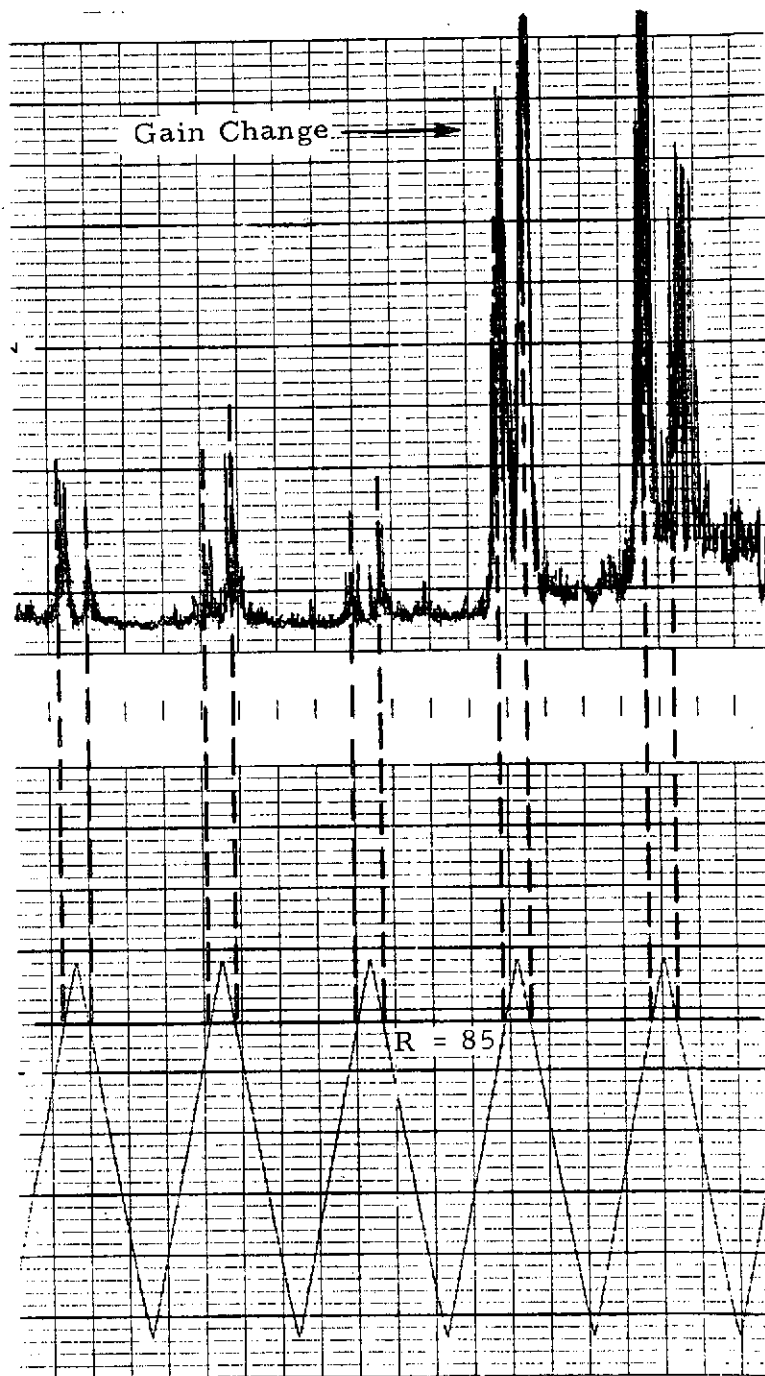
a. 4 Hz Range Scan

b. 0.1 Hz Range Scan

Fig. 2-25 - Range Scan, Propeller at R = 85m, $\theta = 10^{\circ}$ (Constant),
R = 64 to 192 m, Van 2, 11 June 1974

In addition to the data presented in Figs. 2-20, 2-21, and 2-22 which were obtained with the use of a spectrum analyzer, the outputs from the processor were used to obtain estimates of target range and spatial resolution, under the condition of range-only scan with the airstream target at 152 meters range. To obtain these estimates, the signal strength as a function of range was plotted for several scans. The measure of signal strength used was the mean over 10 successive 4 msec integration intervals of the amplitude of the filter which displayed the peak indication (the wind peak being ignored). The data are shown in Fig. 2-26.

The propeller wake was at a range of 152 meters but appears in the data as being at a range of 170 meters due to a scanner range misadjustment. Estimates of the separation between the 3 dB gain points of the curve yields a value (corrected for the range misadjustment error) ∼ 25 meters. If the spatial extent of the flow field (∼ 5 meters) is subtracted an estimate of the spatial resolution of ∼ 20 meters at a range of 150 meters is obtained. This is in excellent agreement with the values obtained using hard targets obtained during the Astrionics testing.

Run 402

●●●●● ⟶

+ + + + ⟵

ᵒᵒᵒ ᵒᵒᵒ ⟶

× × × × × ⟵

⌐◻◻◻◻◻ ⟶

Signal Power (Linear Arbitrary Unit)

80

60

40

110   130   150   170   190   210   230
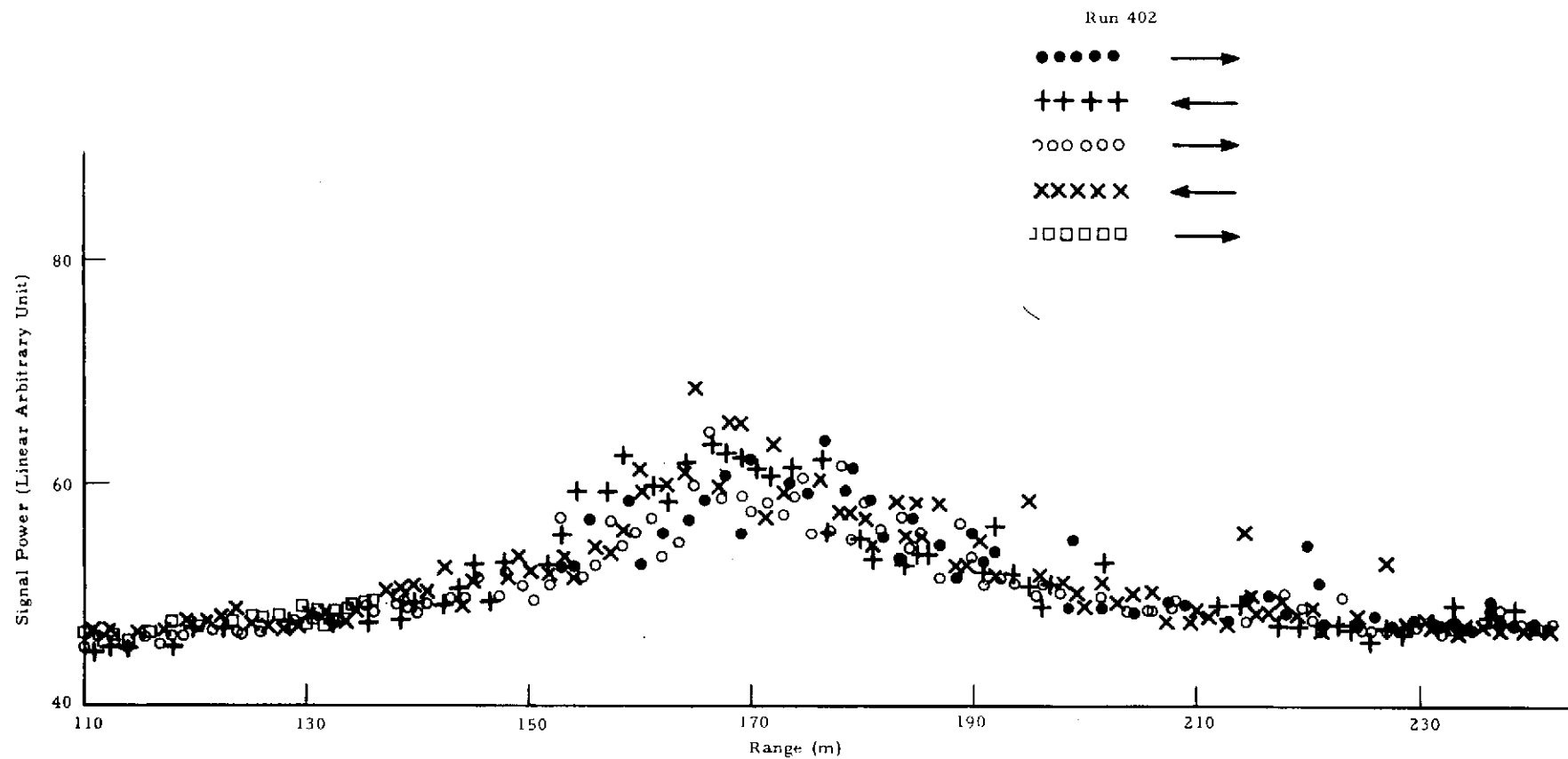
Range (m)

Fig. 2-26 - IPEAK* Versus Range for Propeller Wake Target (*Mean of 10 Consecutive Estimates)

Section 3

LASER DOPPLER SYSTEM OPTICS TESTING AND OPTIMIZATION

Authors: Dr. C-C. Huang
L. K. Morrison
J. L. Jetton

Lockheed-Huntsville personnel have performed numerous laboratory and field tests on the optical components of the laser Doppler system under the subject contract. Laboratory optical tests were performed and documented by C-C. Huang with L. K. Morrison and J. L. Jetton assisting. Various field tests were performed by each of the above individuals. The primary objectives of these tests were to: (1) evaluate Lockheed, Raytheon and other vendor-provided components of the laser Doppler systems; (2) optimize performance of marginal components; and (3) develop new techniques to surmount unforeseen difficulties (such as secondary backscatter).

Section 3.1 includes discussions of the backscatter problem and several approaches which were tried to develop a solution to this problem. Initial Lockheed-Huntsville system calibration tests are discussed in Section 3.2. Spatial resolution and system signal-to-noise ratio tests conducted in the laboratory are presented in Section 3.3. Section 3.4 presents signal-to-noise ratio and spatial resolution measurements made in the field and compares these results with theoretical results. Section 3.5 presents tests results for the interferometer tests and polarization tests of the lasers used in the system. Section 3.6 provides a discussion of ideas for developing bias circuitry. The Isomet acousto-optical translator is discussed in Section 3.7.

3.1 SECONDARY MIRROR BACKSCATTER REDUCTION

Several methods have been suggested by NASA, Lockheed and others for reducing telescope backscatter radiation returns to the detector. These

returns, before reduction, make operation in the Mach Zehnder interferometer configuration impractical with a low power coherent detector. Without reducing the backscattered radiation from the secondary, this backscattered portion of the local oscillator power is larger than the desired local oscillator power.

Methods suggested to reduce this undesirable local oscillator level have included use of:

- Hole in 45-degree mirror
- Spatial filter
- Wire in front of secondary, and
- Location of $\lambda/4$ plate and lens between secondary and primary

The analyses of these techniques are discussed in Section 3.1.1, while actual tests results of the first three techniques are presented in Section 3.1.2.

3.1.1 Analysis of Backscatter Reduction Techniques

- **Hole in 45-Degree Mirror Approach**

A method proposed to reduce the backscatter from the secondary mirror of the LDV is shown in the sketch on top of the next page. The central part of the laser beam will be a "dark" shadow after reflection by the 45-degree mirror with a 1.41 mm hole in the middle. Unfortunately the shadow will close up at a Rayleigh distance (d^2/λ) which is 10 cm away from the 45-degree mirror. The backscatter from the secondary mirror possesses a central "bright" shadow beyond a 10 cm distance.

The diffraction pattern of the 45-degree mirror with a 1.41 mm hole can be produced analogously with aid of a CO_2 laser beam incident upon a 6 mm circular aperture with an opaque ball (1 mm in size). We can therefore investigate the diffraction pattern of that ball as shown on the sketch at the bottom of the next page.

45° Mirror
w/hole

1.41 mm

d = 1 mm

Secondary
Mirror

$\frac{\lambda}{4}$ Plate

Primary
Mirror

Brewster Angle
Ge Coupler

≈ 100 cm

6 mm CO_2
Laser Beam

Opaque Ball

Screen

Diffraction
Limited CO_2
Laser Beam

1 mm

6 mm

100 cm

Circular
Aperture

69
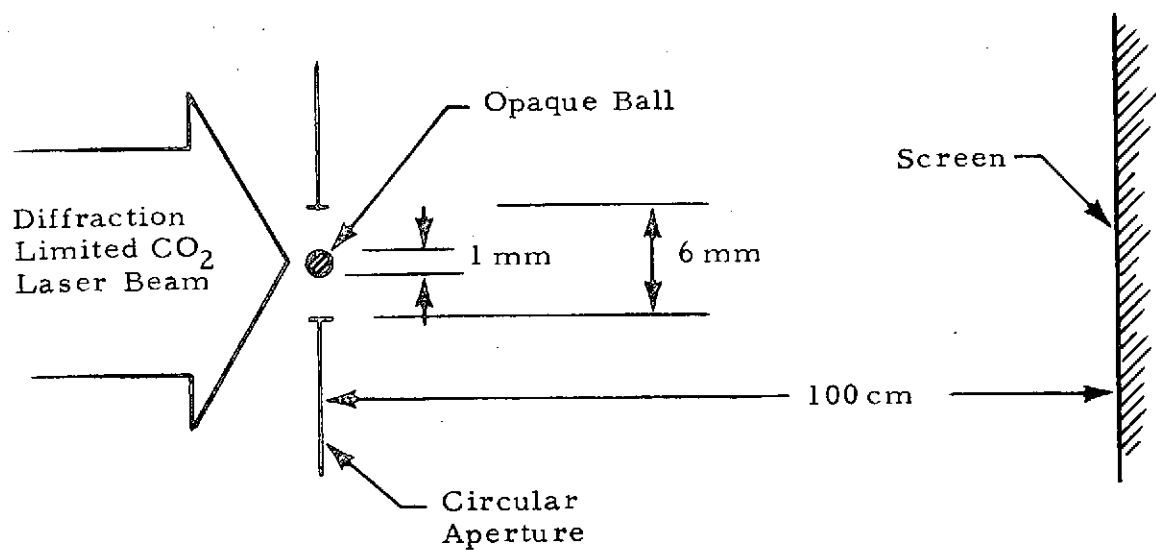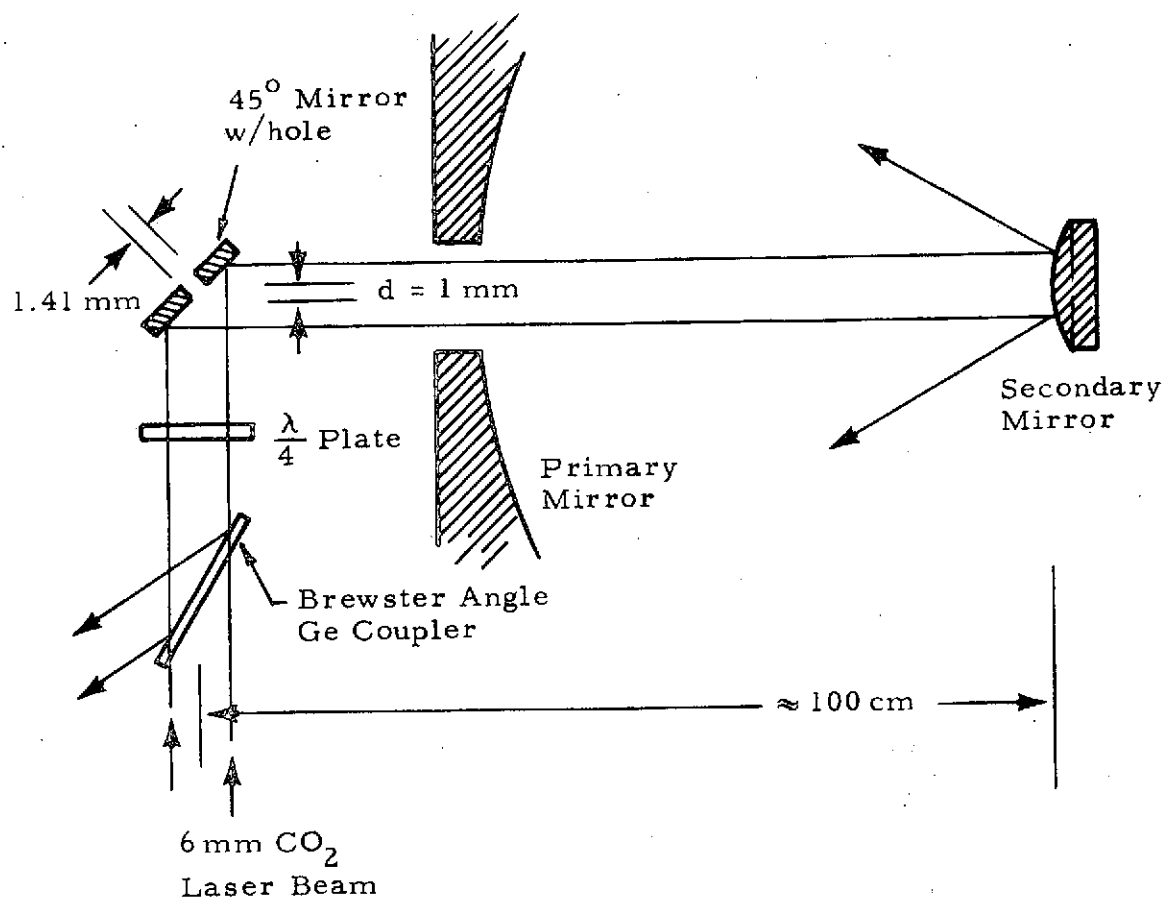
These arrangements can be scaled longitudinally and laterally by a factor of 16.8 for easier diagonistics by utilizing an He-Ne laser rather than a CO_2 laser.

The following arrangement for the 0.6328 μm He-Ne laser should lead to conclusions that can be scaled for CO_2 lasers.
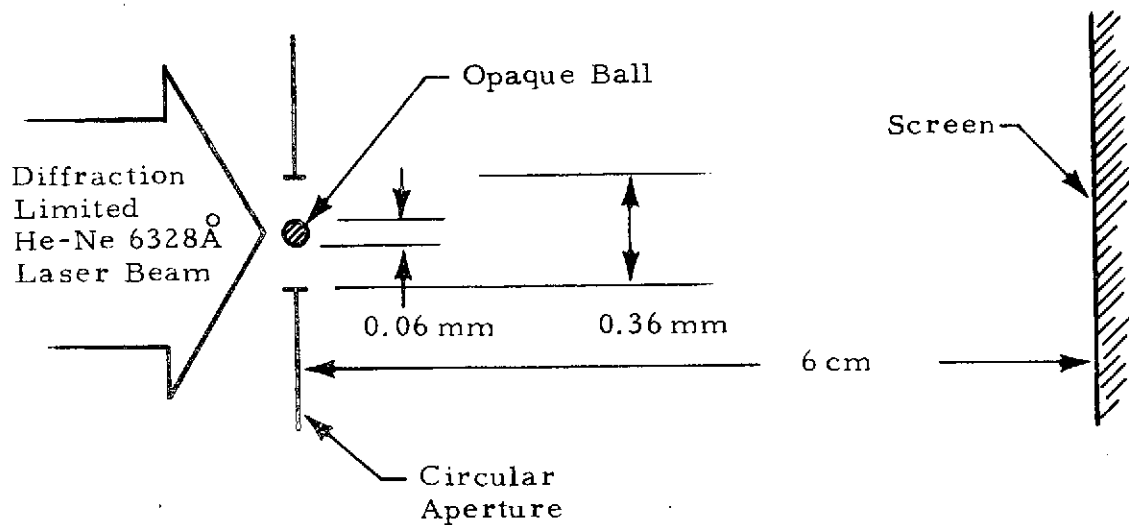
Instead of a 0.36 mm circular opening with an opaque ball (0.06 mm in diameter), a circular opening (0.4 mm) with a metal wire (gauge No. 40 or 0.003 in. or 0.076 mm in diameter) was used in the experiment to measure the diffraction pattern of the wire without loss of generality.

When the screen was located just behind the aperture, the dark shadow of the wire was observed as expected. When the screen was placed 1 cm away from the aperture the central dark shadow could not be observed. A central "bright" shadow of diameter $\sim$0.2 mm was observed on the screen 6 cm away from the aperture and the "bright" shadow extended toward infinity.

We conclude that employing a 45-degree mirror with a hole in the middle is probably not the solution to eliminate the backscatter from the secondary mirror.

● Spatial Filter Approach

Another method proposed to reduce the backscatter from the secondary mirror of the LDV is shown schematically by the following sketch.
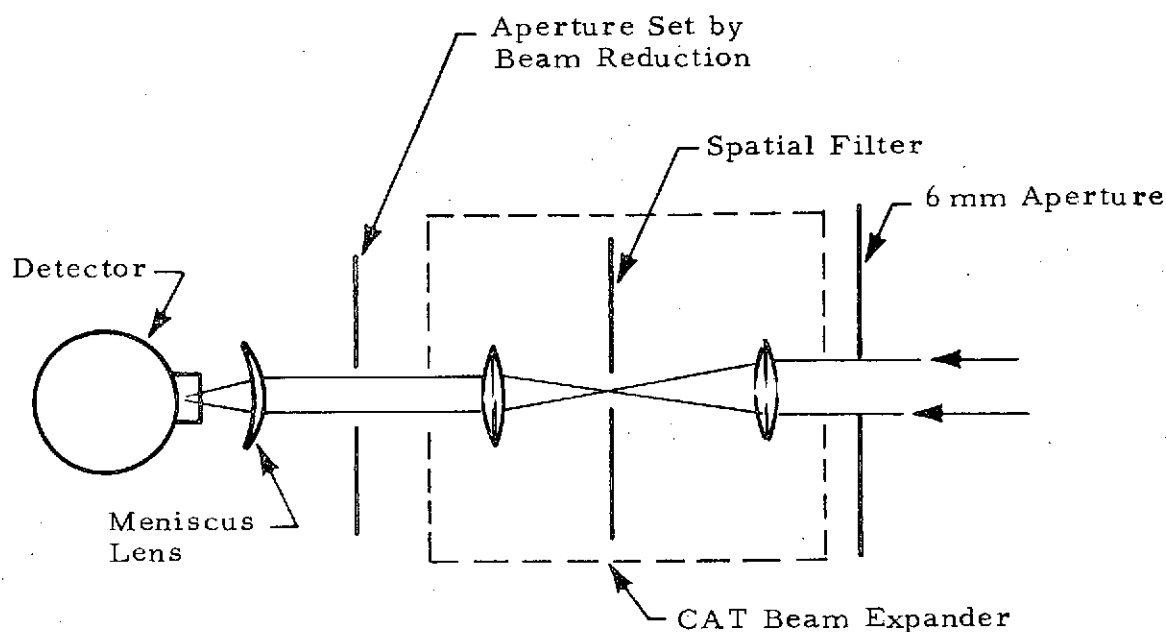
The spatial filter will transmit collimated radiation through the pin hole and block the backscatter from the secondary mirror. In this way the backscatter can be reduced. However, as the actual reduction in back-scatter power is much less than 13 dB under most circumstances as ex-plained in the following analysis.

Since the diffraction limitation can only focus a 6 mm CO_2 laser beam to a diameter $2\omega_{0\infty} = 0.0226$ cm by using a 10 cm focal length lens, a

71

pin-hole size ≥ 0.0226 cm is required for the spatial filter. The back-scatter from the secondary mirror can be regarded as a point source 60 cm away from the 10 cm focal length lens and focused to a point 12 cm behind the lens.

In the following figure we have:

$$\theta = \lambda/\pi\omega_{0\infty}, \quad 2\theta \approx 0.6/10 \text{ rad}$$
$$2\omega_{0\infty} = 4\lambda/2\pi\theta \approx 0.0226 \text{ cm}$$

where $\lambda = 10.6\,\mu\text{m}$.
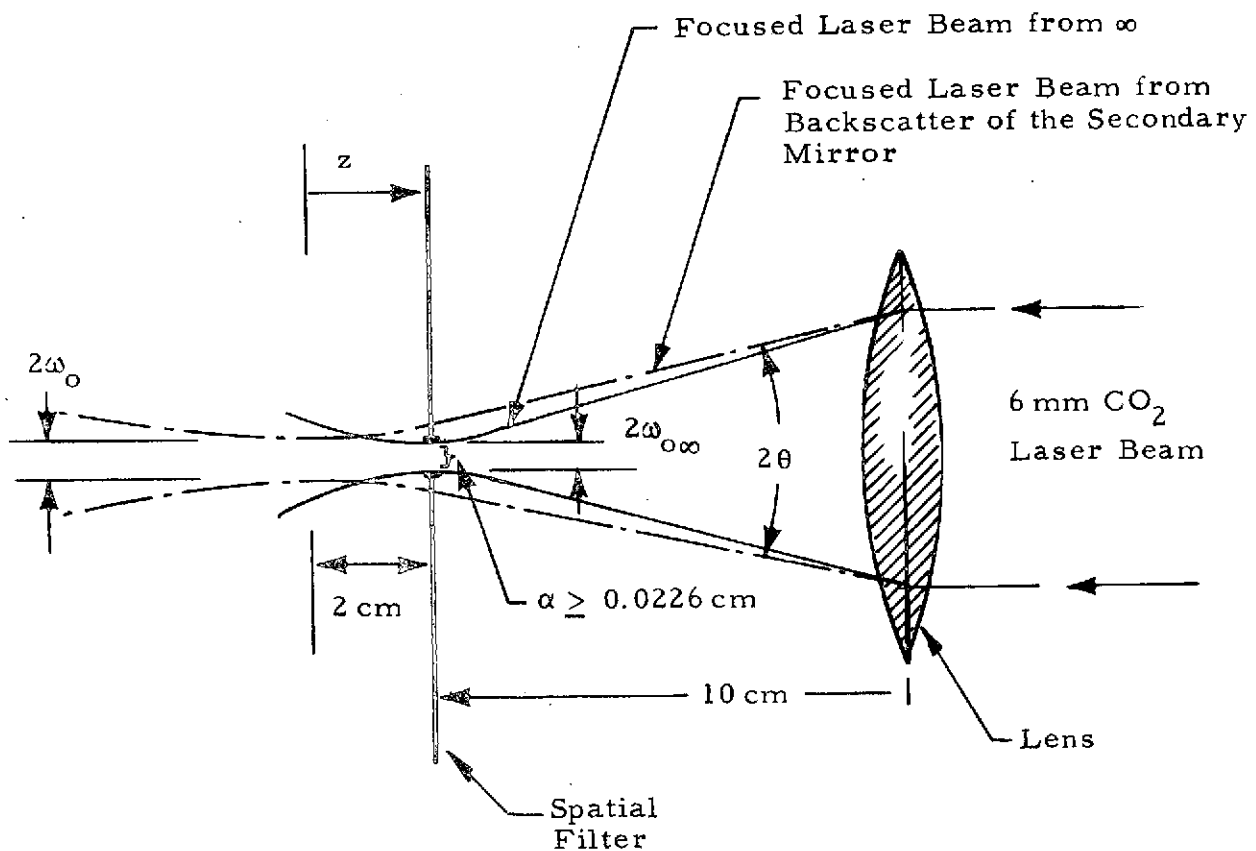
The spot size of the backscatter from the secondary mirror at the spatial filter position can be expressed as[*]

$$2\omega(z) = 2\omega_o \left[1 + (\lambda z/\pi \omega_o^2)^2 \right]^{1/2}$$

where $z = 2.0$ cm in this case and gives $2\omega(z) = 3.84 \times (2\omega_o) = 0.1025$ cm.

The attenuation of the secondary mirror backscatter is much less than $10 \log (2\omega(z)/2\omega_{o\infty})^2 = 10 \log 21.0 = 13.23$ dB because of the Gaussian distribution in laser intensity.

The maximum attenuation of the backscatter from the secondary mirror has been calculated and plotted as shown in the following sketch versus the focal length of the lens used to focus the signal from infinity through a best matched spatial filter.

Secondary Mirror Backscatter Attenuation vs Lens Focal Length
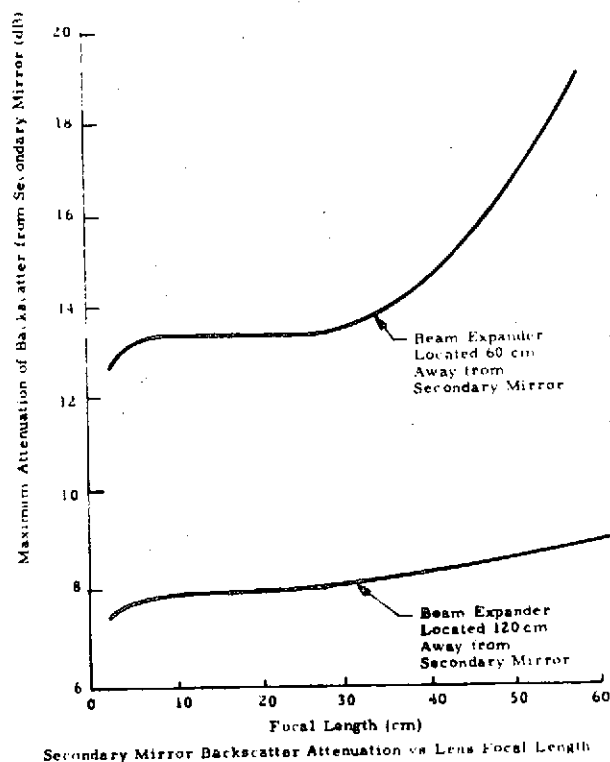
[*]Kogelnit, H., and T. Li, "Laser Beam and Resonators," Proc. IEEE, Vol 54, No. 10, October 1966, pp. 1315-1316.

● Shifted $\lambda/4$ Plate and Lens Approach

In the following paragraphs, a method (untested) is discussed of pre-venting undesired laser power being seen by the detector, the origin being the reflection of laser power from the telescope secondary mirror through the central hole of the telescope primary mirror.

A diagram of this isolation technique is depicted below:
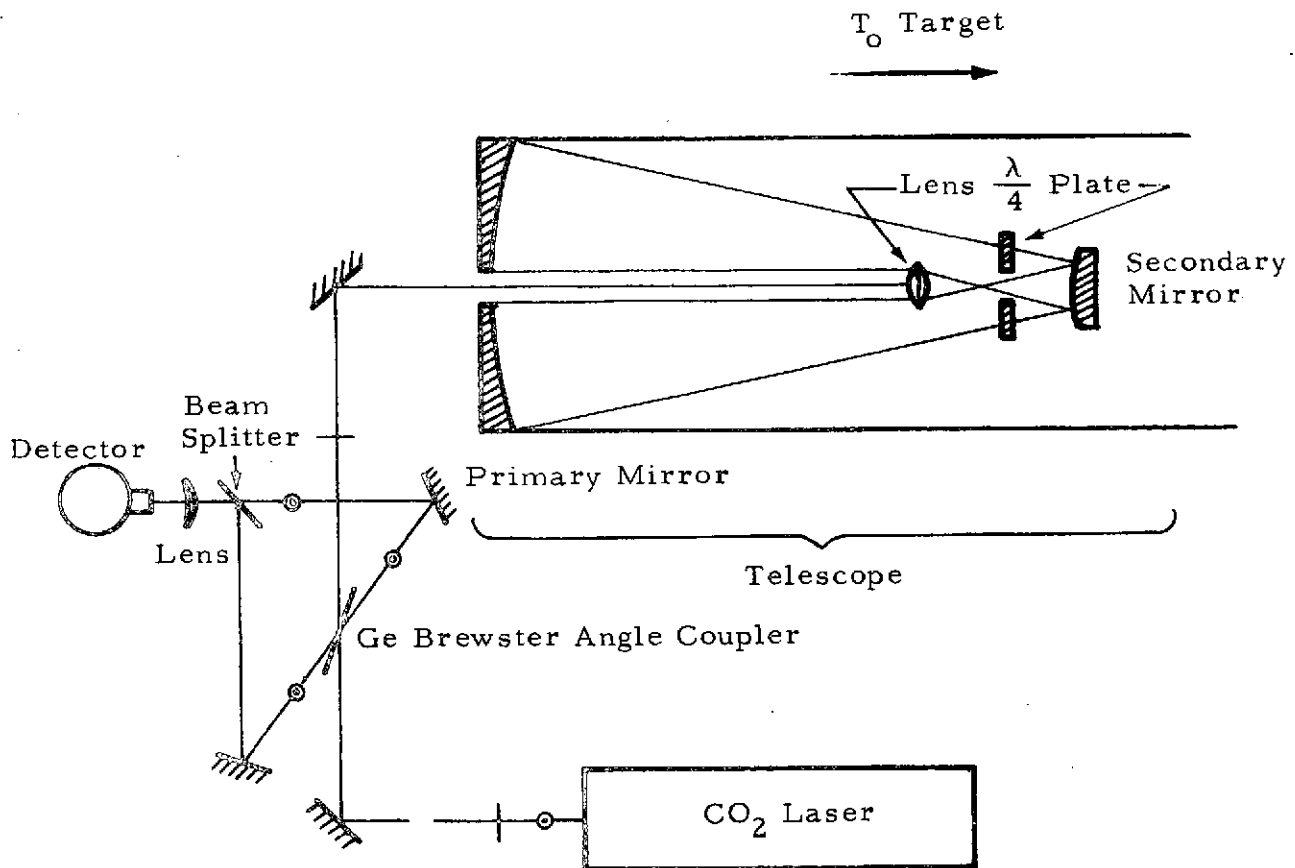
Most of the s-wave from the CO_2 laser is reflected by the Ge coupler. The transmitted CO_2 laser is approximately 100% p-wave. The laser is focused through the central hole of a $\lambda/4$ plate by a lens and then reflected by the secondary mirror. The laser beam through the $\lambda/4$ plate is then circularly polarized and transmitted to targets via the primary mirror. The backscattered laser radiation from target is collected by the primary mirror and passed through the $\lambda/4$ plate. After this stage the radiation from target is changed from circularly polarized radiation into a s-wave. After the collection by the secondary mirror through the central hole of the $\lambda/4$ plate, this s-wave is reflected by the Ge coupler, mirror, beamsplitter and into the detector.

The reflection loss from the central portion of the secondary mirror will retain the same polarization as the incident laser beam and will transmit through the Ge coupler with a polarization that will not be sensed by the detector. We can have nearly 100% isolation between the reflection loss from the secondary mirror and the aerosol signal only under the assumption that the outgoing laser beam through the Ge coupler is 100% linearly polarized.

The configuration of the optics for this system is shown on the following page.

The laser power loss due to this configuration can be estimated by assuming that the intensity distribution of the outgoing laser beam from the telescope secondary mirror is gaussian over the $\lambda/4$ plate. The laser power transmitted through the $\lambda/4$ plate and focused upon the target is

$$P = P_o \frac{2}{\sqrt{\pi}} \int_{u_{min}}^{u_{max}} e^{-u^2} du$$

$$= P_o \frac{2}{\sqrt{\pi}} \int_o^{u_{max}} e^{-u^2} du - P_o \frac{2}{\sqrt{\pi}} \int_o^{u_{min}} e^{-u^2} du$$

4" | 2" | 1.65"

f/2 Outgoing Laser Beam (Extreme Ray)

$\frac{\lambda}{4}$ Plate

Lens

5 mm Incoming
Laser Beam

Telescope
Secondary
Mirror
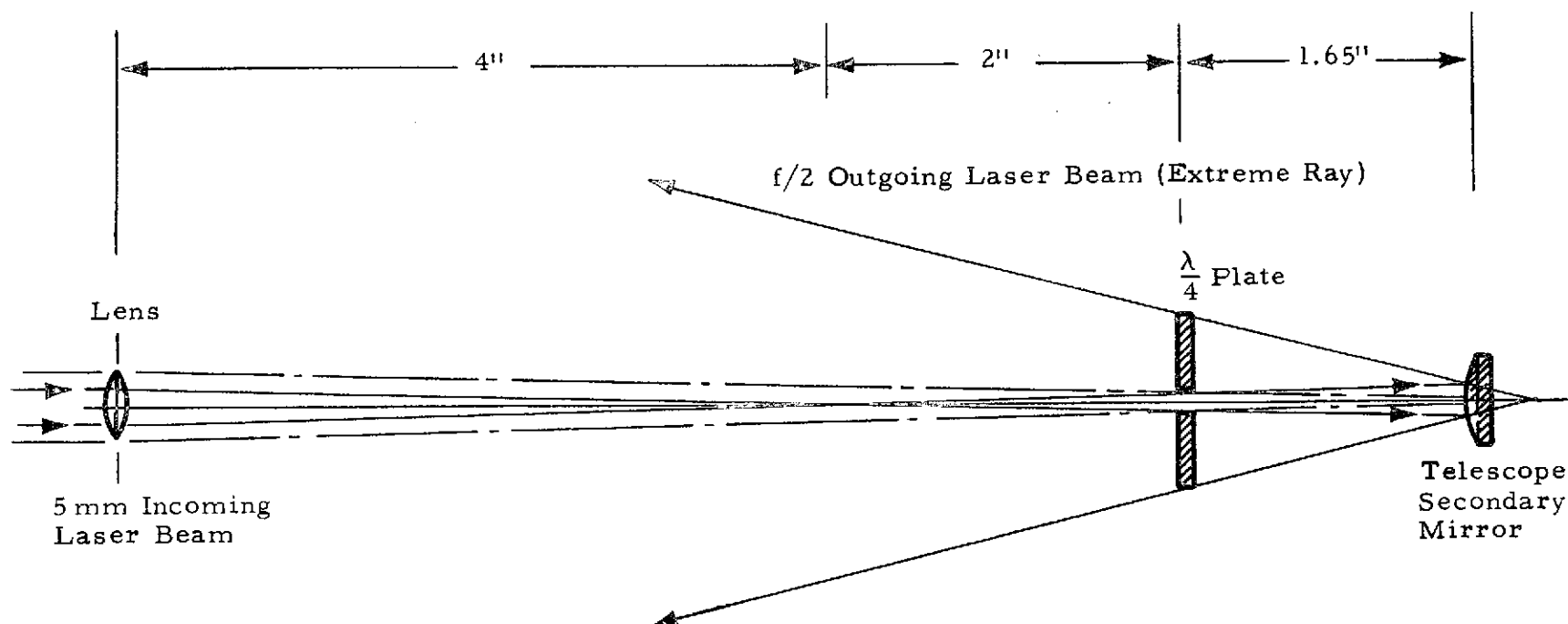
Lens: CdTe Meniscus lens with diameter 1 cm and focal length +4" AR coated on both surfaces at $10.6\,\mu$m; Clear aperture ≥ 7 mm, surface figure better than $\lambda/20$ at $10.6\,\mu$m over 80% area.

CdS $\frac{\lambda}{4}$ Plate: Diameter = 1" ± 0.01", Thickness < 2 mm, diameter of the central hole = 3 mm ± 0.1 mm, Edges chamfered < .5 mm, AR coated on both surfaces at $10.6\,\mu$m, surface figure better than $\lambda/20$ at $10.6\,\mu$m over 90% area.

Secondary Mirror: Diameter = 1/2" parabolic onvex Au coated mirror, f = -1.00 cm, surface figure better than $\lambda/20$ at $10.6\,\mu$m over 80% area.

$$= 0.9545 \, p_o - \frac{2p_o}{\sqrt{2}} \int_o^{\sqrt{2} \cdot \frac{2}{12}} e^{-u^2} du$$

$$\approx 0.70 \, p_o$$

where p_o is the total laser power before entry into the telescope. So we have about 30% loss in laser power for this geometrical configuration.

The $\lambda/4$ plate in this proposed system will change slightly the axial focal depth because of its finite thickness (d), finite index of refraction (n), and the f/2 configuration of optics. The image size (Δp) of a point source seen through a slab of dielectric material with thickness (d) and index of refraction (n) can be expressed as

$$\Delta p = (1 - \frac{1}{n} \frac{\cos i}{\cos r}) d - (1 - \frac{1}{n}) d = (1 - \frac{\cos i}{\cos r}) \frac{d}{n}$$

which is a section of a line in the direction normal to the slab, where i and r are incident and refracted angles respectively for extreme rays and $\sin i / \sin r = n$.

For CdS (n = 2.29) in f/2 system the above equation can be written as

$$\Delta p = (1 - \frac{\cos i}{\cos r}) \frac{d}{n} = (1 - 0.975) \frac{d}{2.29} = 0.011 \, d$$

or $\qquad \Delta p < 0.022 \, mm \quad (= 0.000866") \quad$ for $\quad d < 2 \, mm.$

77
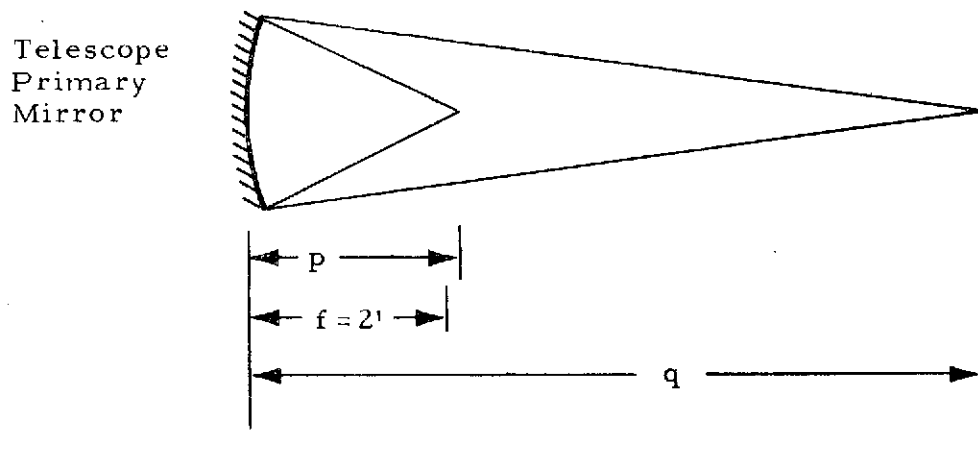
The additional stretch of the axial focal volume (Δq) beyond the diffraction limit due to spherical abberration effects introduced by the CdS $\lambda/4$ plate can be written as:

$$\Delta q = \frac{(q - f)^2}{f^2} \Delta p$$

where

$$p \approx 24''$$

$$f \approx 24''$$

$$\Delta p < 0.000866''$$

and therefore,

$$\Delta q < 1.8 \times 10^{-5} q^2 \quad \text{for} \quad q \gg f.$$

Δq is estimated to be less than 20 feet for a range of 1000 feet. This should be an endurable tolerance. Δq is much smaller at shorter range. (See sketch on the following page.
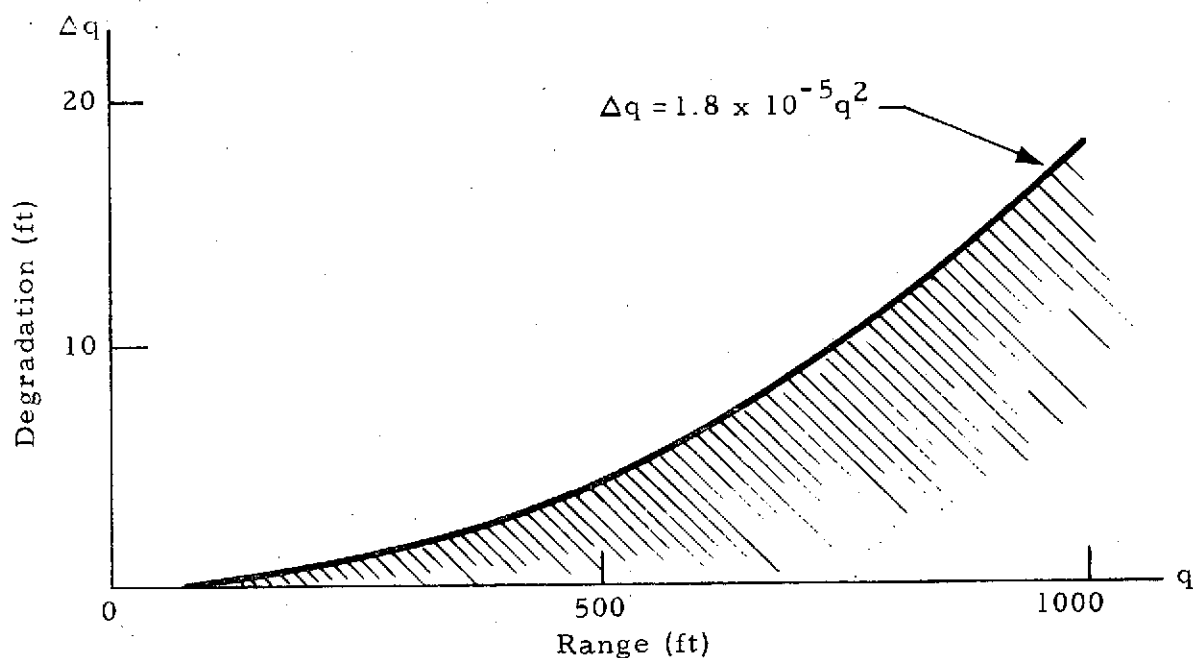
Since the laser beam passes through the $\lambda/4$ plate divergently for the outgoing beam and convergently for incoming beam, a polarization loss is introduced. The polarization loss is the laser power contributed to the original direction of polarization after a round trip through the $\lambda/4$ plate. This part of the power will not be collected by the detector.

The time independent part of the linearly polarized laser beam can be written as

$$
E = \begin{pmatrix} \dfrac{1}{\sqrt{2}} \; E \\[2mm] \dfrac{1}{\sqrt{2}} \; E \end{pmatrix}
$$

79

After a round trip through the $\lambda/4$ plate the extreme rays can be written as

$$\vec{E}_{ex} = \begin{pmatrix} e^{-j\frac{\pi}{2}(\frac{\Delta d}{d})} & 0 \\ 0 & e^{j\frac{\pi}{2}(\frac{\Delta d}{d})} \end{pmatrix} \vec{E}$$

where Δd is the optical path difference between the extreme rays and paraxial rays; in our case

$$\frac{\Delta d}{d} = \frac{1}{\cos 14^\circ} - 1 = \frac{1}{0.97} - 1 = 1.03 - 1 = 0.03 \quad \text{for} \quad f/2 \text{ system,}$$

therefore

$$\vec{E}_{ex} = \begin{pmatrix} e^{-j \cdot 0.015\pi} & 0 \\ 0 & e^{j \cdot 0.015\pi} \end{pmatrix} \vec{E}$$

The electric field which passes through a polarizer with its axis along the original polarization direction is

$$\vec{E}_p = \frac{1}{2} \begin{pmatrix} 1 & 1 \\ 1 & 1 \end{pmatrix} \vec{E}_{ex} = \frac{1}{2} \begin{pmatrix} e^{-j \cdot 0.015\pi} & e^{j \cdot 0.015\pi} \\ e^{-j \cdot 0.015\pi} & e^{j \cdot 0.015\pi} \end{pmatrix} \begin{pmatrix} \frac{1}{\sqrt{2}} E \\ \frac{1}{\sqrt{2}} E \end{pmatrix}$$

The laser power passing through this linear polarizer is

$$
(\vec{E}_p)^* \cdot \vec{E}_p
$$

$$
= \left(\frac{1}{\sqrt{2}} E \quad \frac{1}{\sqrt{2}} E \right) \frac{1}{2} \begin{pmatrix} \dfrac{E}{\sqrt{2}} \, 2 \sin 0.015\pi \\[2ex] \dfrac{E}{\sqrt{2}} \, 2 \sin 0.015\pi \end{pmatrix}
$$

$$
= E^2 \sin 0.015\pi
$$

$$
= E^2 \sin 2.7^{\circ}
$$

$$
= 0.047 \, E^2
$$

This is a rough estimate but we can see that, due to the $\lambda/4$ plate, the polarization loss of the backscattered signal should be less than 5%.

3.1.2 Secondary Mirror Backscatter Reduction Experiments

● 45-Degree Mirror with Hole for Backscatter Reduction

The experimental set-up is shown on the sketch on the following page. A piece of asbestos paper was placed very close to the 45-degree mirror as depicted in the sketch. The diffraction pattern of the laser beam which was produced by the 45-degree mirror appeared on the asbestos paper as a bright doughnut shape. The central dark region filled in and turned bright when the asbestos paper was moved closer to the secondary mirror. Although the 45-degree mirror with the hole was used, the laser beam incident upon the secondary mirror appeared with a Gaussian-like intensity distribution as expected. However, the transmitted laser beam intensity was reduced by a factor of 6.6 (8.2 dB) because of the hole in the middle of the 45-degree mirror.

A smaller attenuation factor should apply to the signal receiving leg because the backscattered power reflected by the 45-degree mirror with
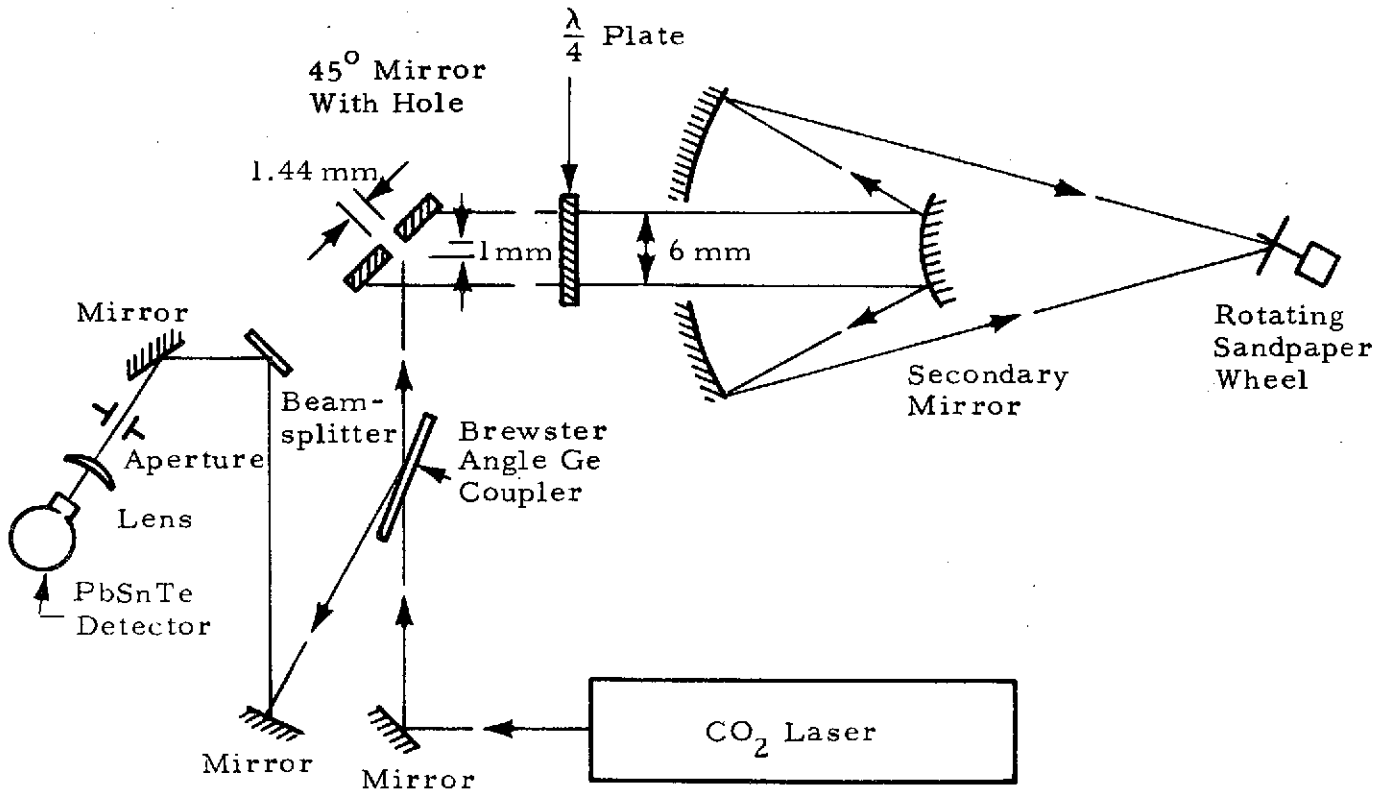
the hole has an approximately uniform illumination of power upon the 45-degree mirror instead of a Guassian beam attenuation in the transmission leg.

The total signal strength is linearly proportional to the product of the signal power and the local oscillator power, but each was reduced by approximately 8.2 dB because of the transmitted power loss through the hole of the 45-degree mirror. A 16.4 dB drop in signal level was expected in addition to the secondary backscatter reduction by this arrangement.

The experimental results are shown in the following two pictures on the next page. The total reduction in signal level was 16 dB which was essentially the same reduction factor as due to the laser power drop without the backscatter reduction effect included (i.e., the system is probably shot noise limited).
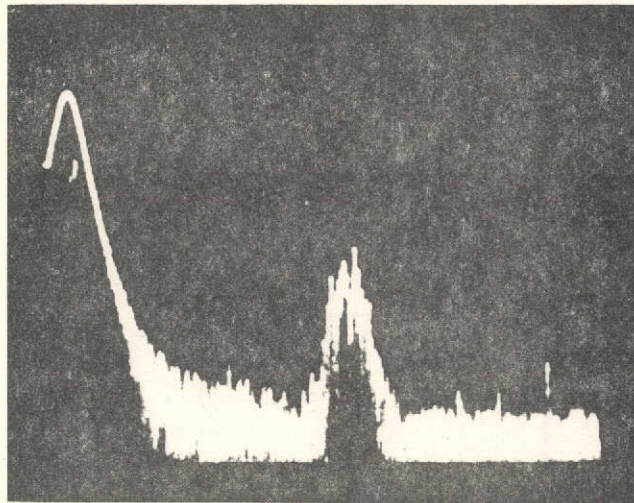
a. 45-Degree Mirror With Hole, Signal Level: -62 dBm
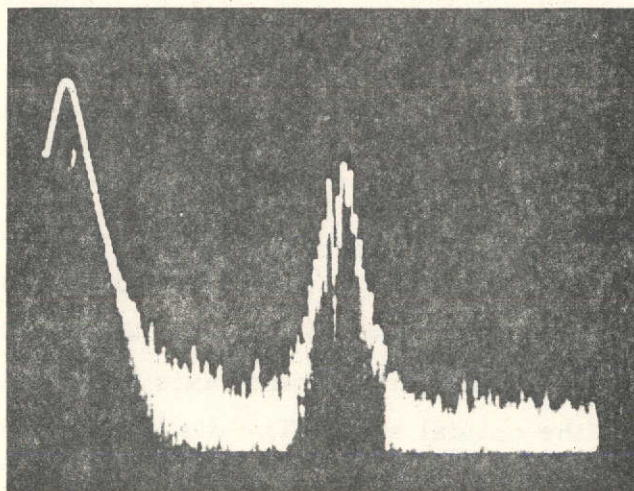
b. 45-Degree Mirror Without Hole, Signal Level: -46 dBm

Sandpaper Wheel Signal and Secondary Mirror Backscatter
Reduction by a 45-Degree Mirror With Hole

A clear conclusion can be drawn, based on experimental and theoretical evidence, that the 45-degree mirror with the hole cannot reduce the backscatter power efficiently.

- Spatial Filter and Backscatter Reduction

The experimental set-up is shown below.
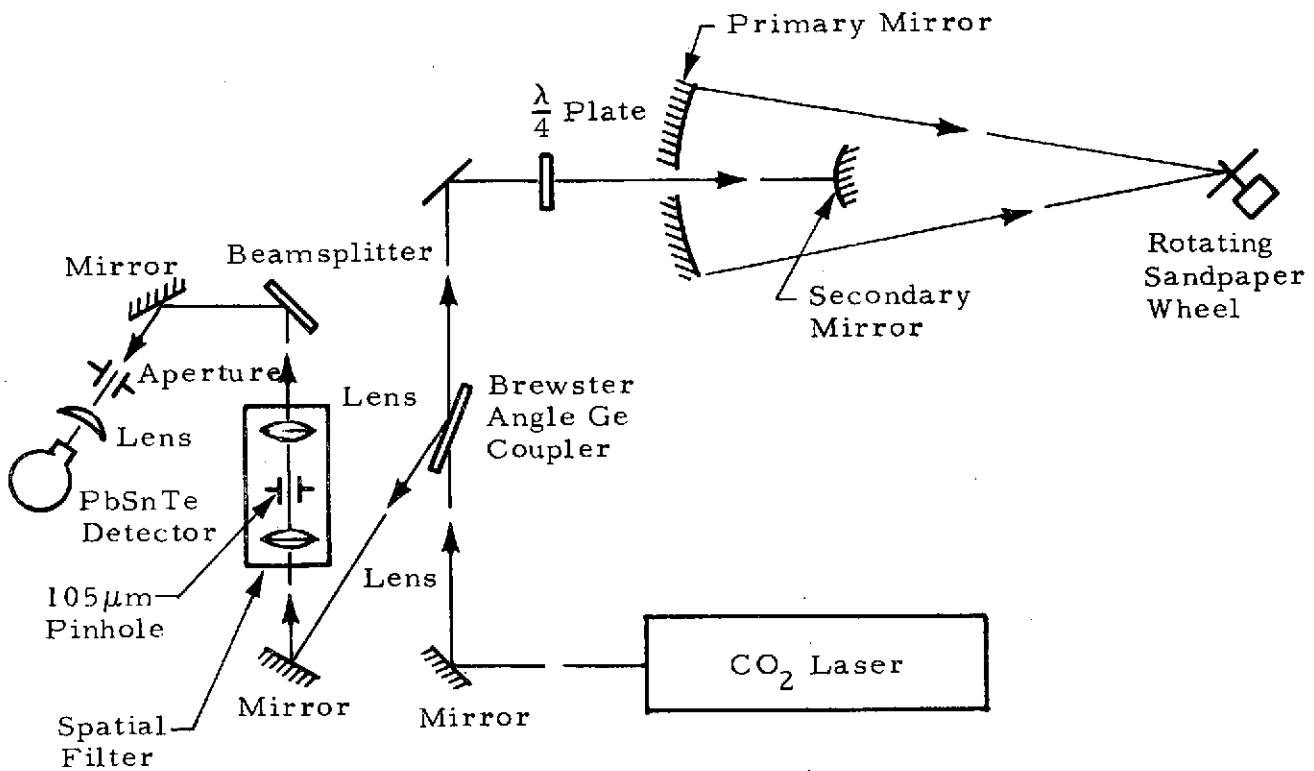
The spatial filter consists of two identical lenses with a focal length of 2" and a 105 μm pinhole. These three pieces were aligned carefully to allow maximum secondary mirror backscatter power through the spatial filter. The 105 μm pinhole could be translated along the optical axis as well as in two directions both perpendicular to the optical axis. The distance between the secondary mirror and the pinhole was 200 cm.

While the signal measurement was taken, the pinhole had been adjusted along the optical axis to peak up the signal reading. The result is shown in

picture (a) on the following page. When the pinhole was removed, the signal was increased by 2.5 dB in picture (b). Another 1 dB increase in signal level appeared when the spatial filter was totally removed as shown in picture (c). These results show that the backscatter reduction using this particular spatial filter set-up was 2.5 dB at most.

● Lamp-Blacked Wire and Backscatter Reduction

The experimental set-up is shown below:
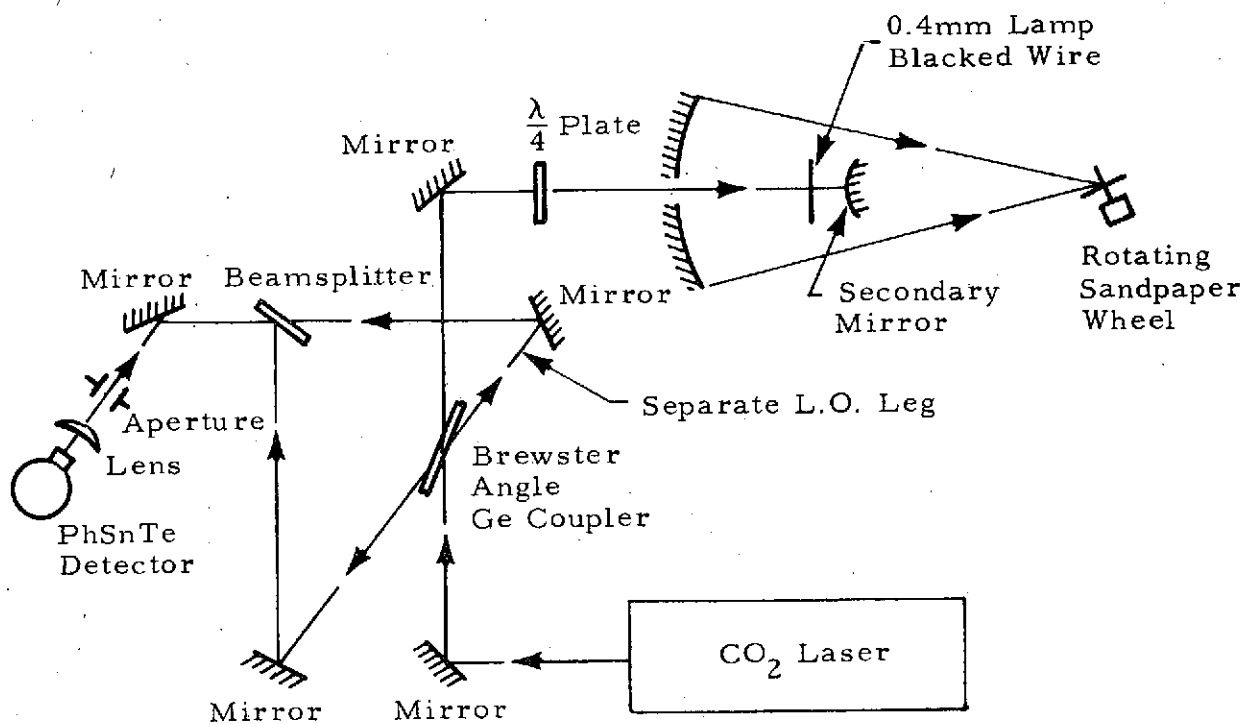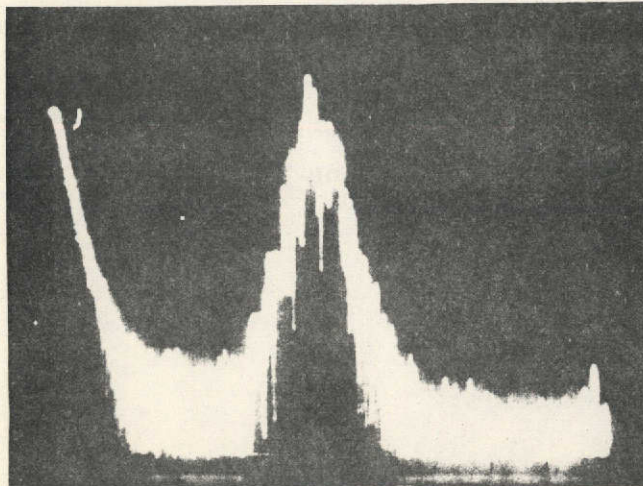
a. Wheel Signal With the Spatial
   Filter Set-Up and Pinhole
   Signal: -35.5 dBm
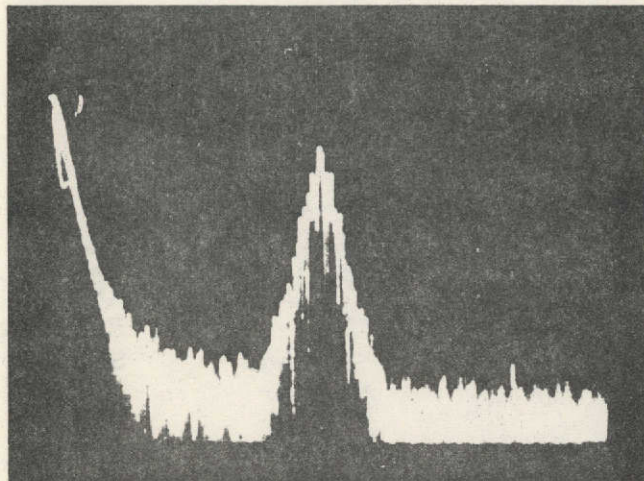
b. Wheel Signal With the Spatial
   Filter Set-Up but Without
   Pinhole
   Signal: -33 dBm
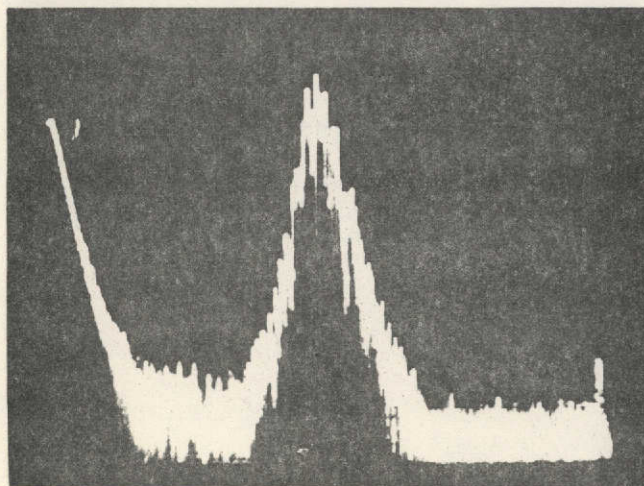
c. Wheel Signal Without Spatial
   Filter and Pinhole
   Signal: -32 dBm

Sandpaper Wheel Signal and Secondary Mirror Backscatter
Reduction by a Spatial Filter

With the separate local oscillator (L.O.) leg blocked, the wheel signal in the backscatter mode was recorded as shown in picture (a) on the the following page. A 0.4 mm lamp-blacked wire was arranged to move across the front surface of the secondary mirror carefully to a position such that the minimum signal was recorded as shown in picture (b). The signal dropped by 16 dB, mostly due to the reduction of secondary backscatter. A small percentage (10%) reduction of the transmitted laser power onto the samdpaper wheel due to the wire was observed.

When the separate L.O. leg was unblocked, the signal level reverted back to almost the same signal level as that of the backscatter mode without the wire (effect shown in picture (c)). The backscatter reduction by a 0.4 mm lamp-blacked wire was around 16 dB. Meanwhile the reduction of the signal was small.

In the sketch shown below, the 0.4 mm lamp-blacked wire was vertically in front of secondary mirror and translated horizontally on the LDV table across the laser beam. The thermopile reading, which was directly proportional to the secondary mirror backscatter power (shown on the following page) is plotted as a function of wire position. When the wire approached the center of the secondary mirror, the edge diffraction pattern of the wire from the divergent backscatter power of the secondary mirror was clearly seen on the dc microvolt meter reading.

a. Backscatter Mode With Wire
   Out

   Signal: -32 dBm
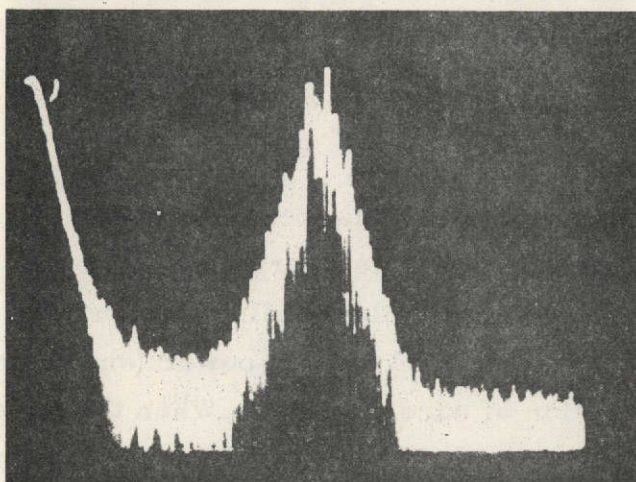
b. Backscatter Mode With Wire
   In

   Signal: -48 dBm
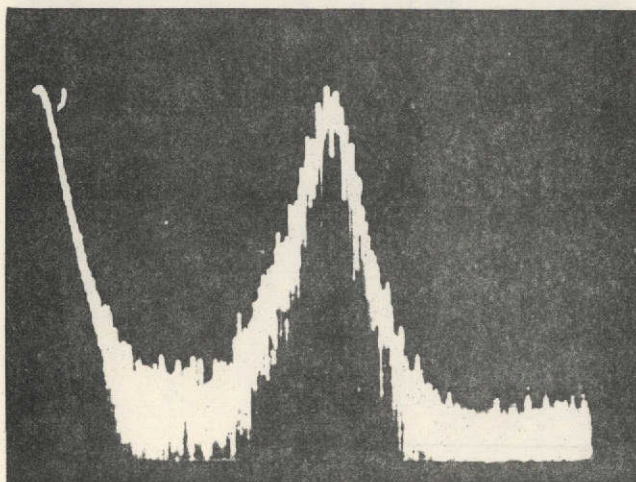
c. Separate L.O. Mode With
   Wire In

   Signal: -30 dBm

Sandpaper Wheel Signal and Secondary Mirror Backscatter
Reduction by a 14 mm Lamp Blacked Wire

Before the wire reached the secondary mirror center, a very strong diffraction peak — almost twice as strong as the backscatter power without the wire — was measured by the thermopile. This strong diffraction peak from the secondary mirror backscatter and the wire is potentially dangerous to a detector which cannot accept this high amount of power. As the wire was moved farther toward the secondary mirror center, a minimum amount of power — 16 dB smaller than the backscatter power with the wire removed — was measured by thermopile. Although the wire diameter was only 0.4 mm, the shadow of the wire will not be "filled in" due to the diffraction because of the large divergent backscatter power of the secondary mirror. Usually a small hump of the thermovoltage is recorded while the wire is placed right at the middle of the secondary mirror. This relates to the fact that the diffraction of a sharp-edged circular opaque disk placed in front of a point source produces a bright spot along the axis which connects the source and the center of the disk. Continued translation of the wire produces another minimum and finally the edge diffraction is seen again. As seen by the results depicted in the following curve, the small hump at the bottom part of the curve is missing due to the coarse incremental translation of the wire. The 16 dB attenuation of the secondary mirror backscatter power recorded by this measurement agrees very well with the coherent method.

3.2   CALIBRATION OF THE LDV SYSTEM AT LOCKHEED

3.2.1   Sulphur Wheel Target Calibration

A 9.5 watt CO_2 laser beam was focused through the LDV telescope onto a rotating sulphur wheel located 100 feet from the telescope. The diffusely reflected radiation from the wheel was collected by a 2-inch focal length BaF_2 lens with a 1.9 cm clear aperture, and focused onto a calibrated thermopile for the incoherent measurement. The distance between the laser spot on the wheel and the collecting lens was 100 cm.

The theoretical value of the diffusely reflected power that the lens should receive can be expressed as shown in Eq. (1) on page 91.
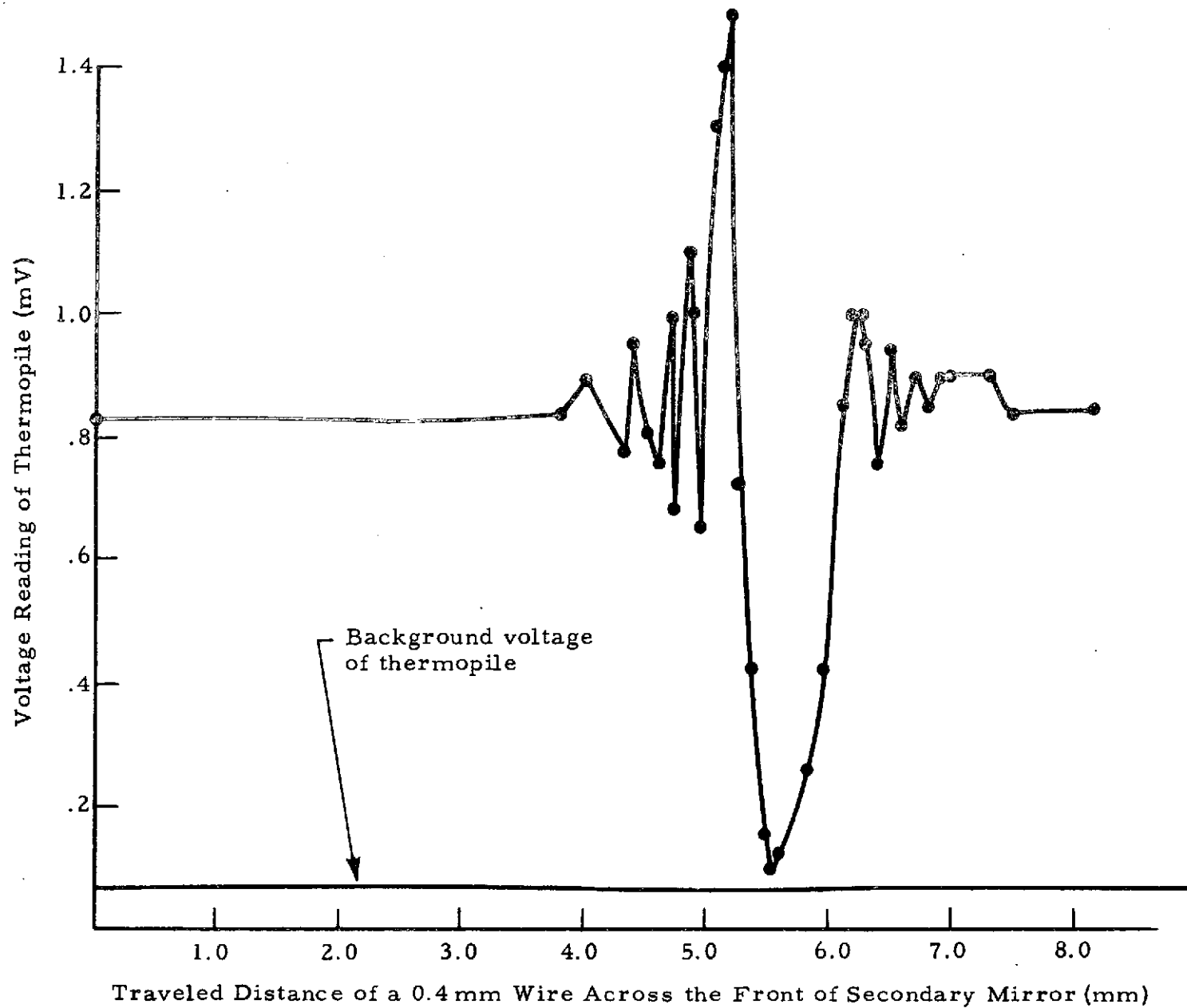
$$P_r = \rho \, \frac{A}{\pi R^2} \, P_i \cos\theta_r \qquad\qquad (1)$$

for a Lambertian surface with reflectivity ρ, where

A = clear aperture area of the collecting lens

R = distance between the laser spot on the wheel and the collecting lens

P_i = incident laser power onto the sulphur wheel

θ_r = angle between the normal of the wheel and the direction of the reflection.

For constant incident power and reflectivity (Eq. 1) the diffusely reflected power from the surface is independent of the incident angle but depends on the reflection angle as $\cos\theta_r$. This has been proven experimentally and the resulting data tabulated in the table below.

Laser Incident Angle (deg)	θ_r (deg)	Experiment		Theory		$\rho = \dfrac{P_{r,\,exp}}{P_{r,\,th}}$ (%)
		P_r, mW	$P_r/\cos\theta_r$, mW	P_r, mW	$P_r/\cos\theta_r$, mW	
0	33	0.54	0.64	0.679	0.810	79
45	12	0.58	0.60	0.792	0.810	74
60	27	0.50	0.56	0.722	0.810	69
0	33	0.54	0.64	0.679	0.810	79
0	48	0.46	0.69	0.542	0.810	85
0	63	0.31	0.69	0.368	0.810	85
0	73	0.20	0.69	0.237	0.810	85

Within the $\pm 10\%$ error of the experiment (because the response of the thermopile was too sensitive to its position) the sulphur wheel surface can be referred to as a Lambertian surface with a reflectivity of 80% on average.

The measured diffuse reflection of various targets as a function of the targets' orientation is shown by the curves on the following page. The experimental configuration is also shown. A stabilized CO_2 laser was directed on the target when at an angle of 15 degrees to a line joining the target and the thermopile. The diffusely reflected power from the target that passed through a calibrated aperture was collected by a Ge lens and focused into the thermopile. The thermopile output voltage was a direct indication of the collected diffuse reflection power from the target. The target was positioned such that a line normal to its surface lay in the same plane with the incident laser beam and the thermopile. The target surface was continuously rotated to avoid local heating by the strong laser beam. The orientation of the target surface could be varied by rotating the target about an axis perpendicular to to the plane which includes the incident laser beam and the thermopile.

The normalized reflectivity (normalized relative to the 0-degree incidence angle condition) is shown for three different targets: (1) sulphur wheel, (2) sandpaper wheel, and (3) belt sander.

The experimental results show that the sulphur wheel provided a uniform reflectivity over a wide range of incidence and reflection angles. This indicates that sulphur provides a good Lambertian surface. The absolute reflectivity of the sulphur wheel was measured to be 80% for the CO_2 radiation as mentioned previously.

The belt sander and the sandpaper wheel also can be regarded as a Lambertian surface for small incidence and reflection angles. The sandpaper with the smaller grain size provides a better match to a Lambertian surface then the coarser sandpaper. The absolute reflectivity of the sandpaper surface is approximately 8%

DIFFUSE REFLECTION OF VARIOUS TARGETS
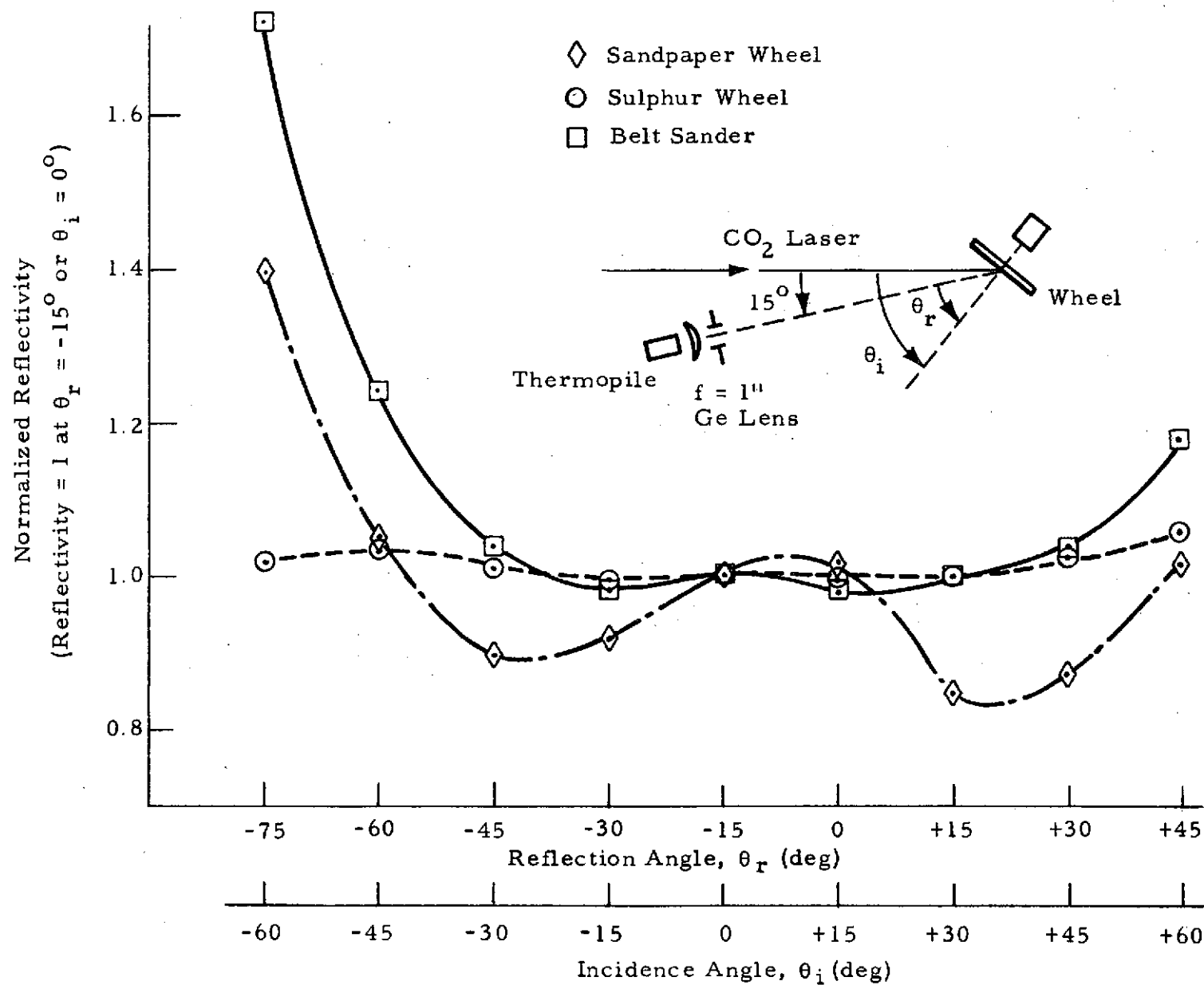
3.2.2   Losses of the LDV System

● **Losses of Optics**

The sketch shown below gives the arrangement of the optics in the LDV set-up.
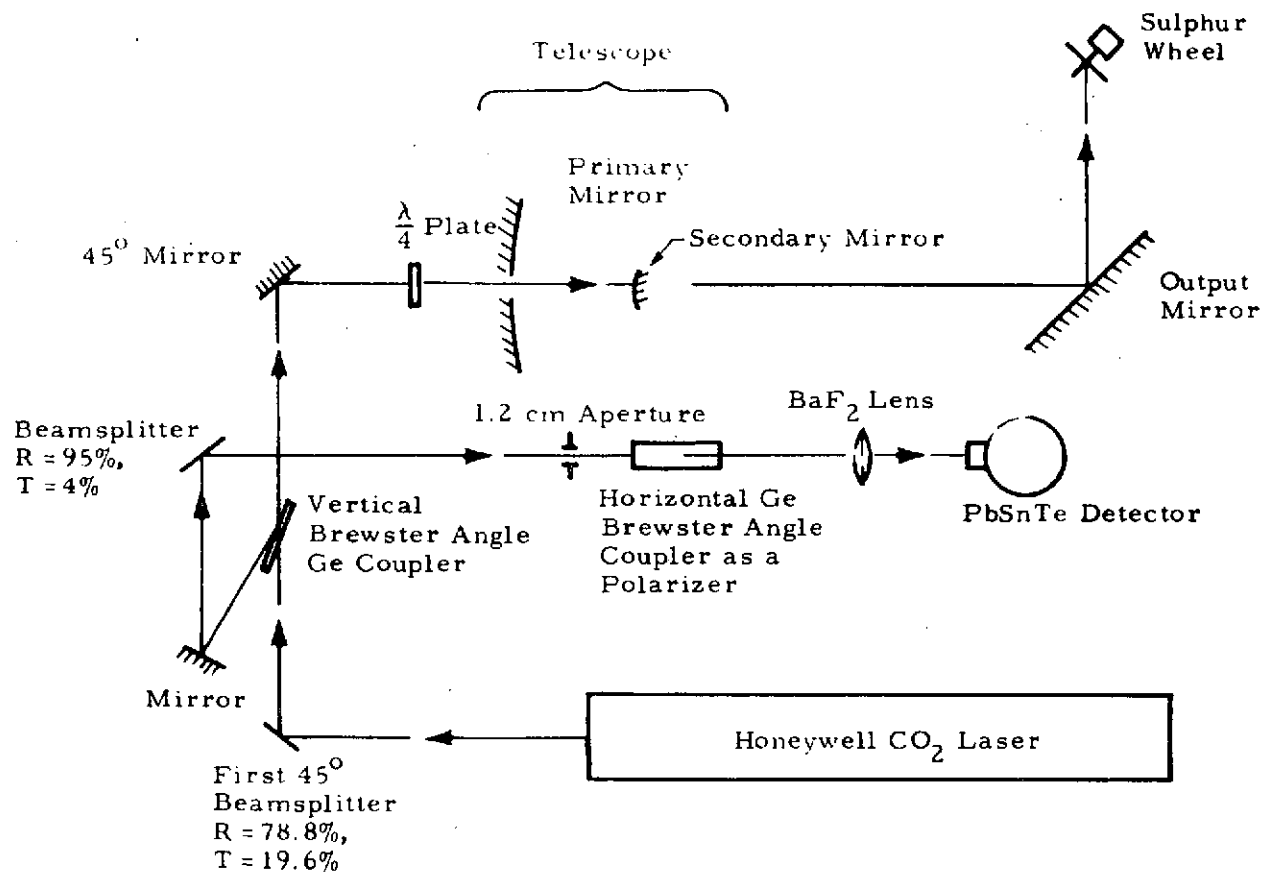
The loss to the outgoing laser beam was 42%, which did not include the first 45-degree beamsplitter transmission loss. (The beamsplitter was installed to provide another leg of the local oscillator (L.O.) power and can be replaced by a highly reflective 45-degree mirror.)

The individual contributions to the total outgoing loss from each optical component were:

Vertical Ge Brewster angle coupler loss: 14%

S-wave component of the laser output: 0.24%

45-degree mirror and $\lambda/4$ plate loss: 10%

Telescope loss: 20%

Output mirror loss: 6.7%

In addition to the spherical aberration and truncation effect, which will be discussed later, the incoming signal undergoes a total loss of 54% through the optics before reaching the detector.

The individual contributions to the loss of the incoming signal due to the optics were:

Output mirror loss: 6.7%

Telescope loss: 20%

45-degree mirror and $\lambda/4$ plate loss: 10%

S-wave coupling loss: 22%

Mirror and beamsplitter loss: 5%

Horizontal Ge Brewster angle coupler loss: 2%

Collecting lens loss: 5%

● Spherical Aberration and Truncation Loss

Analysis of an f/2 system conducted by Lockheed-Huntsville shows that the spherical aberration contribution to the lateral size of the focal volume at a range of 100 feet and below and the spherical aberration contribution to the longitudinal size of the focal volume at a range of 250 feet and below should be considered seriously. A truncation effect exists at any range as long as the LDV telescope destroys the Gaussian nature of the transmitted waveform.

Q-2

Both the lateral and the longitudinal elongation of the focal volume due to the spherical aberration and the truncation effect makes the signal focal volume (which was collected by the primary mirror) a prolonged oval shape. Since the virtual object of the secondary mirror was of a prolonged oval shape the signal beam collimated by the secondary mirror inherited a large divergent angle. The signal power at the detector position could not be fully recovered by using a 6 mm diameter aperture (or even 1.2 cm) in front of the collecting lens for any range. The measured results will be discussed later (Section 3.2.5).

3.2.3 Optimization of PbSnTe Detector Bias Circuitry

The bias circuit used in the LDV system calibration experiment has been modified for better impedance matching between the detector and the preamplifier. The modification of the circuit included adding a pulse trans-former, which has a bandwidth from 10 kHz to 5 MHz and a voltage gain of 15.5 dB, for the correction of the amplifier loading problem. Using the modified bias circuit, the highest signal-to-noise ratio recorded from the sulphur wheel at a 50-foot range was 104.5 dB under the operating condition of 10 mW L.O. power from the backscatter of the secondary mirror, zero bias voltage, 7.5-degree orientation of the wheel to the laser beam, and 10 W laser power incident on the sulphur wheel.

The signal and the noise levels versus bias voltage are shown on the following page for various L.O. power levels for the Raytheon PbSnTe detector 314, chip 1. It is obvious that the highest signal-to-noise ratio of that particular detector was obtained at zero bias voltage condition.

3.2.4 Theoretical Signal-to-Noise Ratio of the Sulphur Wheel Doppler Signal and System Efficiency Tests

The signal-to-noise ratio, S/N, for a reverse-biased photodiode is given by

$$(S/N)_{power} = \eta P_r / h\nu \; f \qquad (2)$$
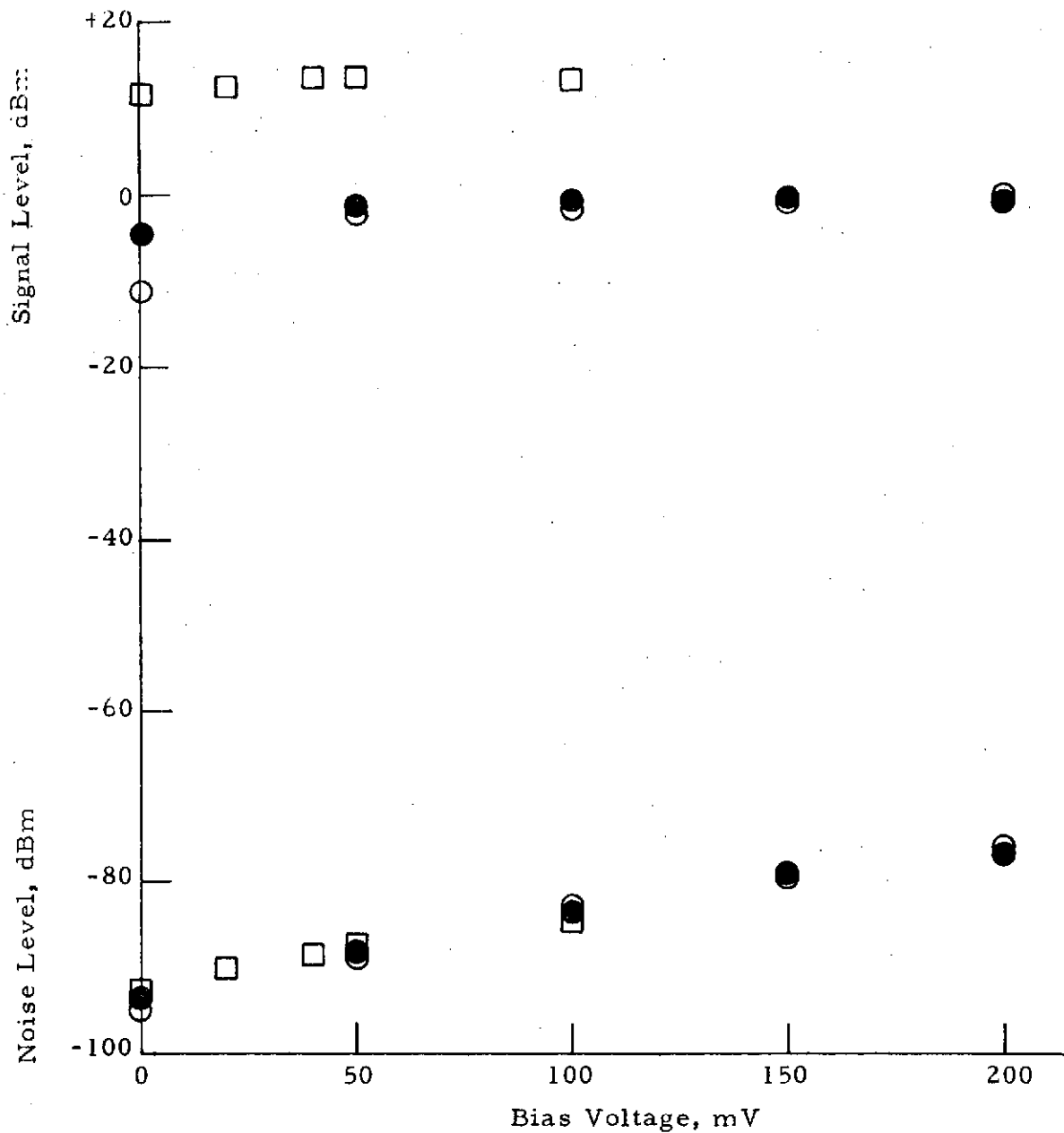
O L.O. power = 1.46 mW   Sulphur wheel signal for a 100 ft range
(213 cm between the secondary mirror
● L.O. power = 2.92 mW   and the 1.2 cm aperture)

□ L.O. power = 10 mW   Sulphur wheel signal for a 50 ft range
(155 cm between the secondary mirror
and the 1.2 cm aperture)

Sulphur Wheel Signal and Noise Levels Under Various
Operation Conditions

where

η = quantum efficiency of the detector $\approx 15\%$

h = 6.625×10^{-34} Joules-sec

ν = 3×10^{13} Hz

Δf = 30 kHz

P_r = signal power incident upon the detector

therefore

$$(S/N)_{power} \approx 2.5 \times 10^{14} P_r \tag{3}$$

With the aid of Eq. (1), Eq. (3) can be rewritten as

$$(S/N)_{power} \approx 2.5 \times 10^{14} \, T\rho \, \frac{A}{\pi R^2} \, P_i \cos\theta_r \tag{4}$$

Typically,

T = transmission of the LDV system to the return signal power $\approx 46\%$ (1 - 0.54)

ρ = 80%

A = area of the telescope primary mirror = $\pi(15\,cm)^2$

R = range = 50 ft = 1500 cm

P_i = 10 W

θ_r = 45 degrees

and we have that

$$(S/N)_{power} \approx 6.5 \times 10^{10}$$

or

$$10 \log (S/N)_{power} \approx 108 \text{ dB}$$

For various calibration arrangements, Eq. (4) can be tabulated as follows:

R (ft)	θ_r (deg)	P_i (W)	$(S/N)_{power}$, dB	
			Theory	Experiment
50	45	10	108.0	--
50	7.5	10	109.5	104.5
100	45	10	102.0	95.5
100	7.5	10	103.5	98.5

The experimental value of the signal to noise ratio was about 5 dB below the theoretical value which can be fully explained in the following section.

3.2.5   Verification of the Spherical Aberration and Truncation Effect

● Incoherent Measurement

The experimental set-up was essentially the same as shown in Section 3.2.2.   The PbSnTe detector was replaced by a Sensors, Inc., thermopile to measure the return signal power.   The distance between the 1.2 cm aperture, which was located in front of the thermopile, and the secondary mirror was 213 cm.   For a 50-foot range, the measured signal power was only about 0.017 mW when a piece of 0.4 mm diameter wire was placed across the front of the secondary mirror to reduce the backscatter power.   This enabled us to measure the slight difference in thermal voltage when the signal power was superposed upon the existing large backscatter power from the secondary mirror.

As the thermopile was moved closer to the secondary mirror from 213 cm to 141 cm, the measured signal power was 0.042 mW which was 2.5 times stronger.   This proves the large divergence of the signal power due to the

spherical aberration and truncation effect. By referring to the table in Section 3.2.2 and the experimental arrangement (shown in Section 3.2.2) used to obtain the above result, we can estimate the signal power that should be received by the thermopile if there were no spherical aberration or truncation effect. Since the lens used in the experiment subtended the same solid angle as the telescope primary mirror for a 50-foot range, the total signal power received by the LDV system should be 0.46 mW. After a 20% two-way loss due to the wire and the 54% one-way transmission loss of the system, the signal power should be 0.17 mW which is four times higher than 0.042 mW.

● Coherent Measurement

For the coherent measurement we maintained the distance from the secondary mirror to the aperture in front of the PbSnTe detector at 155 cm and measured the heterodyne signal from the sulphur wheel which was oriented 7.5 degrees to the incident laser beam and placed 50 feet away from the telescope primary mirror. When the aperture was changed from the diameter of 1.2 cm to a diameter of 6 mm, the signal-to-noise ratio dropped by 3.5 dB. Only 1 dB drop of the signal-to-noise ratio was measured for the same process at a 100 foot range. This illustrated the larger divergence for the closer range due to the spherical aberration and the truncation effect.

3.2.5 Conclusions

The 104.5 dB measured signal-to-noise ratio off the sulphur wheel was only 5 dB below the theoretical value. This is due to spherical aberration and truncation effect. If there were no other additional losses of the signal power because of the range variation, we would expect less than 6 dB reduction in signal-to-noise ratio as the range is changed from 50 feet to 100 feet solely because the spherical aberration decreases with increasing range. The observed reduction in signal-to-noise ratio was still 6 dB (refer to table on preceding page), which illustrated that the truncation loss is more dominant than the spherical aberration loss.

3.3 LDV SYSTEM SPATIAL RESOLUTION AND SIGNAL-TO-NOISE RATIO TESTS

3.3.1 Test Conditions

- A 13-inch folding mirror was placed inside a 100-meter tunnel to achieve the range of 100, 188, 350 and 558 feet. The 700-foot range was achieved when the folding mirror was placed at the outside end of the tunnel.

- A sandpaper wheel was adapted as a hard target which provided a reflectivity of 7% when it was oriented 30 degrees to the incident laser beam.

- The incoherent power measurement at the nominal focal volume was made with various size pinholes attached in front of the power meter head.

- Honeywell stabilized lasers were used during the test.

- The interferometer was Mach-Zehnder Interferometer 1 with modified mount on the detector which provided a three-dimensional translation and also with the modified mount on the recombining beamsplitter which provided rotations along two perpendicular axes and translation along the direction of the separate L.O. beam direction.

- A 12-inch f/2 telescope was used.

- The air turbulence and the mechanical vibration of the LDV table degraded the accuracy of the data.

3.3.2 Incoherent Measurements

- Focused Spot Size vs Range

The focused laser beam diameter at different ranges was determined with the help of a power meter and a pinhole attached in front. Both were moved across the focused beam at the focal plane. The total distance traveled from one $1/e^2$ point (13.5%) to another $1/e^2$ point, in comparison with the peak power reading, was recorded as the diameter of the focused spot size.

Range (ft)	Pinhole Size (mm)	Focused Spot Size (mm)
100	0.5	2.1
188	0.5	4.5
350	1.0	7.5
558	1.8	12.7
700	1.8	13.8

These values are plotted in Fig. 3-1.

● Focal Depth vs Range

The focal depth at different ranges was determined by moving the power meter head, with a pinhole attached, along the optical axis at the nominal focal volume location. Then the distance span between two points was measured where the power meter reading dropped to half of its peak reading.

Due to the lack of a longer optical bench, no attempt was made to measure the focal depth at ranges 558 and 700 feet.

Range (ft)	Pinhole Size (mm)	Focal Depth (ft)
100	0.5	2.9
188	1.0	10.5
350	1.0	45.0

These values are plotted in Fig. 3-2.

● Discussion

The growth of the focused spot size with range is faster than the first power of the range and the growth of the focal depth with range is faster than
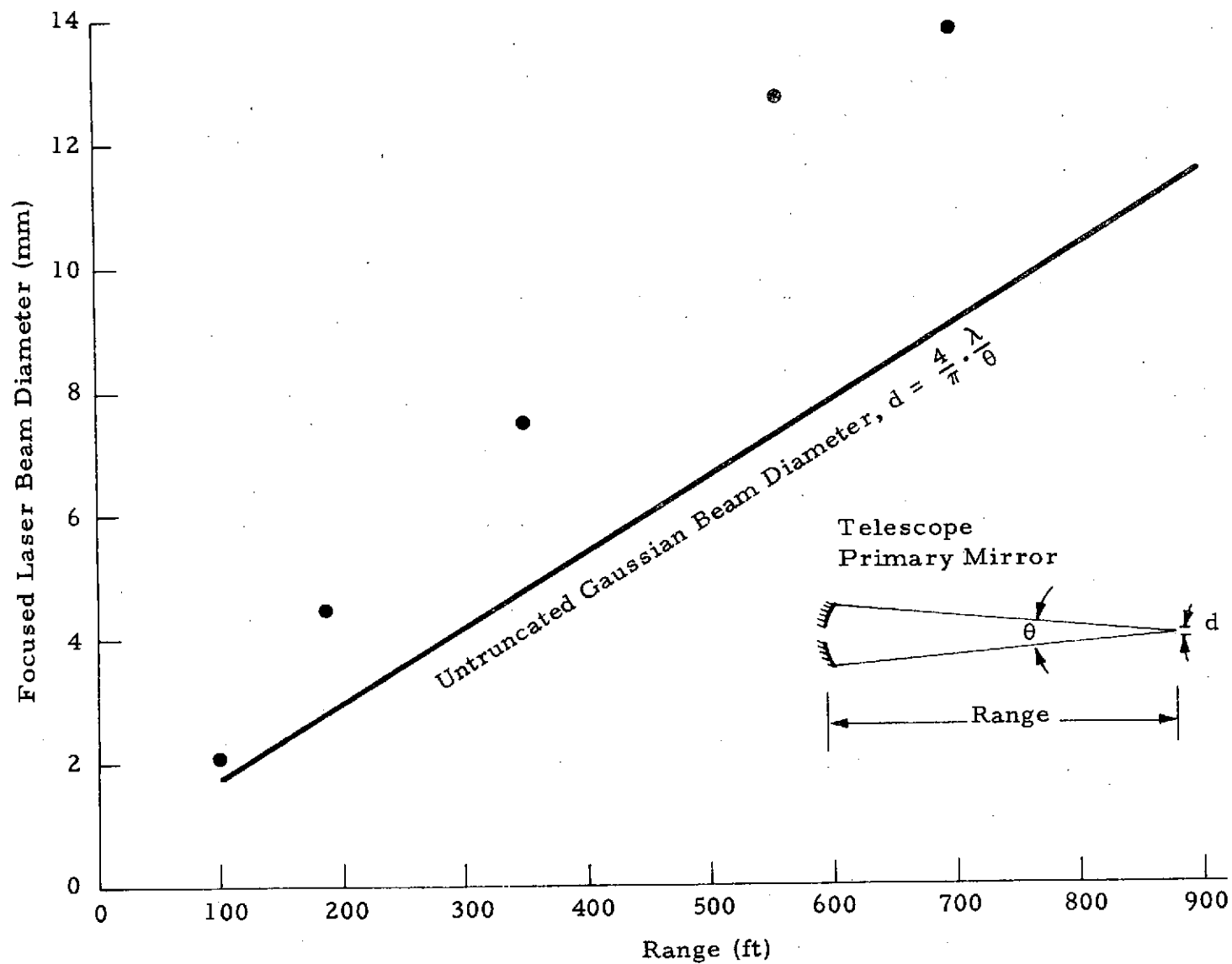
Fig. 3-1 - 12-Inch LDV System Focused CO_2 Laser Beam Diameter as a Function of Range
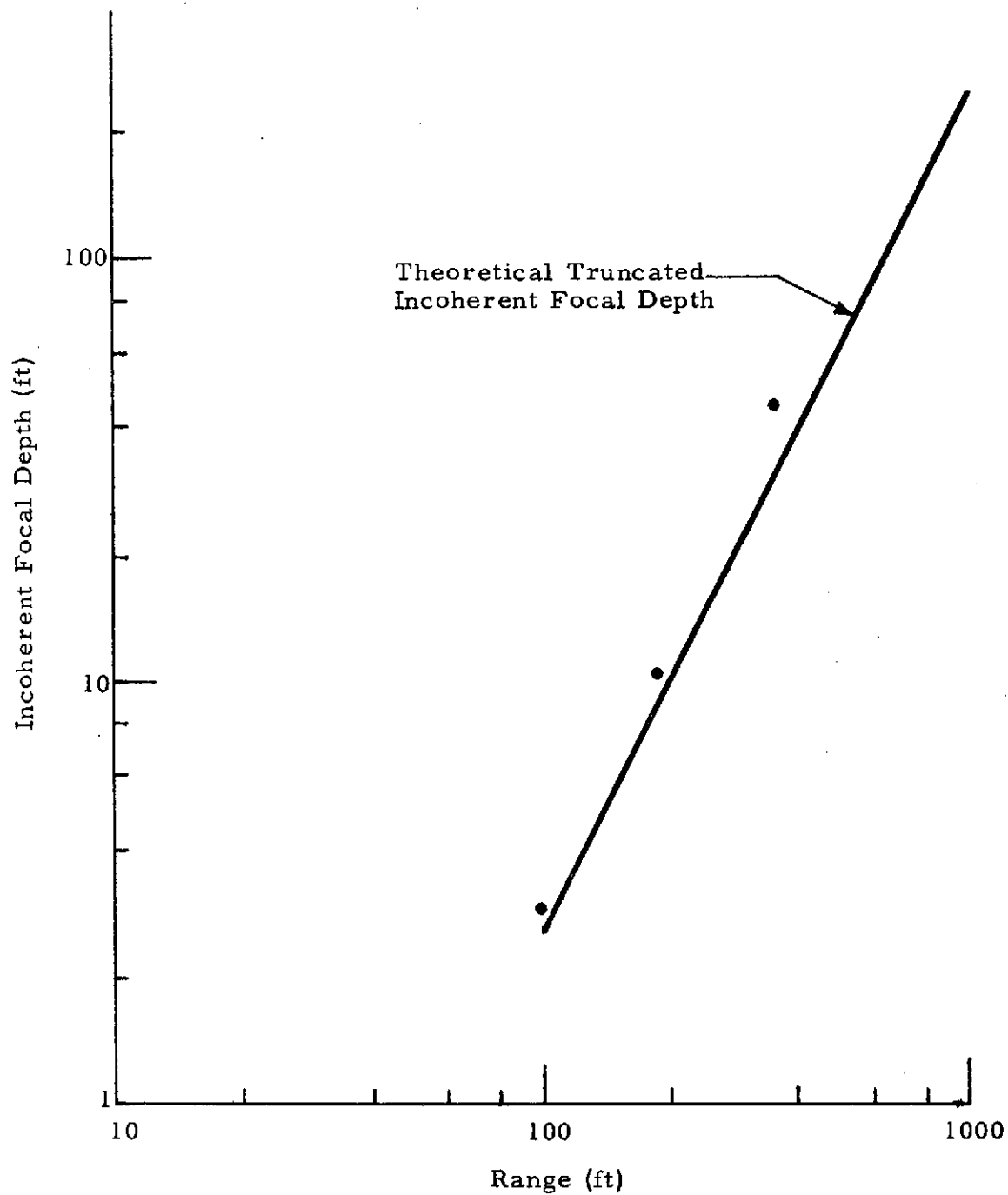
Fig. 3-2 - 12-Inch LDV System CO_2 Laser Beam Focal Depth
as a Function or Range

the range square, which will enable us to explain the signal-to-noise ratio at longer range falling off faster than $1/(\text{range})^2$.

3.3.3 Coherent Measurement

● Previous Measurements

The initial coherent spatial resolution measurements are plotted in Fig. 3-3. When using SAT detector 952, the signal-to-noise ratio measurements at different ranges of that detector were not reliable at the moment the data were taken. As a result, the signal-to-noise ratio fell off unexpectedly fast with range which is shown in Fig. 3-4.

● Recent Measurements

The signal-to-noise ratio as a function of range has been checked by using Pb-Sn-Te detector 314 and another SAT detector PV 1031. The results are shown in Fig. 3-5. The insufficient L.O. power and the possible lower quantum efficiency of the Pb-Sn-Te detector are responsible for the lower signal-to-noise ratio. But the behavior of the signal-to-noise ratio as a function of range should be preserved. In general, a ±2 dB variance on the signal-to-noise ratio is easily introduced into the results because of the laser power fluctuation, beam wandering, optical alignment, and the detector operation conditions.

Signal-to-noise ratio is almost independent of the kind of sand target, i.e., sandpaper wheel or belt sander.

The coherent spatial resolution, as measured in the laboratory, is concluded in Fig. 3-6.

3.3.4 Misalignment Effects on Spatial Resolution

A Pb-Sn-Te detector was used in this test which had a 1.5-inch focal length Ge meniscus lens placed in front. The range was 188 feet.
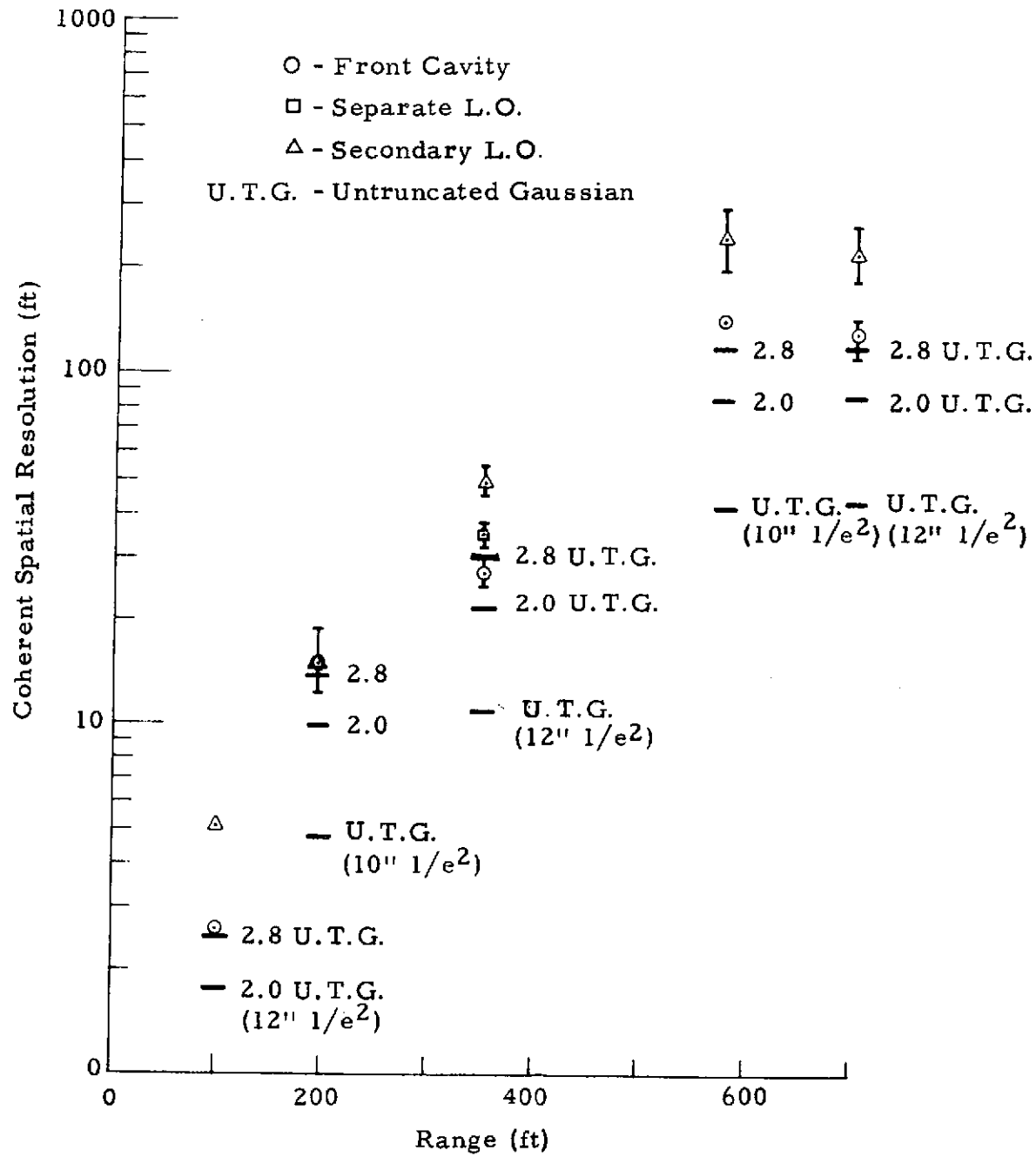
Fig. 3-3 - LDV Coherent Spatial Resolution Measurements
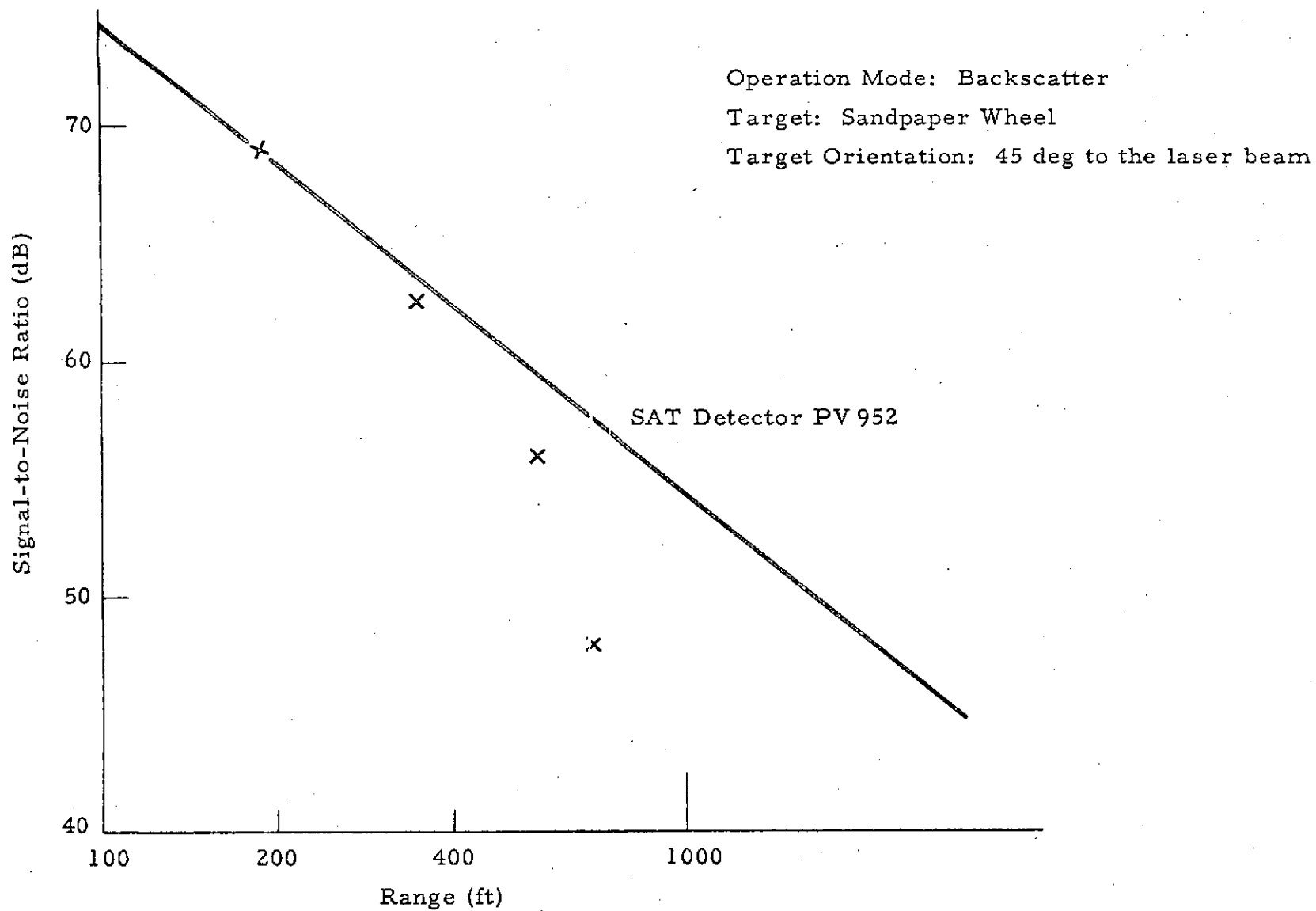
Fig. 3-4 - LDV Signal-to-Noise Ratio Measurements as a Function of Range
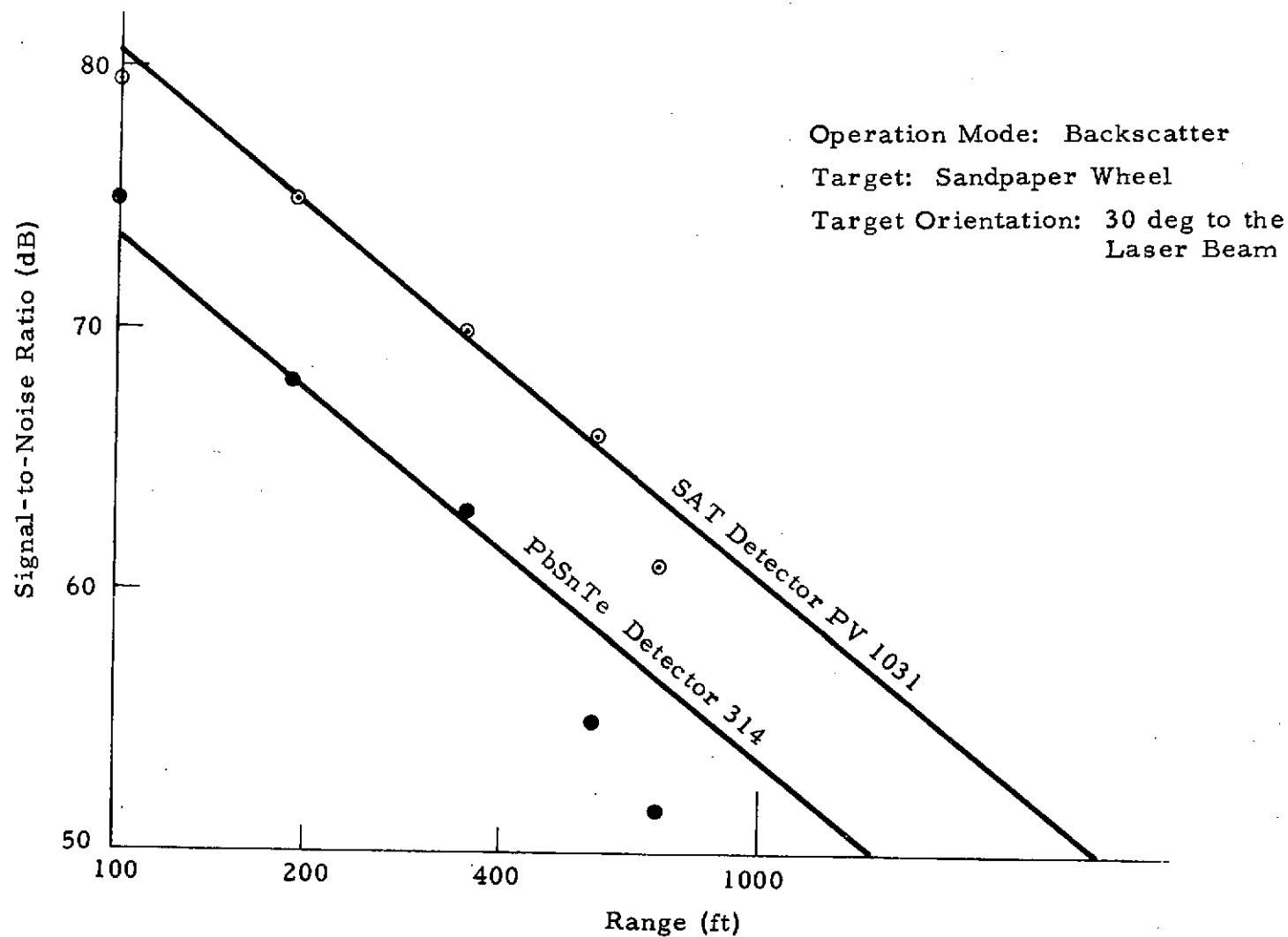
Fig. 3-5 - LDV Signal-to-Noise Ratio Measurements as a Function of Range
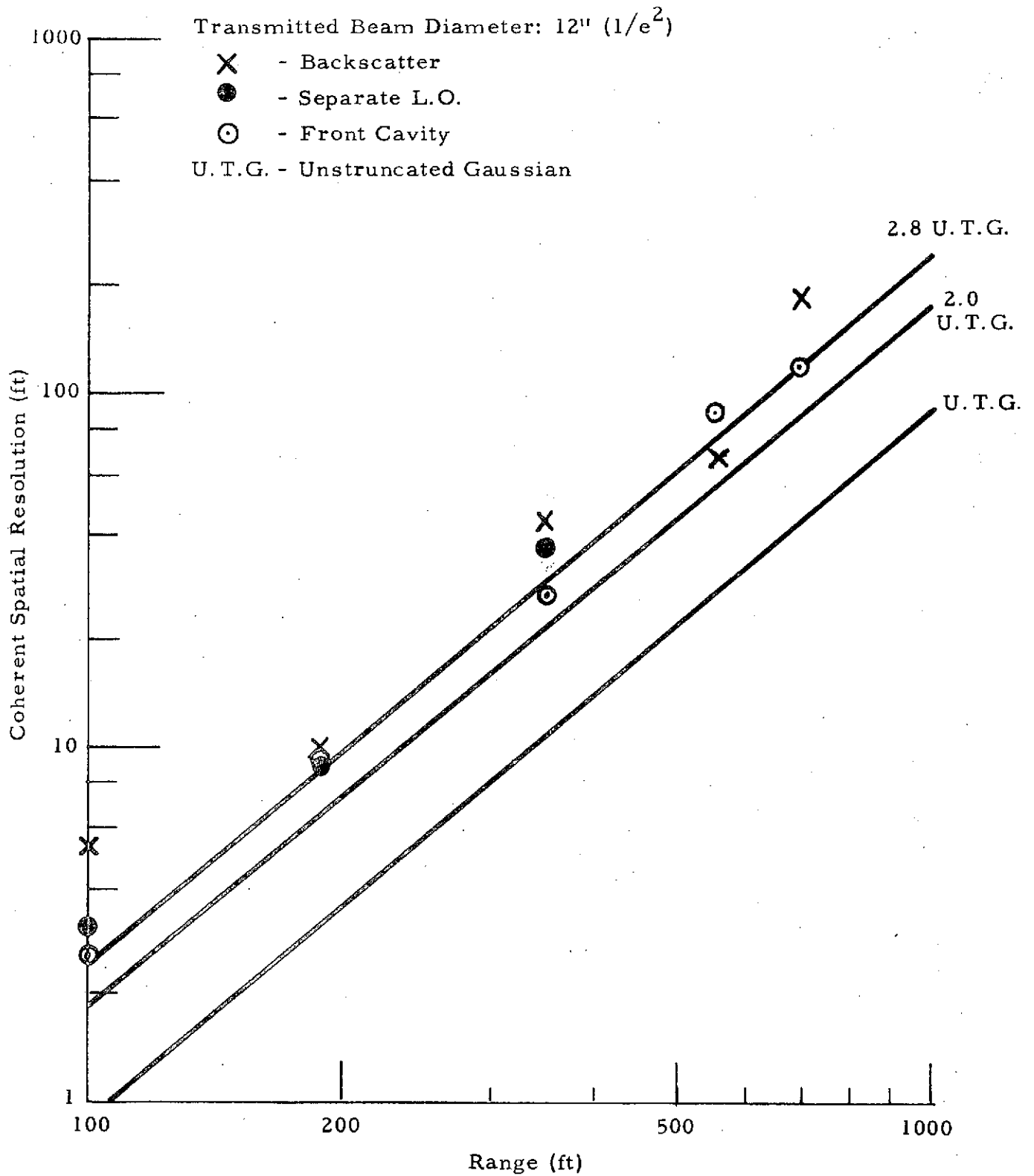
Fig. 3-6 – LDV Coherent Spatial Resolution Laboratory Measurements

● Defocused Detector

The measured coherent spatial resolution was 10.8 feet operated under the backscatter mode. The range resolution was reduced to 9.4 feet when the detector was defocused by 0.20 inch either toward or away from the lens but was within the experimental error.

● Lateral Displacement of Secondary Mirror

The coherent spatial resolution increased from 11.5 to 12.5 feet when the secondary mirror was moved from the optimum position laterally toward the table center by 0.02 inch. The reflected transmission power from the primary mirror was shifted to one side of the optical axis when the above adjustment was made.

● Misalignment of the Secondary Mirror Orientation

Misalignment of the secondary mirror orientation did not affect the spatial resolution measurement by any significant amount when diffraction rings, which indicated good orientation of the secondary mirror, disappeared.

● Misalignment of the Recombining Beamsplitter

By moving the target, the spatial resolution under the separate L. O. mode was 10.5 feet at the optimum position of the recombining beamsplitter. The spatial resolution remained the same when the recombining beamsplitter was rotated by 0.81×10^{-3} radian and consequently lowered the signal level by a factor of 0.43.

3.3.5 Interference Effect Between the Backscatter Power and the Separate Local Oscillator Power

● Experiments

A potential problem with operating the LDV system in the separate L.O. mode is the interference between the backscatter power and the separate L.O. power which will give a fluctuating resultant L.O. power on the detector. The amount of fluctuation due to the scanning secondary — even when the ratio between the separate L.O. and backscattered L.O. powers is increased to 36 to 1 — would still be 3 dB.

The wheel signal level varies with the orientation of the recombining beamsplitter as indicated in Fig. 3-7a. The translation of the recombining beamsplitter along the optical path (x'-axis in Fig. 3-8) was approximately a quarter wavelength. To vary signal level from maxima to minima, or vice versa, at each orientation of the recombining beamsplitter, the amount of the fluctuation, which is the difference between maximum and minimum, at each orientation is indicated in Fig. 3-7b.

By translating the secondary mirror, the same type curves were obtained as shown in Figs. 3-9a and 3-9b. One-quarter wavelength travel of the secondary mirror changes the signal level from maximum to minimum. Rotation of the recombining beamsplitter about the z-axis (Fig. 3-8) by an amount of approximately $\pm 0.5 \times 10^{-3}$ radian gives similar results which are plotted in Figs. 3-10a and 3-10b, respectively.

● Discussion

The ratio of the separate L.O. power level to the backscatter power level should be increased to at least 36 to 1 in order to cure the interference problem.

Wheel Signal Level at 188 Feet (dBm)

1.08×10^{-3} rad.

SAT Detector PV 952
Translation of Recombining
Beamsplitter

Note: Recombining beamsplitter position
about z-axis = 0 rad.

Recombining Beamsplitter Orientation
(rotational adjustment about y-axis in mm)
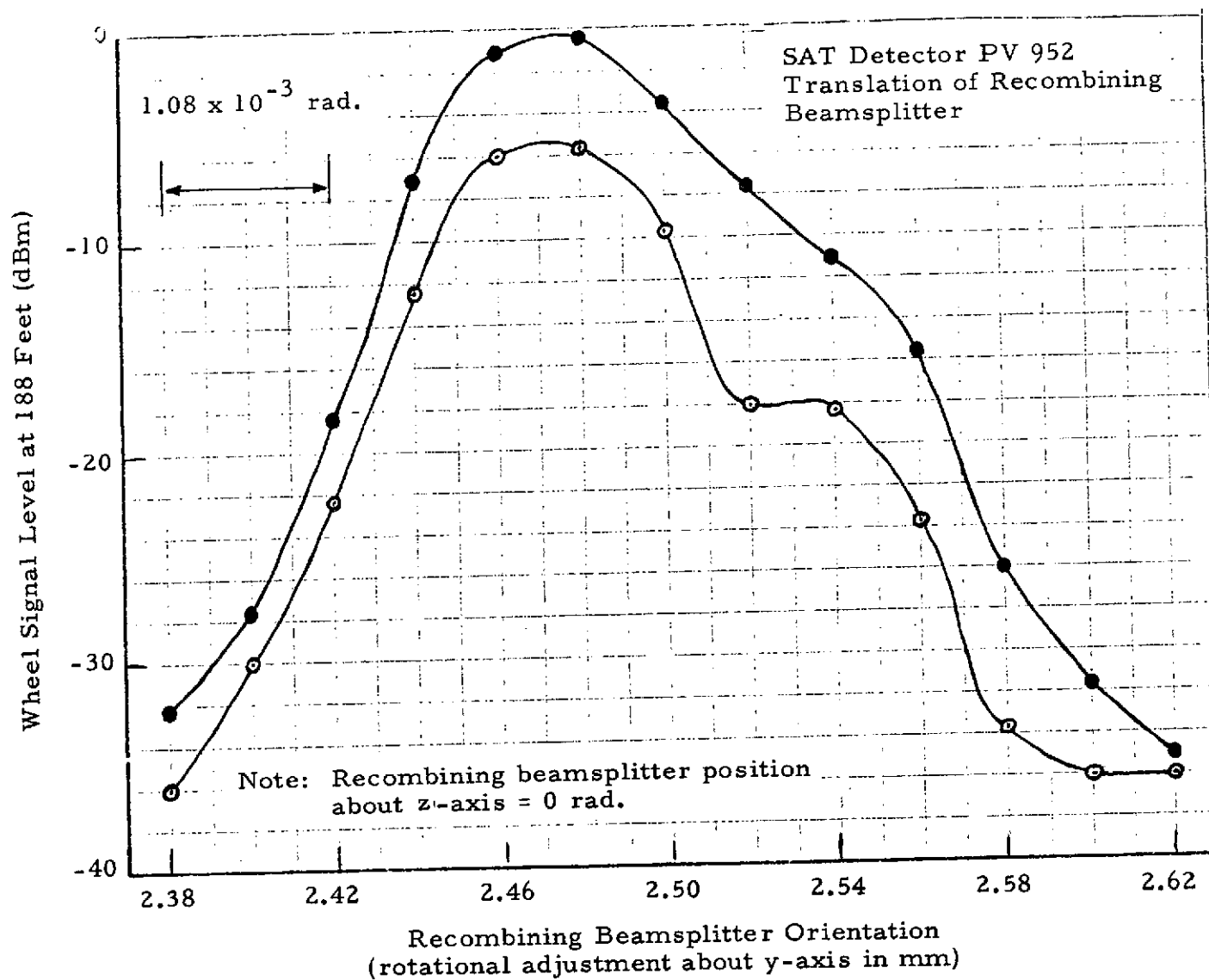
Fig. 3-7a - Interference Effect in the Separate Local Oscillator Mode

Note: Recombining beamsplitter position
      about z-axis = 0 rad.

Fig. 3-7b - Interference Effect in the Separate Local Oscillator Mode

Brewster Angle
Ge Coupler

Top View of the
Interferometer

Backscatter
Power

y

Resultant
L.O.

x′

x

Separate
L.O.

1.5" Ge Lens

Detector

6 mm Iris

Recombining
Beamsplitter

Side View of the
Interferometer

z

y

x′
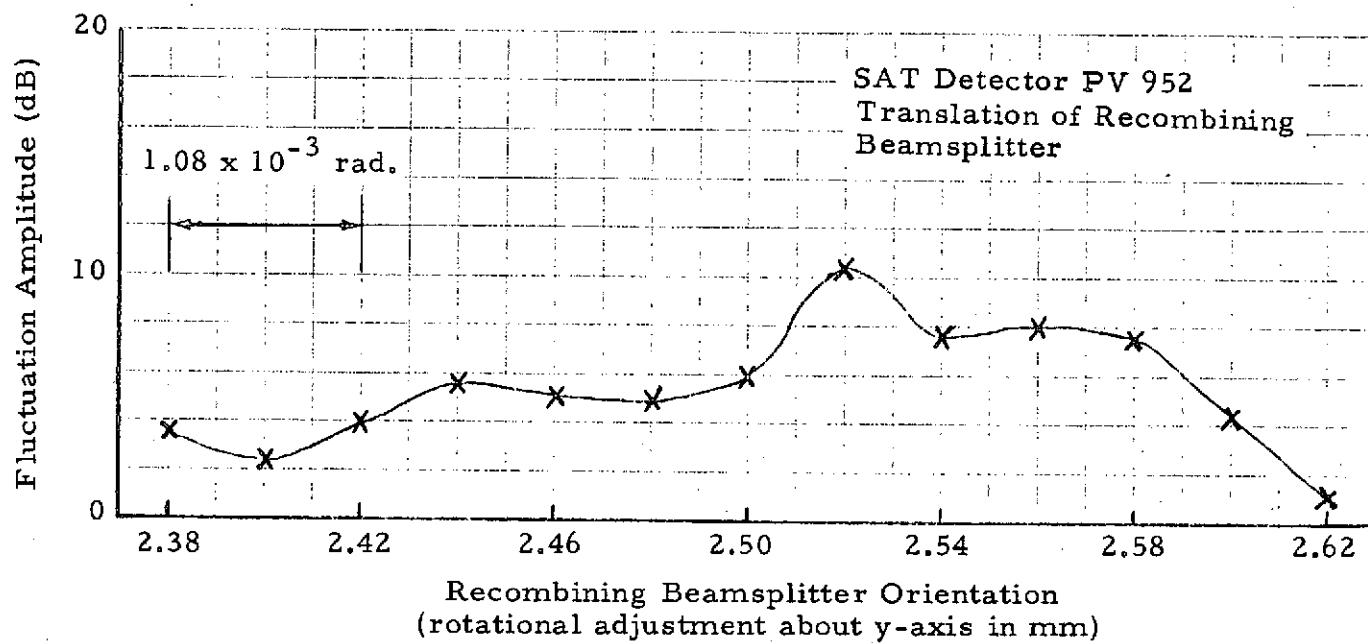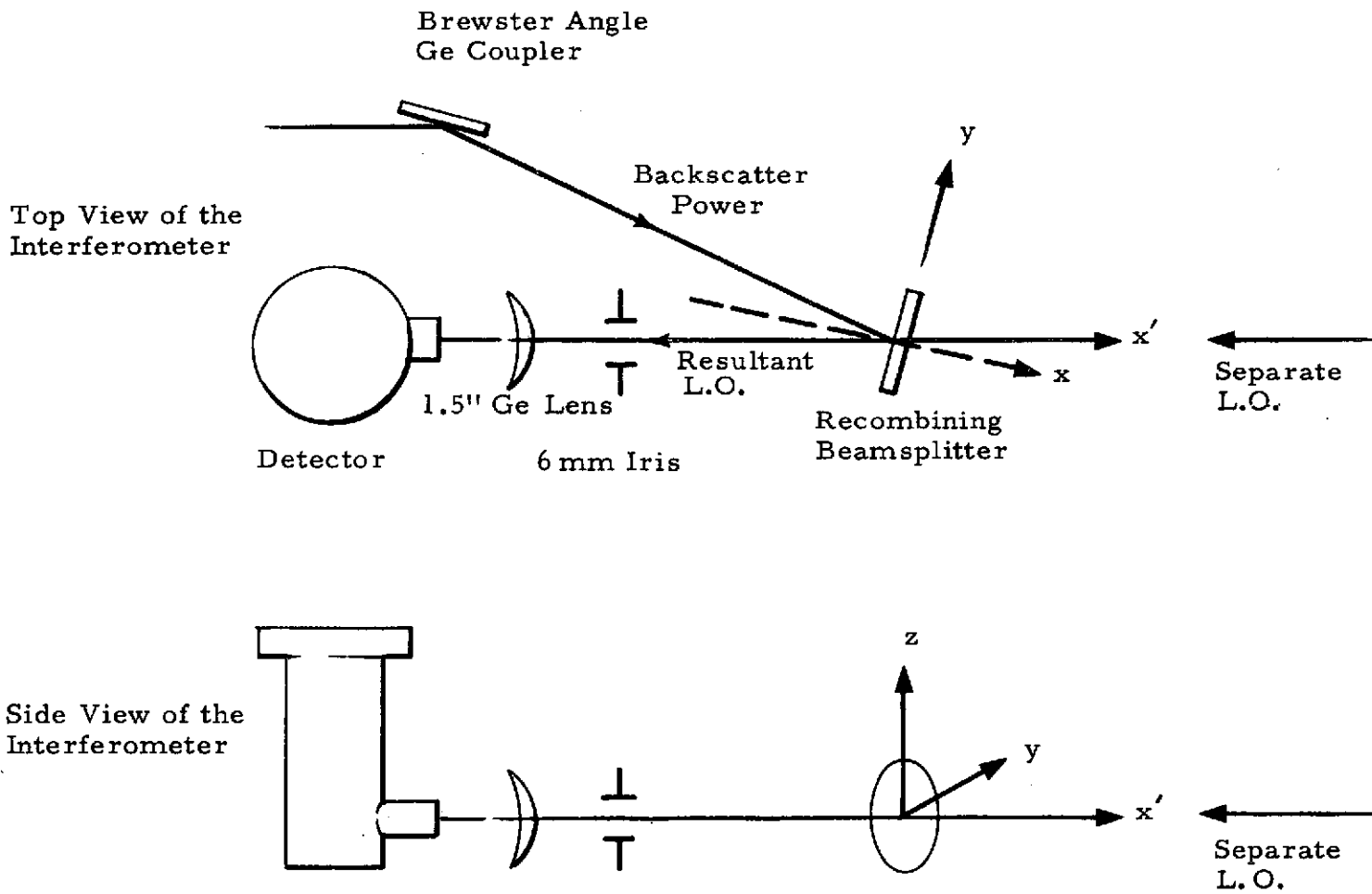
Separate
L.O.

Fig. 3-8 - LDV Interferometer Set-Up for Separate Local Oscillator Operation Mode

Fig. 3-9a - Interference Effect in the Separate Local Oscillator Mode
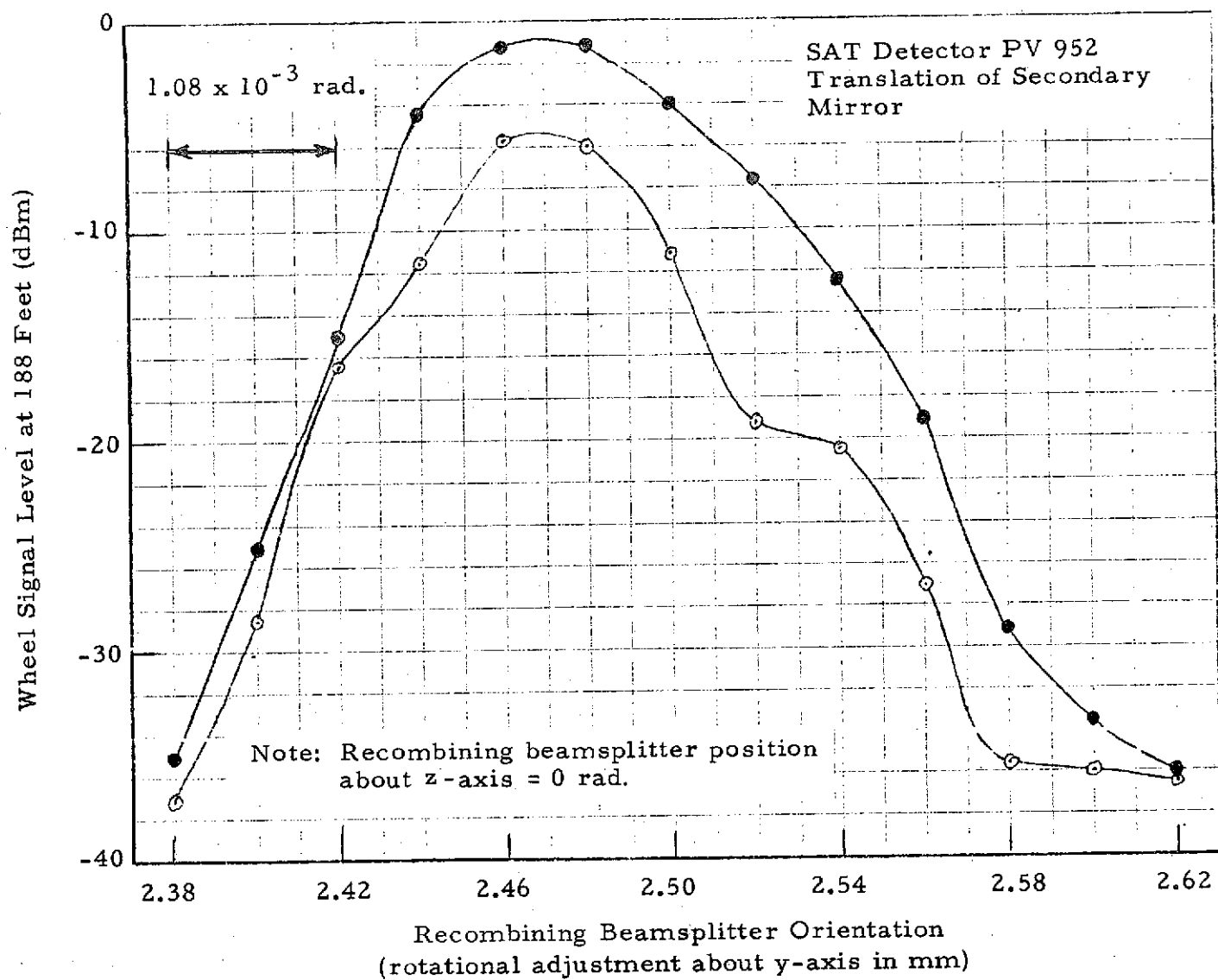
Note: Recombining beamsplitter position
about z-axis = 0 rad.
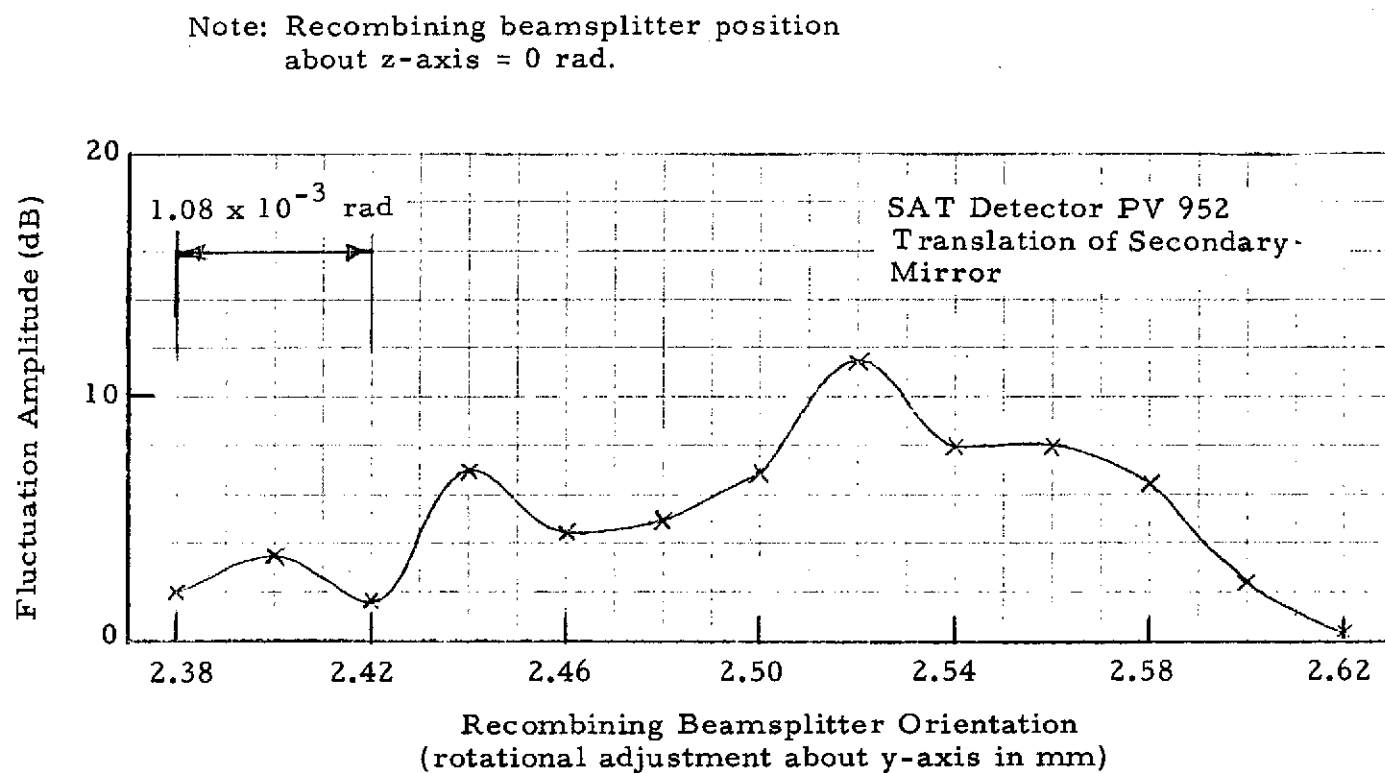
Fig. 3-9b - Interference Effect in the Separate Local Oscillator Mode
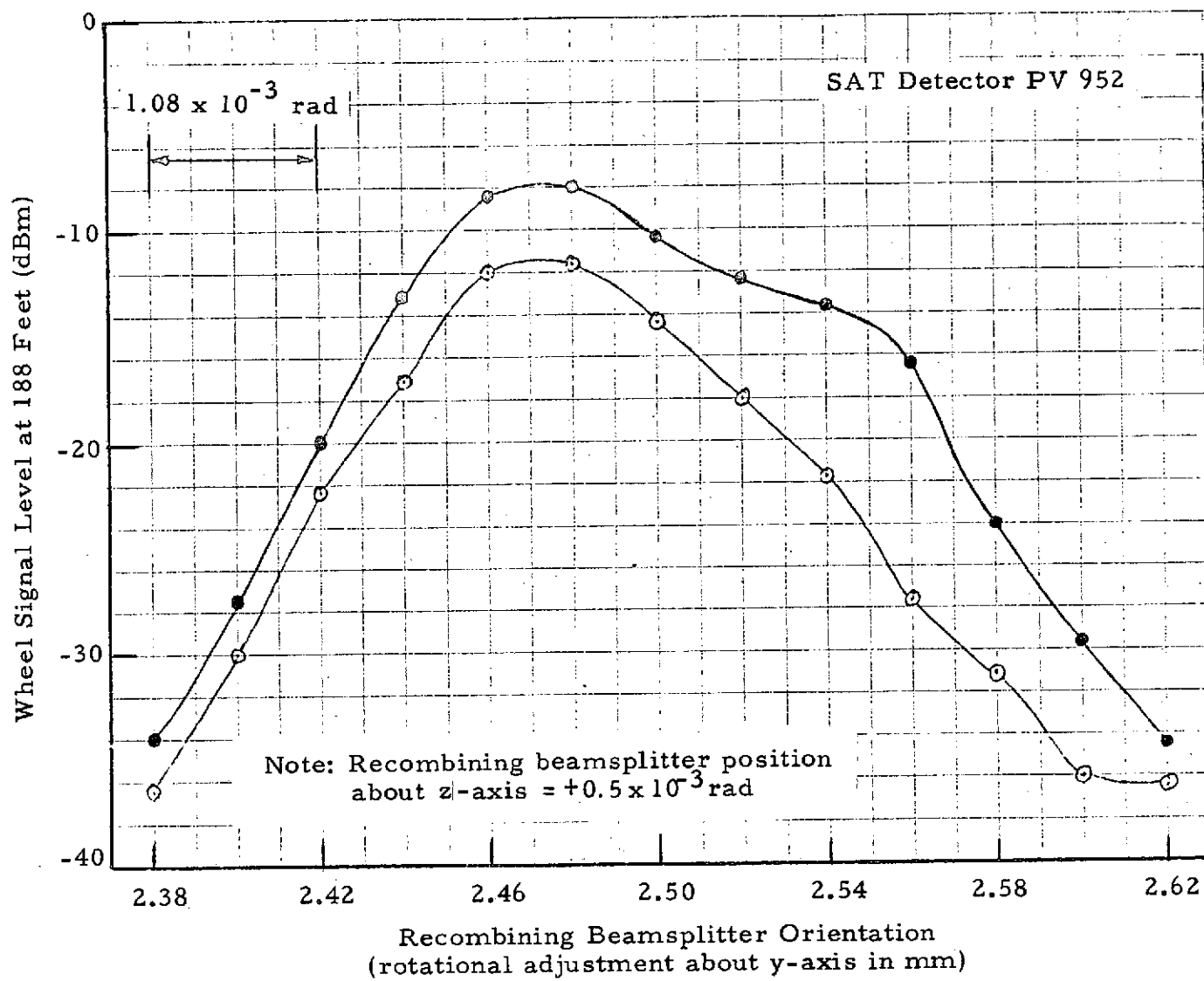
Fig. 3-10a - Interference Effect in the Separate Local Oscillator Mode

Note: Recombining beamsplitter position
about z-axis = $+0.5 \times 10^{-3}$ rad.
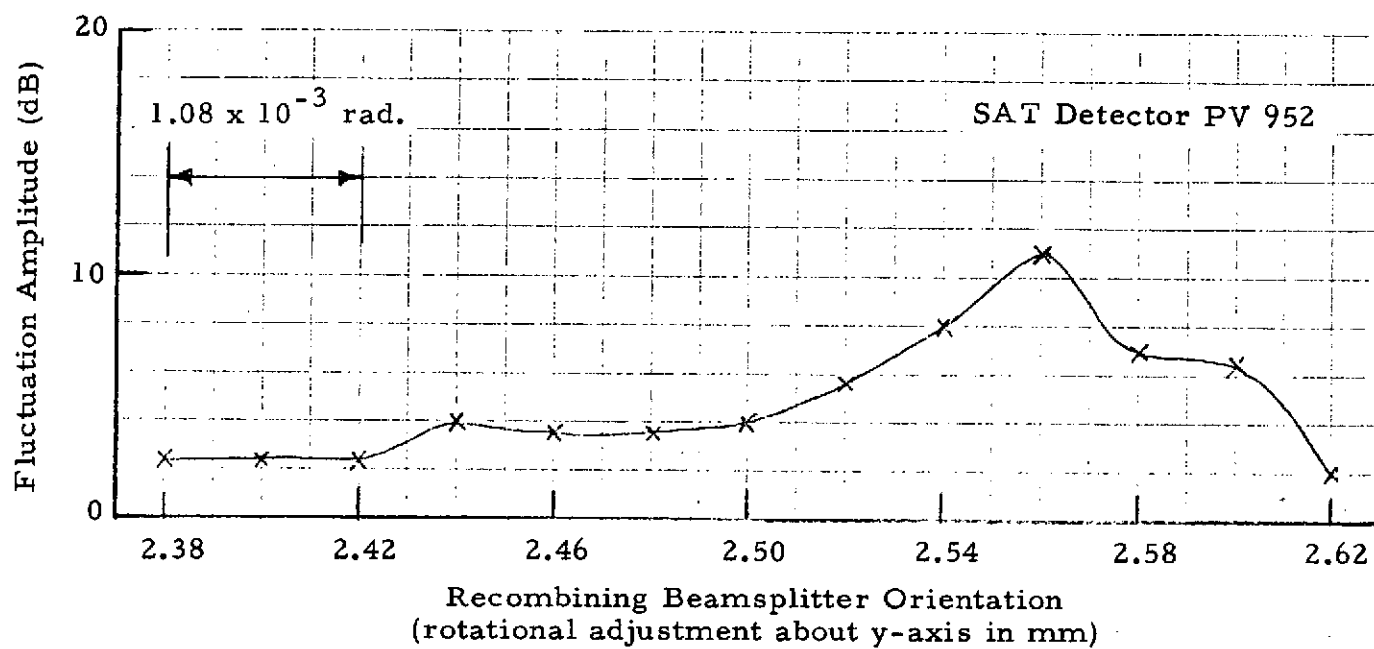
Fig. 3-10b - Interference Effect in the Separate Local Oscillator Mode

The low frequency optical beat of the scanning secondary mirror sepa-rate L.O. mode, can be cured by the following arrangement: (1) introduce the separate L.O. onto a scanning flat mirror which is synchronized with the scanning secondary mirror; and (2) after the reflection by the scanning flat mirror, the separate L.O. can be introduced onto the recombining beamsplitter mixed with the return signal and the backscatter power.* A frequency translated separate L.O. mode will not introduce the interference problem because there is no phase interference between the secondary mirror backscatter power and the frequency translated L.O. power when two frequencies are not equal.

● Extended Measurements

Note in Figs. 3-7a, 3-7b, 3-9a, 3-9b, 3-10a, 3-10b, 3-11a and 3-11b, that the maximum fluctuations of the wheel signal level did not occur when the wheel signal level was maximum and also that the top part of the wheel signal level was somewhat flat. One possible explanation of these results is the saturation of the spectrum analyzer because of the strong signal level.

Switching the input attenuation of the spectrum analyzer from 10 dB to 30 dB corrects the spectrum analyzer saturation. The result of the interference effect in the separate local oscillator mode is shown in Fig. 3-12 where it is seen that the top of the wheel signal is no longer as flat as before and the peak signal fluctuation occurs where the wheel signal is maximum.

A 21 dB fluctuation in signal level was noticed. The destructive inter-ference gives lower resultant local oscillator power, hence the higher voltage across the detector and higher noise level, but higher signal-to-noise ratio that is shown in Fig. 3-13. The constructive interference gives higher resultant local oscillator power, hence lower noise level but also lower signal-to-noise ratio, which is shown in Fig. 3-14.

---

*This technique is probably too complex to be practical.
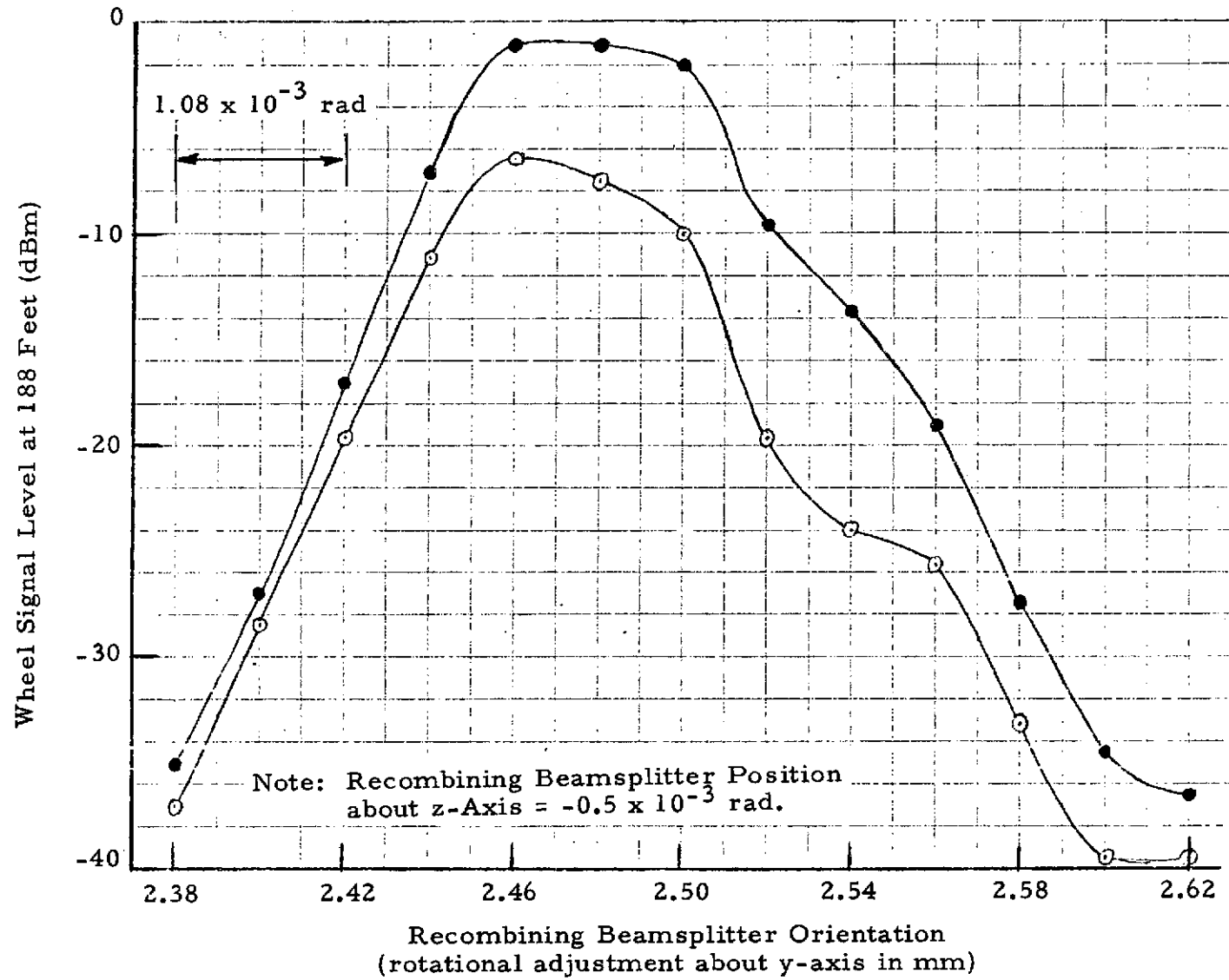
Fig. 3-11a - Interference Effect in the Separate Local Oscillator Mode

Note: Recombining beamsplitter position
about z-axis = -0.5×10^{-3} rad.
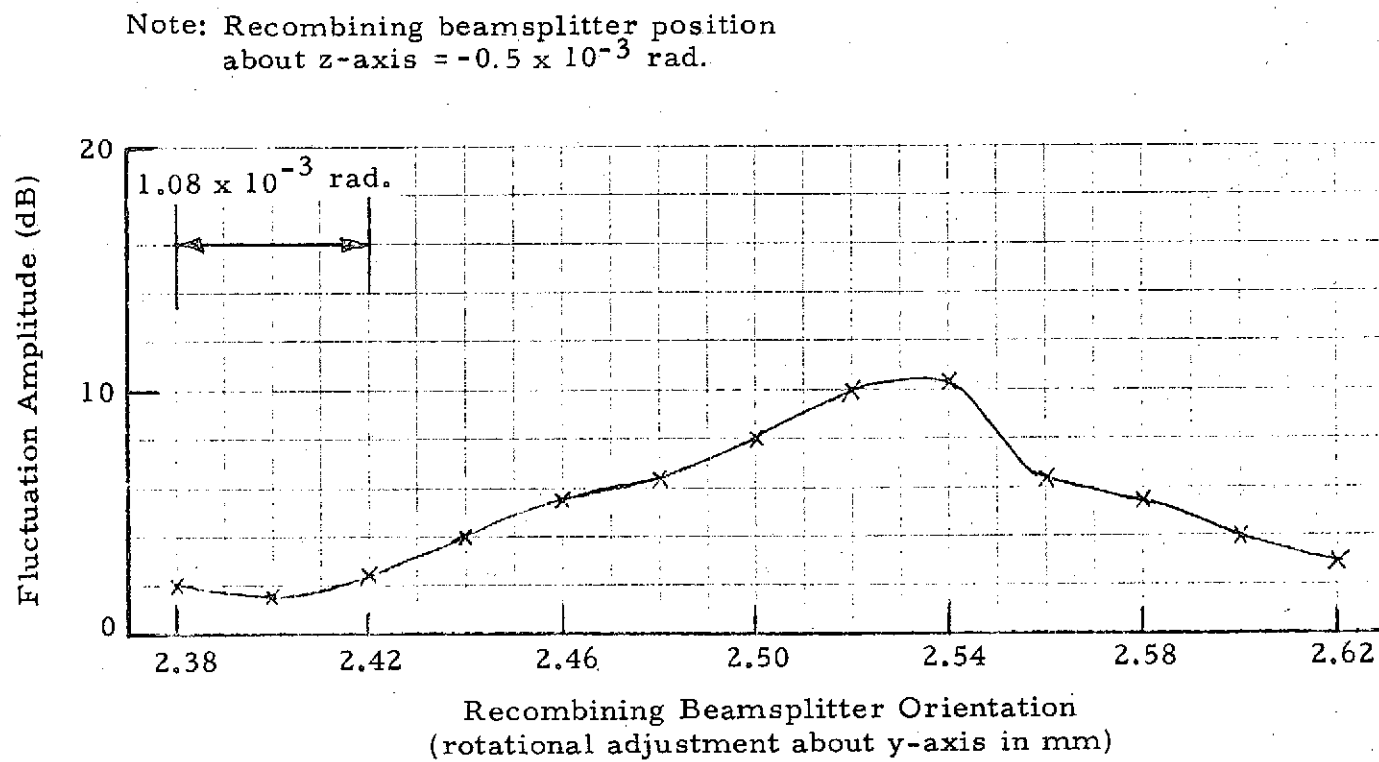
Fig. 3-11b - Interference Effect in the Separate Local Oscillator Mode
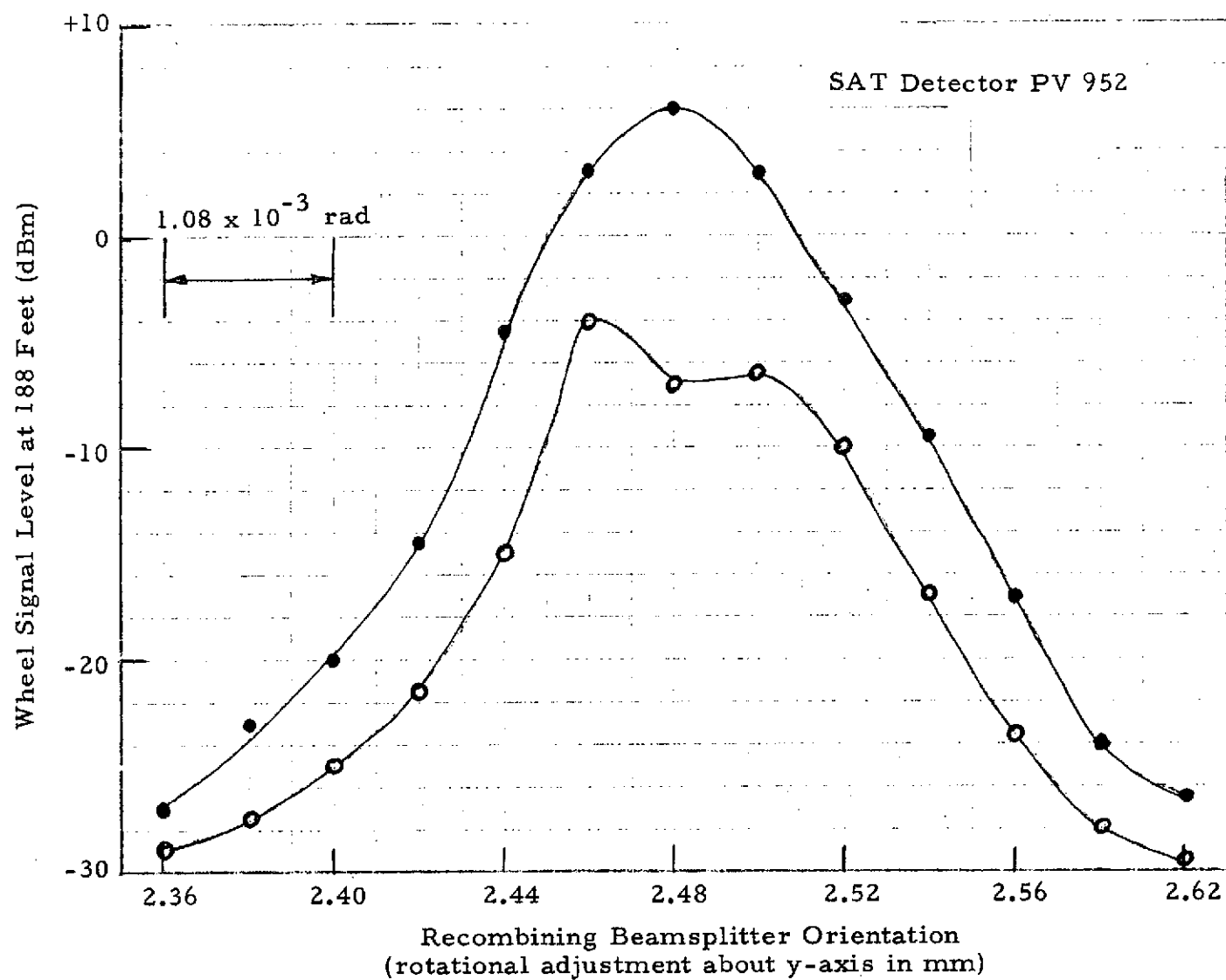
Fig. 3-12a – Interference Effect in the Separate Local Oscillator Mode
After the Spectrum Analyzer Saturation Has Been Corrected
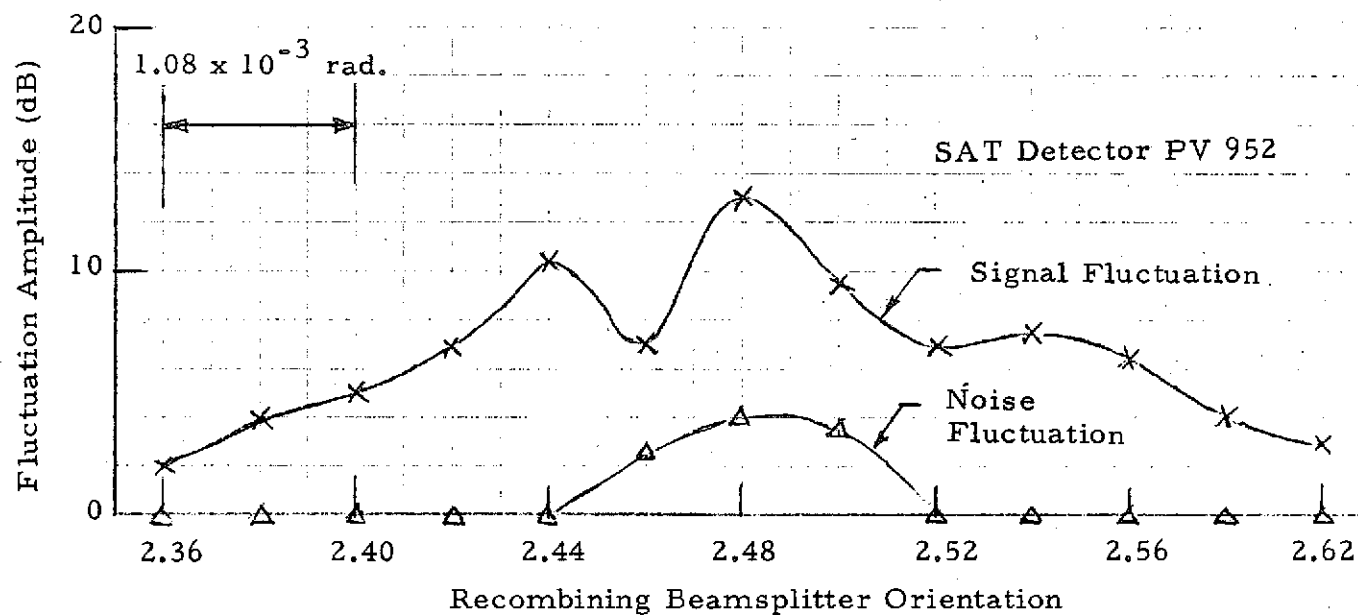
Fig. 3-12b - Interference Effect in the Separate Local Oscillator Mode
After the Spectrum Analyzer Saturation Has Been Corrected

← +10 dBm
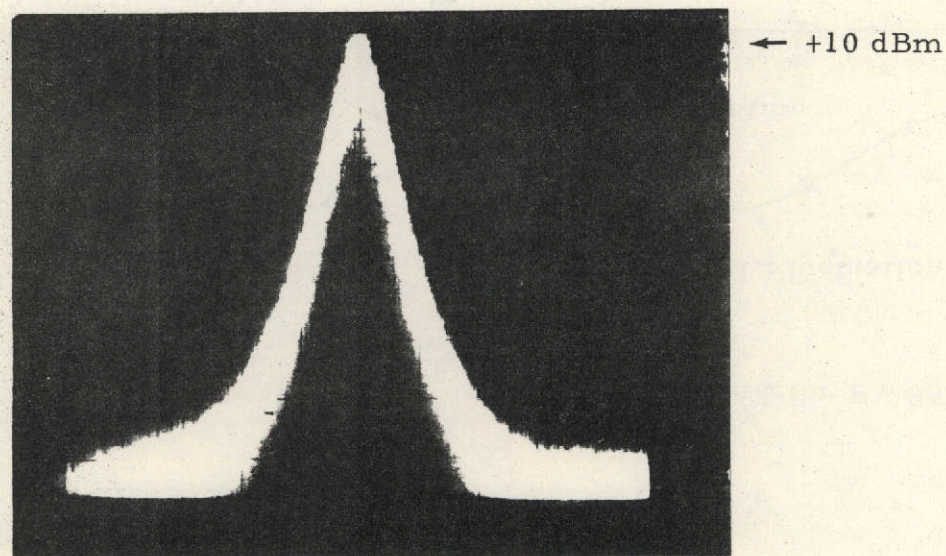
Fig. 3-13a - Sandpaper Wheel Signal Display of the Destructive Interference Between the Separate Local Oscillator Power and the Backscatter Power (Range: 188 ft; detector: SAT PV 952; Signal: +5 dBm; Noise: -71 dBm; S/N: 76 dB; Bandwidth: 30 kHz; Center Frequency 800 kHz; 0.1 MHz/division)

+20 dBm
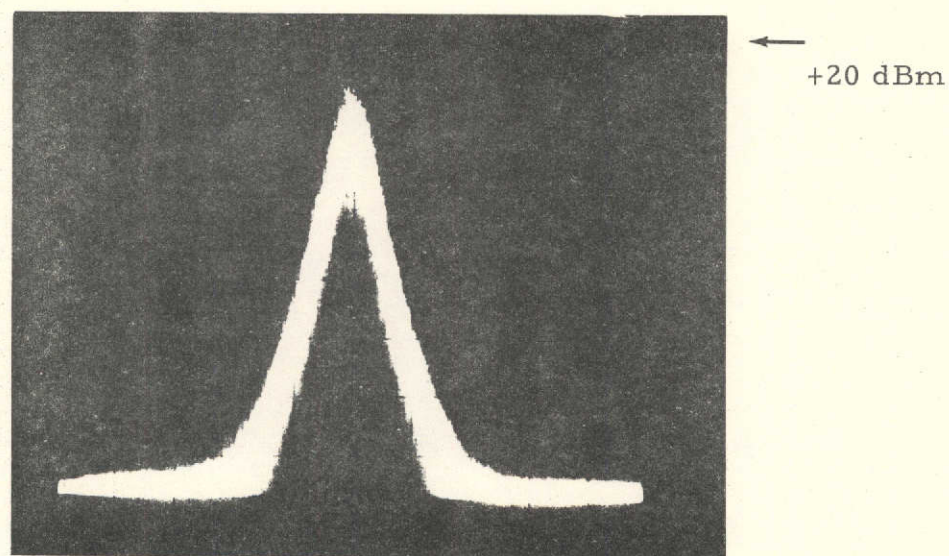
Fig. 3-13b - Sandpaper Wheel Signal Display of the Destructive Interference Between
the Separate Local Oscillator Power and the Backscatter Power (Range:
188 ft; detector: SAT PV 952; Signal: +5 dBm; Noise: -71 dBm; S/N: 76 dB;
Bandwidth: 30 kHz; Center Frequency 800 kHz; 0.1 MHz/division)

← -10 dBm
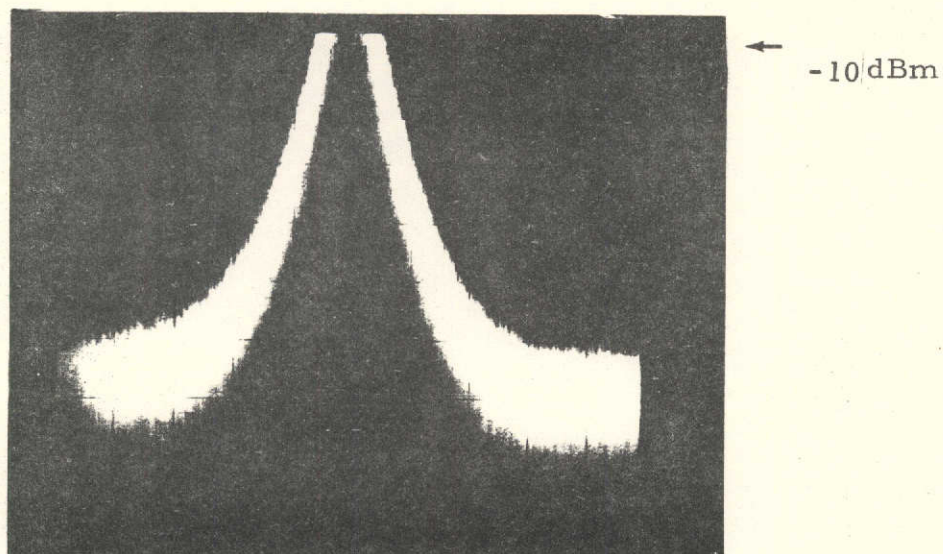
Fig. 3-13c - Sandpaper Wheel Signal Display of the Destructive Interference Between
the Separate Local Oscillator Power and the Backscatter Power (Range:
188 ft; detector: SAT PV 952; Signal: +5 dBm; Noise: -71 dBm; S/N: 76 dB;
Bandwidth: 30 kHz; Center Frequency 800 kHz; 0.1 MHz/division)

-10 dBm
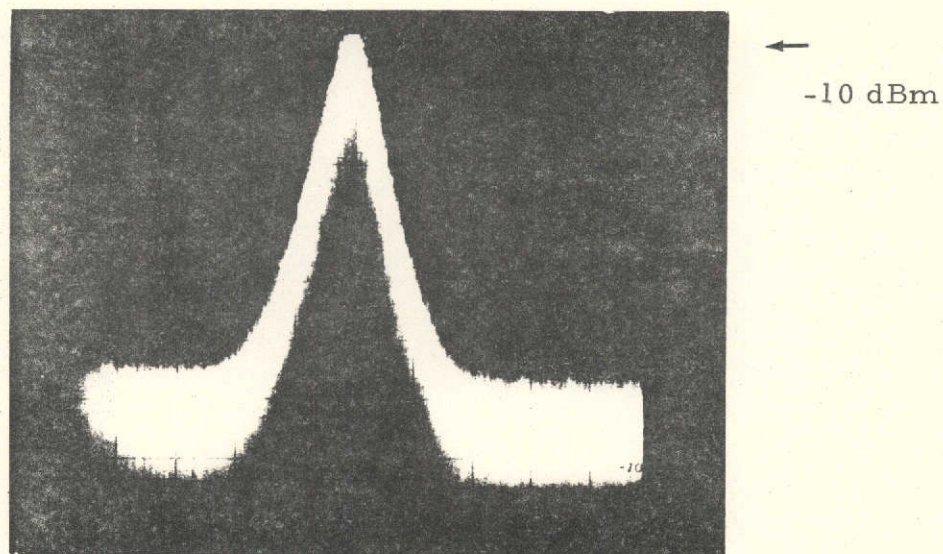
Fig. 3-14a - Sandpaper Wheel Signal Display of the Constructive Interference Between the Separate Local Oscillator Power and the Backscatter Power (Range: 188 ft; detector: SAT PV 952; Signal: -16 dBm; Noise: -76 dBm, S/N: 60 dB; Bandwidth: 30 kHz; 0.1 MHz/division)

0 dBm
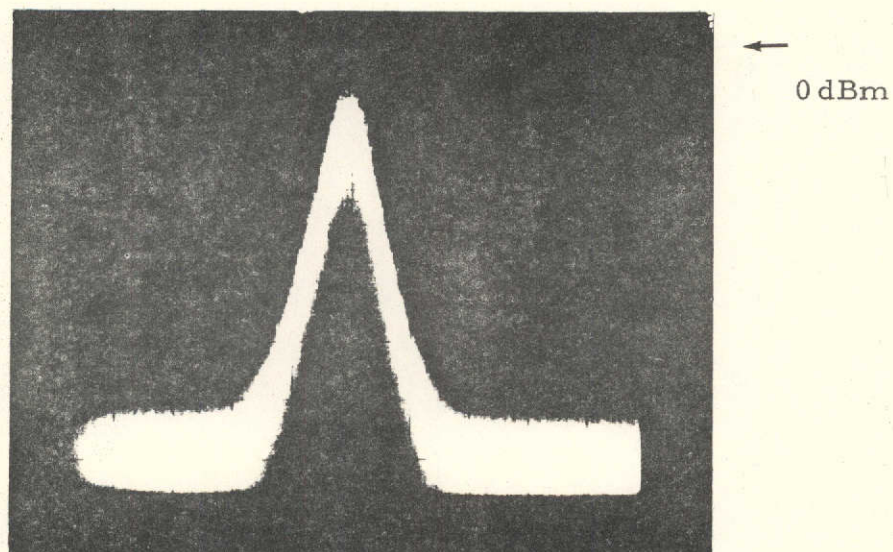
Fig. 3-14b - Sandpaper Wheel Signal Display of the Constructive Interference Between the Separate Local Oscillator Power and the Backscatter Power (Range: 188 ft; detector: SAT PV 952; Signal: -16 dBm; Noise: -76 dBm, S/N: 60 dB; Bandwidth: 30 kHz; 0.1 MHz/division)

-30 dBm
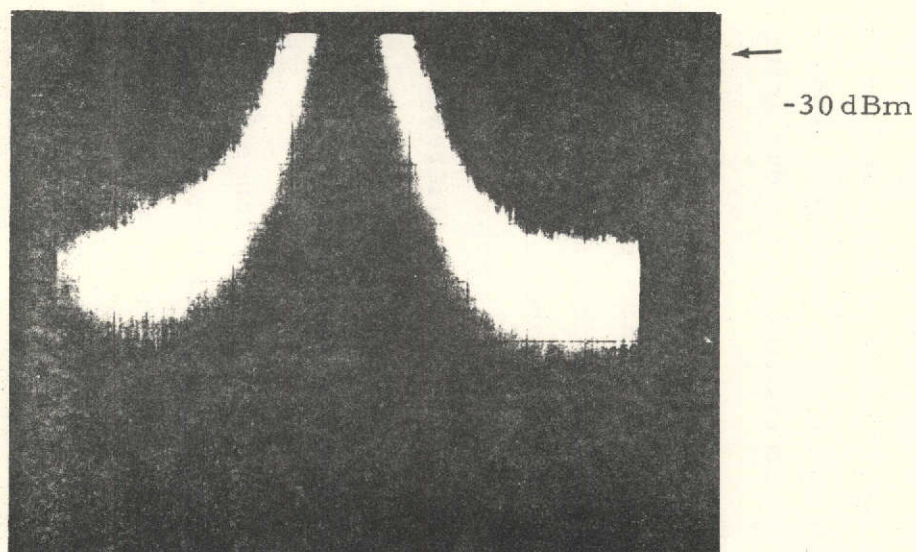
Fig. 3-14c - Sandpaper Wheel Signal Display of the Constructive Interference Between
the Separate Local Oscillator Power and the Backscatter Power (Range:
188 ft; detector: SAT PV 952; Signal: -16 dBm; Noise: -76 dBm, S/N: 60 dB;
Bandwidth: 30 kHz; 0.1 MHz/division)

● Signal-to-Noise Ratio vs Range for SAT Detector PV 952

After the saturation problem for the spectrum analyzer had been cor-
rected, we found that either the local oscillator power was too high or the
amplifier was not designed properly to provide optimized signal-to-noise
ratio for that local oscillator power level which was accepted by the detector.
This was noticed when the secondary mirror was moved laterally approxi-
mately 0.02 in. from its optimum position and the higher signal-to-noise
ratio of the backscatter mode was measured because of the reduced back-
scatter power from the secondary mirror due to this misalignment.

At a range of 188 feet the highest signal-to-noise ratio from a sand-
paper wheel was recorded as 80 dB. Under the normal operation, the signal-
to-noise ratio was only about 75 dB for a total backscatter power of about 0.7
mW accepted by the detector according to the I-V curve of each detector. The
argument that lower local oscillator power gives higher signal-to-noise ratio
was also verified by looking into the interference effect of the separate local
oscillator mode. Destructive interference gives lower local oscillator power,
which gives higher signal-to-noise ratio.

The signal-to-noise ratio versus range for SAT detector PV 952 is shown
in Fig. 3-15. In the figure the signal-to-noise ratio at a range of 188 feet was
78 dB. This value was also reached by SAT detector PV 1031 once before,
which encouraged us to further investigate the signal-to-noise ratio and shoot
for higher values.

3.4 FIELD MEASUREMENTS OF COHERENT SPATIAL RESOLUTION AND SIGNAL-TO-NOISE RATIO

Spatial resolutions of the optical sub-systems of the laser Doppler
units mounted in MSFC's vans 1 and 2 were measured at the field test site
for comparison with theory and laboratory measurements during the month
of June 1974. The results of these measurements are presented in Fig. 3-16.
Signal-to-noise ratio (S/N) measurements were also made. The results of
these tests are depicted in Figs. 3-17 and 3-18.

Operation Mode: Backscatter

Target: Sandpaper Wheel

Target Orientation: 30 deg to the
Laser Beam

Detector: SAT PV 952
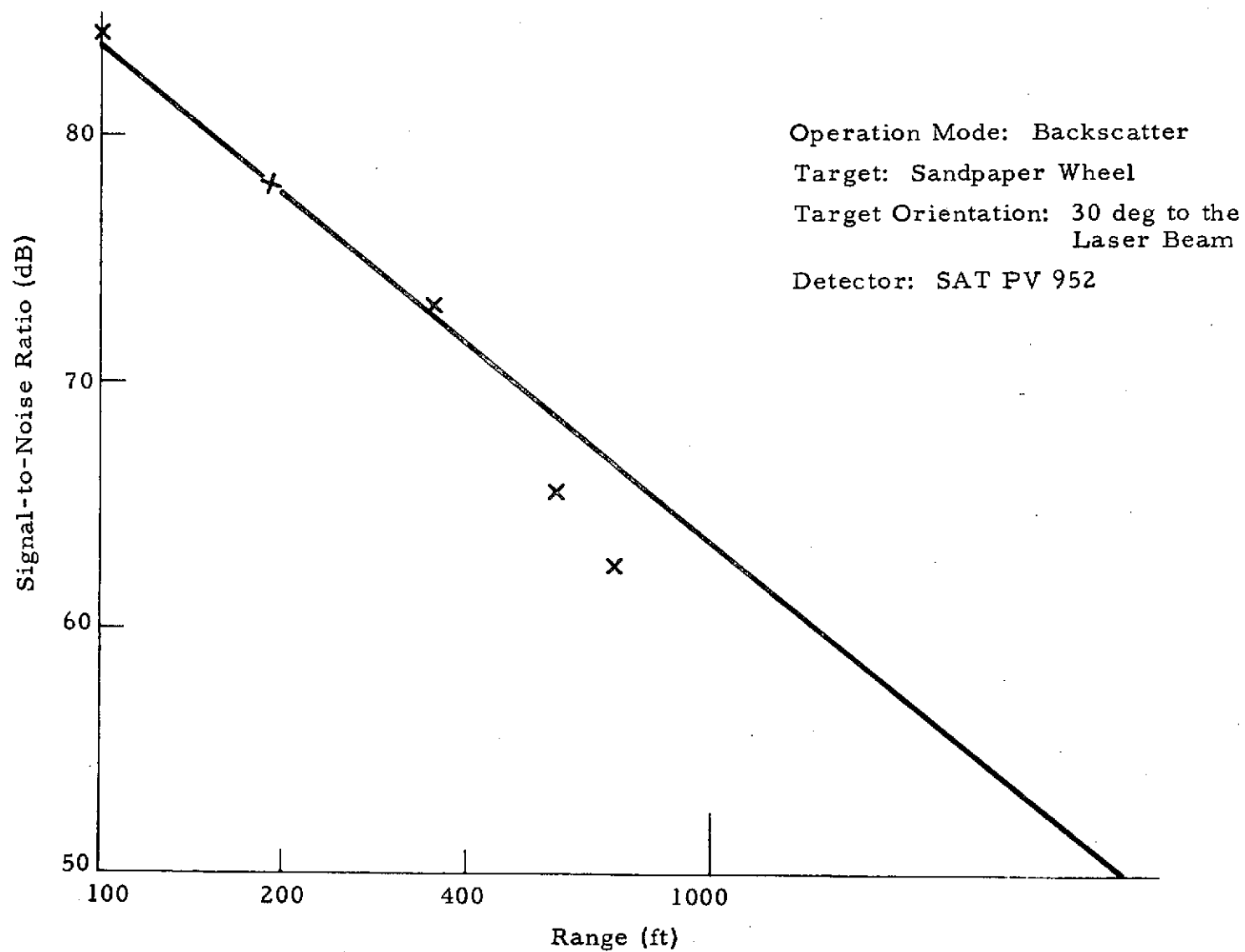
Fig 3-15 - Optimized Signal-to-Noise Ratio for SAT PV 952
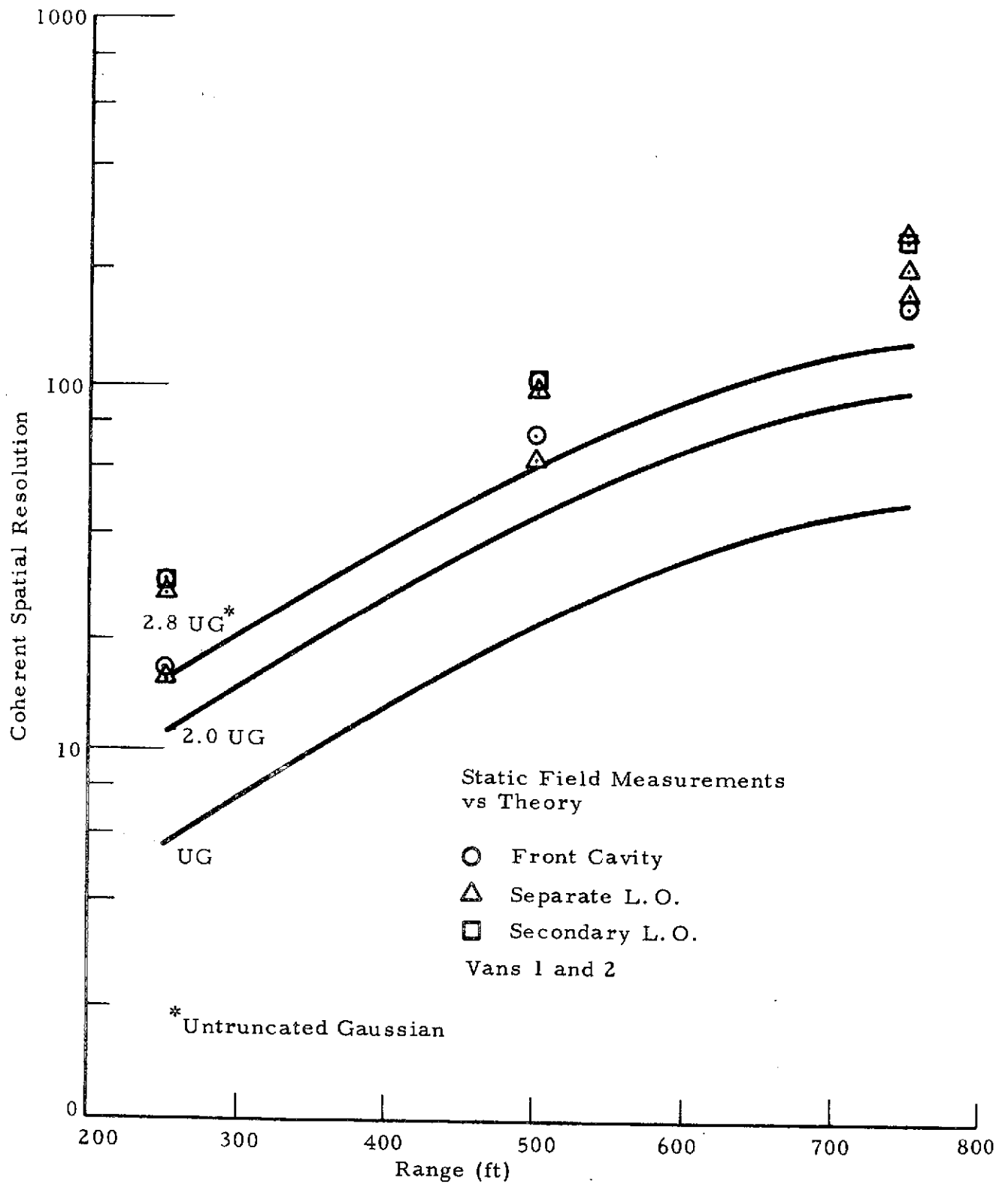
Fig. 3-16 - Coherent Spatial Resolution Measurements versus Theory for LDVs 1 and 2

136

VAN 1
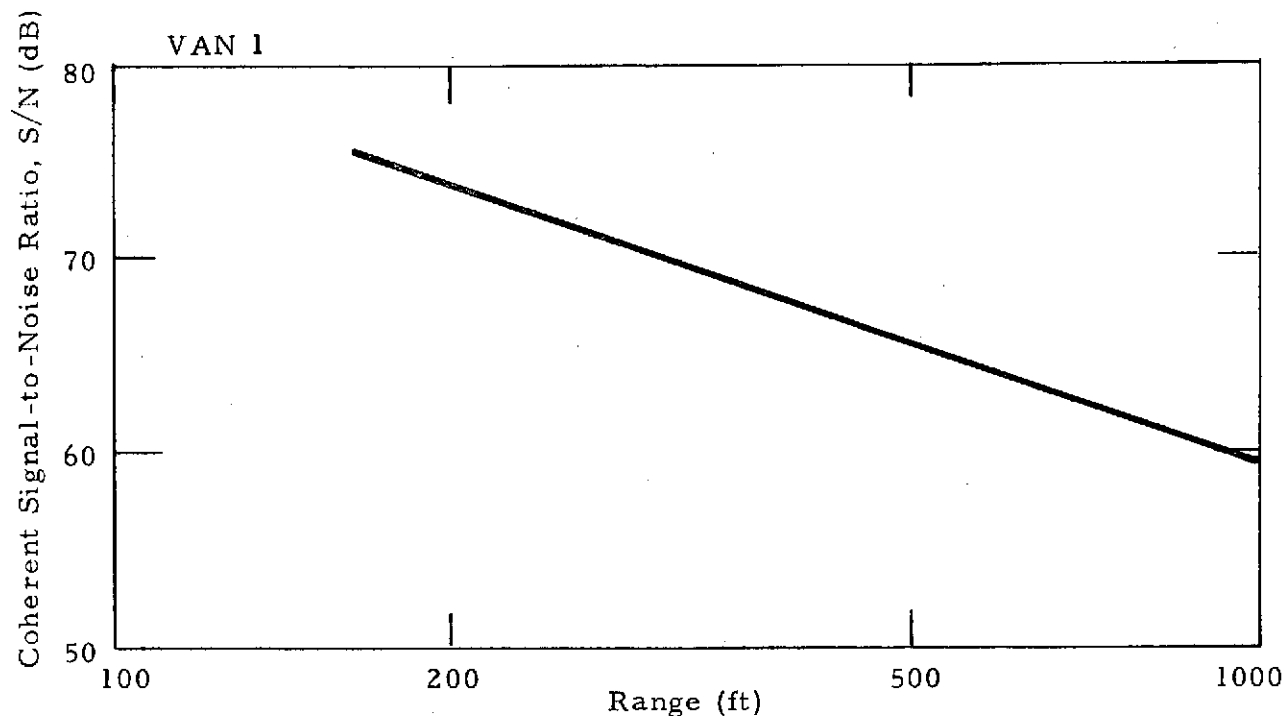
Fig. 3-17- Coherent Signal-to-Noise Ratio versus Target Range for LDV 1

VAN 2
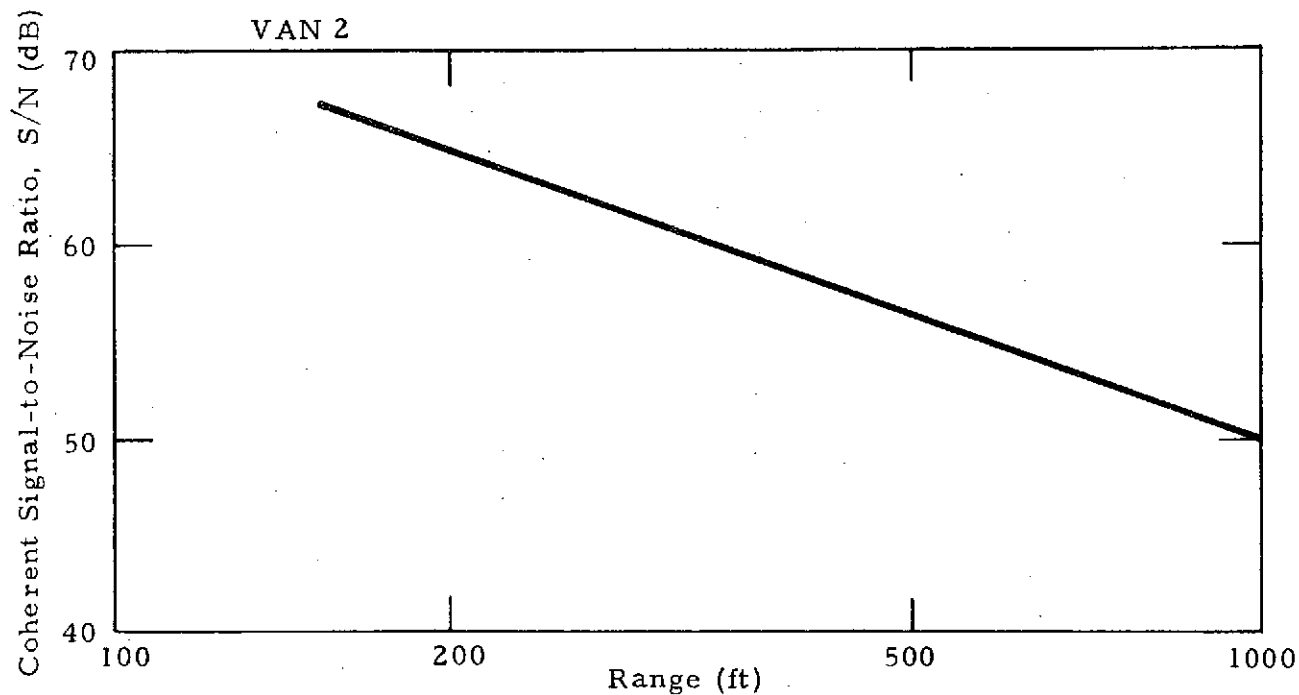
Fig. 3-18 -Coherent Signal-to-Noise Ratio versus Target Range for LDV 2

Calculations of the signal-to-noise (S/N) ratio for untruncated Gaussian theory were made to compare with the actual system efficiency S/N ratio measurements. The results of these calculations and the comparison is depicted as follows.

Untruncated Gaussian Theory

$$(S/N)_{power} = K\alpha\rho\eta (r/R)^2 \; \frac{P_o \cdot \cos\theta_i}{h\nu\Delta f}$$

α	=	optics efficiency
ρ	=	target reflectivity
r	=	telescope radius
R	=	range
P_o	=	laser output power
θ_i	=	incident normal angle on target
Δf	=	bandwidth
$h\nu$	=	photon energy
K	=	Airy receiver efficiency

Quanity	System Number		
	952, Lab	972, Van 1	1031, Van 2
α =	0.24	0.19	0.34
ρ =	0.07	0.07	0.07
η =	0.72	0.30	0.47
r =	0.5 ft	0.5 ft	0.5 ft
R =	200 ft	200 ft	200 ft
P_o =	20 W	15 W	20 W
θ_i =	45 deg	45 deg	45 deg
Δf =	30×10^3 Hz	30×10^3 Hz	30×10^3 Hz
$h\nu$ =	1.87×10^{-20}	1.87×10^{-20}	1.87×10^{-20} J
K =	-6 dB	-6 dB	-6 dB
$(S/N)_{power}$ (calculated) =	86.8 dB	80.7 dB	86.5 dB
(measured) =	80 dB	75 dB	75 dB

3.5 TESTS OF INTERFEROMETER AND CO_2 LASER POLARIZATION

3.5.1 Interferometer Alignment Tests

Lockheed-Huntsville personnel assisted NASA in evaluating the alignment of the Raytheon fabricated Mach Zehnder interferometer (shown in the following sketch). The table below indicates the measured results of this test. These results imply that the system was well aligned when using the secondary backscatter as the local oscillator source, but was non-optimum when using the Mach-Zehnder configuration.
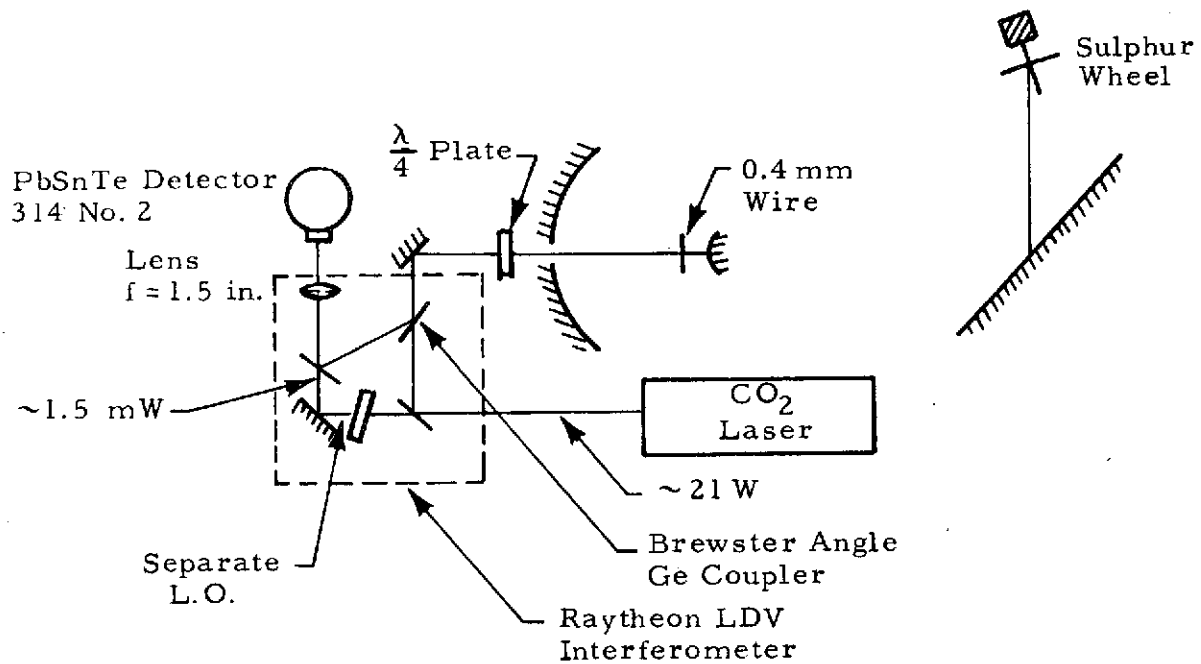
Operation Conditions 200 Range, Bias Voltage = 0	Bias Current (mA)	Signal		Noise (dBm)	S/N (dB)
		p-p(V)	(dBm)		
W/O Wire, W/O Separate L. O.	5.0	0.8	+2	-91.5	93.5
W/O Wire, W/O Separate L.O.	3.8	0.6	0	-91.5	91.5
W/O Wire, W/Separate L.O.	7.0	0.5	-2	-91.0	89.0
W/Wire, W/O Separate L. O.	0.5	0.2	-10	-93.5	83.5
W/Wire, W/Separate L. O.	2.5	0.2	-10	-92.5	82.5

3.5.2 The Degree of Polarization Measurement of a Raytheon CO_2 Laser (Model SL-10A)

The following is a schematic of the experimental arrangement used to evaluate the degree of polarization of Raytheon CO_2 laser.

Coherent Radiation
Model 201 Power Meter

R = 99.9%
Mirror

BaF$_2$ Lens

Attenuator

Sensors
Model C1
Thermopile

Amplifier

Oscilloscope

2nd Brewster
Angle Ge Coupler

1st Brewster Angle
Ge Coupler

Raytheon Model SL-10A
CO_2 Laser

Mirror

140
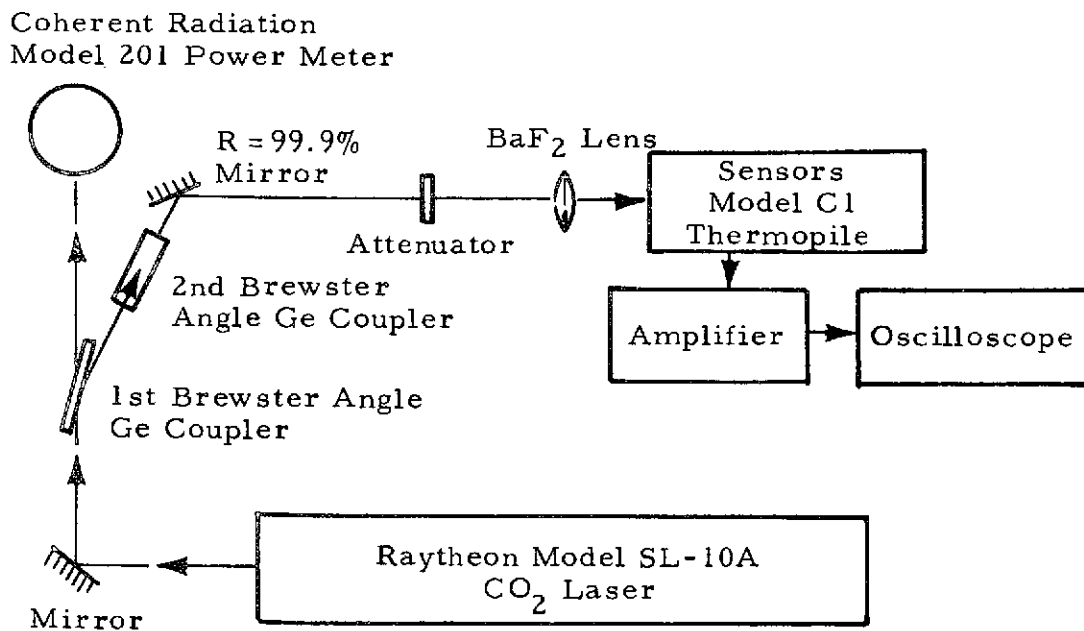
Since the laser power was low (≈ 8 watts, deliberately adjusted), the temperature of the first Ge coupler was low. The absorption of the Ge coupler was therefore also low. Consequently, the laser power received by the coherent radiation power meter was approximately the same as that incident upon the first Ge coupler. The second Ge coupler ensured that the transmitted laser beam through that coupler was a p-wave (which appeared to the first Ge coupler as an s-wave). After the reflection by a high reflectance mirror, this s-wave laser beam was introduced into the model C1 thermopile (Sensors Inc.) through a calcium flouride attenuator (-12.7 dB) and a BaF_2 lens. The output dc voltage of the thermopile was linearly proportional to the power of the s-wave laser beam for this lower power case. The calibrated responsivity of the thermopile enabled us to calculate the power of the s-wave laser beam from the first Ge coupler. The degree of polarization of the laser beam can be calculated as

$$\text{Degree of Polarization} = 1 - \frac{\text{Total s-Wave Power}}{\text{Total Laser Power}},$$

where the s-wave power is much less than the total laser power.

According to the experimental results the degree of polarization of the Raytheon CO_2 laser was 99.20%. Another method was also employed to determine the degree of polarization. This method was a direct measurement of the s-wave power with a Quantronix Model 502 power receiver and a model 504 energy-power meter. This method yielded a value of 99.14% which was comparable to the value measured by the first method.

3.6 DESIGN CRITERIA FOR THE PHOTO VOLTAIC DETECTOR BIAS CIRCUITRY FOR CO_2 COHERENT DETECTOR

The design criteria of the bias circuit for the photovoltaic detector are outlined as shown on the following page.

- Safe operation with the detector
- Maximum photo-induced electrical power coupling from the detector to the preamplifier
- Low noise, flat response preamplifier and circuit
- Sufficient frequency bandwidth
- Minimum radio frequency interference
- Convenient operation

Each design criterion is explained in detail as follows:

3.6.1 Safe Operation With the Detector

- Detector must be cooled using liquid nitrogen before the bias is applied.
- Independent of power failure, optical local oscillator power blockages, or loose wire connections from the detector to the bias supply, the bias voltage generated across the detector must always be less than the maximum allowable voltage applied to the detector.
- The bias current must also be controlled by limiting the amount of optical power incident upon the detector when the safe bias voltage is applied.
- A front panel light bulb is required on the bias box as a reminder to the operator to turn off the bias after each operation.
- A means of achieving these safe operations is to use a small source voltage and small load resistance across the detector as illustrated below.
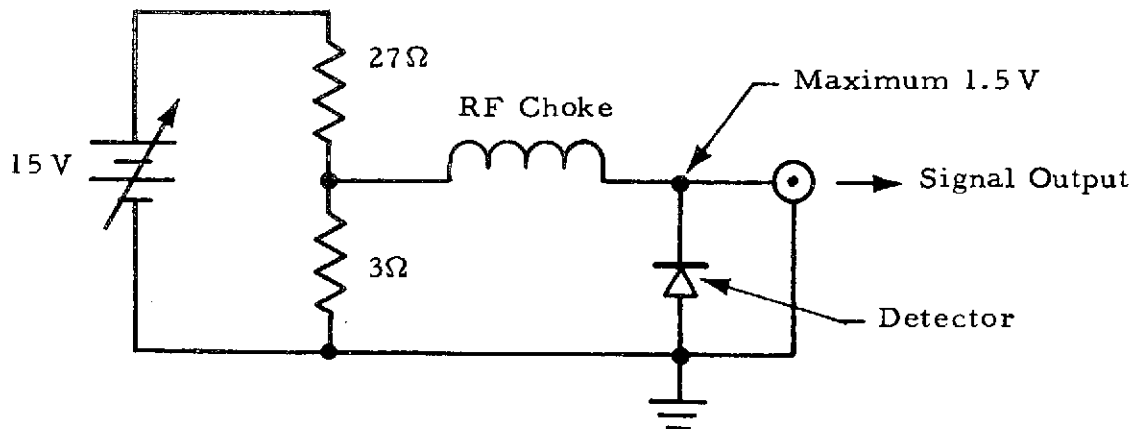
3.6.2 Maximum Photo-Induced Electrical Power Coupling from the Detector to the Preamplifier

- The equivalent circuit of the detector is
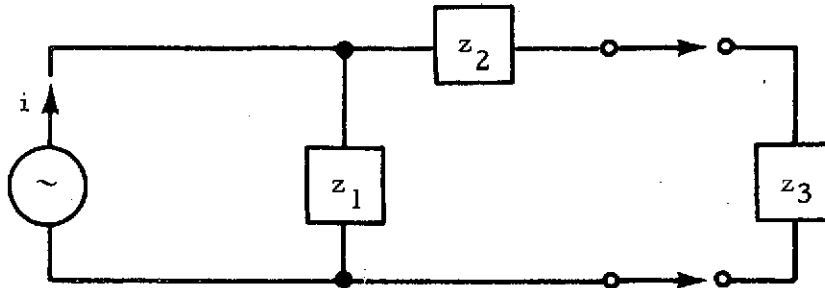
where $z_1 = \dfrac{1}{G_D + j\omega C_D}$

$z_2 = R_s$ = series resistance (dc resistance of the detector)

z_3 = load impedance

G_D = small signal shunt conductance (slope of I-V curve)

C_D = shunt capacitance

ω = IF frequency

i = detector generated IF current

The above circuit can be redrawn as

$$i' = \frac{z_1}{z_1 + z_2}\, i$$
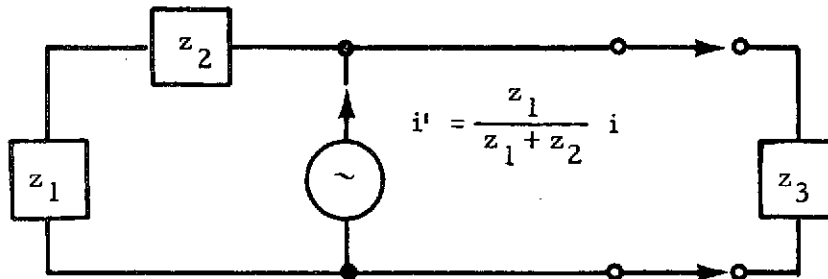
where i' is called short-circuit current. In this circuit
the load impedance will sense the same source current
and impedance as in the previous circuit.

- The condition of maximum power can be coupled by z_3
  from the detector when $z_2 \ll z_1$ if $z_3 \ll z_1$. An amplifier
  having an input impedance equal to the detector impedance
  is preferred in order to provide maximum power coupling;
  however, because of amplifier availability, this is very
  unlikely. An alternative way to achieve the same purpose
  is to use a wide band transformer for matching the detector
  impedance to the input impedance of the amplifier. This
  circuitry is shown below:
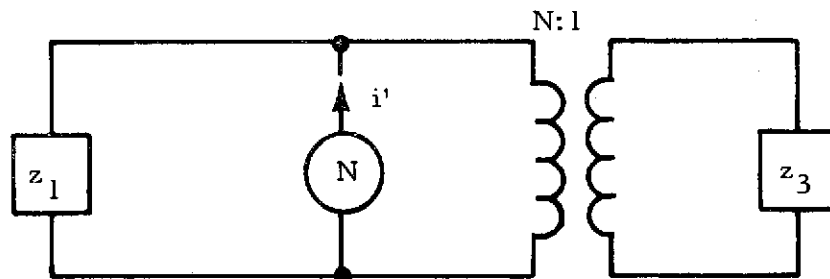
The turn ratio, N, should equal to $\sqrt{z_1/z_3}$ for maximum
power coupling.

3.6.3 Low Noise Flat Response Preamplifier and Circuit

The noise spectrum and the gain of preamplifier must be flat over the
required frequency bandwidth for easier signal processing and calibration of
the system. A low noise preamplifier and circuit is required for shot noise
limited operation of the detector with a moderate optical L.O. power.

3.6.4 Sufficient Frequency Bandwidth

Both the preamplifier and the bias circuit must provide sufficient fre-
quency bandwidth. Electrical component size, arrangement, and connections
should be arranged carefully to avoid stray capacitance and coupling losses
from the detector to the preamplifier.

3.6.5 Minimum Radio Frequency Interference

RF shielding of the detector, bias circuit, and preamplifier must be included in the design of the detector bias circuit. This includes precaution against ground loops, RF isolation of the bias voltmeter and ammeter, and minimum wire lengths. For example, the bias voltmeter can be arranged as depicted below to avoid RF pick-up from the voltmeter:
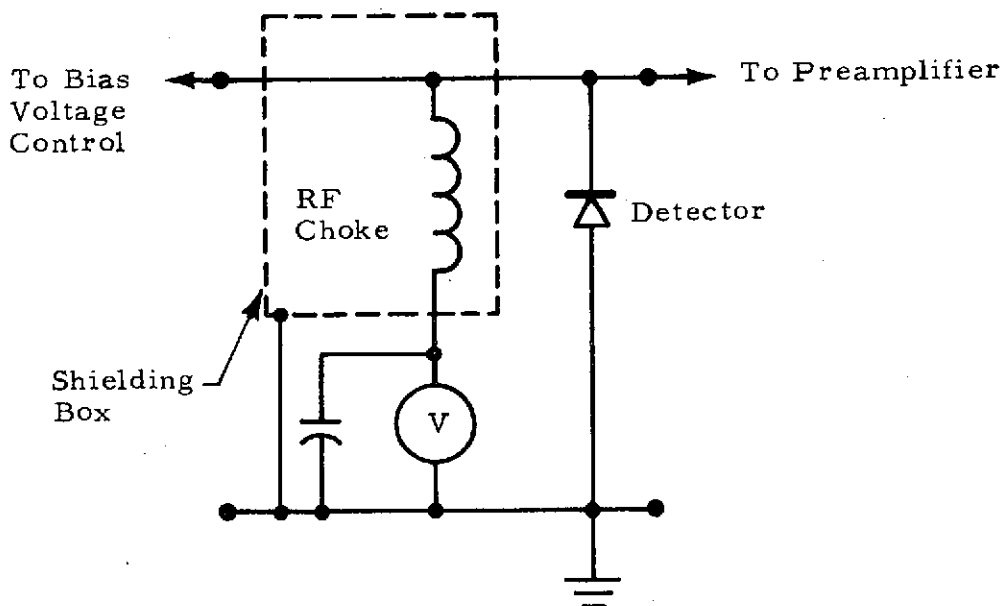
3.6.6 Convenient Operation

The bias box should be compact with bias voltage and current meters attached. The assembly should be designed for easy optical alignment monitoring, optical power monitoring, and ready location of detector optimum operation conditions. Easy adjustment and fine control of the bias should be available. Convenient input and output connectors should be identified with labels. The box should be designed with no exterior exposed voltage terminals.

3.7 ACOUSTIC-OPTICAL TRANSLATOR EVALUATION

3.7.1 Basic Principles

When a laser beam, characterized by its wave vector, $\underline{k}_i$, and its angular frequency, w_i, impinges on a traveling acoustic wave, $\underline{k}_a$, w_a, established in an electro-optic medium, the two waves interact to generate a third wave, $\underline{k}_d$, w_d. This interaction can be represented by a formulation of the conservation of momentum and energy

$$\underline{k}_d = \underline{k}_i \pm \underline{k}_a$$

$$w_d = w_i \pm w_a$$

Figure 3-19 shows schematic and vector diagram of the interaction. The deflected beam exhibits a frequency shift equal in magnitude to the frequency of the acoustic wave.

This interaction, known as the Bragg effect, shifts the incident beam into two beams angularly separated by:

$$\Delta\theta = \lambda f / nv$$

inside the elasto-optic medium, where

$$\lambda = \text{the optical wavelength of the incident beam}$$
$$f = \text{the acoustic frequency applied into the cell}$$
$$n = \text{the index of refraction of the elasto-optic medium}$$
$$v = \text{the acoustic velocity in the elasto-optic medium}$$
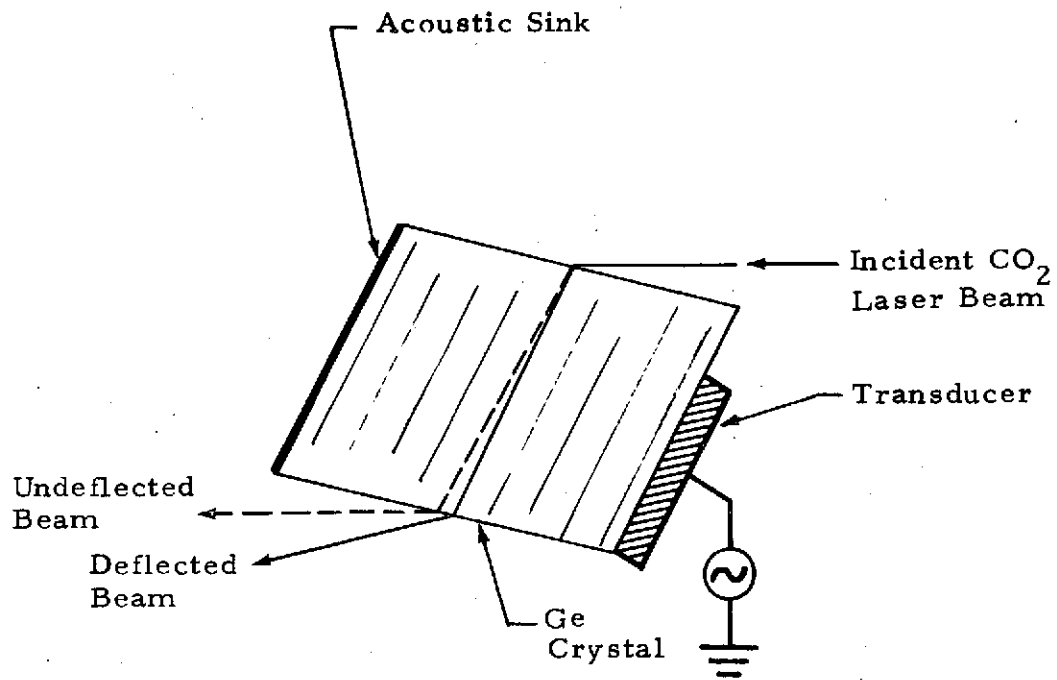
(a)
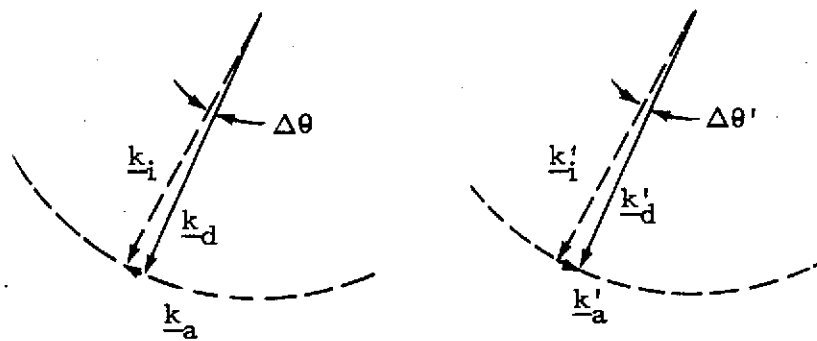
$$\underline{k}_d = \underline{k}_i - \underline{k}_a$$

$$w_d = w_i - w_a$$

$$\underline{k}'_d = \underline{k}'_i + \underline{k}'_a$$

$$w'_d = w'_i + w'_a$$

(b) Down-Shifted in Frequency   (c) Up-Shifted in Frequency

Fig. 3-19 - Acousto-Optic Interaction

147

As shown in Fig. 3-19a the deflected beam will be down-shifted in frequency. This down-shift is shown in Fig. 3-19b. Any amount of reflection of the sound wave, which lies in the same plane as the incident sound wave, by the acoustic sink device will deflect the incident laser beam into the same direction as the beam which is deflected by the transmitted sound wave but up-shifted in frequency (Fig. 3-19c).

An optimum interaction is obtained when the angle of incidence of the laser beam onto the acoustic wave front is set at the Bragg angle

$$\theta_B = \frac{\Delta\theta}{2} = \frac{\lambda f}{2nv}$$

which is equal to 0.36 deg for $\lambda = 10.6 \, \mu m$, $f = 24$ MHz, $n = 4$, and $v = 5.09 \times 10^3$ m/sec.

Although the deflection angle, 9 deg, outside the Ge crystal is large because of the high index of refraction of the Ge, a precise adjustment of the Ge crystal orientation is still required for the optimum operation of the cell.

3.7.2   Acoustical CO_2 Laser Frequency Translator Test

●   Incoherent Measurement

The experimental set-up is shown in Fig. 3-20. The frequency translated separate local oscillator power which is collected by the lens into the detector is shown in Fig. 3-21 for various knob settings of RF driver for the frequency translator.

The efficiency of the frequency translator is defined as the ratio of deflected laser power and incident laser power (see Fig. 3-22).
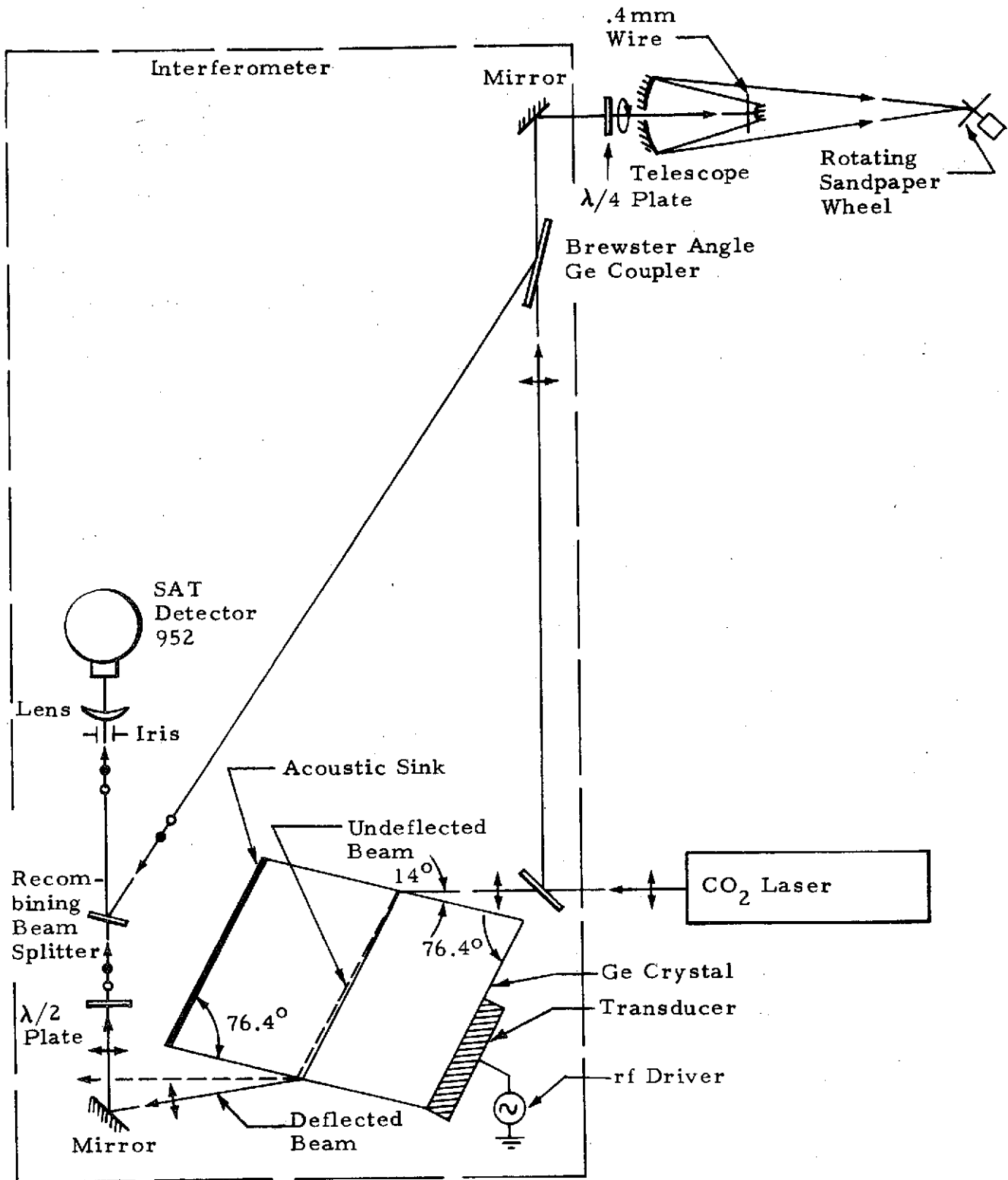
Fig. 3-20 - LDV System with Frequency Translated Separate Local Oscillator
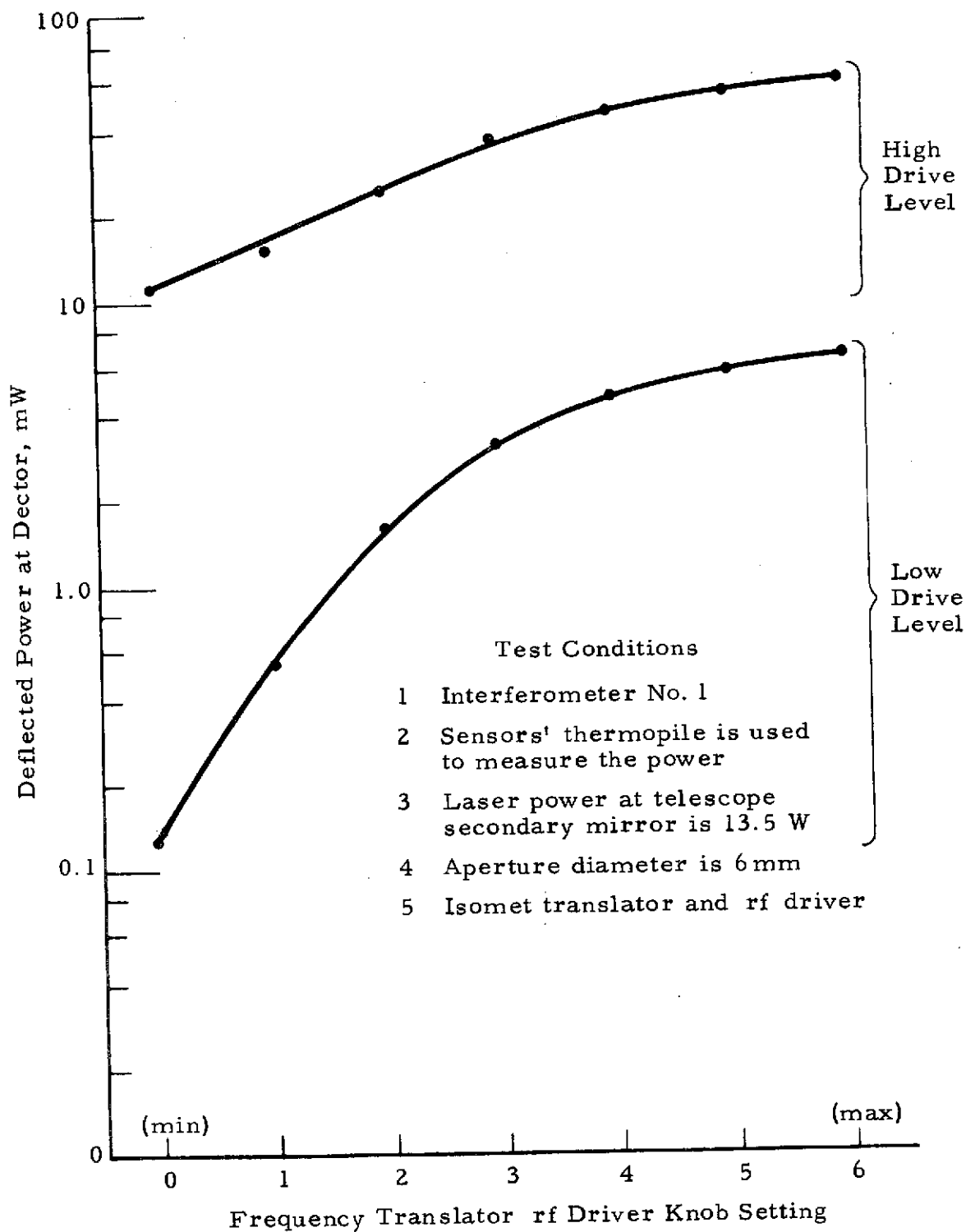
Fig. 3-21 – Frequency Translated Local Oscillator Power as a Function
of Frequency Translator rf Driver Knob Setting

Test Conditions

1   Interferometer No. 1

2   Laser power at separate L. O. Leg
    is 1.9 W with the recombining beam-
    splitter and the frequency translator
    removed.

3   Aperture diameter is 12 mm

4   Isomet translator and rf driver

5   rf power is applied only a short while
    each time when the maximum deflected
    power is recorded.
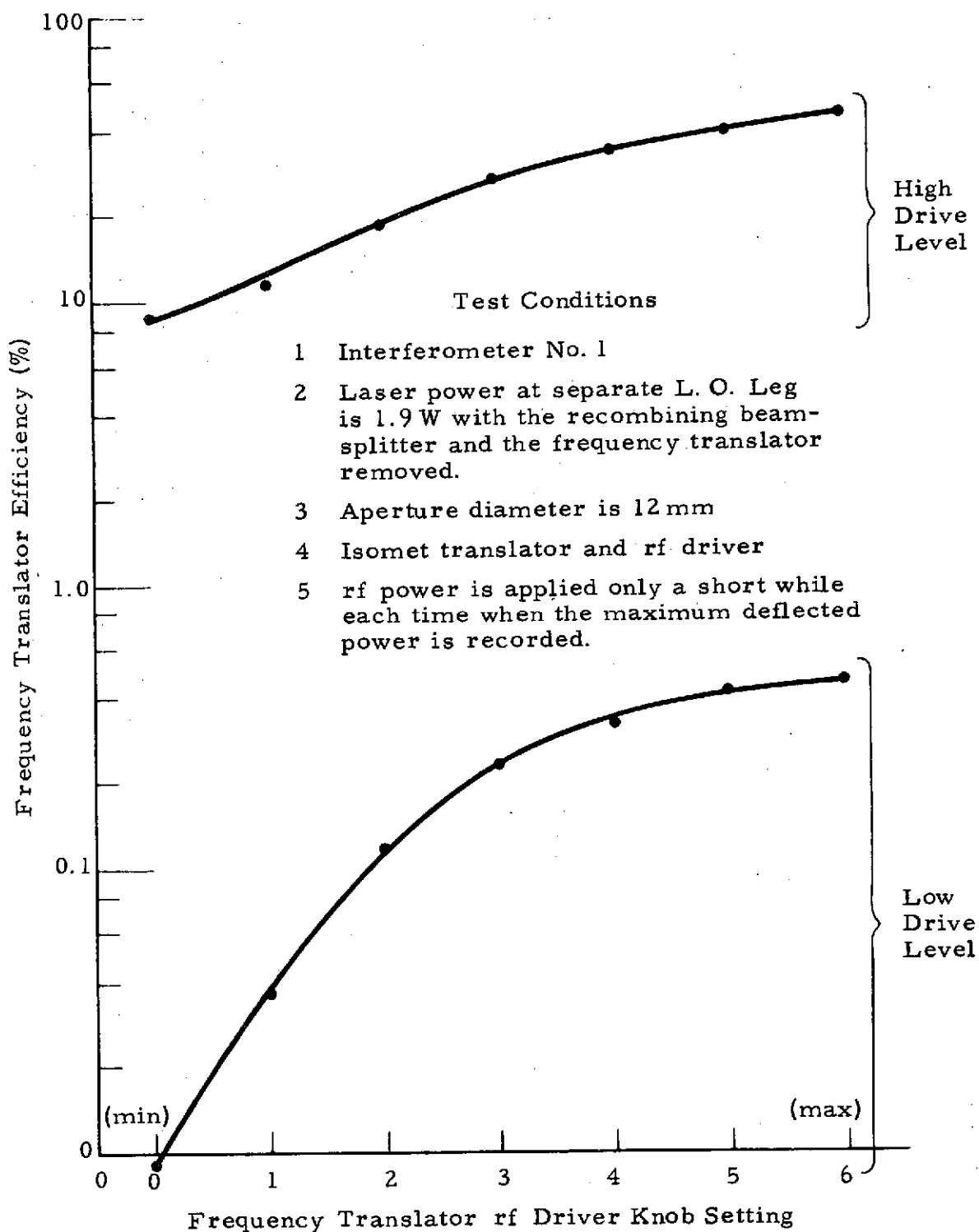
Fig. 3-22 - Acoustic CO_2 Laser Frequency Translator Efficiency Measurement

● Coherent Measurement

The frequency spectrum of the sandpaper wheel signal is shown in Fig. 3-23. The 24 MHz carrier was a beat signal between the translated L. O. laser power and the untranslated laser power. Most of the untranslated laser power was the residual backscatter power from the telescope secondary mirror even when the attenuation wire was in place. As the secondary mirror backscatter was blocked, the 24 MHz beat signal dropped by approximately 42 dB.

The 48 MHz beat signal was due to the beat between the laser beam which is up-shifted in frequency caused by the reflected acoustical wave from the acoustical sink and the laser beam which was down-shifted in frequency produced by the transmitted acoustical wave.

As the laser beam, focused by the telescope, was redirected from the lower part of the rotating sandpaper wheel to the upper part of the rotating wheel, a (24 - 1.4) MHz wheel signal and a (24 + 1.4) MHz wheel signal were seen as photographed in Fig. 3-24a and Fig. 3-24b, respectively.

The "image signal," which is smaller in amplitude, is shown in Figs. 3-24a or 3-24b was a result of the wheel signal beat with the L.O. power up-shifted in frequency which was produced by the reflected acoustical wave from the acoustical sink. The signal strength difference between the "signal" and the "image signal" can be adjusted to as high as 30 dB with extra alignment care.

The noise spectra of the backscatter mode and the frequency translated mode are shown in Figs. 3-25a and 3-25b, respectively, with the telescope output mirror blocked.

The lower noise level and the spikes shown in Fig. 3-25b is due to the strong 24 MHz signal saturating the detector preamplifier and over-driving the spectrum analyzer when the input attenuation of the spectrum analyzer was 0 dB. The noise spectrum is cleaner with higher input attenuation of the spectrum analyzer which is shown in Fig. 3-26.
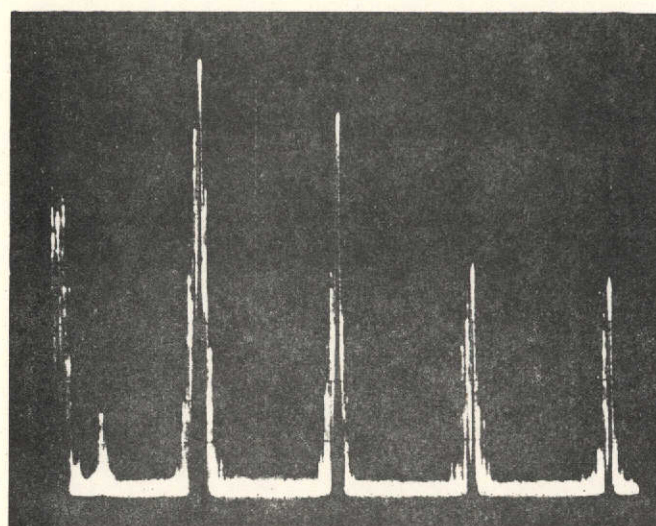
(a) Telescope Output Mirror
Unblocked
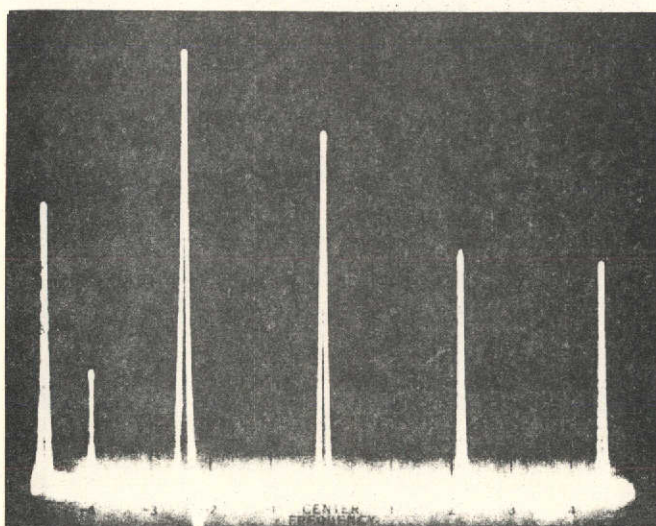
0 Hz   100 MHz

(b) Telescope Output Mirror
Blocked

0 Hz   100 MHz

Bandwidth: 30 kHz
Spectrum Analyzer Input Attenuation: 20 dB
LOG REF Level: 20 dBm
Range of Target: 71 ft (Folding Mirror is Used)

Fig. 3-23 - Frequency Spectrum (0 to 100 MHz) of the Sandpaper Wheel Signal
with Frequency Translated Separate Local Oscillator Power

153

← +10 dBm

→| 1 MHz |←

↑
24 MHz
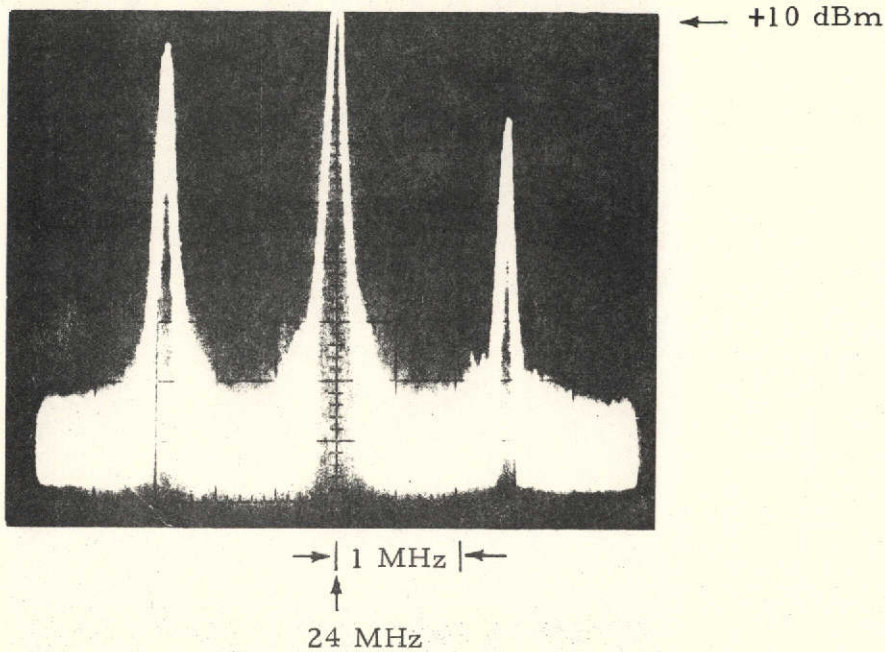
(a) Scattering Particles of the Sandpaper Wheel Move Away from the
Incident Laser Beam

← +10 dBm

→| 1 MHz |←

↑
24 MHz
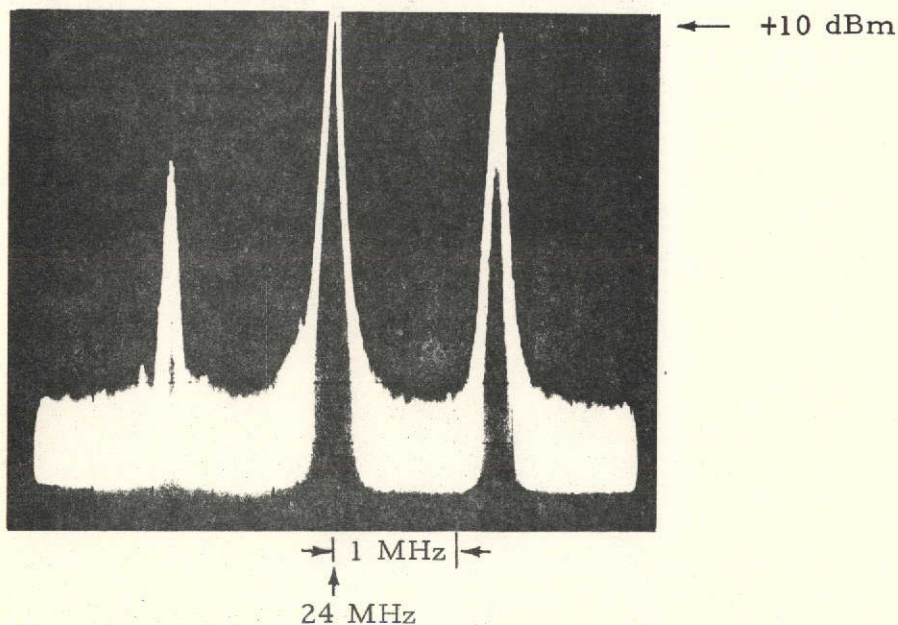
(b) Scattering Particles of the Sandpaper Wheel Move Toward the Incident
Laser Beam

Fig. 3-24 - Sandpaper Wheel Signal in the Frequency Translated
Separate L. O. Mode

← -40 dBm

Input Attenuation: 10 dB

0 Hz   50 MHz

(a) Backscatter Mode

← -50 dBm

Input Attenuation: 0 dB

0Hz   50 MHz

(b) Frequency Translated Mode
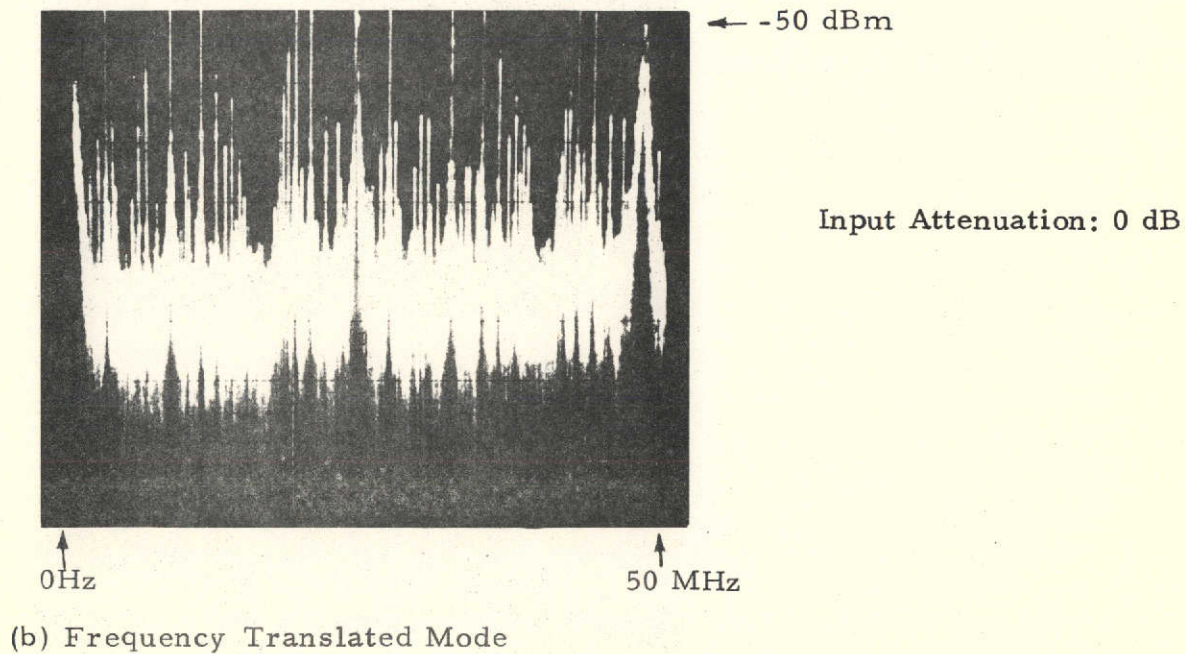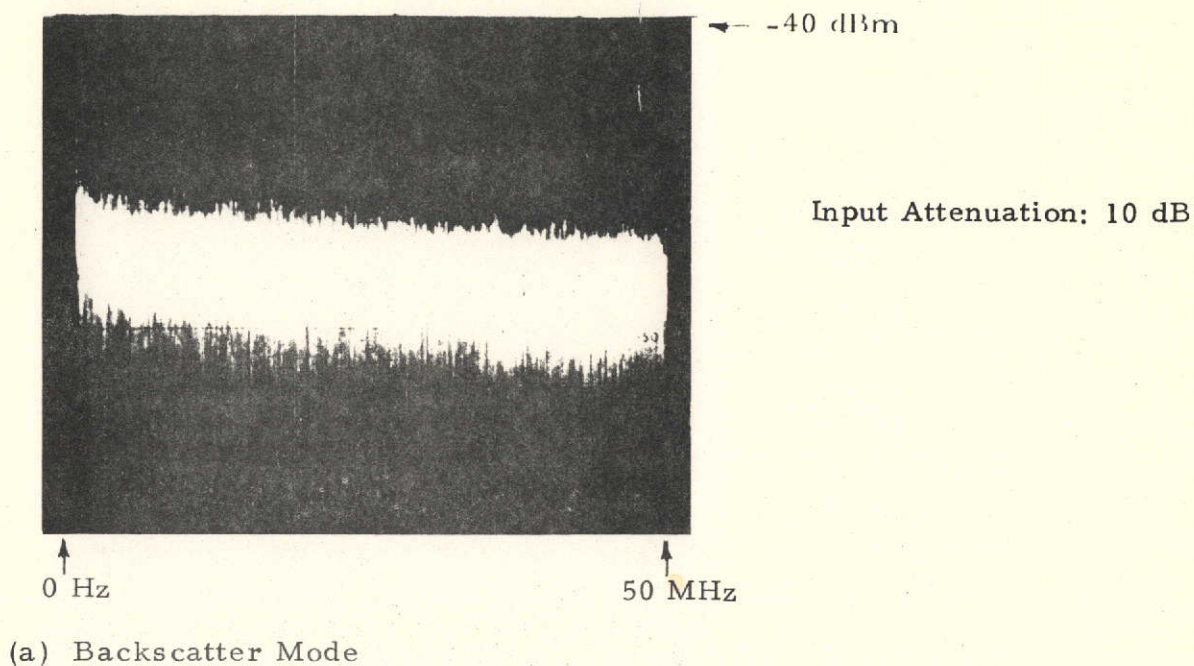
Fig. 3-25 – Noise Spectrum with Telescope Output Mirror Blocked

157

← -40 dBm

Input Attenuation: 10 dB

0 Hz   50 MHz

(a)

← -20 dBm

Input Attenuation: 30 dB

0Hz   50 MHz

(b)
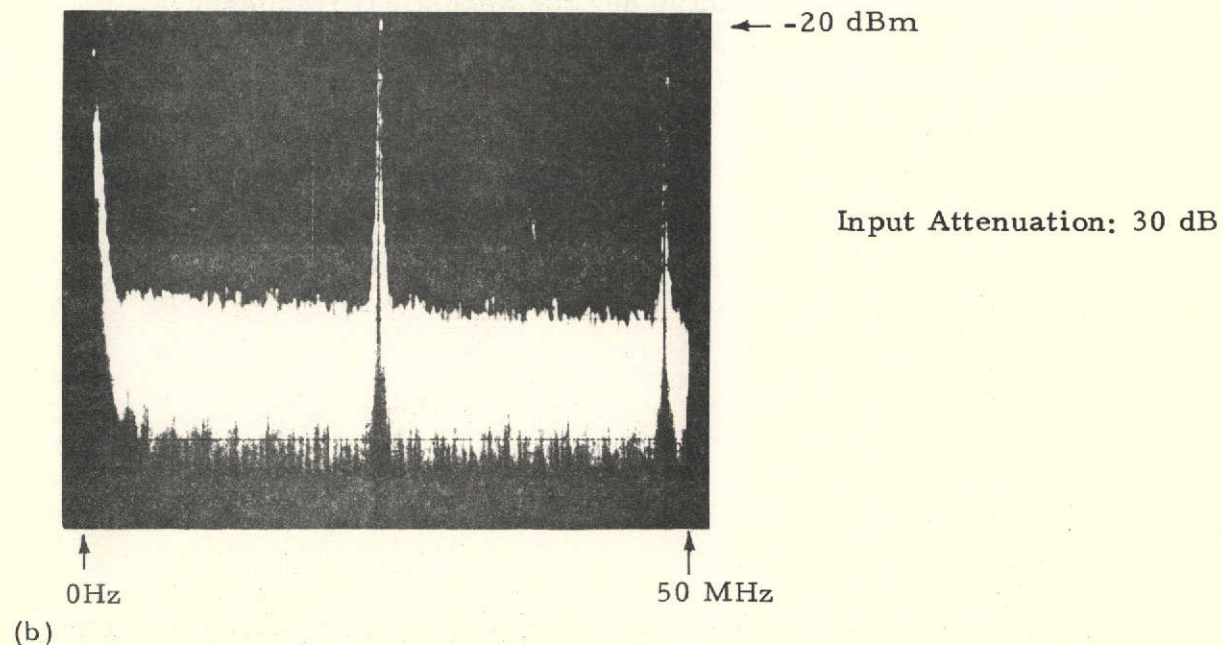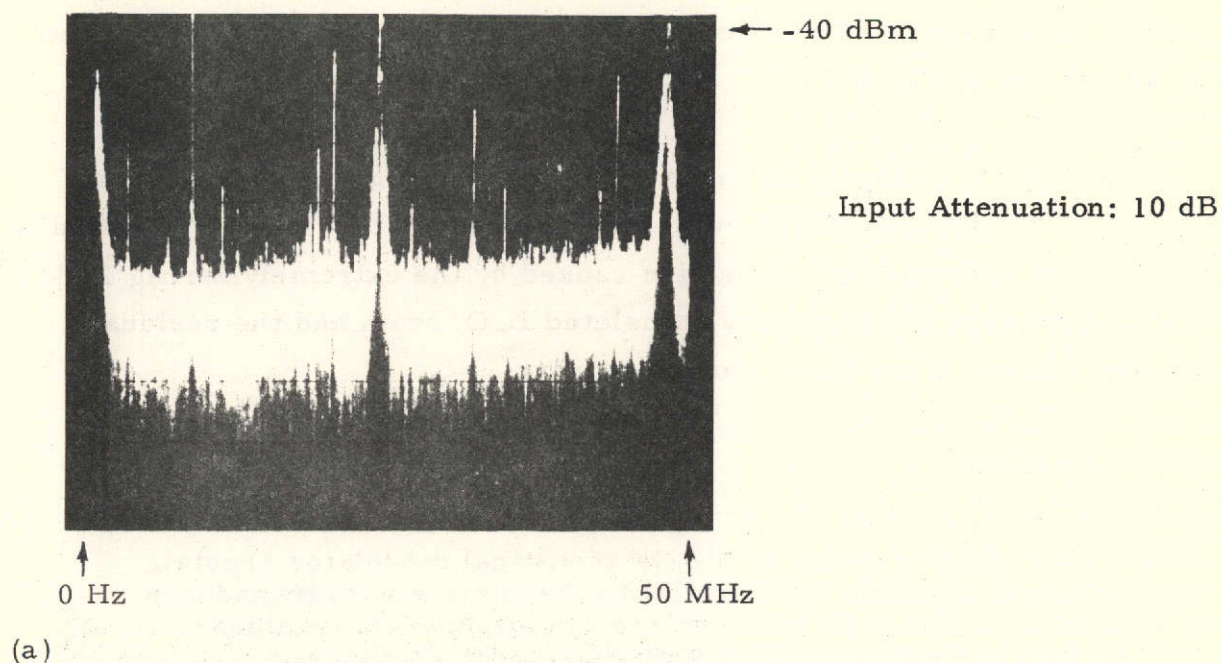
Fig. 3-26- Noise Spectrum of the Frequency-Translated Separate L.O.
Mode with Telescope Output Mirror Blocked and Higher Input
Attenuation of the Spectrum Analyzer

The backscatter mode (untranslated frequency mode) wheel signal and noise are shown in Fig. 3-27.

The frequency translated mode wheel signal and noise are shown in Fig. 3-28. The signal-to-noise ratio measurement in this mode was not valid because of the preamplifier saturation caused by the extremely strong 24 MHz beat signal between the frequency translated L.O. beam and the residual backscatter power from the secondary mirror.

3.7.3 Suggestions

- Cut the back surface of the Ge acoustical modulator crystal, which is opposite and parallel to the surface with transducer attached, into a wedged surface to eliminate the collinear reflection of the acoustical wave from that surface.

- Install a low-noise notch filter with enough attenuation and matched impedance in front of the preamplifier to overcome the amplifier saturation by the 24 MHz strong beat signal.

- Install an adjustable mount under the acoustical frequency translator.

- Install a lower RF power driver for the photovoltaic detector.

+10 dBm

Input Attenuation: 30 dB
Bandwidth: 30 kHz

1 MHz

1.2 MHz

(a) Signal

-30 dBm

Input Attenuation: 10 dB
Bandwidth: 30 kHz

1 MHz

1.2 MHz
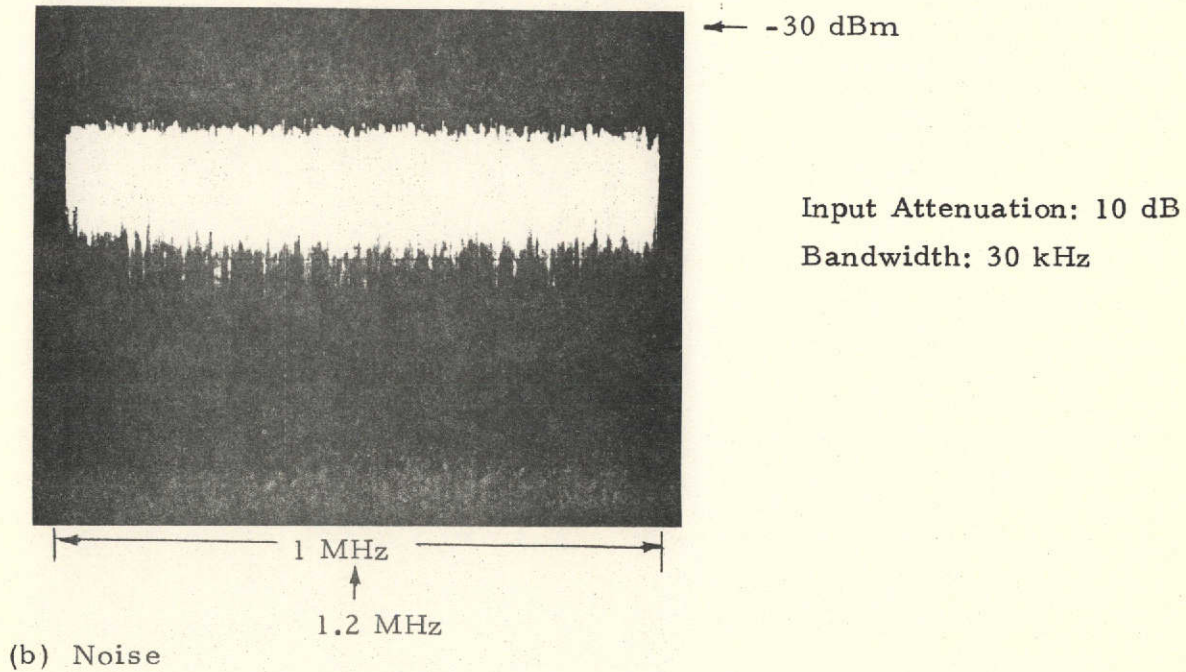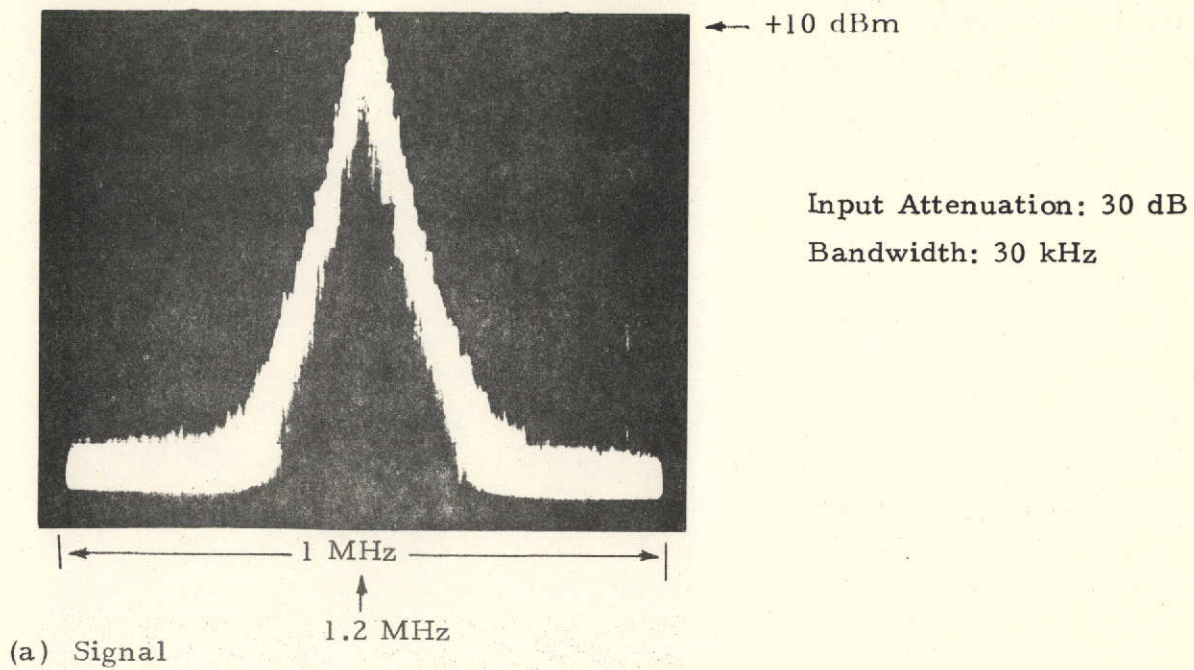
(b) Noise

Fig. 3-27 - Backscatter Mode Sandpaper Wheel Signal and Noise Display

← +10 dBm

Input Attenuation: 30 dB
Bandwidth: 30 kHz

1 MHz
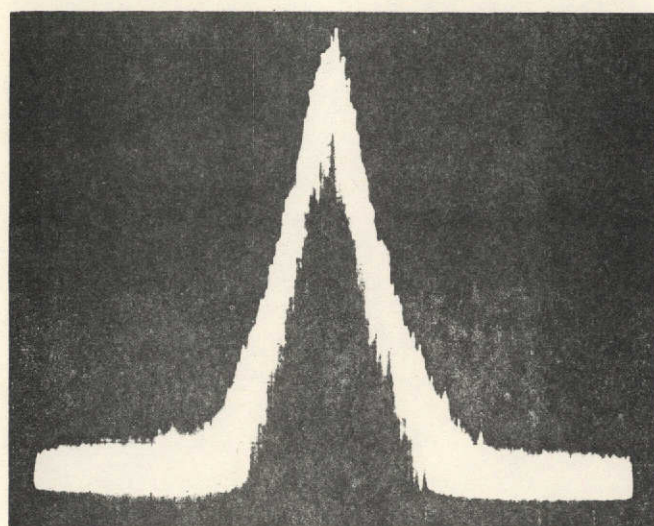
(24-1.2) MHz

(a) Signal

← -50 dBm

Input Attenuation: 10 dB
Bandwidth: 30 kHz

1 MHz
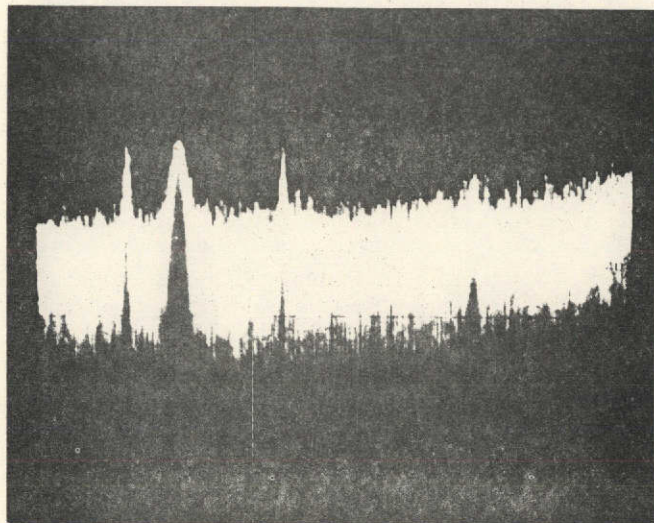
(24-1.2) MHz

(b) Noise

Fig. 3-28 - Sandpaper Wheel Signal in Frequency Translated Separate L.O.
Mode as well as the Noise Display

Section 4

LASER DOPPLER VORTEX SENSOR SIMULATION PROGRAM

Authors: K. Shrider
E. Coffey

4.1   BRIEF DESCRIPTION

The program developed simulates the output of NASA's laser Doppler aircraft wake vortex sensor.

Simulated are the following:

- Air velocity due to the wind and vortices
- Vortex transport
- Particle size distribution in the atmosphere
- Backscatter from particles in the illuminated volume
- Sensing volume motion due to scanning
- Detector response
- Filter response
- Filter integration time
- Digital tape output and printout similar to that of the real data processor.

4.2   DETAILED DESCRIPTION

The simulated parameters are now discussed in more detail.

● Air Velocity

The velocity field in the scanned plane is composed of two vortices and their ground images, superimposed on the wind field. The plane is perpendicular to the axes of the vortices. No wind turbulence model is currently anticipated for this program.

The vortex circulation, Γ_o, is computed from the aircraft's speed, weight, and wing span as follows:

$$\Gamma_o = \frac{4w}{\pi \rho u s} \tag{4.1}$$

where ρ = density of air, w = aircraft weight, u = aircraft speed and s = wing span.

The velocity field of a vortex is represented by

$$V(r) = \frac{\Gamma_o}{2 \pi r} \left(1 - \exp \left(- \frac{r^2}{4 \nu t} \right) \right) \tag{4.2}$$

where

r = the distance from the center of the vortex

t = the time from vortex creation

ν = the eddy viscosity.

The wind field is a curve fit of a set of velocity and direction data points as a function of altitude.

● Particle Distribution

Two types of particle species can be accommodated and are treated separately. Both size distributions are of the following basic shape (see also sketch below) at a sufficient distance from the vortex core. Near the core the centrifuge effect is accounted for.

Particle Size Distribution (log-log scale)
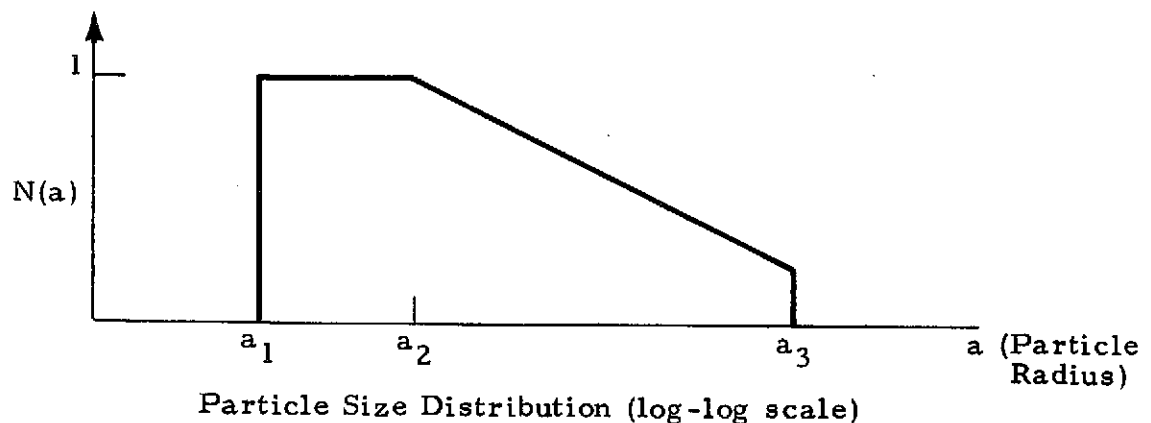
$$N(a) = \bar{N}C \begin{cases} 0 & a < a_1 \\ 1 & a_1 \leq a < a_2 \\ \dfrac{a_2{}^4}{a} & a_2 \leq a < a_3 \\ 0 & a_3 \leq a \end{cases} \qquad (4.3)$$

where

(a) = the radius of the particle in micrometers

N(a) = the number of particles per cubic centimeter within a 1 mm radius increment centered about a radius a

$\bar{N}$ = the total number of particles per cubic centimeter

C = a normalizing factor equal to

$$\left[a_2 - a_1 + \frac{a_2}{3} \left(1 - \left(\frac{a_2}{a_3} \right)^3 \right) \right]^{-1}$$

The redistribution due to the centrifuge effect is a function of age, the velocity distribution of the vortex, the radius and density of the particles, and the temperature and density of the air.

● Backscatter Cross Section, β

β, the equivalent backscatter cross section of the particles per unit volume, is computed from the Mie series and is a function of laser wave length, particle size, particle index of refraction, and the particle number density.

● Detector Response

The range dependence of the response of the LDV is given by

$$I_{(L_1 \ L_2)} = \frac{\tan^{-1}(L_2 - L_o/L_R) - \tan^{-1}(L_1 - L_o/L_R)}{\pi/2 + \tan^{-1}(L_o/L_R)} \qquad (4.4)$$

Line of Sight

Transceiver L_1 L_2 L_o Range
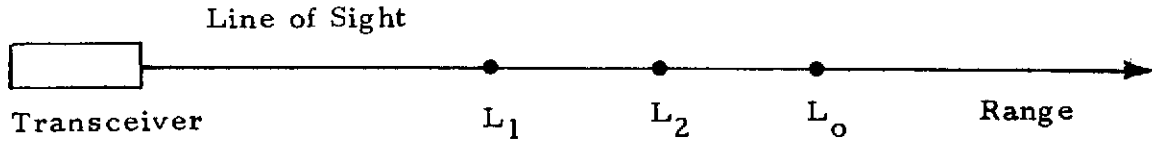
The integration process along the line of sight of the LDV is carried out by summing over length elements L_1 L_2 where

$I_{(L_1, L_2)}$ = the fraction of the detected power at the LDV output arising from the volume between a plane at L_1 and a plane at L_2

L_o = range of maximum response (approximately the focal range, f)

$$L_R = \lambda f^2 / \pi a_b^2 \frac{1}{1 + (\lambda f^2 / \pi a_b^2)}$$

where λ = the wave length of the laser radiation

a_b = the exp(-2) intensity radius of the laser beam at the primary mirror.

The above response function holds true for an infinite mirror without any obstruction. To correct for the finite mirror size and the obstruction in front of the mirror the quantity a_e is substituted for a_b, thus,

$$a_e = a_b (\exp -(a_i/a_b)^2 - \exp - (a_o/a_b)^2) \tag{4.5}$$

where

a_i = radius of obstruction due to the secondary mirror

a_o = radius of primary mirror.

The contribution to the detector output power from between L_1 and L_2 is:

$$P_{(L_1, L_2)} = I_{(L_1, L_2)} \beta P_t \tag{4.6}$$

168

where

$I_{(L_1, L_2)}$ = the fraction of received power from the volume between L_1 and L_2

β = the fraction of the energy backscattered by the particles per unit volume

P_t = a normalizing factor given by

$$P_t = \eta^2 P_o \lambda^3 / (hc)^2 \tag{4.7}$$

to ensure that $P_{(L_1, L_2)}$ has units of power.

where η = the quantum efficiency of the detector

P_o = the output power of the laser

λ = the wavelength of radiation

h = Planck's constant

c = the speed of light

● Filter Bank Response

The illuminated volume is partitioned into contiguous segments (volume between L_i and L_{i+1}) such that the velocity of all the particles in a particular segment can be considered to be traveling at the same velocity. The power $P_{(L_i, L_i+1)}$ from the segment is represented by a Rayleigh distributed random variable to account for phase cancellation caused by the arbitrary separation of the particles in the segment.

The line of sight velocity is computed and converted to a Doppler shift. This frequency is compared to the center frequencies of the filters to locate the signal on the characteristic curve for each filter. The magnitude of the response from each filter is computed by multiplying $P_{(L_1, L_2)}$ by the value of the characteristic curve at the Doppler shift frequency. Also, for each filter response, a random phase angle is assigned.

For each filter the response vectors caused by the illuminated volume segments are added together. Also added is the random shot noise.

The magnitude of the shot noise in each filter is a Rayleigh distribution of the RMS noise where

$$RMS_{noise} = \sqrt{\eta \, \lambda \, B/hc} \qquad (4.8)$$

where

η = detector quantum efficiency

λ = filter bandwidth

h = Plank's constant

c = velocity of light

B = filter bandwidth.

Also a random phase shift is assigned.

● Signal Integrator

Each filter is sampled at 15.625×10^{-6} second intervals. The integrator adds for each filter the sampled magnitude over a specified interval. This summation for each filter is multiplied by a gain factor where the gain factor is given by

$$Gain = \frac{8}{(RMS \ Noise) * (Number \ of \ Samples \ in \ Each \ Summation)} \qquad (4.9)$$

During the integration some correlation of filter output magnitudes is expected since some of the sampled returns are from the same set of particles. Therefore at each partition the cross beam particle velocity relative to the beam is computed. Then, from that computation, the transit times for the particles to cross the beam width are computed. During the transit time the magnitude of signal from a partition is held constant and the phase angle is rotated as a function of the line-of-sight velocity.

170

● Laser Beam Scanning

The range scanning and angular scanning of the focal point are independent of each other. The focal point moves at a constant rate in range and moves at a constant rate in angle.

● Vortex Movement

A vortex moves with a velocity determined by the sum of the velocities at its center due to its ground image, its companion vortex with its ground image, and the wind.

4.3 FLOW OF PROGRAM

Reference is made to Fig. 4-1. Major dots ● indicate the instantaneous location within the program (i.e., the particular routine) and minor dots ● indicate operations within that routine.

● MAIN Program

Call INPUT.

● INPUT Routine

● Reads input (see Section 4.4).
● Computes equivalent beam radius at the primary mirror (Eq. (4.5)).
● Computes preliminary wind calculations for subroutine WINDY.
   If desired, it calculates a "least square" curve fit of wind magnitude to a power law equation.

$$\text{WSPEED(I)} = \text{WSPR} \left(\frac{\text{ALT(I)}}{\text{ALTR}} \right) \text{CPOWER} \tag{4.10}$$

where WSPEED(I) is the wind magnitude at altitude ALT(I).
These are input along with ALTR (a reference height).
WSPR and CPOWER are computed.
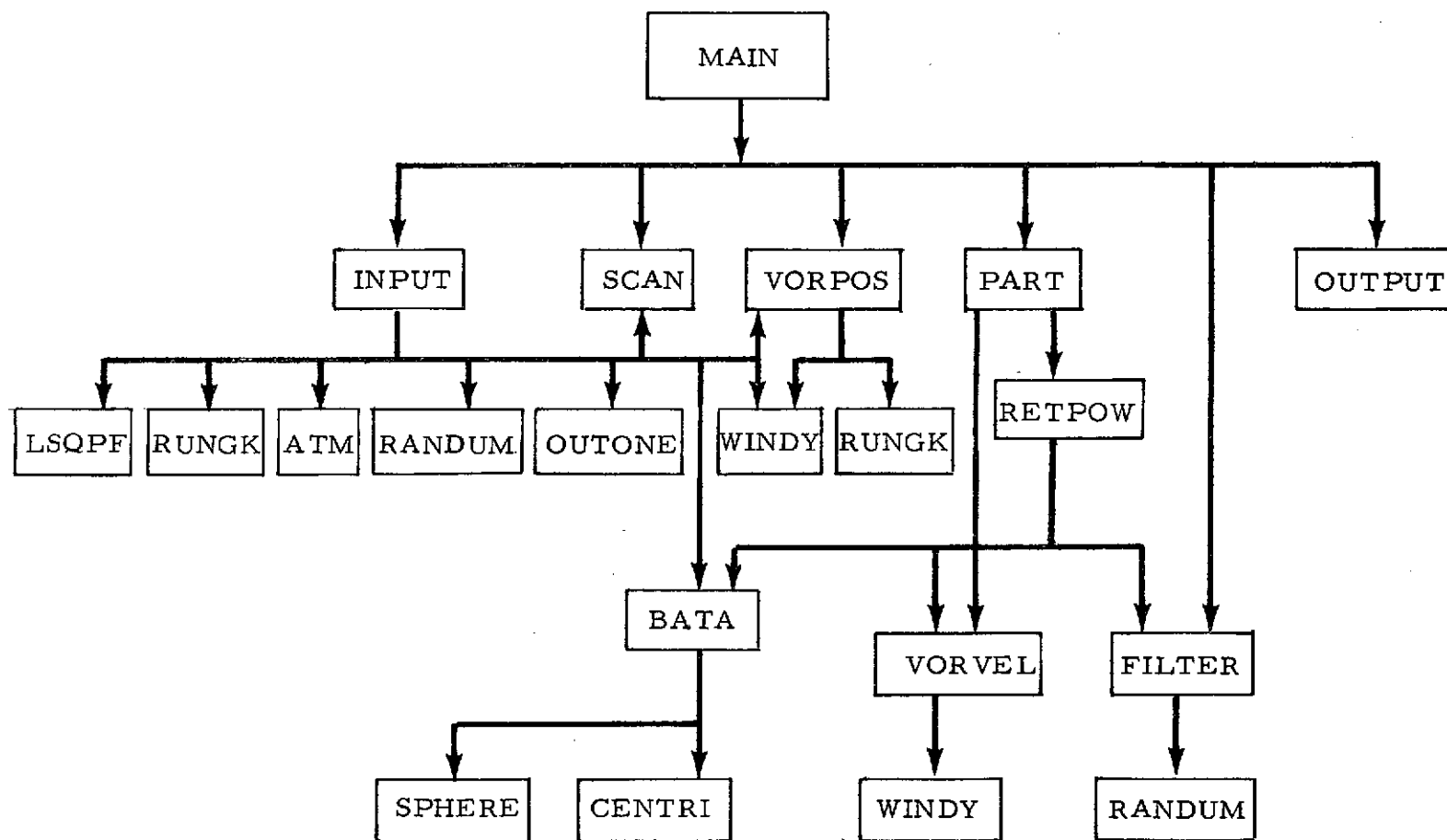
Fig. 4-1 - Flow Diagram of LDV — Vortex Interaction Simulation Program

Also, routine LSQPE is called to compute the least squares curve fit of the wind direction as a function of altitude. This curve is a polynomial. A polynomial least square curve fit is made to represent the temperature field. A pressure and density profile are computed from the pressure at the ground and the temperature profile. This is done by integration using routine RUNGK.

- Vortex circulation is computed using Eq. (4.1), where the atmospheric density is obtained by interrogating routine ATM with the vortex height.

RHO = atmospheric density obtained by interrogating routine ATM with the vortex height.

- Eddy viscosity, UNU, is computed from the temperature, density and recirculation using an empirical relation obtained from the vortex decay literature, thus

$$UNU = \frac{UUU}{RHO} * 10.** \left(.62 * LOG_{10}\left(GAMMA * \left(\frac{RHO}{UUU}\right)\right) - 1.06\right) \quad (4.11)$$

where $UUU = \left(\frac{.3048}{14.5939029}\right) \frac{1.458E-6 * (TH * 5./9.) ** 1.5}{(TH * 5/9 + 110.4)}$

TH is temperature in degrees Rankine from routine ATM.

- Vortex separation is computed assuming elliptically loaded wings, thus

$$\text{Vortex separation} = (\pi/4) * WSPAN. \quad (4.12)$$

- P_t, a normalizing factor is computed using Eq. (4.7).
- RMS noise is computed using Eq. (4.8).
- A gain factor is computed for scaling the output using Eq. (4.9).
- Other initializations and unit conversions are made.
- Call function BATA.

- BATA Function

  - Call SPHERE

● **SPHERE Routine**

    ● Computes the backscatter cross section for a single particle using the Mie series (a function of radiation wave.length particle size and index of refraction).

    ● Return to BATA.

● **BATA Function**

    ● Compute the backscatter cross section per unit volume for the particle distribution. Also, it stores backscatter cross sections for discrete size particles within the distribution. These are used later in conjunction with the centrifuge routine.

    ● Return to INPUT.

● **INPUT Routine**

    ● Routine RANDUM is called to initialize the random number sequence.

    ● Call VORPOS.

● **VORPOS Routine**

    ● Integrates for the vortex position.

    ● Calls routine WINDY for wind velocity.

    ● Calls for the integration routine RUNGK.

    ● Uses standard technique for superimposing air velocity from the vortices, their ground images, and the wind. The velocity at the center of a vortex (neglecting that vortex) is assumed to be the transport velocity of the vortex. The tangential velocity due to a vortex at range, r, from the core is given by Eq. (4.2)

    ● Return to INPUT.

● **INPUT Routine**

    ● Call SCAN.

- <u>SCAN Routine</u>

  - Computes the proper location for the focal point. The angle and range movement are independent. Both move at a constant rate.

  - Return to INPUT.

- <u>INPUT Routine</u>

  - Call OUTONE.

- <u>OUTONE Routine</u>

  - Writes the first record on tape.

    The output unit is 12.
    The record is written in unformatted FORTRAN.
    The record contains 5 words.

    1. NRUN is the run number — Integer
    2. PRTIME is the integration time — Read
    3. IVMODE is the velocity coverage mode — Integer*
    4. LINEAR/CFAR Code — Integer*
    5. TLR CODE — Integer*

  - Prints run number and integration time

  - Return to INPUT.

- <u>INPUT Routine</u>

  - Return to MAIN.

- <u>MAIN Program</u>

  - Determines whether any part of the focal volume is within a distance. VSEP (where VSEP is the initial separation) of the vortices. This is to isolate regions of potentially large velocity gradient (see PART below).

---

*Variables introduced by NASA-MSFC into their readout routines.

- Routine SCAN is called for focus position.

- The location of the focal point is saved periodically (normally every .002 sec). At output time the last saved point is printed.

- Call PART.

● **PART Routine**

- Calculates Gaussian beam parameters. L_o is the range to the maximum intensity point; L_R is the distance along the axis from the L_o point such that 1/2 the returned power is from the interval $(L_o - L_R, L_o + L_R)$.

- Calculates a cell size along the axis of the beam centered at the L_o point. This cell will contain a predetermined (typically .2) fraction of the power collected by the detector. Then if the focal point is close to the vortices, VORVEL will be called to yield the air velocity at the end points of the cell. If the velocity gradient is too large the cell will be cut in half. Cuts will be made until the velocity gradient is not too large.

- Calculates a centroid for the cell weighted by the power returned to the detector. In the case of the first cell the centroid is L_o.

- Calculates the fraction of returned power which comes from this cell.

- Calculates the beam width at the centroid.

- Call RETPOW.

● **RETPOW Routine**

- Call VORVEL.

● **VORVEL Routine**

- Call WINDY.

● **WINDY Routine**

- Calculates wind velocity at specified height
- Return to VORVEL.

- **VORVEL Routine**

  - Computes air velocity at a specified point (centroid of cell) due to the two vortices and their ground images, then adds the wind to get the total air velocity at the point.

  - Return to RETPOW.

- **RETPOW**

  - Computes the cross beam air velocity at a cell centroid relative to the beam (includes scanning motion)

  - From the cross beam air velocity and the beam diameter at the cell centroid the transit time for particles to cross the beam is computed.

  - Computes the line-of-sight air velocity at the cell centroid

  - From the line-of-sight velocity the Doppler shift is computed.

  - The range from the cell centroid to the nearest vortex is computed. (This is to account for the centrifuge effect.)

  - If the centrifuge effect is important call BATA.

  - Call function BATA.

- **BATA Function**

  - If routine CENTRI is called within a certain interval since it was last called (specified in input) it is skipped. (The centrifuge effects needs to be updated only at time intervals large in comparison with the cycle time of other computations.)

  - Call CENTRI or CENTR

    The entry point CENTRI is for the full centrifuge representation and the entry point CENTR is for a short approximation to the centrifuge effect.

- **CENTRI Routine**

  - Computes the radial particle size distribution from the center of a vortex as a function of vortex circulation, temperature, density of air, density of particles, size of particles, and time from creation of vortex.

  - In the case where entry point CENTR is used only the radius of the empty core for one particle size (predetermined in the input) is computed.

- Return to BATA.

● BATA Function

- Using routine CENTRI the backscatter area per unit volume is computed at 250 radii from the center of the vortex.

- The backscatter is then computed for the cell centroid using a polynomial curve fit of three of the 250 points discussed above.

- In the case of the simplified centrifuge model the core is assumed to have no backscatter and outside the core is assumed to have the same backscatter as the undisturbed air.

- Return to RETPOW.

● RETPOW Routine

- The power output from the detector originating from the cell is computed using Eq. (4.6).

- Call FILTER.

● FILTER Routine

- A random detector voltage is selected from a Rayleigh distribution about the mean power computed in routine RETPOW. The random voltage is to take account of power fluctuations due to phase cancellation due to the random motion of the particles.

- Using the Doppler shift frequency and the characteristic curve of the filters the amount of voltage in each filter due to a cell is determined.

- A random phase angle is applied to each filter output originating from the cell. The voltage is resolved into components for summation over all the partition cells.

- When this routine calls for the last cell, a random Rayleigh root-mean-square noise is added to each filter summation. This is to simulate shot noise.

- Return to RETPOW.

- **RETPOW Routine**

  - Return to PART.

- **PART Routine**

  - The next cell in the partitioning which extends from the last cell boundary is now accounted for and routine RETPOW is called. This process continues, the range being increased until the outer boundary of a cell exceeds a range equal to $L_o + 3 L_R$. If the line-of-sight airspeed is increasing, cells will be constructed out to a range $L_o + 6 L_R$. In no case will a cell extend beyond a range $L_o + 6 L_R$. At this point cells are constructed inward from the first cell (toward the laser) to a range $L_o - 3 L_R$ or $L_o - 6 L_R$.

  - Return to MAIN

- **MAIN Program**

  - Time is increased.
  - If sufficient time has elapsed, routine VORPOS is called to reposition the vortices.
  - Routine SCAN is called to re-position the focal point.
  - If the focal point has not moved far enough to justify re-partitioning then routine FILTER is called directly.
  - Call FILTER.

- **FILTER Routine**

  - If the particles at the centroid of the cell have not departed the beam since the routine was last called, the phase angle is rotated by a function of the line-of-sight velocity.
  - If the particles at the centroid of the cell have departed the beam, a new random voltage is selected from the Rayleigh distribution (about a mean power originating from the cell). Also, a new random phase angle is selected.
  - The voltage in each filter due to the cell are summed and noise is added.
  - Now the absolute value of the voltage in each filter for the current cycle is added to the time of the parameter for previous cycles in the integration time.

- Return to MAIN.

● **MAIN Program**

  - If sufficient time has passed, routine OUTPUT is called.
  - Call OUTPUT.

● **OUTPUT**

  - The gain is multiplied by the summed power in the filters.
  - Writes all but first record on tape unit 12. The records are written in unformatted FORTRAN. The logical records contain 107 words of 36 bits.

    Word 1 = frame number — Integer
         2 = x-coordinate of focal point — Integer
         3 = y-coordinate of focal point — Integer
      4-107 = contents of the 103 filters — Integers

  - A printout of this record is made.
  - The summed filter power is zeroed.
  - Return to MAIN.

● **MAIN Program**

  - The time is increased and the program continues in the above manner.

4.4 VORTEX SCAN PROGRAM INPUT GUIDE

TITLE CARD   72 COLUMNS OF COMMENT
                  (IF FIRST 6 COLUMNS ARE BLANK, PROGRAM TERMINATES)

AIRCRAFT CARD   CHOOSE STANDARD AIRCRAFT WITH FIRST 6 COLUMNS
               (LEFT JUSTIFIED)
                THE CHOICES ARE B747 B707 B727 DC10 DC9 DC8 CV880
               L1011 C5A
                ALL BLANKS INDICATES AIRCRAFT FROM PREVIOUS CASE
               WILL BE USED

NAMELIST (RUN)

NRUN	RUN NUMBER
EPS1	CRITERION FOR CELL DIVISION
	FRACTION OF RETURN RADIATION
EPS2	CRITERION FOR CELL DIVISION
	DELTA VELOCITY IN CELL (METERS/SEC)
PARMAX	MAXIMUM CELL SIZE (METERS)
NRAN	STARTING NUMBER FOR RANDOM NUMBER GENERATOR

NAMELIST (VORTEX)

IVORTX	NUMBER OF VORTICES (CURRENTLY ONLY CHOICE IS 2)
HEIGHT	VORTEX ALTITUDE ABOVE GROUND (FT)
SPEED	SPEED OF AIRCRAFT RELATIVE TO GROUND (FT/SEC)
	IF NEGATIVE, (SPEED) IS TAKEN AS AIR SPEED
WEIGHT	WEIGHT OF AIRCRAFT (POUNDS)
WSPAN	WING SPAN OF AIRCRAFT (FT)
AIRHD	AIRCRAFT HEADING IN DEGREES CLOCKWISE FROM
	MAGNETIC NORTH
XVORT	CROSS RUNWAY POSITION FOR CENTER OF VORTEX PAIR (M)

NAMELIST (WINDS)

JWIND	FLAG
	JWIND = 1 WIND IS PROVIDED BY TAPE 10 AS A
	FUNCTION OF TIME
	(CURRENTLY NOT AVALABLE)
	JWIND = 2 WIND IS PROVIDED BY TABLE WITH LINEAR
	INTERPOLATION AND LINEAR EXTRAPOLATION
	AS A FUNCTION OF ALTITUDE
	JWIND = 3 WIND IS PROVIDED BY LEAST SQUARE CURVES
	OF TABLE VALUES
SWINDT	TIME ON WIND TAPE WHICH CORRESPONDS TO ZERO TIME OF
	SIMULATION
WINDD	DIRECTION OF WIND REFERENCE ON TAPE IN DEGREES
	CLOCK-WISE FROM (-Y)
NW	NUMBER OF ALTITUDES
ALT(30)	ALTITUDES AT WHICH THE WINDS ARE SPECIFIED (FT)
WSPEED(30)	WIND SPEED (FT/SEC)
WDIREC(30)	DIRECTION FROM WHICH WIND IS COMING.

	DEGREES ARE MEASURED CLOCKWISE FROM MAGNETIC NORTH
WSV(30)	VERTICAL WIND SPEED (FT/SEC)
ALTR	REFERENCE ALTITUDE FOR LEAST SQUARES CURVE OF WIND SPEED (FT)
WSPR	WIND SPEED AT REFERENCE ALTITUDE (FT/SEC) (COMPUTED WHEN NW IS GREATER THAN 0)
CPOWER	IS VARIABLE IN LEAST SQUARES CURVE WSPEED/WSPR = (ALT/ALTR)**CPOWER (COMPUTED WHEN NW IS GREATER THAN 1)
NPOLY	ORDER OF POLYNOMIAL TO BE FITTED TO WIND DIRECTION. MAXIMUM VALUE FOR NPOLY IS 7
COEF(9)	COEFFICIENTS OF POLYNOMIAL FOR WIND DIRECTION (COMPUTED WHEN NW IS GREATER THAN NPOLY)
PRESSG	PRESSURE AT GROUND LEVEL IN MILLIBARS
JTEMP	FLAG JTEMP = 1 TEMPERATURE IS PROVIDED BY TABLE WITH LINEAR INTERPOLATION AND LINEAR EXTRAPOLATION AS A FUNCTION OF ALTITUDE JTEMP = 2 TEMPERATURE IS PROVIDED BY A LEAST SQUARES POLYNOMIAL OF TABLE VALUES
NA	NUMBER OF ALTITUDES AT WHICH THE TEMPERATURE IS SPECIFIED.
ALTIT(30)	ALTITUDES AT WICH THE TEMPERATURE IS SPECIFIED.(FT)
TEMP(30)	TEMPERATURE I DEGREES C
NPOLYT	ORDER OF POLYNOMIAL TO BE FITTED TO TEMPERATURE MAXIMUM VALUE FOR NPOLYT IS 7
COEFT(9)	COEFFICIENTS OF POLYNOMIAL FOR TEMPERATURE PROFILE (COMPUTED WHEN NA IS GREATER THAN NPOLYT)

NAMELIST (LASER)

POWER	LASER OUTPUT CW POWER (WATTS)
BANDW	FILTER BANDWIDTH (HZ)
WAVE	WAVE LENGTH OF LASER RADIATION (METERS)
RADIBE	RADIUS OF LASER BEAM AT PRIMARY LENS (METERS)
RADIOT	OUTER RADIUS OF PRIMARY LENS (METERS)
RADIIN	INNER RADIUS OF PRIMARY LENS (METERS)
QUANEF	QUANTUM EFFICIENCY (DIMENSIONLESS)

NAMELIST (SCANER)

YLASER	HEIGHT OF SCANER FROM GROUND (METERS)
XLASER	CROSS RUNWAY POSITION OF SCANER (METERS) POSITIVE IS TO PORT OF AIRCRAFT
FOCALL	MINIMUM RANGE FOR SCANER (METERS)
FOCALU	MAXIMUM RANGE FOR SCANER (METERS)
THETAL	MINIMUM ANGLE ABOVE HORIZONTAL FOR SCANER (DEGREES)

THETAU	MAXIMUM ANGLE ABOVE HORIZONTAL FOR SCANER (DEGREES)
FREQR	FREQUENCY OF RANGE SCAN (CYCLES/SEC)
FREQT	FREQUENCY OF ANGLE SCAN (CYCLES/SEC)
SFOCAL	STARTING RANGE OF FOCAL POINT (METERS)
STHETA	STARTING ANGLE FROM HORIZONTAL FOR FOCAL POINT (DG)
SIGNR	STARTING DIRECTION OF RANGE SCAN.
	+1.0 FOR POSITIVE −1.0 FOR NEGATIVE
SIGNT	STARTING DIRECTION OF ANGLE SCAN.

+1.0 FOR POSITIVE   −1.0 FOR NEGATIVE

NAMELIST (PARTIC)

NTYPE	NUMBER OF PARTICLE TYPES (1 OR 2)
INDEX(2)	INDEX OF REFRACTION FOR EACH TYPE OF PARTICLE
	INDEX IS COMPLEX
PRHO(2)	DENSITY OF PARTICLES KG/M**3
A1(2)	LOWER LIMIT OF PARTICLE RADII (M)
A2(2)	CONSTANT DISTRIBUTION BETWEEN A1 AND A2
A3(2)	RECIPROCAL OF FOURTH POWER BETWEEN A2 AND A3
XNUMBR(2)	TOTAL NUMBER OF PARTICLES
JCENT	FLAG
	JCENT = 0 NO CENTRIFUGE NO MIE SCATER
	JCENT = 1 NO CENTRIFUGE YES MIE SCATER
	JCENT = 2 YES CENTRIFUGE NO MIE SCATER
	JCENT = 3 YES CENTRIFUGE YES MIE SCATER
	JCENT = 4 FULL CENTRIFUGE YES MIE SCATER
BETA	EQUIVALENT BACK SCATER AREA OF PARTICLES M**2/M**3
	BETA IS COMPUTED IF JCENT = 1,3 OR 4
	FOR CENTRIFUGE. RADIUS IN METERS
PSIZET	PARTICLE SIZE USED IN DETERMINING STEP FUNCTION
	(ONLY USED WHEN JCENT = 2 OR 3)

NAMELIST (TIME)

STIME	PROCESSOR START TIME (SEC)
FTIME	PROCESSOR CUTOFF TIME (SEC)
VSTIME	VORTEX START TIME (VSTIME MUST BE .LT. STIME) (SEC)
SSTIME	SCAN START TIME (SSTIME MUST BE .LE. STIME) (SEC)
VDTIME	STEP SIZE FOR VORTEX POSITIONING (SEC)
PRTIME	INTERVAL BETWEEN OUTPUTS (SEC)
SMTIME	FILTER SAMPLING TIME
DLTIME	INTERVAL BETWEEN POSITION SAMPLING FOR OUTPUT (SEC)
NPRINT	NUMBER OF OUTPUT FRAMES TO EACH PRINTOUT

PRESET INPUT VALUES

NAMELIST NAME	VARIABLE	VALUE
RUN	NRUN	
	EPS1	0.2
	EPS2	0.5
	PARMAX	2.5
	NRAN	1.0
VORTEX		
	IVORTX	2.0
	HEIGHT	250.0
	SPEED	-247.0
	WEIGHT	565000.0 } for B747
	WSPAN	195.7
	AIRHD	0.0
	XVORT	100.0
WINDS		
	JWIND	2.0
	SWINDT	0.0
	WINDD	0.0
	NW	2.0
	ALT(30)	0., 10000.0
	WSPEED(30)	0.0
	WDIREC(30)	0.0
	WSV(30)	0.0
	ALTR	23.0
	WSPR	0.0
	CPOWER	0.27
	NPOLY	2.0
	COEF(9)	0.0
	PRESSG	1013.0
	JTEMP	1.0
	NA	2.0
	ALTIT(30)	0.0, 2000.0
	TEMP(30)	20.0
	NPOLYT	1.0
	COEFT(9)	0.0
LASER		
	POWER	12.0
	BANDW	120000.0
	WAVE	0.0000106
	RADIBE	0.15
	RADIOT	0.15
	RADIIN	0.01905
	QUANEF	0.25

SCANER

YLASER	0.0
XLASER	0.0
FOCALL	40.0
FOCALU	250.0
THETAL	5.0
THETAU	35.0
FREQF	6.0
FREQT	0.1
SFOCAL	40.0
STHETA	5.0
SIGNR	1.0
SIGNT	1.0

PARTIC

NTYPE	2.0
INDEX(2)	(1.212, 0.06), (1.650,0.09)
PRHO(2)	1000,1192
A1(2)	.02E-6, .02E-6
A2(2)	.1E-6, .1E-6
A3(2)	10E-6, 10E-6
XNUMBR(2)	1.378E+9, 1.378E+9
JCENT	0.0
BETA	5.601492E-8
PSIZET	1.35E-6

TIME

STIME	0.0
FTIME	20.0
VSTIME	-5.0
SSTIME	0.0
VDTIME	1.0
PRTIME	0.002
SMTIME	15.625E-6
DLTIME	0.0002
NPRINT	1

4.5   OUTPUT DESCRIPTION

Two types of output are possible, a line printer record and digital magnetic tape.

A typical line printer output is shown in Fig.4-2 and includes:

- Integration time (milliseconds)
- Time (seconds)
- x (horizontal position in meters of focal point from LDV)
- y (vertical position in meters of focal point from LDV)
- RADIUS (range in meters to focal point from LDV)
- THETAD (beam elevation angle — degrees)
- The column under CELL is the filter number.
- The column under AMP is the integrated power from the corresponding filter.

The digital magnetic tape is similar to that produced by the real data processor program. The tape contains record one, which has five words written in unformatted FORTRAN form. The five words are:

1. Run number — Integer
2. Integration time — Real
3. Velocity coverage mode — Integer[*]
4. Linear/CFAR code — Integer[*]
5. TLR code — Integer[*]

Record two, three, etc., contain 107 words written in unformatted FORTRAN form. The 107 words are:

1. Frame number — Integer
2. x-coordinate of focal point — Integer
3. y-coordinate of focal point — Integer
4. 107.   Integrated voltage from the 103 filters.

---

[*]Variables introduced by NASA-MSFC into their readout routines.

PRINT AMPLITUDE PROGRAM

RUN NUMBER   19   EVERY   1 POINT TO BE PRINTED . STARTING AT POINT NUMBER   1

INTERGRATION TIME   4.00   MODE   1   LINEAR   TRANSLATOR OUT

FRAME=   1   TIME=   26.77165   X=   182.013   Y=   24.944   RADIUS=   183.325   THETAD=   6.860

CELL	AMP	CELL	AMP	CELL	AMP	CELL	AMP	CELL	AMP	CELL	AMP	CELL	AMP	CELL	AMP
1	0	14	0	27	77	40	17	53	10	66	10	79	10	92	10
2	0	15	0	28	65	41	13	54	11	67	10	80	10	93	10
3	0	16	0	29	56	42	14	55	10	68	10	81	10	94	10
4	0	17	0	30	38	43	22	56	11	69	10	82	10	95	10
5	0	18	0	31	32	44	23	57	10	70	10	83	10	96	0
6	0	19	0	32	24	45	17	58	10	71	11	84	11	97	0
7	0	20	0	33	26	46	19	59	10	72	10	85	11	98	0
8	0	21	0	34	25	47	23	60	10	73	10	86	10	99	0
9	0	22	0	35	26	48	25	61	10	74	10	87	10	100	0
10	0	23	0	36	28	49	27	62	10	75	10	88	10	101	0
11	0	24	109	37	23	50	17	63	10	76	10	89	10	102	0
12	0	25	212	38	17	51	10	64	10	77	10	90	10	103	0
13	0	26	126	39	20	52	10	65	10	78	10	91	10	104	0

FRAME=   2   TIME=   26.77562   X=   175.417   Y=   23.968   RADIUS=   176.660   THETAD=   6.801

CELL	AMP	CELL	AMP	CELL	AMP	CELL	AMP	CELL	AMP	CELL	AMP	CELL	AMP	CELL	AMP
1	0	14	0	27	68	40	19	53	10	66	10	79	10	92	10
2	0	15	0	28	68	41	23	54	10	67	10	80	10	93	10
3	0	16	0	29	56	42	25	55	10	68	10	81	10	94	11
4	0	17	0	30	52	43	24	56	10	69	9	82	11	95	10
5	0	18	0	31	33	44	26	57	10	70	10	83	10	96	0
6	0	19	0	32	48	45	27	58	10	71	10	84	10	97	0
7	0	20	0	33	30	46	27	59	10	72	10	85	10	98	0
8	0	21	0	34	43	47	22	60	10	73	10	86	10	99	0
9	0	22	9	35	27	48	29	61	10	74	10	87	10	100	0
10	0	23	0	36	29	49	42	62	9	75	10	88	10	101	0
11	0	24	76	37	32	50	24	63	10	76	10	89	10	102	0
12	0	25	166	38	29	51	10	64	10	77	10	90	10	103	0
13	0	26	122	39	21	52	10	65	10	78	10	91	10	104	0

FRAME=   3   TIME=   26.77959   X=   168.819   Y=   23.006   RADIUS=   169.995   THETAD=   6.742

CELL	AMP	CELL	AMP	CELL	AMP	CELL	AMP	CELL	AMP	CELL	AMP	CELL	AMP	CELL	AMP
1	0	14	0	27	95	40	34	53	11	66	10	79	9	92	9
2	0	15	0	28	81	41	43	54	10	67	10	80	10	93	10
3	0	16	0	29	56	42	11	55	10	68	10	81	10	94	10
4	0	17	0	30	53	43	11	56	10	69	10	82	10	95	10
5	0	18	0	31	49	44	37	57	9	70	10	83	10	96	0
6	0	19	0	32	40	45	48	58	10	71	10	84	10	97	0
7	0	20	0	33	45	46	12	59	10	72	10	85	10	98	0
8	0	21	0	34	47	47	21	60	10	73	10	86	10	99	0
9	0	22	0	35	24	48	61	61	10	74	10	87	10	100	0
10	0	23	0	36	37	49	44	62	10	75	10	88	10	101	0
11	0	24	75	37	53	50	22	63	10	76	10	89	10	102	0
12	0	25	133	38	13	51	10	64	10	77	10	90	10	103	0
13	0	26	130	39	11	52	10	65	10	78	10	91	10	104	0

Fig. 4-2 - Typical Line Printer Output

4.6   SUMMARY

The main handicap in using this program is the long run time required (approximately 20 minutes, for 0.5 second of real time). Therefore, to simulate a 20-second run would take over 13 hours of 1108 central processor time. However, short runs have shown some interesting phenomena, such as the large variations that the random particle distributions make on the signal amplitude in the various filters. More runs using the program are desirable. Possibly some program changes can be made to speed up the program.

Appendix
ACCEPTANCE TEST PROCEDURE

A.1 ELEVATION

A.1.1 Automatic Mode

A.1.1.1 Upper Scan Limit Set

For test purposes the scan limit is defined as being the angle determined by the voltage output of the D/A converter for the command word when the latter voltage is at its maximum positive value. The maximum angle is given by:

$$\theta_{max} = 10.24 \ V_{max} \ \text{(degrees)} \qquad (A.1)$$

The value of θ_{max} as determined by (A.1) shall be functionally related to the angle set on the upper thumbwheel in accordance with Table A-1. Table A-1 gives the effect of the 5 bit truncation used in the comparator.

A.1.1.2 Automatic Mode — Lower Scan Limit Set

For test purposes the scan limit is defined as being the angle determined by the voltage output of the command word D/A converter when the latter is at its minimum value. The minimum angle is given by

$$\theta_{max} = 10.24 \ V_{min} \ \text{(degrees)} \qquad (A.2)$$

The value at θ_{min} is given by (A.2) and shall be functionally related to the lower limit thumbwheel setting as given in Table A-2.

Table A-1
ELEVATION SCAN UPPER LIMIT

Actual Scan Upper Limit (Digital)	Angle Value (θ_{max})	Thumbwheel Setting (Upper Limit)	
10010	57.6	59, 58	Note 1
10001	54.4	57, 56, 55	
10000	51.2	54, 53, 52	
01111	48.0	51, 50, 49, 48	
01110	44.8	47, 46, 45	
01101	41.6	44, 43, 42	
01100	38.4	41, 40, 39	
01011	35.2	38, 37, 36	
01010	32.0	35, 34, 33, 32	
01001	28.8	31, 30, 29	
01000	25.6	28, 27, 26	
00111	22.4	25, 24, 23	
00110	19.2	22, 21, 20	
00101	16.0	19, 18, 17, 16	
00100	12.8	15, 14, 13	
00011	9.6	12, 11, 10	Note 2

Note 1: Mechanical stops limit thumbwheel to 59 deg maximum

Note 2: Mechanical stops limit thumbwheel to 10 deg minimum

Table A-2
ELEVATION SCAN LOWER LIMIT

Actual Scan Lower Limit (Digital)	θ_{max}	Thumbwheel Setting (Lower Limit)	
01111	51.175	49, 48	Note 1
01110	47.975	47, 46, 45	
01101	44.775	44, 43, 42	
01100	41.575	41, 40, 39	
01011	38.375	38, 37, 36	
01010	35.175	35, 34, 33, 32	
01001	31.975	31, 30, 29	
01000	28.775	28, 27, 26	
00111	25.575	25, 24, 23	
00110	22.375	22, 21, 20	
00101	19.175	19, 18, 17, 16	
00100	15.975	15, 14, 13	
00011	12.775	12, 11, 10	
00010	9.575	9, 8, 7	
00001	6.375	6, 5, 4	
00000	3.175	3 or smaller	

Note 1: Table applies so long as the difference between upper and lower limits on the thumbwheel is at least 10 deg; if not, then $\theta_{LL} = \theta_{UL} - 9.6$ which is accomplished automatically.

A.1.1.3   Limit Tests and Procedure — Automatic Mode

<u>Test E-1</u>

The output at the command word D/A converter shall be connected to a calibrated strip chart recorder with a convenient scale factor. The control settings should be as follows:

    a.   Mode — automatic

    b.   Frequency — 0.1 Hz

    c.   Lower limit — 0 deg

Starting at 10 deg, the upper limit shall be increased manually by 1 deg at the completion of at least one complete scan cycle. The values of θ_{max} as read from the recorded data (using Eq. (A.1)) shall conform to Table A-1 within ±2 deg.

<u>Test E-2</u>

Using the same test set-up, the controls should be set as follows:

    a.   Mode — automatic, normal

    b.   Frequency — 0.1 Hz

    c.   Upper limit 59 deg

Starting at 0 deg, the lower limit should be increased manually by 1 deg at the completion of at least one scan cycle. The values of θ_{min} should conform to Table A-2 within ±2 deg. (Note: the difference between upper and lower limits should not be made less than 10 deg.)

Test E-3 — Scan Frequency

For each of the conditions given in Table A-3 below, manually program the scan frequency through the five available values, and determine the scan frequency from the strip chart recording, using time calibration marks or known chart speed. The frequency should correspond to the dial setting to within ±10 percent.

Table A-3

Test Condition	Upper Limit (deg)	Lower Limit (deg)	Span (deg)	Center (deg)
1	59	44	15	51.5
2	39	24	15	31.5
3	19	4	15	11.5
4	59	29	30	44.0
5	34	4	30	19.0
6	59	9	30	20.0

Test E-4 — Crossover

    a. Control settings: automatic, manual

    b. Frequency: 0.1 Hz

With the same test set-up, set the upper limit successively to 20, 40, and 59 deg. At each setting, move the lower limit toward the upper limit; the lower limit on the thumbwheel should be automatically replaced by $\theta_{UL} = 9.6$ deg whenever the difference is less than 10 deg.

A.1.2   Manual Mode

The command voltage should be recorder monitored as in the previous tests.

Test E-5

Depression of the up/down slewing switches should produce monotone variation of the command voltage between the limits of 89.6 and 3.2 deg in the selected direction. The indicated read-out angle should correspond to the chart recording to within ± 0.20 deg. The slew speeds should be 34 deg/sec and 3.4 deg/sec to within $\pm 10\%$.

Depression of the single increment button, when the speed setting is "fast," should enable single increments of no greater than 0.2 deg in either selected direction.

A.1.3 Sector Scan Mode

Tests of this mode shall employ the same recorder test set up as in the previous tests

    a. Mode — automatic, sector

    b. Frequency — 0.1 Hz

Test E-6

Press the "clear" button to index the control counters.

a. Depress the "span increase" lever for several seconds to move the counter control word to maximum.

b. Depress the "span diminish" lever for several seconds to run the span counter down to its automatic limit of 3.175 deg.

c. Depress the "center location" lever in the up and down directions: the upper and lower limits as observed on the recorder should move in unison (within ± 3.2 deg) maintaining a span of 6.4 deg.

d. With the center of the scan excursion stopped, depression of the span control in the selected direction should provide monotone expansion or contraction of the scan excursion about the original center angle.

e. The span should be capable of expansion to +30 deg maximum and the center should be capable of excursion from 10 to 50 deg. The upper limit should be automatically restrained from falling below 3.2 deg (these will inhibit symmetry of the scan limits about the center line under the appropriate circumstances).

A.2 RANGE

The definitions and tests for range are identical to those for elevation, with the following exceptions.

a. Range values correspond to ten times the counterparts in angle.

b. Tests specifying 0.1 Hz scan frequency for θ should be run at 1 Hz for range. Due to the higher speeds, changes in limit settings should be made every 5 seconds rather than once per cycle.

c. The frequency tests of test E-3 should be run at 0.1, 1, 2, 3, 4 and 5 Hz.

A.3 SERVO PERFORMANCE

A.3.1 Elevation Servo

A.3.1.1 Static Accuracy — Manual Mode

Test E-7

With the elevation system in the manual mode, the angle shall be slewed manually in 5-deg increments from 5 to 55 deg, as indicated on the LED read-outs, and returned down through the same values. The angle indicated on the vernier dial should correspond to the LED reading to +0.2%.

A.3.1.2 Dynamic Response — Automatic Mode

At the highest scan rate (0.5 Hz) and maximum excursion ($\approx$ 55 deg) the phase shift between driving sawtooth command and mirror motion should not exceed 20 deg. The scan excursion should be within 5 deg of the command angle at both turn-around points. The period during which the scan velocity falls in absolute value to less than 75% of the command velocity shall not occupy more than 10% of the scan period.

These values shall be determined by the strip chart recording of the command voltage and feedback pot voltage after the latter has been aligned and the gains and offsets adjusted.

A.3.2   Range Servo

A.3.2.1   Static Accuracy

Since the actual location of the focus (point of maximum intensity of the illumination) is not observable within the control system, static accuracy tests should encompass at least one determination of the correspondence be-tween the secondary mirror position and the location of the actual physical focus, using the following technique.

Test R-8

a. A Doppler wheel target shall be setup externally at range R_i; the range servo shall be manually set to give an LED readout corresponding to R_i, and, with the loop closed and elevation angle correctly aimed, the secondary mirror platform position is adjusted to give maximum voltage from a fixed I.F. bandwidth (non-scanning) spectrum analyzer signal power output terminal.

b. The target is moved to range R_2 and the spectrum analyzer output is again maximized by manually slewing the range to whatever new value is required to accomplish this. Both the LED readout and the optical encoder D/A converter voltage output correspond-ing to this maximum should be recorded. The latter value (after multiplication by the scale factor relating encoder angle to mirror translation) is to be taken as the mirror position that the positions should satisfy.

$$(d_1 - d_2) = F^2 \left(\frac{1}{R_1} - \frac{1}{R_2}\right)$$

where

$$d_i = \text{mirror position}$$
$$F = \text{system focal length}$$
$$R = \text{target range}$$

For this test, $R_1 = 100$ meters, $R_2 = 200$ meters.

Test R-9

The output of the optical encoder D/A converter (which measures the secondary mirror position) shall be measured with a precision digital voltmeter while the range is slewed to successive positions 50 meters apart, from 50 meters to 550 meters, and back to 50 meters stopping at the same values and maintaining monotone directional sense. The range values are those indicated by the LED range readouts. After conversion by the scale factor, the mirror position values should satisfy.

$$d_i = F^2/R_i$$

(within an additive constant) to within 1% of the corresponding values based on the R_i observed on the LED. At each position of static range, the reconstructed range voltage shall also be measured, and after scale factor conversion, this should be within 1% of the command range.

A.3.2.2   Dynamic Performance

Test R-10

The command range input voltage and D/A (mirror position) voltage shall be simultaneously recorded on strip chart. The excursion shall be set to span 6.4 to 480 meters. A run shall be made at 0.1 Hz scan frequency for comparison purposes. When the scan frequency is increased to 5 Hz, the phase shift (between input sawtooth minima and mirror position maxima) shall not exceed 10 deg, and the excursion shall not depart from the low frequencies by more than 5%.